

**MARINE GEOPHYSICAL STUDIES
OVER A PART OF THE
CENTRAL INDIAN BASIN, INDIAN OCEAN**

**SUBMITTED TO THE GOA UNIVERSITY
FOR THE DEGREE OF
DOCTOR OF PHILOSOPHY**

BY

**KATTOJU ATCHUTA KAMESH RAJU
*NATIONAL INSTITUTE OF OCEANOGRAPHY***

RESEARCH GUIDE

MR. R. R. NAIR

DEPUTY DIRECTOR AND HEAD,

GEOLOGICAL OCEANOGRAPHY DIVISION

574.467

RAJ/MAR

T-063

**NATIONAL INSTITUTE OF OCEANOGRAPHY
DONA PAULA, GOA - 403 004, INDIA.**

SEPTEMBER 1993



~~T-88~~

**MARINE GEOPHYSICAL STUDIES
OVER A PART OF THE
CENTRAL INDIAN BASIN, INDIAN OCEAN**

**SUBMITTED TO THE GOA UNIVERSITY
FOR THE DEGREE OF
DOCTOR OF PHILOSOPHY**

BY

**KATTOJU ATCHUTA KAMESH RAJU
NATIONAL INSTITUTE OF OCEANOGRAPHY**

RESEARCH GUIDE

MR. R. R. NAIR

DEPUTY DIRECTOR AND HEAD,
GEOLOGICAL OCEANOGRAPHY DIVISION

**NATIONAL INSTITUTE OF OCEANOGRAPHY
DONA PAULA, GOA - 403 004, INDIA.**

SEPTEMBER 1993

574.467

RAJ/MAR

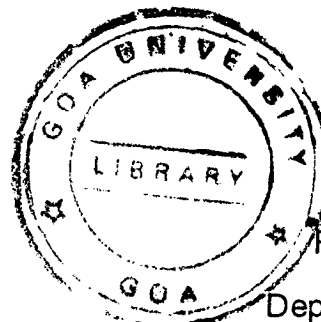
T-063

~~F-86~~



CERTIFICATE

Mr. K.A. Kamesh Raju has been working under my guidance since 1991. The Ph.D. thesis entitled '*Marine geophysical studies over a part of the Central Indian Basin, Indian Ocean*', submitted by him contains the results of his original investigation of the subject. This is to certify that the thesis has not been the basis for the award of any other research degree or diploma of other University.



(*R. R. Nair*)

Research Guide

Deputy director and
Head, Geological Oceanography Division
National Institute of Oceanography

DONAPAULA, GOA-403004

CONTENTS

Page No.

Acknowledgements	
List of Figures	
List of Tables	
Statement	
CHAPTER I. GENERAL BACKGROUND	1-22
1.1 Introduction	1
1.2 The Indian Ocean	3
1.3 The Mid-Ocean Ridge System	4
1.3.1 The Carlsberg Ridge	6
1.3.2 The Central Indian Ridge	7
1.3.3 The Southeast Indian Ridge	9
1.3.4 The Southwest Indian Ridge	10
1.3.5 The Indian Ocean Triple Junction	12
1.4 The Ocean Basins	13
1.4.1 The Central Indian Basin	14
1.5 Fracture Zones	16
1.6 Study Area and Objectives of the present investigations	18
CHAPTER II. MARINE GEOPHYSICAL INVESTIGATIONS	23-45
2.1 Introduction	23
2.2 Details of the Equipment used for data acquisition	24
2.2.1 Position Fixing	24
2.2.2 Echosounding	29
2.2.3 Proton precession Marine Magnetometer	30
2.2.4 Marine Gravimeter	33

	Page No.
2.3 The Multibeam Sonar Investigations	35
2.3.1 The Hydrosweep System	37
2.4 Layout of the Cruise Tracks	40
CHAPTER III. DATA PROCESSING	46-58
3.1 Introduction	46
3.2 Underway Data Processing	48
3.2.1 Processing of data acquired in analog mode	48
3.2.2 Processing of data acquired in digital mode	51
3.3 Processing of Hydrosweep data	54
CHAPTER IV. INTERPRETATION OF MARINE MAGNETIC ANOMALIES	59-109
4.1 Introduction	59
4.2 Geomagnetic Polarity Time Scale	62
4.2.1 Selection of Geomagnetic polarity time scale for the model studies	66
4.3 Model Studies: Marine magnetic anomalies	71
4.3.1 Factors influencing the marine magnetic anomalies	71
4.3.2 Description of the observed magnetic anomalies and bathymetry. Identification of marine magnetic anomalies	78
4.4 Delineation of tectonic features from the magnetic anomaly identifications and bottom topography	99
4.4.1 Stacked magnetic anomalies	99
4.4.2 Bottom topography	103
4.5 Summary	108

	Page No.
CHAPTER V. MULTIBEAM BATHYMETRY AND FREE-AIR GRAVITY OBSERVATIONS IN THE VICINITY OF 79°E FRACTURE ZONE	110-131
5.1 Introduction	110
5.2 Morphotectonic elements	116
5.3 Free-air gravity observations near 79°E fracture zone	128
5.4 Distribution of seamounts in the Central Indian Basin	129
CHAPTER VI. MODEL STUDIES: THERMAL STRUCTURE OF THE OCEANIC LITHOSPHERE AND FREE-AIR GRAVITY MODEL STUDIES AT 79°E FRACTURE ZONE	132-152
6.1 Thermal models of oceanic lithosphere	132
6.2 Thermal structure of the lithosphere at a fracture zone	136
6.2.1 Flexural response of the lithosphere	137
6.3 Computation of thermal structure at a fracture zone	141
6.3.1 Flexural rigidity	144
6.3.2 Density structure	145
6.4 Free-air gravity model studies	148
CHAPTER VII. DISCUSSION	153-188
7.1 Evolution of the Indian Ocean	153
7.1.1 Breakup of Gondwanaland (Late Jurassic to Late Cretaceous)	153
7.1.2 Late Cretaceous to Middle Eocene	154
7.1.3 Middle Eocene	158
7.1.4 Middle Eocene to Present	160
7.2 Evolution of the Central Indian Basin	161
7.2.1 Tectonic implications of magnetic lineations, spreading rates and fracture zones	161

	Page No.
7.2.2 Influence of Indian Ocean Triple Junction	170
7.3 Implications of Seamount distribution	174
7.4 Morphotectonics of the 79°E Fracture Zone	178
7.5 Factors influencing the evolution of morphotectonic features at a Fracture Zone	184
CHAPTER VIII.SUMMARY AND CONCLUSIONS	189-203
8.1 Summary	189
8.2 Conclusions	198
REFERENCES	204-221
PUBLICATIONS OF THE AUTHOR	222-224

DEDICATED TO
MY BELOVED PARENTS

ACKNOWLEDGEMENTS

I am indebted to my research guide *Mr. R.R. Nair*, Deputy Director, N.I.O., for his constant encouragement and thought provoking suggestions. I am grateful to him for providing me an opportunity to work with multibeam system. I am fortunate to have his guidance and support.

My gratitudes to *Dr. B.N. Desai*, Director, N.I.O., for permission and facilities extended to carry out this work. I record my gratitudes to late *Dr. H. N. Siddiquie*, former director of N.I.O., who has motivated me to pursue research in Marine Geophysics.

My friend and colleague *Mr. T. Ramprasad* has been a constant source of encouragement, I thank him for all the help, together we had many fruitful discussions. I gratefully acknowledge the friendly gestures of my colleagues in the *Polymetallic Nodules Project*. Special thanks to *Mr.M. Shyam Prasad*, *Dr. V. Purnachandra Rao*, *Mr. P.S. Rao*, *Dr. V.K. Banakar*, *Mr. M. Sudhakar*, *Mr. B. Nagender Nath* and *Dr.B. Chakraborty* for their encouragement, which helped in keeping my morale high. I am thankful to *Mr.B. Nagender Nath* for critically reading the first draft and for his valuable suggestions. I extend my sincere thanks to *Dr. V.N. Kodagali*, who gave some useful tips on the processing of *Hydrosweep* data and for helpful discussions.

I am thankful to colleagues in the Geophysics group. I am grateful for the suggestions and advices of *Dr. Gopala Rao, Mr. L.V. Subba Raju, Mr. G.C. Bhattacharya, Dr. M.V. Ramana and Dr. V.Subrahmanyam. Mr. K. Sreekrishna, Mr. A.K. Chaubey, Mr. G.P.S.N. Murthy and Dr. K.V.L.N. Sarma* are thanked for their suggestions. I am grateful to *Mr. G.C. Bhattacharya*, who introduced me to underway data processing techniques. My sincere thanks to *Prof. P. Rajendraprasad*, Department of Geophysics, Andhra University for his valuable suggestions.

I extend my thanks to *Mr. N. Prabhakaran, Mr. K. Sivakholondu* for their assistance in underway data processing. *Mr. K. Srinivas, Mr. B. R. Rao, Mr. S. Jaishankar* are thanked for their assistance. I am thankful to the staff of N.I.O. *Computer Center* for the system support during various stages of data processing.

I record my thanks to *Instrumentation group, Marine survey group and the Mechanical engineering groups* of the *Geological Oceanography Division*, for their support at sea during the data acquisition. I am thankful to *Dr. S.M. Karisiddaiah and Dr. A.B. Valsangkar* for their encouragement during the early scientific voyages of my career. I thank the *Hydrosweep* maintenance group, comprising of *Mr. G. Ranade, Dr. B. Chakraborty, Mr. Y.S.N. Raju and Mr. T. Sudhakar* for their excellent support during the acquisition of multibeam bathymetric data. *Mr. V.D. Khedekar and Mr. D. Pathak* are thanked for the instrumentation support during the acquisition of

gravity and magnetics data. The staff of G.O.D. office are thanked for their assistance from time to time.

I thank *Mr. Ravindranath Uchil* for neatly drafting the illustrations with good care and patience.

This thesis would not have been completed but for the encouragement from my parents and enduring support of my wife *Vani*. I record my appreciation to my wife and son *Siddharth* for tolerating my absence at home for long hours.

LIST OF FIGURES

Page No.

- Figure 1.1** Physiographic map of the Indian Ocean with 1000 and 4000m bathymetric contours, depicting the major topographic provinces. The study area is indicated by hatched box. 5
- Figure 1.2** Magnetic anomalies and fracture zones as delineated from the earlier studies (*Schlich*, 1982). The thin line with numbers indicate the magnetic anomalies, doubtful identifications are shown with dotted lines. Thick dots represent the location of the ODP sites and the triangles represent the DSDP sites. Bathymetric contours of 1000 and 4000 m are shown. The study area is marked. 17
- Figure 1.3** The study area (hatched box) with respect to the mid-ocean ridge system and magnetic anomalies (*Schlich*, 1982; *Munschy and Schlich*, 1989). The thick hatch within the box represents the area covered with multibeam bathymetry and gravity observations. Star symbol with number denotes the DSDP site locations. 21
- Figure 2.1** The 1,50,000 km² area in the Central Indian Basin, allocated to India for the exploration and exploitation of the Polymetallic Nodule resources, by the *PrepCom* of the *United Nations*. 25
- Figure 2.2** Schematic diagram showing the configuration of the *Integrated Navigation System (INS)*, onboard *ORV Sagar Kanya*. 28
- Figure 2.3** Photograph showing the *Geometrics G 801/3* proton precession marine magnetometer. The bottom part of the figure illustrates the schematics of various modules of the system. 31
- Figure 2.4** Photograph showing the *Bodenseewerk KSS 30* marine gravimeter and the sensor mounted on gyro-stabilized platform. The bottom part of the figure shows the principal elements within the sensor. 34
- Figure 2.5** Schematic diagram showing various modules of the *Hydrosweep system*. 38

	Page No.
Figure 2.6 Swath coverage during the survey and calibration modes. The principle of calibration illustrated.	41
Figure 2.7 Cruise tracks are shown with dotted lines along which total magnetic intensity and bathymetric data were collected. The hatched box shows the area covered by multibeam sonar investigations. The 3000, 4000 and 5000 bathymetric contours are from the <i>Hydrographic chart</i> .	43
Figure 2.8 The cruise tracks at 5 mile interval along which multibeam bathymetric and gravity data were collected.	44
Figure 2.9 Swath coverage map. The swath coverage along the survey tracks is indicated by horizontal line segments.	45
Figure 3.1 Schematic illustration of the data processing scheme followed for the processing of underway data collected in analog form.	47
Figure 3.2 Processing sequence followed to process the <i>Hydrosweep</i> data.	55
Figure 4.1 Conceptual model of the seafloor spreading process. Symmetric bands of normally and reversely magnetized blocks would be produced due to the combined effect of earth's magnetic field reversals and the seafloor spreading process.	61
Figure 4.2 The geomagnetic polarity time scales of Cox (1969), <i>Heirtzler et al.</i> (1968), <i>LaBrecque et al.</i> (1977) and <i>Berggren et al.</i> (1985). The blocks indicate normal polarity events, anomaly numbers are shown.	67
Figure 4.3 Synthetic magnetic anomalies generated by varying the thickness of the assumed blocks of the model. A constant susceptibility of 0.01 cgs units is used.	73
Figure 4.4 Synthetic magnetic anomalies generated by varying the susceptibility of the model blocks. The thickness of the blocks is kept constant at 500m.	74
Figure 4.5 Synthetic magnetic anomalies as observed at various latitudes (see text for explanation). Note that the positively magnetized blocks give rise to negative anomalies when observed in the northern hemisphere.	77

- Figure 4.6** The synthetic anomalies generated by assuming the ridge axis to be at 35°S. Susceptibility of the model blocks is assumed to be 0.01 cgs units and the thickness of the block is kept at 500m (*McKenzie and Sclater, 1971; Talwani et al., 1971*). A variable spreading rate of 3.6 cm/yr between anomalies A21 and A23 and 8.0 cm/yr between anomalies A23 and A25 were inferred. *Berggren et al. (1985)* time scale was used to generate the synthetic anomalies. The observed magnetic anomaly profile *CB-1* and the bathymetry are shown. 79
- Figure 4.7** Observed magnetic anomaly and bathymetry along the profile *CB-2* along with the synthetic anomalies and the model. Model parameters are same as mentioned in figure 4.6. 81
- Figure 4.8** Observed magnetic anomaly and bathymetry along the profile *CB-3* along with the synthetic anomalies and the model. Model parameters are same as mentioned in figure 4.6. 82
- Figure 4.9** Observed magnetic anomaly and bathymetry along the profile *CB-4* along with the synthetic anomalies and the model. Model parameters are same as mentioned in figure 4.6. 83
- Figure 4.10** Observed magnetic anomaly and bathymetry along the profile *CB-5* along with the synthetic anomalies and the model. Model parameters are same as mentioned in figure 4.6. 85
- Figure 4.11** Observed magnetic anomaly and bathymetry along the profile *CB-6* along with the synthetic anomalies and the model. Model parameters are same as mentioned in figure 4.6. 86
- Figure 4.12** Observed magnetic anomaly and bathymetry along the profile *CB-7* along with the synthetic anomalies and the model. Model parameters are same as mentioned in figure 4.6. 87
- Figure 4.13** Observed magnetic anomaly and bathymetry along the profile *CB-8* along with the synthetic anomalies and the model. Model parameters are same as mentioned in figure 4.6. 89

- Figure 4.14** Observed magnetic anomaly and bathymetry along the profile *CB-9* along with the synthetic anomalies and the model. Model parameters are same as mentioned in figure 4.6. 90
- Figure 4.15** Observed magnetic anomaly and bathymetry along the profile *CB-10* along with the synthetic anomalies and the model. Model parameters are same as mentioned in figure 4.6. 91
- Figure 4.16** Observed magnetic anomaly and bathymetry along the profile *CB-11* along with the synthetic anomalies and the model. Model parameters are same as mentioned in figure 4.6.. 93
- Figure 4.17** Observed magnetic anomaly and bathymetry along the profile *CB-12* along with the synthetic anomalies and the model. Model parameters are same as mentioned in figure 4.6. 94
- Figure 4.18** Observed magnetic anomaly and bathymetry along the profile *CB-13* along with the synthetic anomalies and the model. Model parameters are same as mentioned in figure 4.6. 95
- Figure 4.19** Observed magnetic anomaly and bathymetry along the profile *CB-14* along with the synthetic anomalies and the model. Model parameters are same as mentioned in figure 4.6. 97
- Figure 4.20** Observed magnetic anomaly and bathymetry along the profile *CB-15* along with the synthetic anomalies and the model. Model parameters are same as mentioned in figure 4.6. 98
- Figure 4.21** The observed magnetic anomalies stacked with respect to position. Synthetic anomalies and model are shown at the bottom. Identified magnetic anomalies are indicated with dashed line, inferred fracture zones are marked. 100
- Figure 4.22** Observed magnetic anomalies plotted perpendicular to the cruise tracks. The identified magnetic lineations and fracture zones are indicated. 101

	Page No.
Figure 4.23 Magnetic anomaly contour map depicting well defined near E-W lineations. Contour interval is 100 nT.	104
Figure 4.24 Bathymetric profiles stacked with respect to position.	105
Figure 4.25 Bathymetric contour map. Contour interval 100 m.	106
Figure 5.1 Colour coded bathymetric contour map generated by using multibeam sonar data. Contour interval 100 m, colour change at every 300 m.	111
Figure 5.2 Simplified bathymetric map of multibeam sonar data along with the magnetic anomaly markings. Contour interval 100 m.	112
Figure 5.3 Magnetic anomalies plotted perpendicular to the cruise tracks in the vicinity of 79°E fracture zone.	113
Figure 5.4 High resolution bathymetric map at 25 m contour interval, depicting prominent E-W bathymetric lineations and bending of these lineations into the fracture zone.	114
Figure 5.5 High resolution bathymetric map at 25 m contour interval, depicting steep gradient expression of the fracture zone.	115
Figure 5.6 Isometric view of a part of the 79°E fracture zone generated from the Hydrosweep data.	117
Figure 5.7 Multipeaked seamount. Contour interval 50 m.	118
Figure 5.8 Bathymetric profiles generated from the gridded depth data.	119
Figure 5.9 Free-air gravity and center beam depth along the tracks of multibeam sonar survey. See figure.2.8 for the location of the tracks.	122

- Figure 5.10** Map showing the distribution of seamounts in the Central Indian Basin. Open triangles represent the locations of the seamounts identified based on multibeam data and the solid dots from echosounding data. The inferred fracture zones are shown with dashed line. 131
- Figure 6.1** Schematic thermal models of the oceanic lithosphere. A) Boundary layer model. B) Constant plate model. (after *Sclater et al.*, 1980). T_M indicates the deep mantle temperature. The solid lines represent isothermal surfaces within the cooling lithosphere. 134
- Figure 6.2** Thermomechanical model of the oceanic lithosphere at a fracture zone (after *Sandwell*, 1984). 138
- Figure 6.3** Schematic illustration of the flexural response of the lithosphere at a fracture zone. Subsidence curves of the ridge segments are shown at the right. 140
- Figure 6.4** Computed isotherms at 79°E fracture zone. Stress relaxation temperature (T_E) 450°C and deep mantle temperature (T_M) 1365°C are considered. The bottom part of the figure shows the variation in flexural rigidity across the 79°E fracture zone. 147
- Figure 6.5** Free-air gravity model showing the lithospheric section at 79°E fracture zone. (a) The isotherms of T_E and T_M are shown. (b) Computed and observed free-air gravity along a profile AA-AA' (see figure 2.8). The bottom part of the figure shows the difference between the computed and observed free-air gravity for different assumed thicknesses of the lithosphere. 150
- Figure 7.1** (a) Initial position of the southern continents before breakup (b) Reconstructed positions of the continents during Early Cretaceous (after *Norton and Sclater*, 1979). 155
- Figure 7.2** Reconstruction during Late Cretaceous (80 Ma) (after *Norton and Sclater*, 1979). 157
- Figure 7.3** (a) Early Paleocene (65 Ma) reconstruction indicating the separation of Seychelles from India. (b) Reconstructed positions during Early Eocene (53 Ma) (after *Norton and Sclater*, 1979). 159

	Page No.
Figure 7.4 Reconstructed positions during (a) Early Oligocene (38 Ma) and (b) Present day positions (after <i>Norton and Sclater, 1979</i>).	162
Figure 7.5 Paleoposition of the Southeast Indian Ridge during a) Eocene b) Oligocene and c) Present (<i>Fisher et al., 1971</i>).	164
Figure 7.6 The Indian plate movement during the geological past. The magnetic anomalies corresponding to various stages are marked (<i>Patriat and Acha�che, 1984</i>).	165
Figure 7.7 The computed spreading direction and spreading rates with respect to Central Indian, Southeast Indian and Southwest Indian Ridges (<i>Patriat and Segoufin, 1988</i>). The inferred spreading rates in the present study are shown with small dashed line. Note the sudden decrease in spreading rate around anomaly 23.	169
Figure 7.8 The identified magnetic lineations and fracture zones during the present study. The triple junction trace as delineated by <i>Sclater et al. (1982)</i> and the fracture zone trends on Southeast Indian Ridge (<i>Royer and Schlich, 1988</i>) are shown.	173
Figure 7.9 Summary tectonic map showing the results from the present study with magnetic lineations, fracture zones and seamount locations along with results from other studies. The magnetic lineations along SEIR are from <i>Royer and Schlich (1988)</i> . The inset shows the traces of the Reunion and Kerguelen hot spot traces in the Indian Ocean (after <i>Duncan and Richards, 1991</i>).	175
Figure 7.10 Summary tectonic map of the area encompassing the 79 ^o E fracture zone. Bathymetric lineations as delineated from the multibeam bathymetric study, the identified magnetic anomalies (numbered solid lines), the fossil transform tectonized zone (stippled area) and the location of seamounts (solid dots) are shown.	180
Figure 7.11 (a) The proposed model: summary of factors influencing the morphotectonics at a fracture zone.	187
Figure 7.11 (b) Schematic illustration of the evolution of the fracture zone.	188

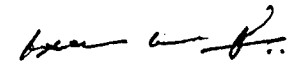
LIST OF TABLES

	Page No.
Table T4.1 Geomagnetic polarity reversal time scale for the Cenozoic and Late Cretaceous (<i>Hirtzler et al.</i> , 1968)	68
Table T4.2 Geomagnetic polarity reversal time scale for the Cenozoic and Late Cretaceous (<i>LaBrecque et al.</i> , 1977)	69
Table T4.3 Geomagnetic polarity reversal time scale for the Cenozoic and Late Cretaceous (<i>Berggren et al.</i> , 1985)	70
Table T6.1 Physical constants and model parameters used in thermal model studies.	146

STATEMENT

As required under the University ordinance 19.8, I state that the present thesis entitled '*Marine geophysical studies over a part of the Central Indian Basin, Indian Ocean*', is my original contribution. To the best of my knowledge, the present study is the first comprehensive study of its kind from the area mentioned.

The literature concerning the thesis has been cited. Due acknowledgements have been made wherever facilities have been availed of.



(K. A. Kamesh Raju)

CHAPTER I

GENERAL BACKGROUND

CHAPTER I

GENERAL BACKGROUND

1.1 INTRODUCTION

Early attempts to synthesize geological history of the earth were severely handicapped by the complete absence of information about the nature of the seafloor. During the early stages, towards the beginning of the 20th century, the oceans were believed as the sunken continents, differing only in their elevation. Based on the available few marine gravity observations, *Alfred Wegener* (1929) (well known for his theory of drifting continents, 1912), suggested that the ocean crust to be qualitatively different from that of continents. This question persisted till 1950's, until it was conclusively demonstrated by the geological and geophysical observations at sea that the ocean crust was very much different from the continental crust. The *International Geophysical Year* (IGY), 1958-1959, was the first major program which realized the need for the studies of the oceans and incorporated research programs dealing with oceans. The initial major efforts have resulted in the mapping of the ocean floor and the realization of the world encircling mid-ocean ridge system (*Heezen and Tharp, 1965*).

The knowledge of the mid-ocean ridge system and the perception that the oceanic crust is generated at these active ridges, coupled with the observation of linear magnetic patterns across the ridges resulted in the

formulation of *Plate Tectonics* theory. The theory of plate tectonics is a synthesis of the Alfred Wegener's *Continental drift* and the ideas of *Seafloor spreading* (Dietz, 1961; Hess, 1962). The most definitive evidence for the seafloor spreading came from the observations of magnetic lineations that characterize the ocean floor. *Vine and Matthews* (1963), envisaged a simple model consisting of crustal blocks, magnetized alternatively in the normal and reverse directions of the earth's magnetic field to explain the linear magnetic anomalies. They proposed that the oceanic crust created by the emplacement of upcoming magma at the axial rift zone of the mid ocean ridges, acquires the direction of the earth's magnetic field prevailed at that time as it cools through the Curie temperature. The fresh injections of magma splits the existing block and forces it apart. As the earth's magnetic field is reversed periodically crustal blocks of alternating polarity are generated. According to the plate tectonic theory, the earth's lithosphere, the outer 100-250 km layer, breaks up into a set of rigid plates that move with respect to each other and these lithospheric plates drift over the underlying less rigid asthenosphere. The lithospheric plates are created at the mid-ocean ridges from the ascending magma and are consumed at the trenches by the processes of subduction. The plate tectonic model revolutionized the geological thinking and offered explanation to many geological and geophysical observations. Studies that are made in the world oceans applied the plate tectonic model to understand their evolution. These studies involving the geophysical measurements, sediment coring, dredging, deep-sea drilling and underwater photography have resulted in the broad

reconnaissance knowledge of the development of the major ocean basins. The following sections briefly describe the geophysical investigations that were carried out in the Indian Ocean.

1.2 THE INDIAN OCEAN

Indian Ocean the third largest of the world oceans lies in the southern part of the Asia, between Africa and Australia, and extends up to Antarctica in the south. It is estimated to have a total area of about 74 million square kilometers.

The *International Indian Ocean Expedition* (IIOE) sponsored by the special committee on Ocean Research which was officially designated between 1959 and 1966, marked the beginning of systematic geological and geophysical investigations in the Indian Ocean. Before IIOE, the only major geological and geophysical studies resulted from the expeditions of *Dana* (1928-1930), *Snellius* (1929-1930), *Mabahiss* (1933-1934), *Challenger* (1949-1950), *Albatros* (1950-1952), and *Ob* (1955-1957). The major contributions from these studies came from *Wiseman and Seymour-Sewell* (1937) on the Arabian Sea, and *Fairbridge* (1948 and 1955) on the southeastern Indian Ocean. *Gutenberg and Richter* (1954), tabulated and interpreted earthquake data. The IIOE has prompted many analyses of the data. Primarily based on the study of the earthquake epicenters derived from the U.S. Coast and Geodetic Survey between 1963 and 1968 and the results

from the IIOE cruises, major physiographic features of the Indian Ocean are outlined (*Heezen and Tharp, 1965; Udintsev, 1965; Kanaev, 1967*). The outstanding contribution by *Heezen and Tharp (1965)* and the later compilations by *Udintsev, (1975)* defined major physiographic regions.

These studies have revealed the complexity of the Indian Ocean, with several features such as the micro continents and N-S trending ridge systems. The most prominent of these features are the Ninetyeast Ridge, the Chagos-Laccadive ridge, the Seychelles bank which is attached to the Mascarene plateau, the Madagascar and Mozambique ridges, the Agulhas plateau, the Crozet plateau, the Kerguelen-Heard plateau and to the south Ob, Lena and Marion Dufresne seamounts (*Laughton et al., 1970*). Many of these features trend in a north-south direction and together with the active ridges and surrounding continents, demarcate the Indian Ocean into number of ocean basins (Figure.1.1).

1.3 THE MID-OCEAN RIDGE SYSTEM

The world wide studies of morphology and seismicity of the ocean floor revealed the wide extent and continuity of the mid-ocean ridge, an active geotectonic feature of global significance. The mid-ocean ridge system, about 70,000 km long world encircling belt, passes through the Atlantic, Indian and Pacific oceans. The structure and origin of the mid-ocean ridge

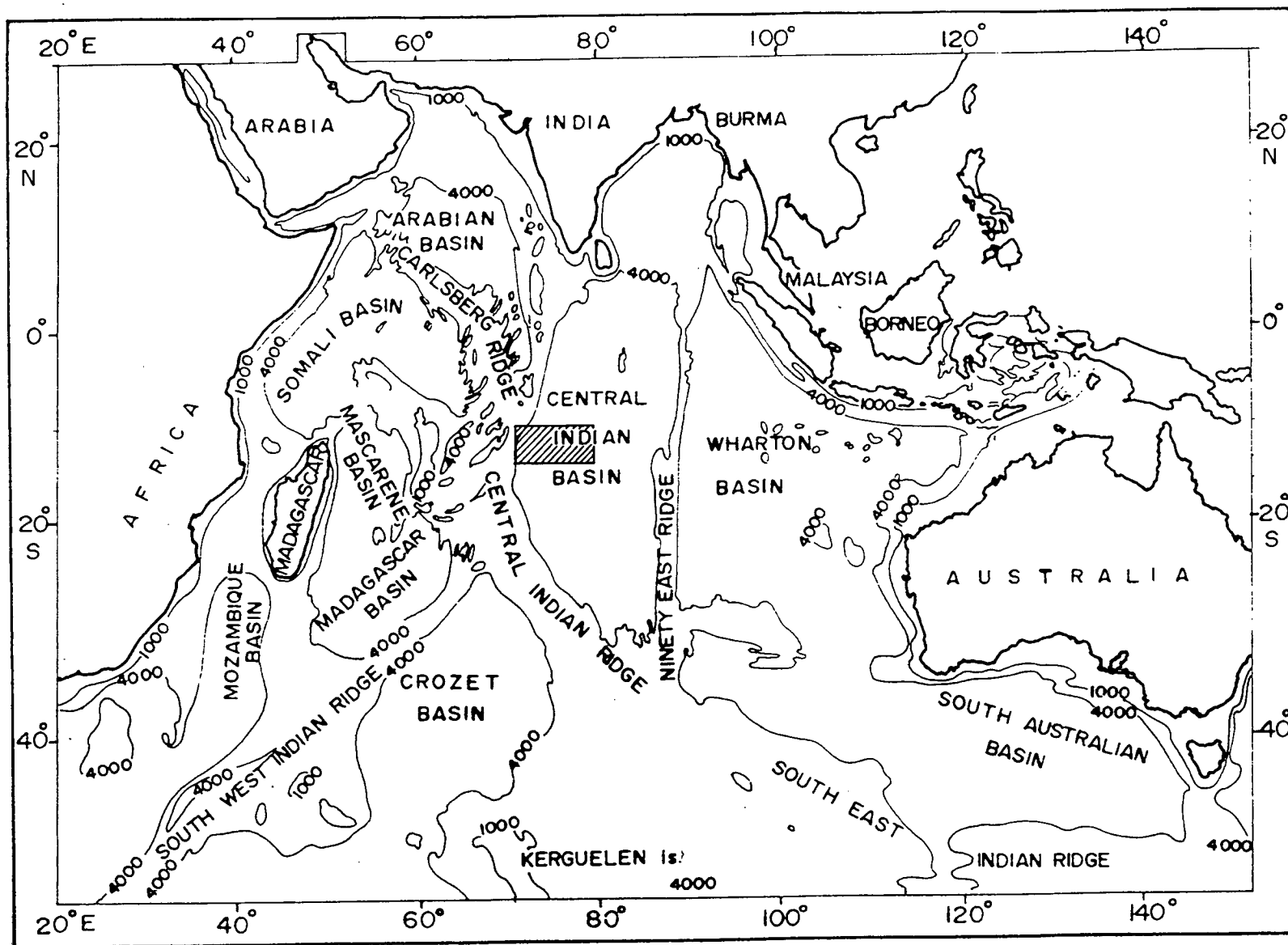


Figure 1.1 Physiographic map of the Indian Ocean with 1000 and 4000 m bathymetric contours, depicting the major topographic provinces. The study area is indicated by hatched box.

system is fundamental to the understanding of the origin of oceans and control the tectonics of the individual ocean basins.

The existence of a mid-ocean ridge in the Indian Ocean was first postulated by *Schmidt* (1932), following the expedition of *Dana* in the Arabian Sea. The name Carlsberg Ridge was given to the northwestern part of it. Subsequent observations by *Farquharson* (1935), *Wiseman and Seymour-Sewell* (1937) confirmed the presence of the ridge.

Seismically active mid-ocean ridge system in the Indian Ocean consists of the Sheba Ridge in the Gulf of Aden, Carlsberg Ridge in the Arabian Sea, the Central Indian Ridge between equator and 20°S, the Southeast Indian Ridge that joins the Pacific-Antarctic ridge in the southeast and the Southwest Indian Ridge that branches to southwest from the Rodriguez island and joins the Bouvet triple junction in the Atlantic. The following sections briefly describe the mid-ocean ridges in the Indian Ocean, in the light of the marine geophysical studies.

1.3.1 THE CARLSBERG RIDGE

The Carlsberg Ridge trends northwest-southeast between the Owen fracture zone and the equator across the middle of the Arabian Sea. The Sheba Ridge and the Carlsberg Ridge are offset by about 300 km at the Owen fracture zone (*Matthews*, 1963; 1966). Carlsberg Ridge was studied in

some detail by *Matthews et al.*(1965), *Cann and Vine* (1966), *Vine* (1966), *Le Pichon and Heirtzler* (1968), *Fisher et al.*(1968) and *McKenzie and Sclater* (1971). Besides the major Owen fracture zone there are small fractures zones in the central region of the ridge and some major faults at the southern end of the ridge. *Le Pichon and Heirtzler* (1968) and *McKenzie and Sclater* (1971) attributed a spreading rate of 1.2 to 1.3 cm/yr based on the axial magnetic anomalies.

Anomalies 6 and 7, followed by a magnetic quiet zone on either side were identified across the Carlsberg Ridge (*Tisseau*, 1978). *McKenzie and Sclater* (1971) recognised complete sequence of Paleocene and Late Cretaceous magnetic anomalies (A20 to A28) in the Arabian Sea. The strike of these lineations are 90°E and differ significantly with the present trend of the Carlsberg Ridge. The older anomalies (A20 to A28) were suggested to have formed due to the symmetric spreading between India and Seychelles (*Schlich*, 1982). *Le Pichon and Heirtzler* (1968) and *McKenzie and Sclater* (1971) considered the absence of the anomalies (A8 to A20) due to very slow spreading or a complete halt of spreading from Eocene to Miocene times.

1.3.2 THE CENTRAL INDIAN RIDGE

The Central Indian Ridge broadly follows north-south trend extending from the equator at the southern end of the Carlsberg Ridge to the Indian

Ocean Triple Junction near latitude 25.5°S and longitude 70°E . *Langseth and Taylor* (1967) and *Fisher et al.* (1967, 1968, and 1971), have shown that the Central Indian Ridge is dominated by numerous northeast-southwest trending transform faults. The direction of these transform faults change from 35°E at equator to 60°E at 20°S latitude (*Fisher et al.*, 1971). The most conspicuous transform faults correspond to the Vema Trench at about 9°S latitude (*Heezen and Nafe*, 1964) which displaces the ridge axis by about 200 km and the Argo transform fault at 14°S latitude with a smaller offset. In the southern part of the ridge system at about 18°S latitude, Marie Celeste transform fault displaces the ridge axis by about 220 km (*Engel and Fisher*, 1969, 1975). The studies carried out by *Chaubey et al.* (1990) at the southern end of the Central Indian Ridge, revealed northwest-southeast trending median valley and a new transform fault around 21°S latitude.

Magnetic anomalies up to 5 have been identified on both sides of the ridge and the spreading rate computed from these identifications varies from north to south between 1.8 cm/yr to 2.4 cm/yr (*Fisher, et al.*, 1971). The fracture zones which offset the ridge axis extend beyond the anomaly 5 and ⁰about the Chagos-Laccadive Ridge in the northeast and the Mascarene Plateau in the southwest (*Fisher et al.*, 1971). The striking similarities between the Chagos-Laccadive Ridge and the Mascarene Plateau which are symmetrically displaced on either side of the Central Indian Ridge, lead to the suggestion that they were formed at the same time during the beginning of the present spreading episode (*Fisher et al.*, 1971). *McKenzie and Sclater*

(1971) suggested that the Chagos-Laccadive Ridge and the Mascarene Plateau are the result of intense volcanism in the region, during Eocene and Early Miocene, when there was a slowdown or even complete halt of spreading. Prior to this volcanic activity, the Chagos-Laccadive Ridge and the Mascarene Plateau were part of a major transform fault offsetting the Paleocene and Late Cretaceous magnetic anomaly patterns in the Arabian Sea and the Central Indian Basin.

The anomaly 6 (20 Ma), 8 (29 Ma) and possibly 13 (37 Ma), related to the Central Indian Ridge were recognized by *Schlich* (1982). The Deep Sea Drilling Project (DSDP) site 238, located at the extreme end of the Argo fracture zone, beyond anomaly 9 (30 Ma), yielded an age of middle Oligocene (31 Ma) for the sediment at the basalt contact (*Schlich*, 1982).

1.3.3 THE SOUTHEAST INDIAN RIDGE

The Southeast Indian Ridge from the Indian Ocean Triple Junction to about 100°E longitude, has been an active spreading ridge with the spreading direction trending northeast-southwest for the last 45 Ma (*Schlich and Patriat*, 1967, 1971; *Le Pichon and Heirtzler*, 1968). The axial magnetic anomaly has been clearly identified and is offset by several transform faults running in a northeast-southwest direction.

Major transform faults with large offsets are located in the vicinity of Amsterdam and Saint Paul islands. *Schlich and Patriat* (1971) observed several small changes in the spreading rate accompanied by minor spreading direction changes from the studies made in the Crozet Basin between anomalies 1 and 11 (35 Ma). Two distinct major spreading rates are identified between 0 and 40 Ma with a rate of 3.4 cm/yr for anomalies 1 to 5 (10 Ma) and 2.5 cm/yr for anomalies 5 and 17 (40 Ma) (*Le Pichon and Heirtzler*, 1968; *Schlich and Patriat*, 1971; *Schlich*, 1975). The later studies have identified older anomalies between 5 and 22 (*Sclater and Fisher* 1974; *Sclater et al.*, 1976; *Schlich*, 1982). The identified younger magnetic lineations trend at about 135°E (NW-SE), beyond anomaly 15 the trend changes to 100°E (near E-W). The change in the trend of the magnetic lineations has been attributed a major spreading direction change of the Southeast Indian Ridge during early to middle Eocene period (*Schlich*, 1975, 1982). The studies carried out by *Royer and Schlich* (1988) over a segment of the ridge, between the Indian Ocean Triple Junction and the Amsterdam and Saint Paul islands indicated that the spreading along the ridge is essentially asymmetric since Miocene, resulting in a regional migration of the ridge axis towards north.

1.3.4 THE SOUTHWEST INDIAN RIDGE

The existence of the Southwest Indian Ridge was first suggested by *Rothe* (1954), from the distribution of earthquake epicenters. The subsequent

studies by *Ewing and Heezen* (1960) confirmed its presence. The ridge trending northeast-southwest is characterized by extremely rugged topography with relief in excess of 4000 m and is offset by numerous north-south trending fracture zones. The magnetic signature associated with the Southwest Indian Ridge has a very low relief and the axial anomaly is not very conspicuous. These observations are interpreted as due to the complex faulting along this ridge coupled with very slow spreading rates of the order of 0.8 to 1.3 cm/yr (*Vine*, 1966; *Le Pichon and Heirtzler*, 1968; *Ewing et al.*, 1969). *Schlich and Patriat* (1968) suggested north-south spreading across the Southwest Indian Ridge assuming an east-west trending ridge axis which split into short segments by numerous north-south trending transform faults. *Schlich and Patriat* (1971b) computed a spreading rate of 0.6 to 0.9 cm/yr based on axial magnetic anomalies observed between latitudes 25 °S and 45°S.

Recent studies on the Southwest Indian Ridge include the detailed investigations carried out by *Sclater et al.* (1976a), *Norton* (1976) and *Sclater et al.* (1978) in the vicinity of Bouvet Triple Junction; by *Bergh and Norton* (1976), north of Marion and Prince Edward islands between 35 °E and 42°E longitudes; by *Patriat* (1974), north of Crozet islands between longitudes 43°E and 53°E; by *Sclater et al.* (1981), between 54°E and 62°E longitudes and by *Tapscott et al.* (1980) in the vicinity of the Indian Ocean Triple Junction. These studies, besides reconciling the very slow spreading rates, have also indicated that the ridge is dominated by fracture zones which can

be traced over a distance as large as 2000 km from their active transform region. The trends of these fracture zones change progressively from northeast in the vicinity of Bouvet Triple Junction to north-south west of the Indian Ocean Triple Junction.

1.3.5 THE INDIAN OCEAN TRIPLE JUNCTION

The Indian Ocean Triple Junction, which is also known as the Rodriguez Triple Junction, the meeting point of the Central Indian Ridge, Southeast Indian Ridge, and the Southwest Indian Ridge is located at about 25.5°S and 75°E . Even though the existence of the triple junction was suggested along with the mid-ocean ridge system (*Heezen and Tharp, 1965; McKenzie and Sclater, 1971*), very few detailed studies have been carried out on the Indian Ocean Triple Junction. The major studies in the vicinity of the Indian Ocean Triple Junction are made by *Tapscott et al. (1980)*, *Sclater et al. (1981)* and *Fisher and Sclater (1983)*. *Tapscott et al. (1980)* have analyzed in detail the morphology and magnetic pattern of the triple junction and modelled the development of the triple junction in time. *Sclater et al. (1981)*, have presented the Eocene to Recent development of the Southwest Indian Ridge between 55°E longitude and the Indian Ocean Triple Junction. These studies have shown that the Southwest Indian Ridge has evolved as a consequence of the rapid eastward migration of the triple junction.

At the Indian Ocean Triple Junction, the Indian, African and Antarctic plates converge. *Sclater et al.* (1981) delineated the trace of the triple junction on the Indian, African and Antarctic plates. An RRR(ridge-ridge-ridge) configuration has been proposed on a regional scale for the evolution of the triple junction (*Tapscott et al.*,1980). *Patriat and Courtillot* (1984) suggested that the triple junction evolved in two preferred modes of 1 Ma duration. Based on the detailed Seabeam studies, *Munsch and Schlich* (1989) proposed ridge-ridge-transform fault (RRF) model for the evolution of the triple junction since last 1 Ma and suggested an RRR model at a regional scale (0-80 Ma). *Mitchell* (1991) used GLORIA images and explained the deeper Southwest Indian Ridge rift valley at the triple junction, in terms of distributed mechanical extension of the triple junction.

1.4 THE OCEAN BASINS

The major ocean basins in the Indian Ocean include, the Arabian sea and the Bay of Bengal in the north, the Somali basin in the southwest; to the east of Madagascar main land and the Madagascar ridge, the Mascarene and Madagascar basins. Further to the south and west, the Mozambique basin extend to the north as the Mozambique channel and to the south into Agulhas basin. To the east of the Chagos-Laccadive ridge, the Central Indian Basin and Wharton Basins are separated by the Ninetyeast ridge. In the south between Southwest Indian Ridge and Southeast Indian Ridge, the Crozet basin extends up to the African-Antarctic basin. The Wharton Basin is

bounded in the east by the Indonesian Island arc, which extends from Burma to the northwestern edge of the Australia. This major feature which correspond to the Sunda-Banda arc system represents a typical subduction zone separating the Indo-Australian plate from the Eurasian plate (Figure 1.1)

1.4.1 THE CENTRAL INDIAN BASIN

The Central Indian Basin extends from the Central Indian Ridge to the Ninetyeast Ridge bounded in the south by the Indian Ocean Triple Junction and the Southeast Indian Ridge. In the northeast, the basin merges with the Bay of Bengal. Bathymetric and magnetic data acquired by *Vema* (1963) and *Argo* (1968), together with the *Project Magnet* tracks were analyzed by *McKenzie and Sclater* (1971). They observed distinct magnetic anomalies on several north-south profiles and identified two fracture zones along 79 °E and 83°E longitudes between latitudes 2°S and 10°S. The trends of these fracture zones parallel the Ninetyeast Ridge and the identified magnetic anomalies strike 96°E with a spreading rate of about 8.0 cm/yr between anomalies 23 and 30, and 5.6 cm/yr between older anomalies 30 and 33. Later studies by *Sclater and Fisher* (1974) suggested a third fracture zone along 86°E longitude, west of Ninetyeast Ridge and were able to identify complete sequence of anomalies in the eastern part of the Central Indian Basin. They proposed a spreading rate of 4.0 cm/yr between anomalies 17 to 22, 8.0 cm/yr between anomalies 23 to 27 and spreading rates of 12.0 cm/yr

and 5.7 cm/yr were suggested between anomalies 27 to 30 and anomalies 31 to 33. *Sclater et al.* (1976b) from the studies of the magnetic lineation pattern in the southern part of the Central Indian Basin, identified a fracture zone south of 27°S trending N45°E between 82°E and 85°E longitudes which appears to change its direction to N10°E and joins the 86°E fracture zone. They explained this change in the trend of the fracture zone by the reorientation of the Southeast Indian Ridge from east-west to northwest-southeast between anomalies 15 and 18 (39 to 43 Ma).

The other characteristic feature of the Central Indian Basin is the existence of an intraplate deformation zone. The deformation zone, well developed around 2°S between Chagos Laccadive Ridge and the Ninetyeast Ridge, manifests itself as a zone of high seismicity (*Bergmen and Solomon*, 1985), anomalous heatflow (*Stein and Weissel*, 1990). This zone is characterized by E-W undulations deforming the oceanic crust and the overlying Bengal Fan sediments (*Weissel et al.*, 1980; *Geller et al.*, 1983; *Neprochnov et al.*, 1988; *Bull and Scrutton*, 1990).

The studies by *Patriat and Segoufin* (1988), *Royer and Schlich* (1988), *Royer et al.* (1989) provided the synthesis of the magnetic anomalies and the reconstructions of the Indian Ocean. The detailed studies carried out by *Kamesh Raju and Ramprasad* (1989), *Kamesh Raju* (1990), *Kamesh Raju* (1993) and *Kamesh Raju et al.* (1993) have contributed to the understanding of the tectonic processes at work in the middle part of the Central Indian

Basin. Figure 1.2 gives summary of the previous studies that were carried out in the Indian Ocean.

1.5 FRACTURE ZONES

Fracture zones on the ocean floor are originally defined as long and narrow "band of grossly irregular topography", characterized by volcanoes, linear ridges, scarps and typically separating distinctive topographic provinces (*Menard, 1954*). Fracture zones are linear scars in the seafloor produced by transform faulting (*Wilson, 1965*). Topography along their segments consist of long ridges, troughs and scarps which separate regions of different depths (*Menard and Atwater, 1969*).

Fracture zones were first identified in the Pacific Ocean with the delineation of Mendocino fracture zone (*Menard and Dietz, 1952*). Subsequently a whole system of subparallel fracture zones were mapped (*Menard, 1955; Menard and Fisher, 1958*). Fracture zones similar to the Pacific were identified in the Atlantic (*Heezen and Tharp, 1961; Krause, 1965*) and the Indian oceans (*Matthews, 1963; Heezen and Tharp, 1965*). The offsets in the magnetic lineations help to identify fracture zones, even with less detailed bathymetric mapping. It is believed that almost all the fracture zones are genetically related to the mid-ocean ridges (*Menard and Chase, 1968*). As detailed in the previous sections, several fracture zones

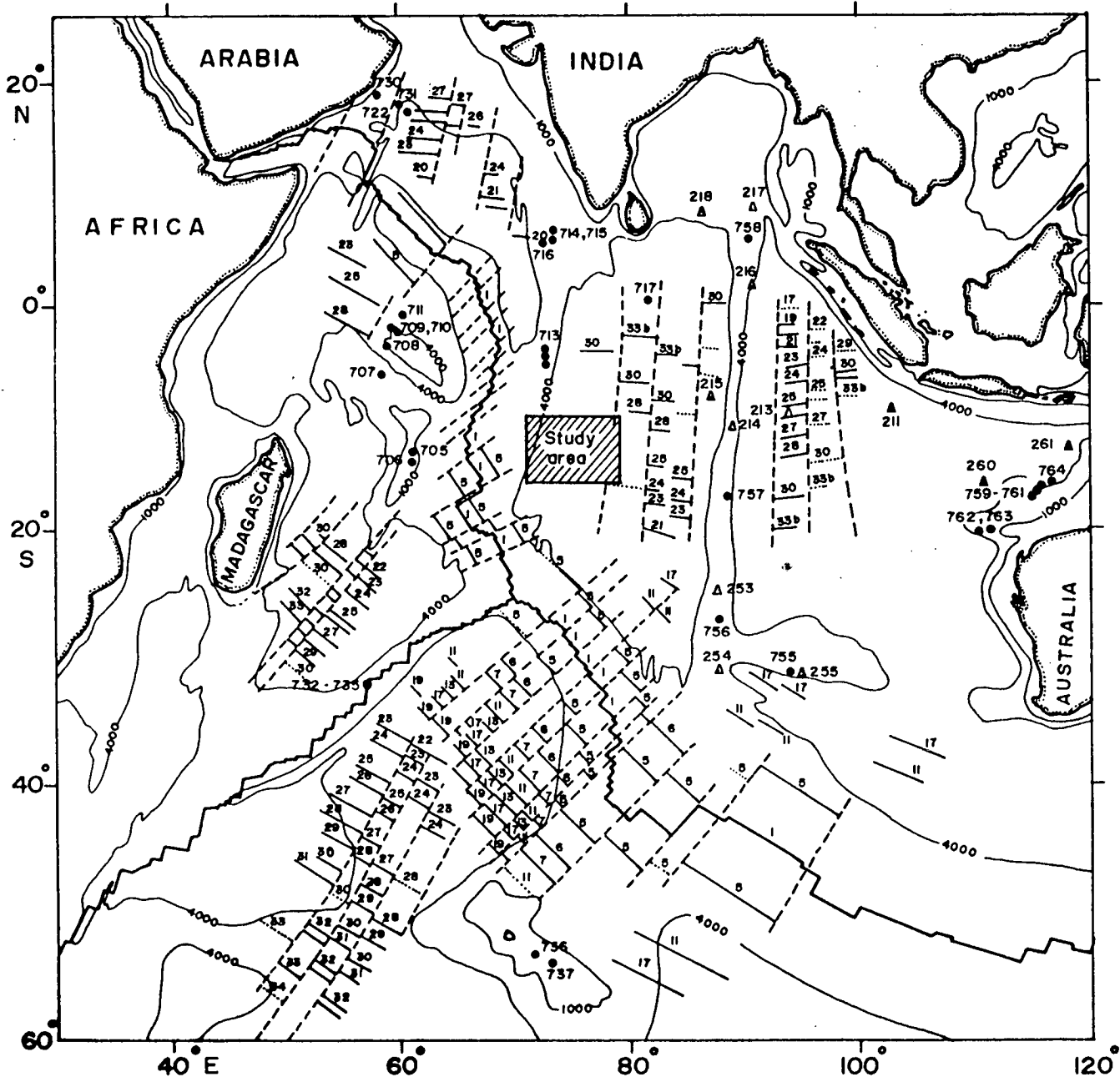


Figure 1.2 Magnetic anomalies and fracture zones as delineated from the earlier studies (Schlich, 1982). The thin line with numbers indicate the magnetic anomalies, doubtful identifications are shown with dotted lines. Thick dots represent the location of the ODP sites and the triangles represent the DSDP sites. Bathymetric contours of 1000 and 4000 m are shown. The study area is marked.

were identified in the Indian Ocean. Fracture zones appear to be the characteristic feature of all ocean basins.

There is an overlap of the terms used to indicate the transform fault and the fracture zone. "Transform fault" refers to any plate boundary undergoing strike slip motion, whereas the aseismic extension of the transform fault is referred as the "Fracture zone" (*Kastens, 1987*). The terminology used in the recent studies by *Fox and Gallo (1984, 1986)* and *Gallo et al. (1986)* has been followed in this thesis. The term fracture zone will be used for the aseismic extension of the ridge-ridge transform fault, whereas the transform fault refers to the active transform fault region undergoing the strike slip motion defining the plate boundaries.

1.6 STUDY AREA AND OBJECTIVES OF THE PRESENT INVESTIGATIONS

A part of the Central Indian Basin has been the focus of study following the discovery of polymetallic nodule rich areas by the *National Institute of Oceanography (NIO)*, Goa. As it can be seen from the previous sections above, a broad regional picture in terms of the tectonic evolution of the Central Indian Basin has emerged from the studies carried out using widely spaced survey tracks, in the Indian Ocean by various groups. However, there are vast areas still left unexplored, the Central Indian Basin is one such region. In the Central Indian Basin the earlier studies as summarized by

Schlich (1982) (Figure 1.2), indicate a large gap between the Central Indian Ridge and the 79°E fracture zone, where no anomaly identifications are available. The southern extension of the 79°E fracture zone is poorly constrained with questionable magnetic anomaly identifications.

The present studies are taken up in order to fill the knowledge gaps in terms of the anomaly identifications and fracture zones. These studies are envisaged to provide better constraints to the evolution of the Central Indian Basin. The conventional geophysical methods such as magnetics and bathymetry have been extremely successful in delineating various tectonic features. However, detailed knowledge about the processes responsible for the evolution these features is not clear. More detailed investigations with high resolution techniques are necessary to understand these processes. In the present study the high resolution swath bathymetric techniques are employed to study the evolution of various morphotectonic elements associated with 79°E fracture zone.

1 Study Area

The present studies are carried out over a part of the Central Indian Basin between latitudes 10°S and 16°S and 71°E and 80°E longitudes. This region is extensively studied using closely spaced survey tracks along which magnetics, gravity and bathymetric data were collected. A part of the area encompassing the 79°E fracture zone is selected for detailed multibeam

bathymetric and gravity studies, between latitudes 10°15'S to 14°45'S and 78°E to 79°20'E longitudes (Figure 1.3).

These studies are carried out as a part of the *Polymetallic Nodule Project*, undertaken by the *National Institute of Oceanography* in which the author is a participant.

ii Objectives

The present studies are carried out with closely spaced tracks in order to decipher the evolution of the Central Indian Basin, in terms of the geodynamic processes at work in the region. The specific objectives of the present investigations are as follows.

- To identify linear marine magnetic anomalies and to establish the trends of the magnetic lineations in the region.
- To delineate the fracture zones and to establish the southern extension of the 79°E fracture zone, based on the bathymetric and magnetic data.
- To study the tectonic implications of the fracture zones and other bathymetric features.

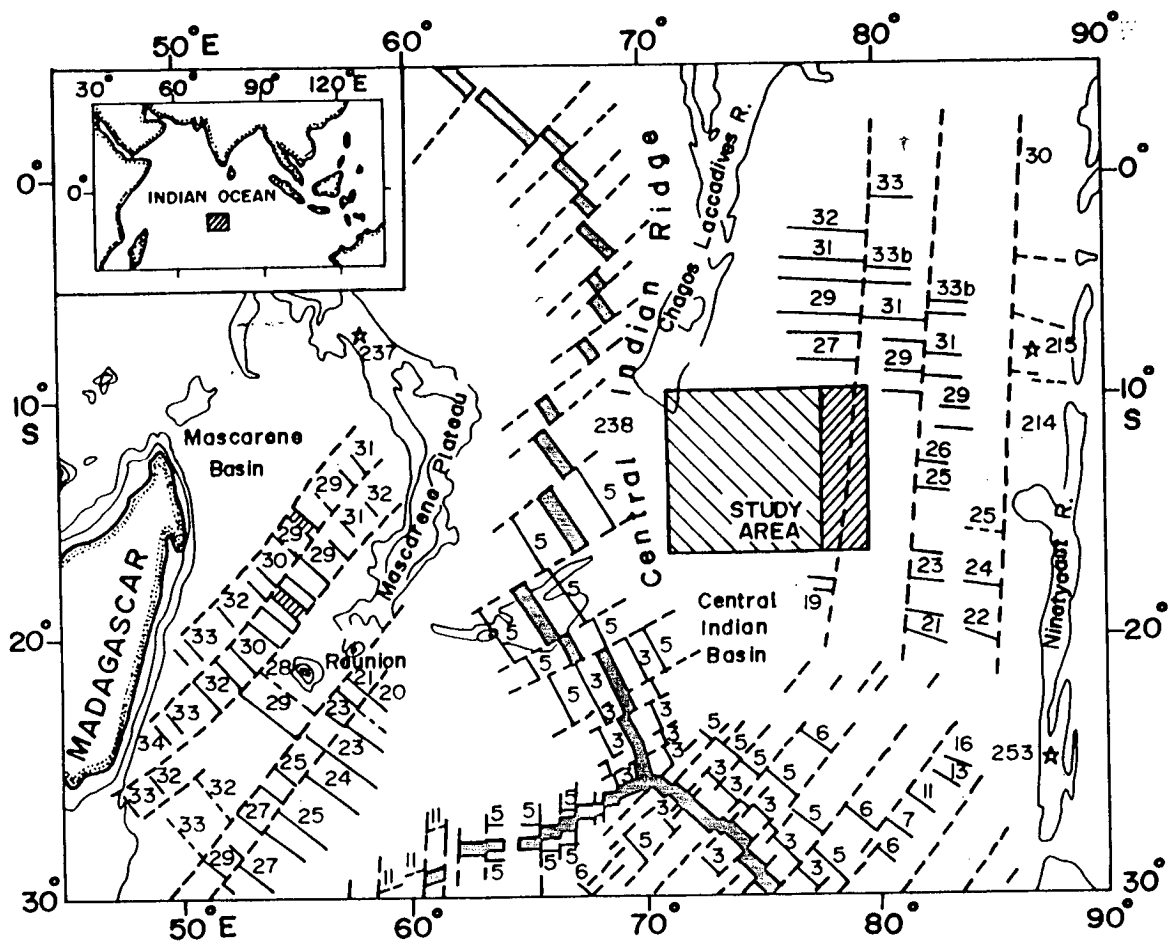


Figure 1.3 The study area (hatched box) with respect to the mid-ocean ridge system and magnetic anomalies (*Schlich, 1982; Munsch and Schlich, 1989*). The thick hatch within the box represents the area covered with multibeam bathymetry and gravity observations. Star symbol with number denotes the DSDP site locations.

- To delineate various morphotectonic features associated with a fracture zone on a moderately old ocean floor using multibeam swath bathymetric mapping.
- To decipher various stages of evolution of the fracture zone by an integrated study of magnetic and multibeam bathymetric data.
- To generate a thermal structure model of the oceanic lithosphere across the 79°E fracture zone.
- To generate probable density model of the oceanic lithosphere across the 79°E fracture zone and to provide lithospheric thickness estimates with the constraints from thermal structure and free-air gravity observations.
- To develop a model to explain the evolution of various morphotectonic elements associated with 79°E fracture zone.

CHAPTER II

MARINE GEOPHYSICAL INVESTIGATIONS

CHAPTER II
MARINE GEOPHYSICAL INVESTIGATIONS

2.1 INTRODUCTION

The *National Institute of Oceanography* (N.I.O), has launched a major program for the delineation of polymetallic nodule rich areas in the Central Indian Basin in 1982, following the initial success of recovering the nodules during the 86 th cruise of *R.V. Gaveshani* in 1981. For this purpose, besides the Institute's vessels *R.V. Gaveshani* and *ORV Sagar Kanya*, four more chartered vessels namely *MV Farnella*, *MV G.A.Raey* from U.K., *MV Skandi Surveyor* from Norway and *DSV Nand Rachit* from India, were deployed. The exploration program involved the collection of nodule and sediment samples by free fall grabs, coring, dredging, under water photography and the collection of underway data. As a part of the Polymetallic Nodule project the Central Indian Basin between latitudes 10°S and 16°S and 71°E to 80°E longitudes was covered extensively with conventional echosounding, magnetics and in part by gravity surveys.

Integrated analysis of the data acquired under the project, led to the delineation of nodule rich prime area of 300,000 km² and enabled India to claim Pioneer Investor status from PrepCom (Preparatory Commission for the International Seabed Authority & International Tribunal for the Law of the

Sea). In August, 1987 India acquired the Pioneer Investor status and was allocated an area of 150,000 Km² (Figure 2.1), to carry out Pioneer activities involving detailed investigations.

The second phase of exploration is aimed at more detailed studies. One of the advanced swath bathymetric data acquisition system, Multibeam Sonar System, was used to map the seabed in detail during the second phase of exploration.

For the purpose of present study, bathymetric, magnetic, gravity and multibeam sonar data has been used. The bathymetric and magnetics data were collected during the cruises of *MV Farnella* and *DSV Nand Rachit*. Multibeam sonar, magnetics and gravity data were collected during the expeditions of *ORV Sagar Kanya*.

2.2 DETAILS OF THE EQUIPMENT USED FOR DATA ACQUISITION

2.2.1 POSITION FIXING

A dual channel satellite receiver, *MX1107*, was used for achieving position fixing during the surveys on the chartered vessels *MV Farnella* and *DSV Nand Rachit*. On *ORV Sagar Kanya* an Integrated Navigation System (INS) was used for the accurate navigation.

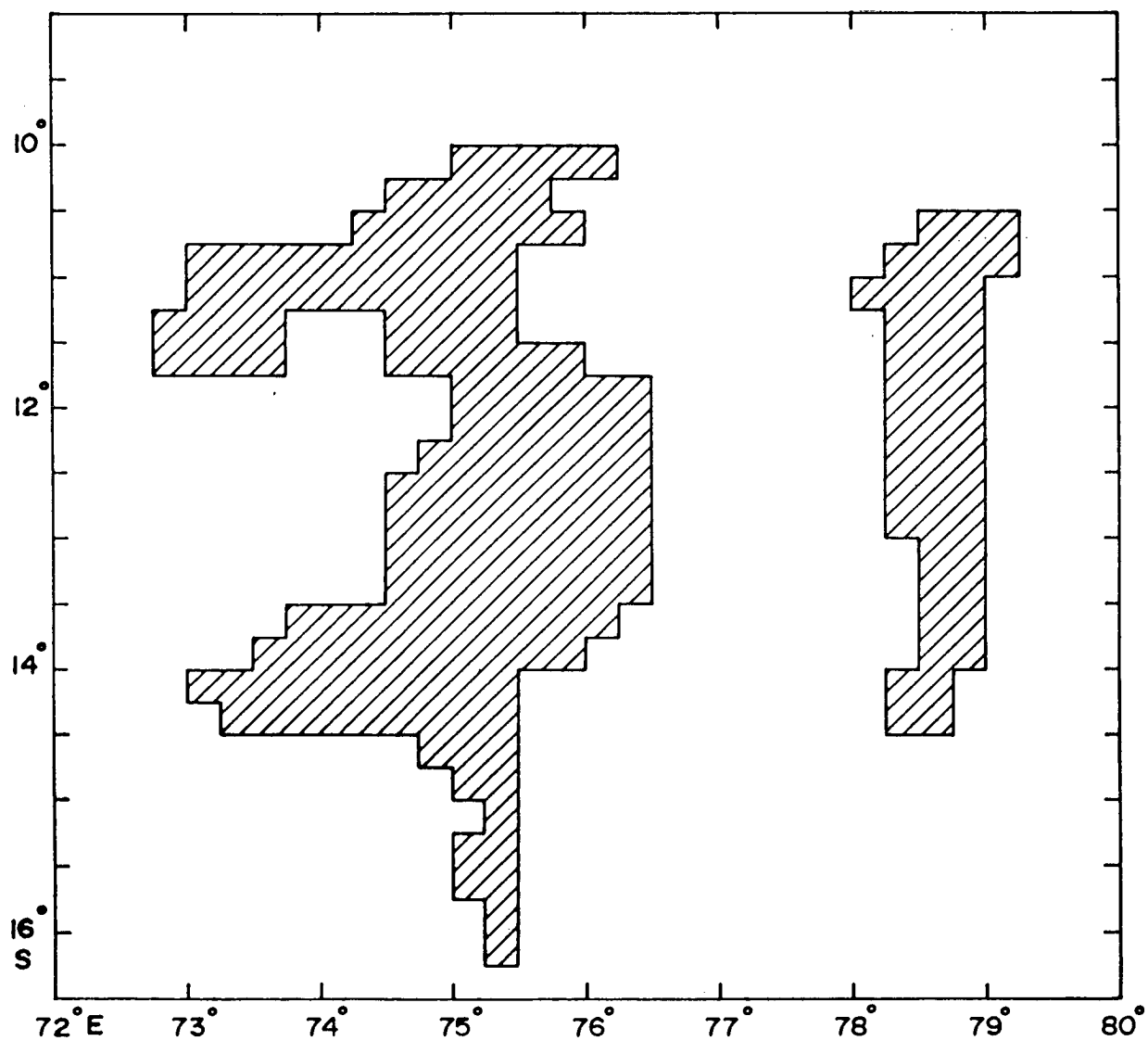


Figure 2.1 The 1,50,000 km² area in the Central Indian Basin, allocated to India for the exploration and exploitation of the Polymetallic Nodule resources, by the *PrepCom* of the *United Nations*.

1 MX1107 Satellite Navigation System

The *Magnavox MX1107* satellite navigation system contains a dual channel satellite receiver with a digital processor and an antenna. The system makes use of the satellite signals transmitted from the Navy Navigation Satellite System (NNSS), often known as the Transit Satellites to compute the position of the vessel. The transit satellite system consists of six polar orbiting satellites at an altitude of 600 nautical miles. These satellites transmit very stable 400 and 150 MHz signals which are phase modulated with several types of information. A part of the message from the satellite signal contains the navigation data which precisely describes the position of the satellite as a function of time.

The transit satellites travel roughly at a speed of 4 miles/sec and this motion with respect to an observer on earth causes a Doppler shift in the ^{transmitted} (radiated) 400 and 150 Mhz signals. This Doppler shift is measured by the satellite receiver to compute the slant range between the observer and the satellite. The slant range data and the satellite position data are used to compute the position of the receiver vessel at that time. Thus accurate position fixing can be achieved only when the satellite passes above the horizon of the user. The availability of satellite fix depends on the latitude of operation and varies between 30 minutes at poles to 110 minutes at the equator. The satellite receiver computes the position of the vessel in between

the satellite passes with the aid of gyro and speed log information. These positions are called as the dead reckoning positions. The accuracy of the position during a satellite fix is about ± 50 m RMS and the positional accuracy deteriorates during dead reckoning process.

ii Integrated Navigation System (INS)

The research vessel *ORV Sagar Kanya* is equipped with Magnavox series 5000 Integrated Navigation System (INS). The INS integrates the data from several navigational aids such as MX1107 satellite receiver, the Global Positioning System (GPS) receiver, Omega etc., to achieve most accurate position of the vessel. A schematic network of the INS is shown in Figure 2.2. Prior to the installation of Global Positioning System (GPS) receiver, the basic reference for the INS was the transit satellites. *Hewlett Packard* HP2117F computer serves as the processing control of the system. It accepts data from various navigational aids and control the devices attached to it and communicates with the operator. The system software provides optimal position information and also logs the underway data at user specified intervals on magnetic tape.

iii The Global Positioning System (GPS)

The basic system of *Global Positioning System* consists of satellite signal receiver *MX4400* with a microprocessor and an antenna. The system

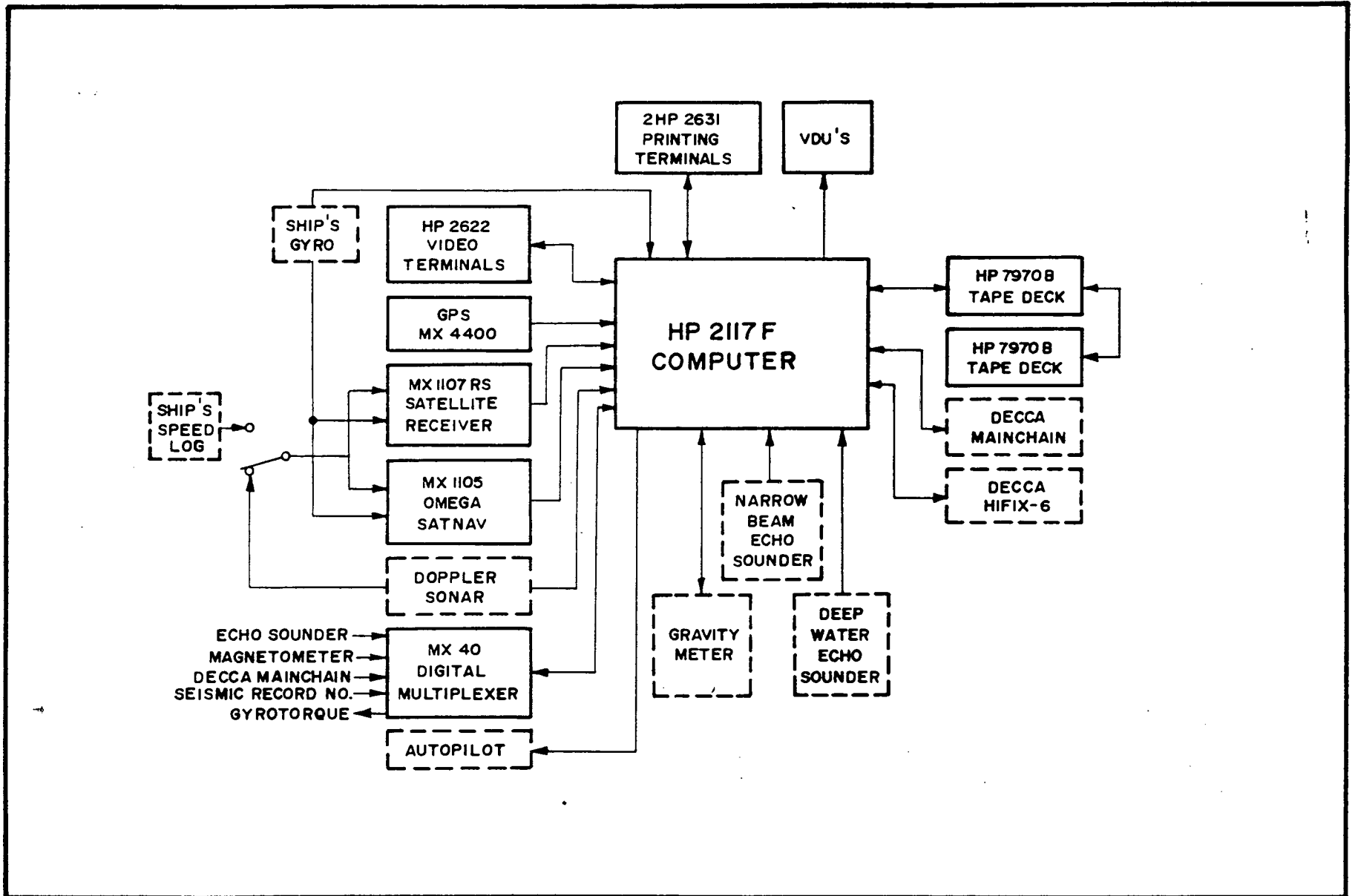


Figure 2.2 Schematic diagram showing the configuration of the *Integrated Navigation System (INS)*, onboard *ORV Sagar Kanya*.

is based on a set of satellites called *NAVSTAR* (Navigation System with Time and Ranging), satellites. These satellites orbit the earth at an altitude of about 10,900 nautical miles with an orbital period of 12 hours. This system is based on 18 satellites in six orbital planes. These orbits are configured to make a constellation covering the earth in such a way, that at least four satellites are in line of sight from any point at any given time.

Determining position involves recovery of time of arrival (TOA) measurement on satellite signal and the use of satellite ephemerides to compute the position of the satellite being tracked. Navigation is accomplished by using Kalman filter, a software based navigation model stored in receiver processor. It provides continuous navigation solutions based on TOA and Doppler measurements. The satellite derived position has an accuracy of 15 meters RMS. The dead-reckoning process may not be required as the GPS is aimed at giving 24 hours coverage. However, the *MX4400* satellite receiver has the capability of providing dead-reckoning positions from the speed and heading information of the vessel.

2.2.2 ECHOSOUNDING

The echosounder consists of a transceiver, control electronics and a graphic recorder. The system continuously transmits acoustic pulses and receives the reflected signal from the seabed. The time elapsed between the transmission and reception of the acoustic pulse is measured. The elapsed

time is converted into depth considering the velocity of sound (1500 m/sec) in sea water.

The following echosounders were used for the collection of bathymetric data. On *ORV Sagar Kanya*, the *Honeywell-Elac* narrow beam echosounder (NBS) system which can operate at frequencies 12 kHz, 20 kHz and 30 kHz was used. The system was operated at 12 kHz frequency. On the chartered vessels *MV Farnella* and *DSV Nand Rachit*, *Raytheon* echosounder with precision depth recorder was used at 12 kHz frequency

2.2.3 PROTON PRECESSION MARINE MAGNETOMETER

Marine proton precession magnetometer model *G801/3*, manufactured by *EG&G Geometrics*, was used for the acquisition of total magnetic intensity data. The system consists of a sensor, cable, control electronics cabinet and a recorder (Figure 2.3).

The principle of proton precession magnetometer is based on the fundamental properties of atomic nucleus and the phenomenon of Larmour precession. The protons (hydrogen nuclei) have a spin which makes each nucleus equivalent to a tiny magnet. Under the normal conditions the spin axes are randomly oriented and their individual fields cancel each others. When a polarizing field is applied perpendicular to the earth's field, the spin axes of the protons get aligned in the direction of the polarizing field. When

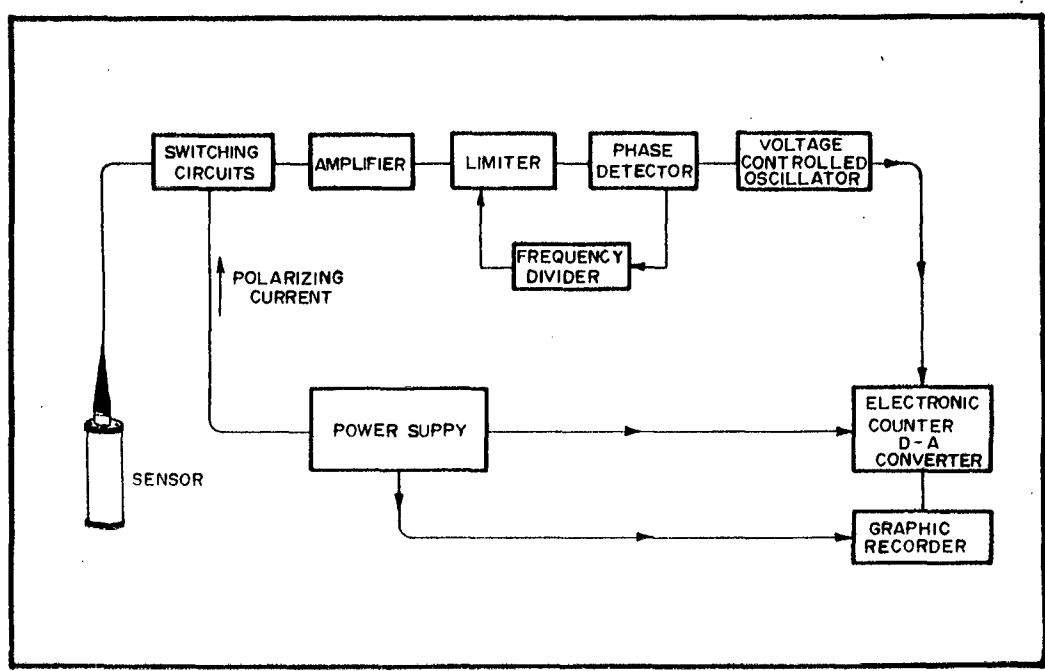
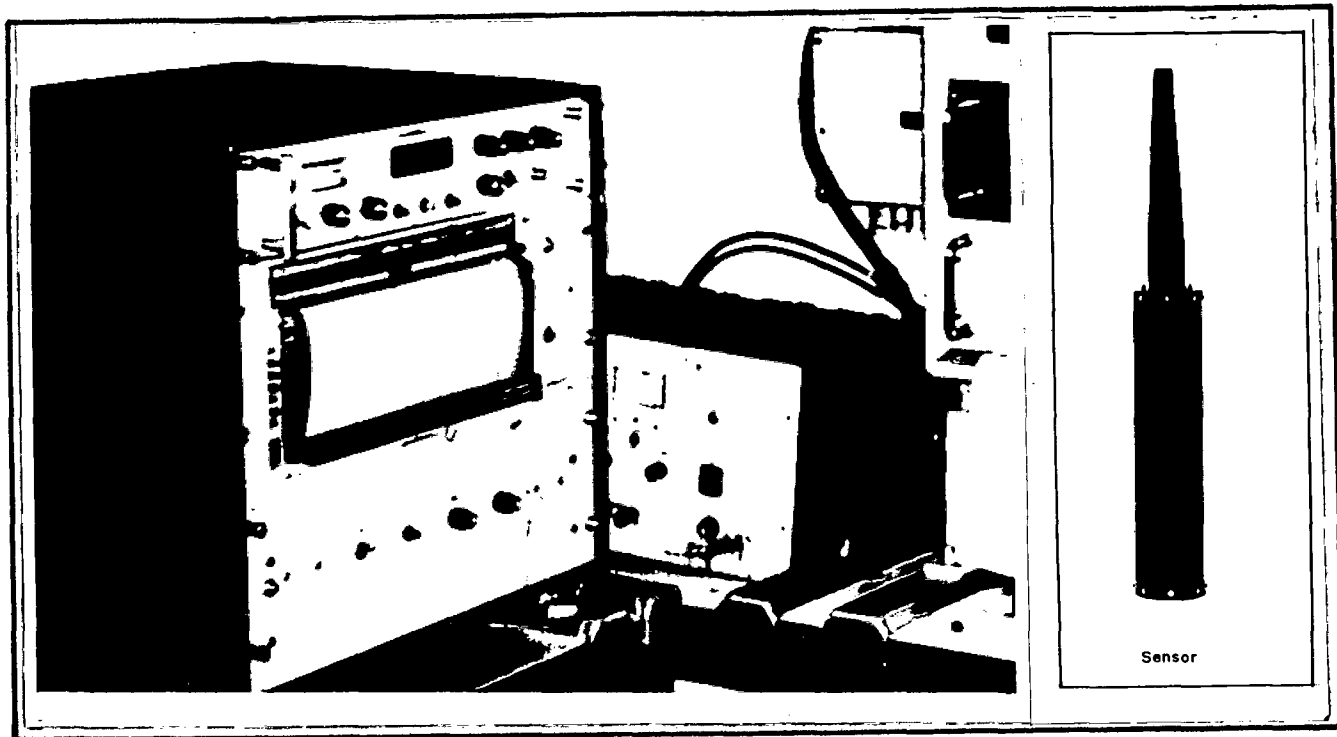


Figure 2.3 Photograph showing the *Geometrics G 801/3* proton precession marine magnetometer. The bottom part of the figure illustrates the schematics of various modules of the system.

the external polarizing field is removed, the spinning nuclei behave like tiny tops and precess towards earth's field at a frequency, that is proportional to the magnitude of the ambient field.

The frequency of precession F is given as:

$$F = \frac{\gamma}{2\pi} \cdot T$$

Where,

T is the total field of the Earth

γ is the gyromagnetic ratio, given as $0.267513 \text{ gamma}^{-1} \text{ sec}^{-1}$

The total magnetic field of the earth in gammas = $23.4874 F$

In modern proton precession magnetometers this frequency (F) is measured with high accuracy and displayed. A schematic diagram showing the working principle of magnetometer is illustrated in Figure 2.3.

During the data acquisition the sensor is towed behind the ship and the measurements are made continuously. The sensor was towed at a distance of three times the ship's length in order to avoid the magnetic noise generated by the ship.

2.2.4 THE MARINE GRAVIMETER

The marine gravimeter *KSS-30* manufactured by the *Bodenseewerk* of *Germany* was used for the acquisition of gravity data. This system consists of three major subsystems, the gravity sensor subsystem *GSS 30*, the stabilization subsystem *KT 30* and the data handling subsystem *ZE 30*.

The sensor consists of a tubular shaped mass attached to a zero length spring guided by five ligaments in a friction less manner and the motion of the sensor mass is limited to one degree of freedom in vertical direction. The tubular mass forms the moving plate of a capacitive transducer (Figure 2.4). Any change in the gravity varies the capacitance and is balanced by passing equivalent current through an electromagnetic system which brings back the spring mass to the original position. The current required for the electromagnetic system is a measure of change in gravity. The sensor is mounted on gyrostabilized platform in order to compensate for the roll and pitch motions of the vessel. The platform is controlled by stabilization subsystem and the stabilization is achieved with the aid of vertical gyros and the two accelerometers mounted in the pitch and roll axes.

The data handling subsystem *ZE 30* represents the command and control part of the total system. The *ZE 30* microprocessor acts as the control unit and monitors the logic of the sensor stabilization platform, performs signal processing, logging of the data and error handling of the system. The

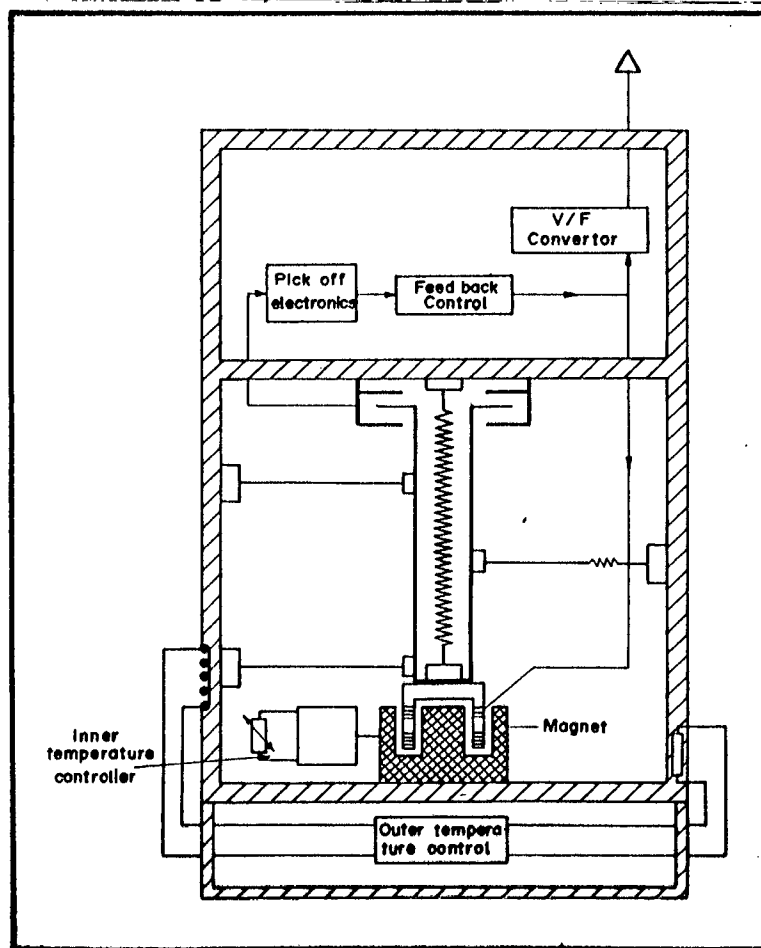
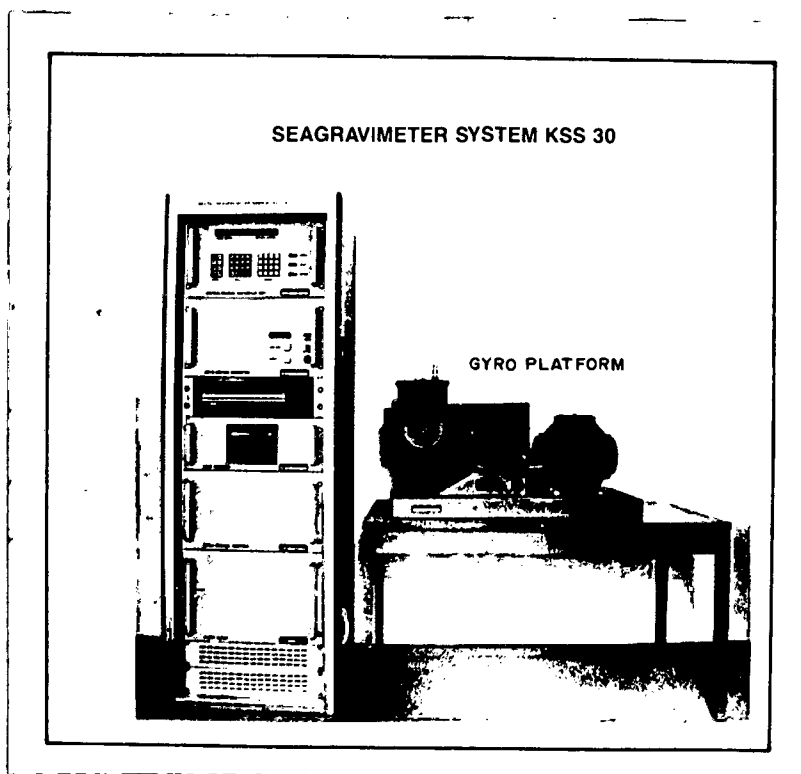
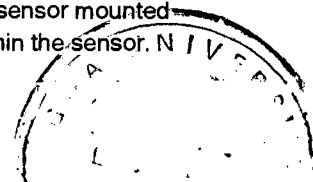


Figure 2.4 Photograph showing the *Bodenseewerk* KSS 30 marine gravimeter and the sensor mounted on gyrostabilized platform. The bottom part of the figure shows the principal elements within the sensor.



control electronics cage the sensor automatically in case of failure to any sub system or in case of ship exceeds the tolerable limits of rolling and pitching. The ZE 30 is interfaced with navigation computer and receives various data, in order to perform gyro erection, turn manoeuvre compensation and on-line processing to make Eotvos, Free-air and Bouguer corrections.

The accuracy of the system is about 0.02 mgals which is the minimum change in gravity that can be detected. However, the effective accuracy, which depends on the accuracy of navigation and sea conditions is about 0.8 to 1.0 mgals.

During data acquisition, at the start of the cruise, the gravimeter is calibrated to check the performance of the system and the gravity reading at harbour is taken while the ship is at the berth and the absolute gravity at that place is noted. The harbour gravity reading and absolute gravity values are entered into the system. The absolute gravity values at Marmugao harbour were established by tying to the nearest network of known gravity bases (*Subbaraju and Sreekrishna, 1989*).

2.3 MULTIBEAM SONAR INVESTIGATIONS

The extensive use of echosounders on research vessels during years following World War II have contributed immensely towards the general understanding of the bottom topography of the world oceans and resulted in

the compilation of regional bathymetric maps (*Heezen and Tharp, 1965; Udintsev, 1975; GEBCO, 1983*). These maps played an important role in the development and acceptance of the ideas of seafloor spreading and plate tectonics in the mid and late 1960's. Once the first order features were delineated, the attention of the researchers shifted to the more detailed mapping of the seafloor with an objective of investigating the volcanic, tectonic and sedimentological processes of the ocean basins.

The need for much higher resolution bathymetric maps and new techniques for rapidly covering large areas led to the development of new instruments like *Seabeam, Sea MARC I and II* during late 1970's. The *Sea MARC I and II* are medium range (6 km swath) and long range (10 km swath) side looking sonars which can operate at moderate towing speeds and can provide images of large areas.

The *Seabeam* system, introduced in 1977 was the first multibeam bathymetric equipment which operates at 12 kHz and provides real time contour maps of the seafloor. This system makes use of 16 pre-formed beams and provides a swath coverage of 73% of the water depth. During 1986, a new and more efficient multibeam bathymetric system was introduced by the *Krupp Atlas Electronic of Germany* by the name *Hydrosweep* (cf. *Gutberlet and Shanke, 1989; Grant and Schreiber, 1990*). The major advantage of this system is that it provides a swath coverage of twice the depth of operation by making use of 59 pre-formed beams and

incorporates cross fan calibration method for the compensation of variation of sound velocity in the sea water.

2.3.1 THE HYDROSWEEP SYSTEM

The *Hydrosweep* multibeam sonar system was acquired by the Government of India and was installed on the vessel *ORV Sagar Kanya*, during 1990. The system consists of hydroacoustic transducer arrays, the transmission/reception electronics cabinets, an EPR 1300 process computer, two magnetic tape drives, a control and display console and a printer/plotter (Figure 2.5). The system receives position information from navigation computer (INS), heading information from Gyro, roll, pitch and heave information from Heave platform. The operational frequency of the system is 15.5 kHz, a swath is surveyed for each sounding, covering an area of twice the depth of operation ensuring 59 depth samples, resulting from one center beam and 29 beams on both port and starboard sides of the vessel.

The transducer assembly consists of two transducer arrays composed of several individual elements. These arrays are mounted flush to the bottom of the vessel in a T-shaped configuration. The array which acts as the transmission array during the survey mode is installed parallel to the longitudinal axis of the vessel and the reception array is perpendicular to this axis. The functions of the transmission and reception arrays are interchanged during the calibration mode by means of change over switches.

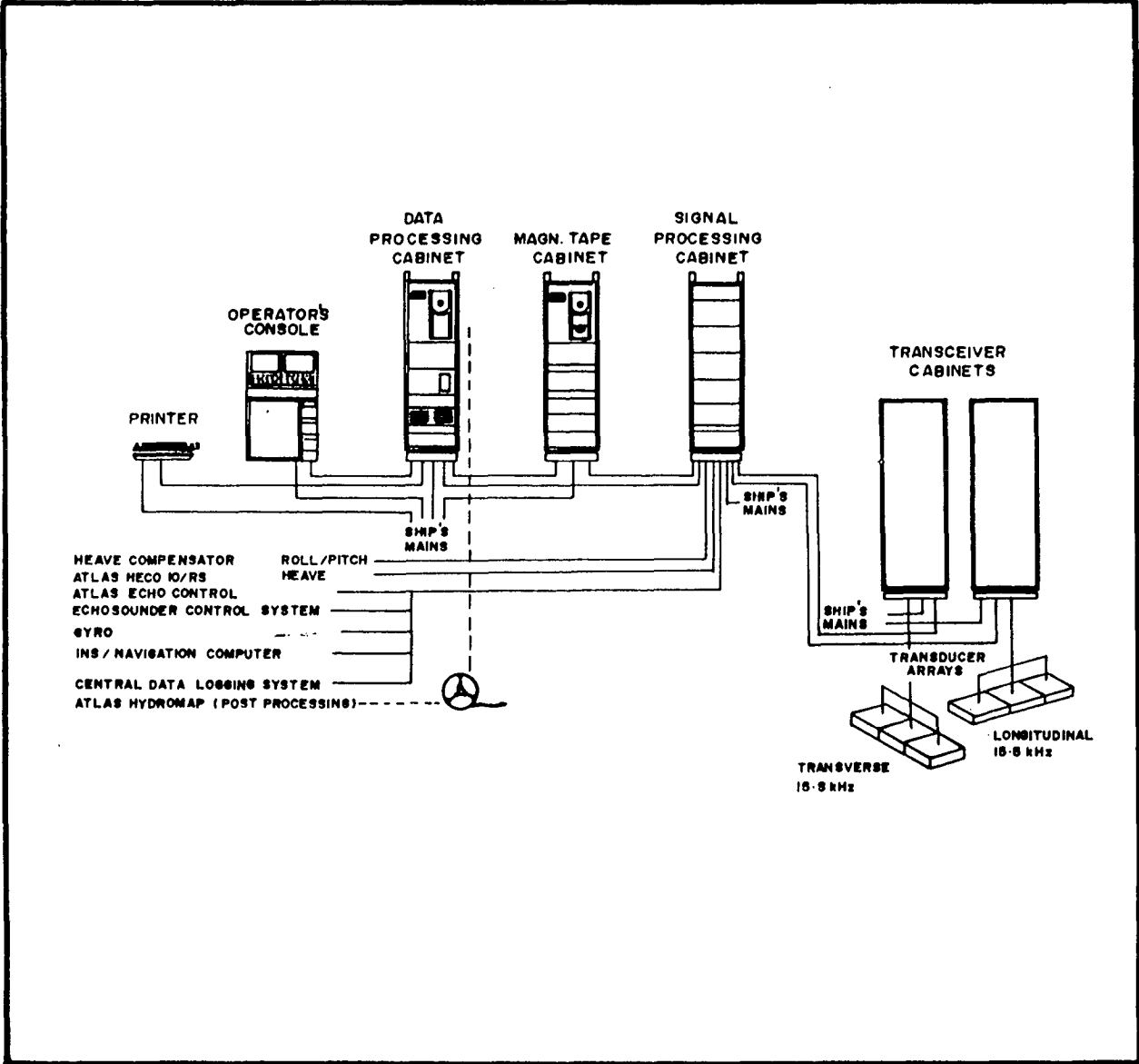


Figure 2.5 Schematic diagram showing various modules of the *Hydrosweep* system.

The preamplified transducer signals are passed through TVC (time varied gain control) amplifiers and fed to the beamformer. In the beamformer 59 pre-formed beams (PFB's) are generated by phased addition of the signals, taking into account the roll and pitch angles and sound velocity dependent corrections. The PFB's are filtered with a band width in accordance with the measuring range and these signals are passed to the echo logic unit. In this part several processors run while the echo evaluation process is active. These include the bottom detection by using echo processing, computation of digital depth to each of the 59 PFB's and assignment of positions to the depth data.

One distinctive feature of the *Hydrosweep* system is the provision to correct the errors resulting from sound velocity variations during the data acquisition without interrupting the survey. In the conventional echosounders a constant value of sound velocity (1500 m/sec) is used to compute the measured depth. The sound velocity varies in the water column and affects the travel time of the acoustic pulse, resulting in errors in the measured depth. This problem is accentuated in multibeam echosounders as the outer beams deviate from their actual angle of transmission/ reception. Sound velocity information is required to correct for these effects. In some of the multibeam echosounders this information is provided by separately measuring the sound velocity in the region of survey at regular intervals. This procedure is time consuming and expensive. The *Hydrosweep* system uses a patented calibration process to estimate the sound velocity. During the

survey mode the center beam depths are stored in the system memory. The system at regular intervals (for every 1000m distance traversed) enters into calibration mode, during which the transmission and reception arrays are inter-changed, resulting in a swath along the longitudinal axis (Figure 2.6). The depth values obtained along the longitudinal axis are compared with the stored center beam values collected during survey mode. A correction factor is applied to produce best fit result and an estimate of the average sound velocity is obtained. This sound velocity value is used by the system to compute the water depth till next calibration is performed.

The system's process control computer *EPR 1300* continuously monitors the performance of the system besides communicating with the user through the consol/display unit and providing data to various output devices. The depth data from all the 59 beams along with the position and related information is recorded on magnetic tapes for the purpose of post processing. A real time contour map is generated by the system and is plotted on the printer as isobath lines and displayed on the console as a colour coded bottom map.

2.4 LAYOUT OF THE CRUISE TRACKS

Earlier studies in the Central Indian Basin by *McKenzie and Sclater* (1971) and *Fisher and Sclater* (1974), have indicated near east-west trending magnetic lineations. As the magnetic anomalies are best reflected when

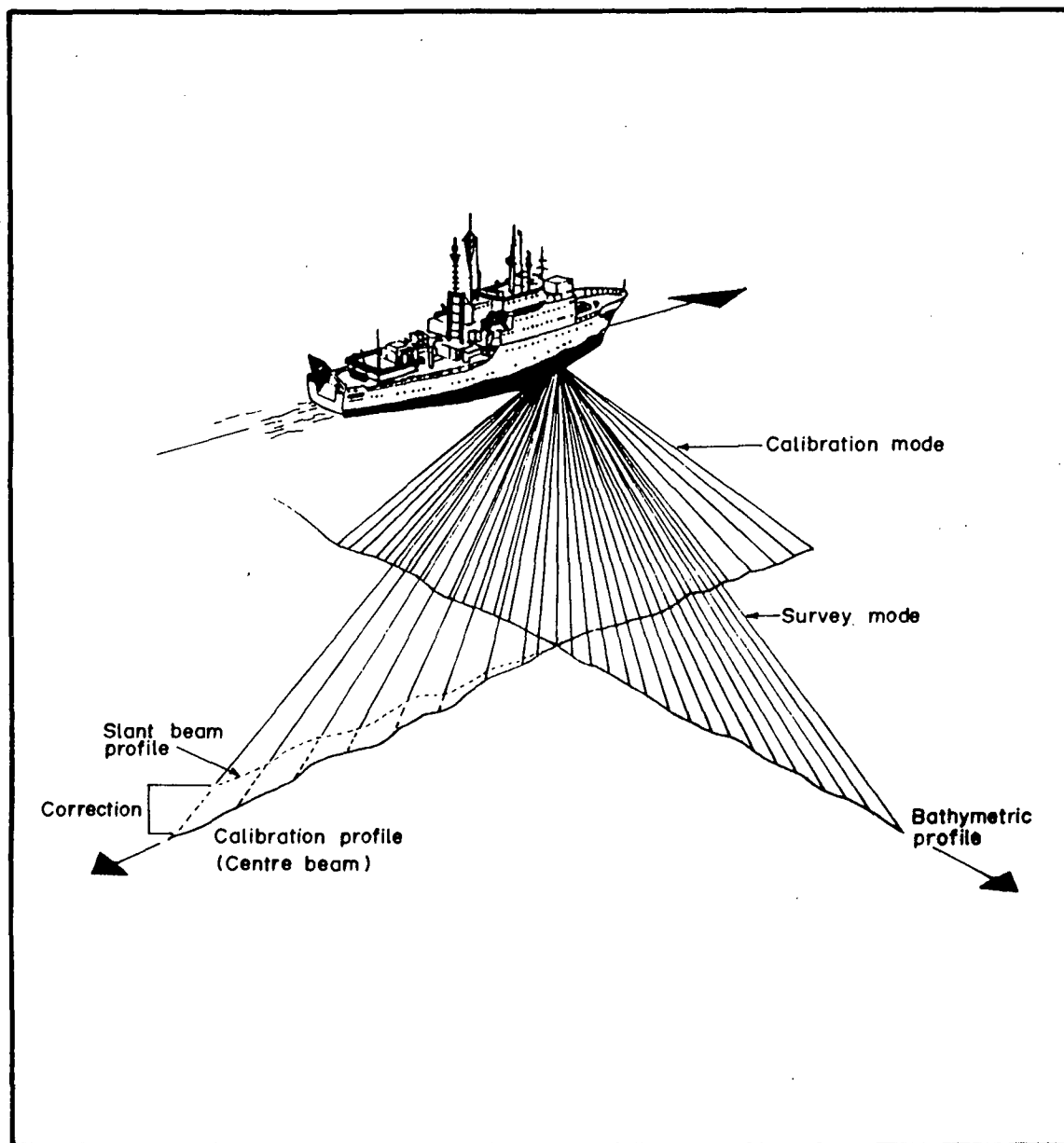


Figure 2.6 Swath coverage during the survey and calibration modes. The principle of calibration illustrated.

surveyed perpendicular to the lineation pattern, a set of 15 profiles in the north-south direction were planned between latitudes 10°S and 16°S and longitudes 70°E and 80°E. Bathymetric and magnetic data were collected along these tracks which are spaced at 30 miles (Figure 2.7). This set of 15 profiles consisted of about 8494 line kms (lkms) of total magnetic intensity and bathymetric data.

A part of the study area encompassing the 79°E fracture zone was selected for detailed studies using multibeam sonar surveys by the *Hydrosweep* system. The area selected is between 10°15'S, 14°45'S latitudes and 78°E to 79°20'E longitudes. The *Hydrosweep* cruise tracks are planned to ensure 100% coverage of the seabed. Accordingly north-south tracks were planned with a spacing of 5 miles (9.2 Km) (Figure 2.8). As the average depth is about 5000 m in the region, this track spacing has resulted in 100% coverage of the seabed with considerable overlap between the swath coverages of the individual tracks (Figure 2.9). With this layout a total number of 16 profiles were covered along which multibeam bathymetric and gravity data were collected. These surveys resulted in 8000 lkms of Hydrosweep data and 4100 lkms of gravity data. The total area insonified by these investigations is about 73000 Km².

In total about 8494 lkms of magnetics and bathymetric data, 4100 lkms of gravity data and 73000 Km² of multibeam bathymetric data comprised the data set for the present investigations.

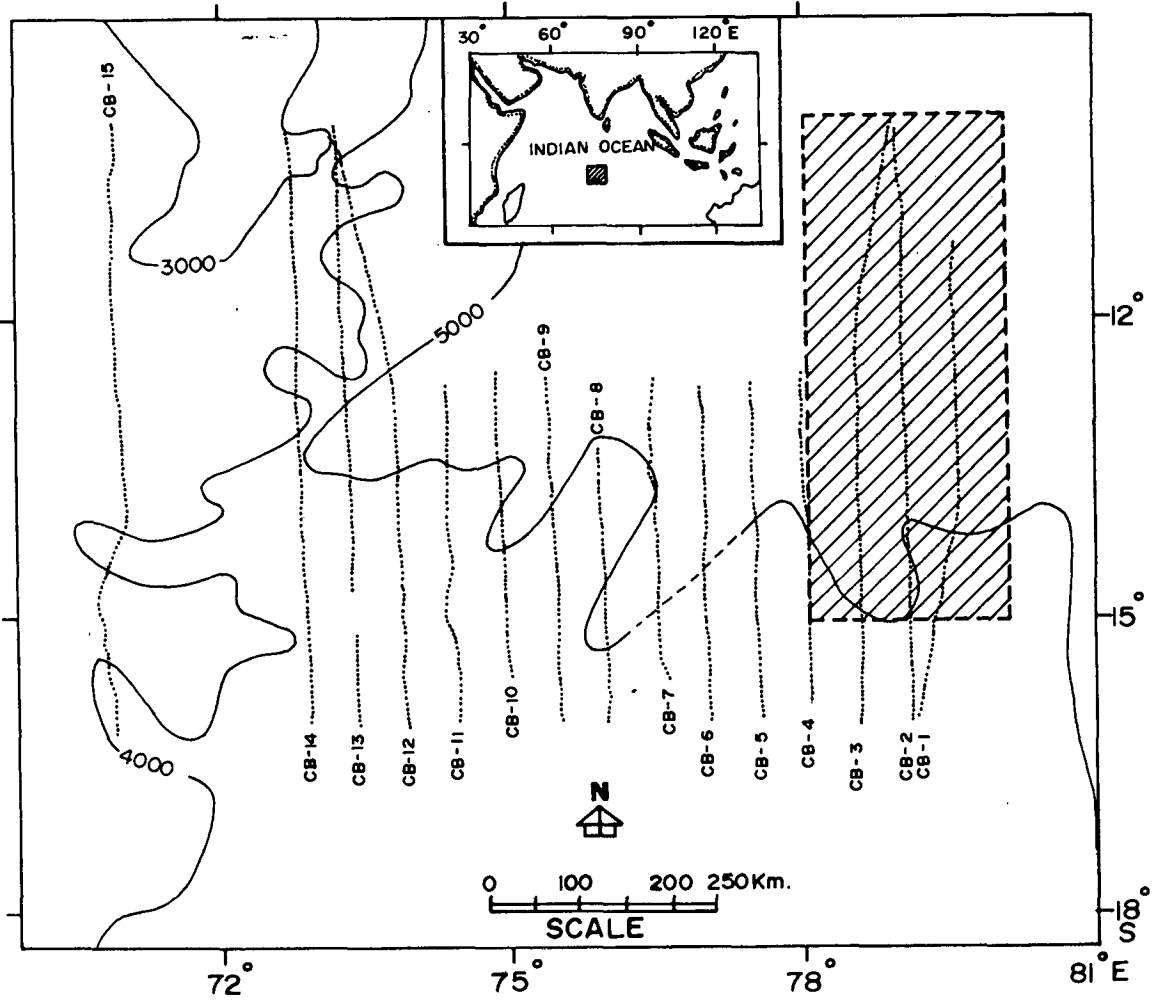


Figure 2.7 Cruise tracks are shown with dotted lines along which total magnetic intensity and bathymetric data were collected. The hatched box shows the area covered by multibeam sonar investigations. The 3000, 4000 and 5000 m bathymetric contours are from the *Hydrographic chart*.

T-201

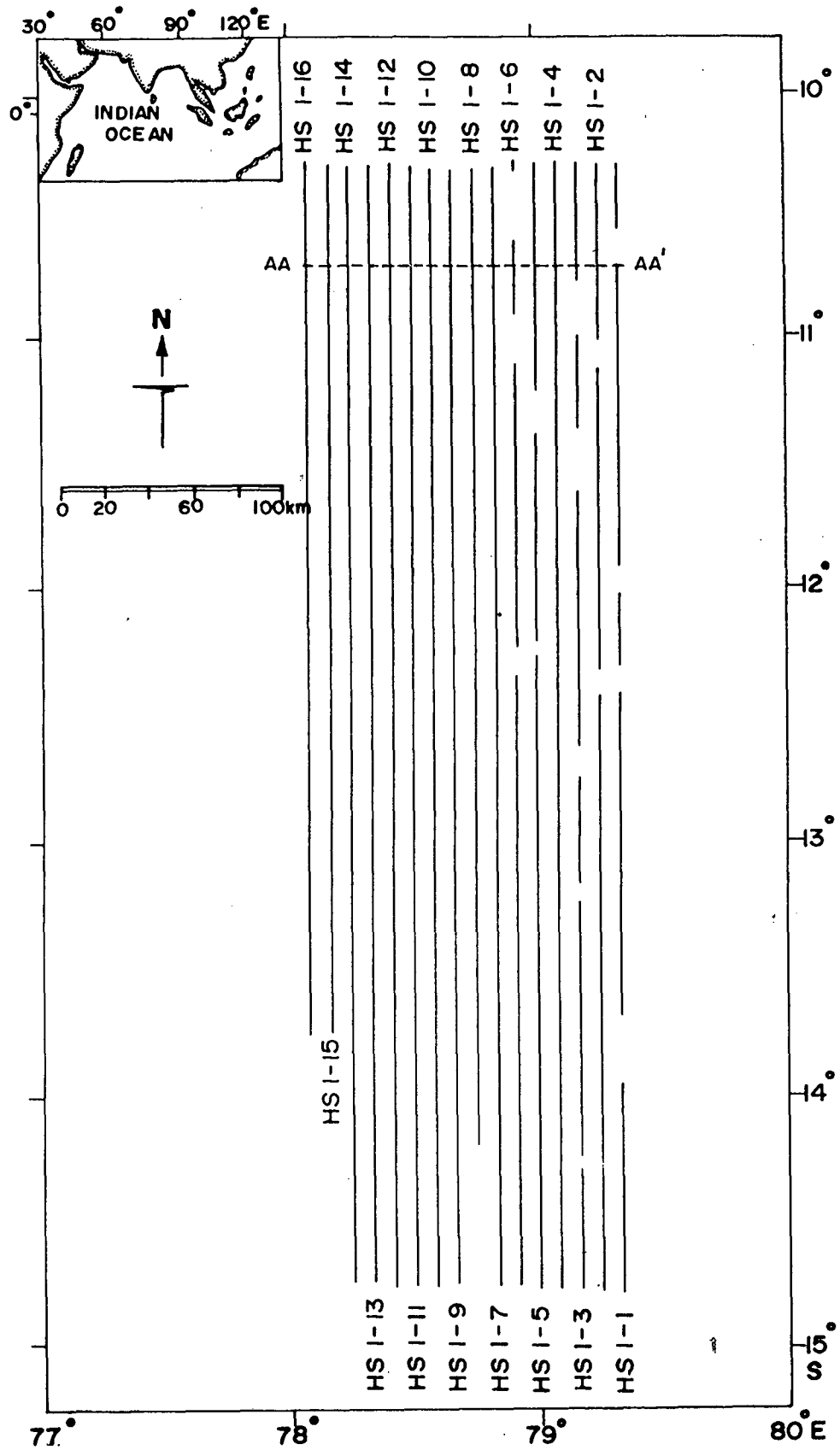


Figure 2.8 The cruise tracks at 5 mile interval along which multibeam bathymetric and gravity data were collected.

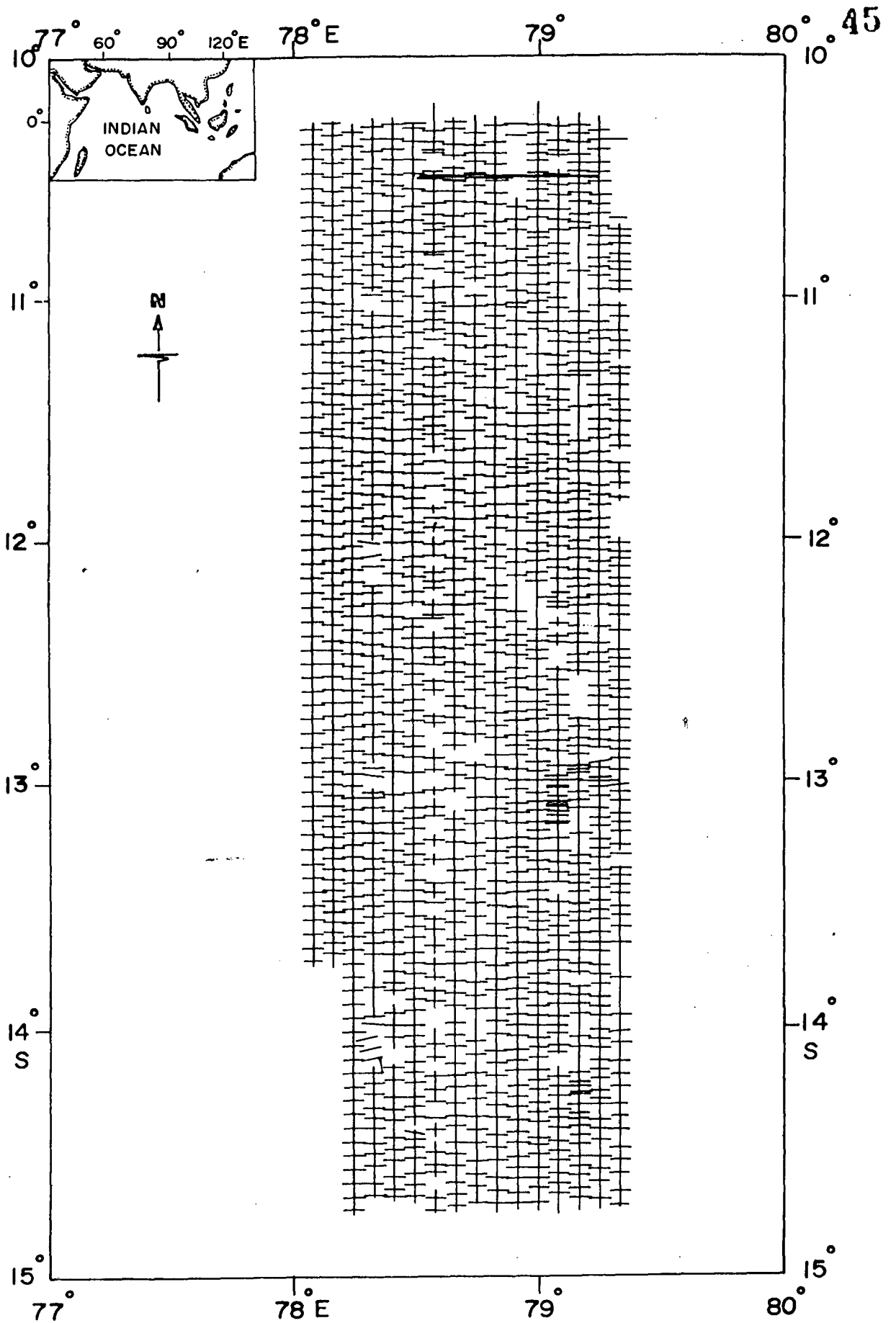


Figure 2.9 Swath coverage map. The swath coverage along the survey tracks is indicated by horizontal line segments.

CHAPTER III

DATA PROCESSING

CHAPTER III
DATA PROCESSING

3.1 INTRODUCTION

Processing of underway marine geophysical data demands additional attention as voluminous data are collected during a single cruise. In order to process large amounts of data a computer oriented approach is followed. The data are routinely processed onboard during the survey is in progress, primarily to check the quality of the data and to make decisions onboard regarding the track spacing, areal extent and also to improve the data quality. In addition, onboard processing gives an opportunity to work with the data while on location. However, onboard post processing requires appropriate computer and software facilities. Additional processing is carried out in the laboratory to further refine the data and to merge various types of data in order to generate maps. These maps aid interpretation and meet the requirements of presentation.

Essentially three different approaches have been followed to process the data during the present study, depending on the mode of collection and the type of data. The data acquired using the chartered vessels which do not have onboard computer facilities for data logging are in the form of analog records and navigation print outs. A scheme (Figure 3.1), for processing of

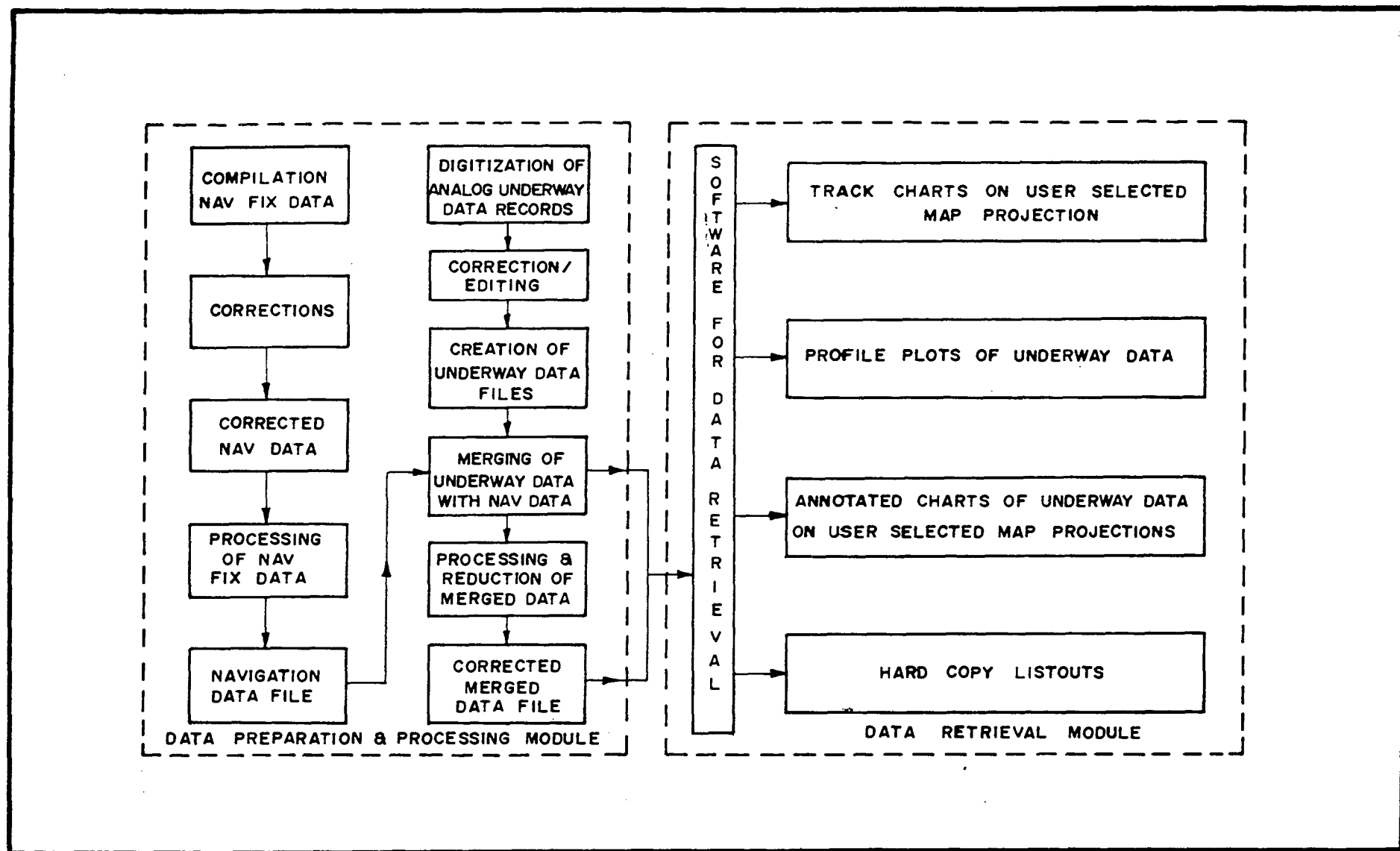


Figure 3.1 Schematic illustration of the data processing scheme followed for the processing of underway data collected in analog form.

9

these data was designed by me in association with other colleagues (*Kamesh Raju et al.*, 1986). MECON (Metallurgical Engineering Consultants, India), has developed the computer programs based on this scheme. This software was initially developed and used on *UNIVAC 1100/60* system at MECON, Ranchi and subsequently it was installed on NIO's Norsk Data computer, ND570. Onboard *ORV Sagar Kanya*, the bathymetric, magnetic and gravity data are logged by the Integrated Navigation System and are digitally recorded on magnetic tapes. These data are processed onboard by making use of HP 1000 general purpose computer and the Magnavox supplied software and at the laboratory by using ND570 system.

The multibeam sonar data which requires specialized processing was processed onboard by using the Krupp Atlas Electronics supplied *Hydromap* System, based on *EPR1300* computer. The various steps involved in each of these approaches are briefly described in the following sections.

3.2 UNDERWAY DATA PROCESSING

3.2.1 PROCESSING OF DATA ACQUIRED IN ANALOG MODE

The data outputs from the chartered vessels are in the form of analog records of total magnetic intensity data, bathymetry in the form of echograms and navigation data as position printouts. The post processing of these data involved digitization of the analog records and merging these digitized

records with corrected navigation data. Position dependent corrections such as the IGRF correction (*IAGA, I Division study group, 1985*) and Matthews correction (*Carter, 1980*) were applied to these merged data files. The merged and corrected files were used for the generation of various types of outputs. Figure 3.1 shows the schematic representation of the scheme followed.

1 Digitization

Digitization of the Analog records of magnetic and bathymetric data were digitized by using digitizer boards. The digitization was accomplished by manually moving the digitizer's cursor along the curve defining the data, and picking the representative data points by activating the cursor switch. This procedure resulted in digitized values at random time intervals. At places of rapid variations, the data points were picked at very closely spaced intervals in order to ensure true representation of the field data. After digitizing each segment of the record the digitized data were checked using graphics display to detect erroneous values and to check the quality of digitization. When fully satisfied the data were saved and the digitization process is continued. The digitized values are converted into time series data files by linearly interpolating the data in between the digitized points.

ii Navigation Data

The chartered vessels are equipped with dual channel Magnavox MX1107 satellite receivers to provide navigation. These systems are based on Transit satellites, as mentioned in the preceding chapter, accurate position information can be obtained only during a satellite fix and the accuracy of positioning deteriorates during dead-reckoning process. At the time of post processing, only good satellite fix data are considered and the positions in between the satellite fixes are computed. This process involved computation of distance, speed and course in between the satellite position fixes over a spherical surface, by taking into account WGS 72 spheroid constants. Satellite fix data are compiled using the print outs from the satellite receiver. While compiling these data, besides the good satellite fix data, the positions at the start of a line and at places of sudden speed increase and course change are also taken, in order to avoid erroneous interpolation of navigation data. From these position data, time series navigation data files were generated.

iii Merging and Reduction

The time series data files of bathymetry, magnetics and navigation are merged to assign corrected position information to the measurements. While merging, the ship code, date and time were used as reference parameters

(these parameters are incorporated in all the time series data files), to make appropriate merging. The merged data file thus contained ship code, line code, date, latitude, longitude, speed, course, water depth, total magnetic intensity values and the cumulative distance travelled along the line of survey. The merged data file was then used to apply position related corrections to magnetics and bathymetric data. The total magnetic intensity values are reduced by subtracting International Geomagnetic Reference Field (*IAGA, I Division study group, 1985*) computed at each observation point and the bathymetric data are corrected for regional variations in the sound velocity by applying Matthews correction (*Carter, 1985*). The processed data file contains reduced magnetic anomaly and corrected depth values in addition to the data fields in the uncorrected merged file.

The processed data file was then used for generating various types of outputs, such as the cruise tracks, profile plots, annotated charts and hard copy listings. Mercator Projection was used for the representation of data on maps on user selectable scales.

3.2.2 PROCESSING OF DATA ACQUIRED IN DIGITAL MODE

The INS system onboard *ORV Sagar Kanya* logs the digital data on magnetic tape from various geophysical sensors along with the navigation information in a merged format. These data are required to be post processed to correct for the uncertainties in the position data and to reduce

gravity, magnetic and bathymetric data by applying position dependent corrections. The post processing of the data has been carried out both onboard and at the laboratory. The processing procedure remains essentially same as that applied to the data collected in analog mode, for the position correction, IGRF correction and Matthew's correction are concerned. The processing of gravity data is outlined below.

1 Processing of Gravity Data

The on-line processing of gravity data is performed by the ZE 30 data handling subsystem of the Gravimeter using the position information obtained from INS system. During on-line processing, Eotvos correction, free-air correction and Bouguer corrections are applied to the measured gravity to compute Eotvos corrected gravity, Free-air anomaly, and Bouguer anomaly. As there are uncertainties in the navigation data, these values are computed again during post processing using the corrected navigation data. The following formulae were used during post processing to compute these anomalies:

$$\text{Free-air anomaly, } F = (G - G_H) \cdot K + G_{ABS} - G_N + E$$

Where,

G is the measured gravity in mgal

G_H is the measured gravity at harbour in mgal

G_{ABS} is the absolute gravity at harbour in mgal

G_N is the normal gravity computed from
International gravity formula.

K is the gravimeter sensor constant.

E is the eotvos correction

Among the above parameters G_H is noted at the start of the cruise while the ship is in the berth and the G_{ABS} is the absolute gravity tied to the Marmugao harbour (*Subbaraju and Sreekrishna, 1989*).

$$E = 7.508 V \sin \alpha \cdot \cos \phi + 0.004154 V^2$$

(after *Nettleton, 1976*)

Where,

E is the Eotvos correction in mgals

V is the speed of the vessel in knots

α is the course of the vessel

ϕ is the geographical latitude

$$G_N = 978.03185 [1 + 0.005278895 \sin^2 \phi + 0.000023462 \sin^4 \phi]$$

(after *Garland, 1979*)

Where,

ϕ is the geographical latitude

Eotvos corrected gravity, $E_G = G.K + E$

Bouguer anomaly, $B = F + B K$

Where $B_K = 2\pi G\sigma h$

$G = 6.6732 \times 10^{-8}$; σ = density ; h = water depth

where B_K is the Bouguer correction applied to remove the effect of water by replacing the water column with a material of the same density of the crust. In the present study, this correction is not applied to the data due to the uncertainties in assuming the crustal densities. For all interpretation purposes free-air gravity anomalies are used.

3.3 PROCESSING OF HYDROSWEEP DATA

The post processing of the *Hydrosweep* data was carried out by making use of the Krupp Atlas Electronics *Hydromap* system. The *Hydromap* system consists of a EPR 1300 computer with alphanumeric and colour graphics monitors, winchester drive, a floppy drive, a function key board, a text key board and a roll ball. The system has a magnetic tape drive to read in the *Hydrosweep* field tapes and to take backup of the processed data. The system has *Fortran 77* and *META* compilers and software to process the *Hydrosweep* data. The post processing software is written in *Fortran 77* and *META* languages. The post processing is accomplished by making use of the menu driven software to correct the raw data and to generate various types of outputs such as, the swath coverage plots, depth contour maps, profile plots and 3-D plots. A typical processing sequence (Figure 3.2) involves,



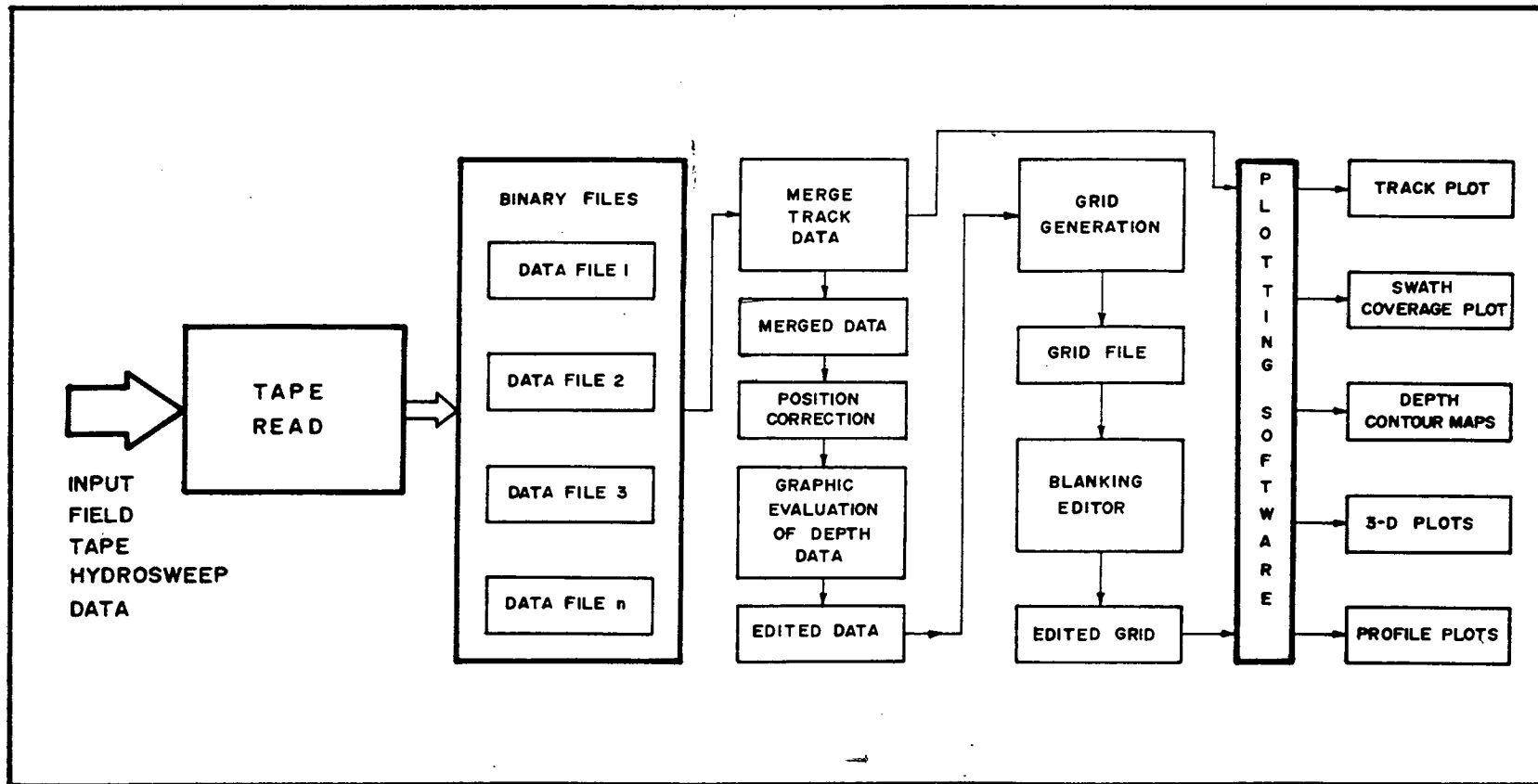


Figure 3.2 Processing sequence followed to process the *Hydrosweep* data.

reading the Hydrosweep field tape, performing position correction, editing of the erroneous data by graphic evaluation and produce various types of outputs. These steps are briefly described below.

i Read Hydrosweep Data

The *Hydrosweep* field data tape contains data records with a maximum record length of 132 characters in ASCII. These data contain the tape header, measurement section header, event records and measurement data records. Various combinations of these records are written on the tape (cf. *Operators manual, Hydrosweep system*). The measurement data records are always written as a combination of four records in the following order:

- Measurement data for starboard cross-track deviations,
ie., lateral distances to the starboard preformed beams
- Measurement data for starboard depth data
- Measurement data for port cross-track deviations
ie., lateral distances to the port side preformed beams
- Measurement data for port depth data

When the read option is selected from the menu, all the event records with position information and the measurement data records are transferred

to the Hydromap system from the tape. These data are stored in binary data files with a record length of 168 words and are organized with reference to tracks.

ii Position Correction

After the data are loaded into the system, a position correction is performed to correct for the uncertainties in the position data. This correction is very critical if transit satellites are used as the primary navigation. However, with 24 hours GPS coverage this correction is required, if there are gaps in GPS coverage during the survey. The position corrected data are used to generate track plot and swath coverage plots.

iii Editing of Depth Data

During the course of survey, data from all the 59 preformed beams may not get registered and some times the depth data from the outer beams result in erroneous data. These errors arise due to a variety of reasons resulting from a combination of instrument errors, sea conditions and bottom topography. Therefore, it is important that the recorded data are checked before they are actually used for the generation of maps. The checking is accomplished through the Profile Editor option. With the selection of this option, it is possible to display the depth data corresponding to each swath on the graphics monitor and to correct the erroneous data points using the

roll ball and function keyboard. The edited/corrected data are stored for further processing.

iv Grid Generation

The grid generation option permits comprehensive processing of several tracks at a time, to create grid file containing depth values over a selected area. In this option, grid cells are created with discrete depth values from the measured depth values and the missing depth values are computed by interpolation. After the creation of the grid file, if there are data gaps in the area covered, these gaps can be blanked by using the blanking editor option, in order to avoid erroneous extrapolation of gridded data while contouring. The edited grid file serves as the basic input file for the generation of contour maps, profile plots and 3-D plots. The various outputs can be displayed on the graphics monitor before actually plotting on the plotter. Mercator projection has been used for the generation of contour maps.

CHAPTER IV

**INTERPRETATION OF
MARINE MAGNETIC ANOMALIES**

CHAPTER IV
INTERPRETATION OF
MARINE MAGNETIC ANOMALIES

4.1 INTRODUCTION

Typical profiles showing the bathymetry and the associated total magnetic intensity anomalies observed in the world ocean basins have essentially exhibited (1) a pronounced central anomaly associated with the ridge crest/median valley, (2) short period anomalies over the rugged flanks of the ridge and (3) long period anomalies over the exposed or buried foothills of the ridge. Marine magnetic anomalies of these characters were initially observed in the North Atlantic (*Heezen et al.*, 1953; *Keen*, 1963), the Antarctic (*Adams and Christoffel*, 1962) and the Indian Ocean (*Matthews*, 1963).

The increase in wave length of the anomalies away from the ridge axis was related to the general increase in depth to the magnetic crustal material (*Heezen et al.*, 1957^{2 in depth!}). The local anomalies of short period were correlated with bathymetry and were explained in terms of reasonable crustal configuration and susceptibility contrasts. However, the long period anomalies could not be explained satisfactorily. With the availability of more data from the ocean basins, the existence of magnetic stripes with alternate

bands of high and low intensity magnetic anomalies have become apparent. These stripes were observed for several thousands of kilometers and a common explanation for them was sought. The observation of magnetic stripes in the world oceans emphasized the need for an alternate explanation and interpretation of the marine magnetic anomalies. In 1963, *Federick Vine* and *Drummond Matthews*, while interpreting the magnetic anomalies across the Carlsberg ridge in the Indian Ocean, offered a simple explanation in terms of a block model to explain the marine magnetic anomalies. This model was conceived by combining the theory of seafloor spreading and the observations of periodic reversals of the earth's magnetic field (*Cox et al.*, 1963). The proposed model of *Vine and Matthews* (1963), suggested that the alternate stripes of positive and negative magnetic anomalies were caused by bands of basaltic rock of the oceanic crust that were alternately magnetized in normal and reversed direction of the earth's magnetic field. It was proposed that the lithosphere is formed over convective upcurrents beneath the oceanic ridges by magmatic processes. As magmas emplaced in the axial rift zone cool through Curie temperature of magnetic minerals, they acquire a magnetization in the direction of the existing magnetic field of the earth. The newly magnetized crust then splits and is forced apart to make room for the fresh injections of magma. The simple block model of *Vine and Matthews* (1963), has received wide acceptance and laid foundation to the plate tectonic theory. Schematic illustration of the Vine and Matthews concept is shown in Figure 4.1. The Vine and Matthews model is widely used in interpreting the marine magnetic anomalies. The model studies conducted

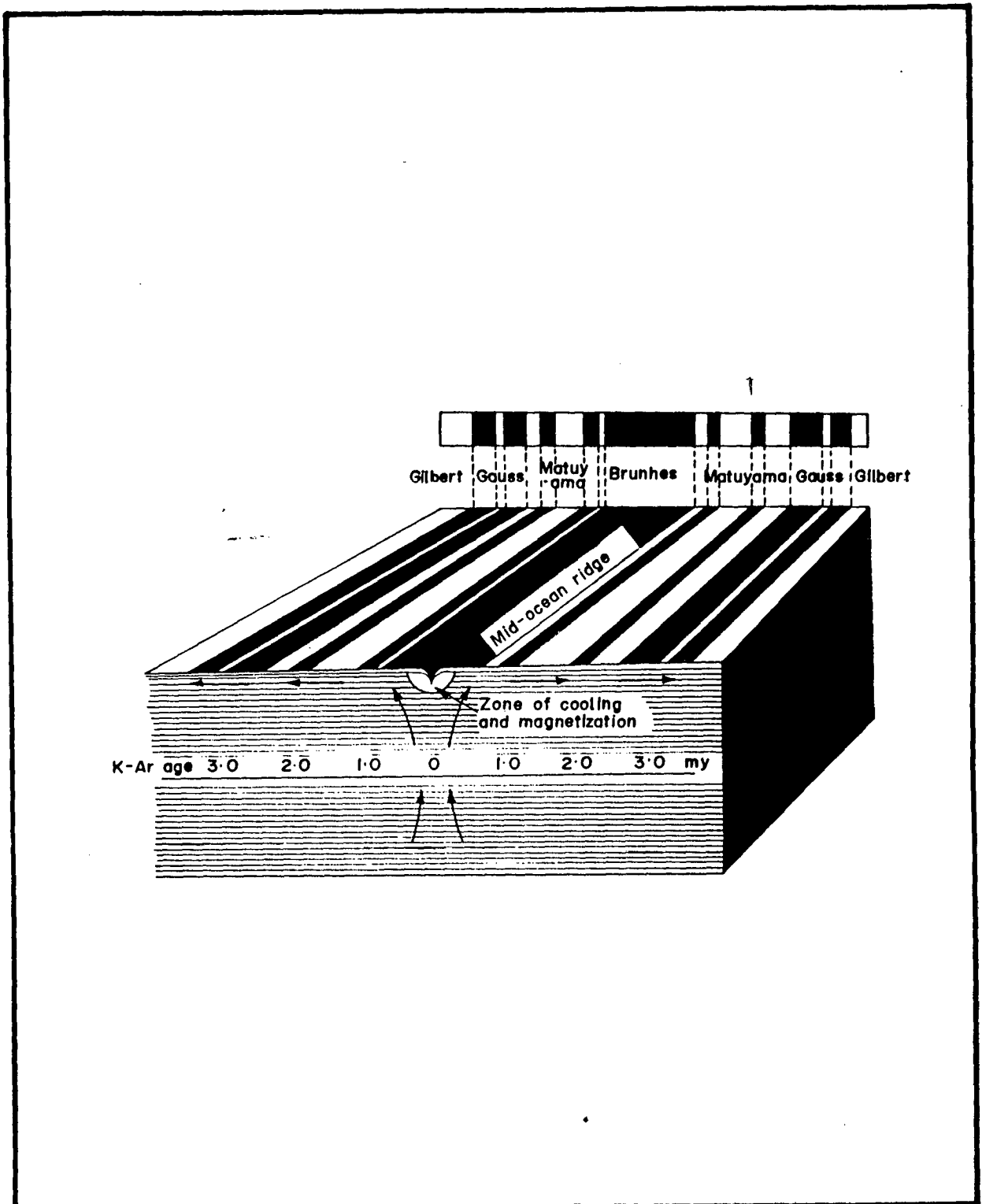


Figure 4.1 Conceptual model of the seafloor spreading process. Symmetric bands of normally and reversely magnetized blocks would be produced due to the combined effect of earth's magnetic field reversals and the seafloor spreading process.

in the present investigations were carried out based on the Vine and Matthews model.

In order to interpret the marine magnetic anomalies it is necessary to select a geomagnetic reversal time scale, which will serve as a reference frame to interpret and compare magnetic profiles. The following sections describe the geomagnetic reversal time scale and the model studies conducted on the observed magnetic anomalies in the Central Indian Basin.

4.2 GEOMAGNETIC POLARITY TIME SCALE

The paleomagnetic studies carried out on the volcanic rocks indicated that some of the rock samples exhibited a reverse magnetization i.e., about 180° from the present direction of the earth's magnetic field. It was proposed that, at the time of formation of these rocks the direction of the earth's field had been opposite to the present direction (*Brunhes, 1906; Mercanton, 1926*). These early observations have provided firm observational support to the concepts of seafloor spreading and plate tectonics more than half a century later. Application of the paleomagnetic reversal observations to determine geological time was first proposed by *Matuyama (1929)*. By using the available age information of the rock samples, he suggested that the earth's field had reversed polarity during early Pleistocene. Several other studies that followed (*Hospers, 1953; Sigurgeirsson, 1957; Kharmov, 1957; Cox, 1959*) have confirmed the periodic polarity changes in the earth's

magnetic field. These studies have laid foundation to the conceptualization of geomagnetic polarity time scale.

Between 1963 and 1969, several radiometrically dated polarity time scales were proposed (*Cox et al.*, 1963a; *Cox et al.*, 1963b; *Cox et al.*, 1964; *Doell et al.*, 1966; *Doell and Dalrymple*, 1966; *McDougall and Chamalaun*, 1966; *Cox et al.*, 1968; *Cox*, 1969), extending up to 4.5 Ma. These are based on paleomagnetic parameters and the Potassium - Argon (K-Ar) dating. *Pitman and Heirtzler* (1966) have generated a time scale extending up to 10 Ma using the marine magnetic anomalies over a profile across Pacific - Antarctic ridge by generating synthetics based on Vine and Matthews model, which is consistent with the radiometric time scale. The studies by *Pitman and Heirtzler* (1966) and *Vine* (1968), have clearly suggested that an extended magnetic reversal time scale can be constructed using seafloor magnetic anomalies.

Heirtzler et al., (1968), compared the relative distances to particular magnetic anomalies from the crests of spreading ridges in the North and South Pacific, the South Atlantic and the Indian Oceans. This was done in order to select a profile to generate standard magnetic anomaly time scale. South Atlantic profile was selected for its continuity and uniform spreading in the region. The profile was calibrated for the age of the anomaly at 3.35 Ma consistent with radiometric age determinations made on sub-areal basalts by

T. 201

Doell et al. (1966) and *McDougall and Chamalaun* (1966). *Heirtzler et al.* (1968) assumed a uniform half spreading rate of 1.9 cm/yr for the profile and extrapolated the spreading rate versus distance relationship to generate a time scale extending up to 80 Ma. This time scale was consistent with the Cretaceous age determination of a sediment core from the South Atlantic near anomaly 31. The time scale thus derived from a calibration at 3.35 Ma and supported by a single Late Cretaceous sediment core is remarkably well balanced and served as the basic time scale till date. Hereafter, this time scale will be referred as HDHPL-68. The time scales published after HDHPL-68, are only modest revisions, additions or recalibrations to the original scale. The plate reconstructions made using the HDHPL-68 time scale are still valid.

Revisions to the HDHPL-68 time scale were proposed by *Talwani et al.*(1971); *McKenzie and Sclater* (1971); *Blakely and Cox* (1972); *Blakely* (1974); and *Klitgord et al.* (1975). The recent revision to the HDHPL-68 time scale was proposed by *LaBrecque et al.*(1977). They incorporated parts of previously published time scales selecting the studies which provided increased resolution to the HDHPL-68 scale and those based on exclusively marine magnetic anomalies.

In addition to the approaches of radiochronology, which emphasized radiometric dating to calibrate the time scale and the magnetostratigraphy based on the characteristic binary sequence of normal and reversed polarity

of the geomagnetic field and the extrapolation of marine magnetic anomalies, one more approach that gained importance and which is comparable in resolution with magnetostratigraphy is biostratigraphy. Biostratigraphy is the organization of geologic time scale according to the irreversible process of biotic evolution and provides an ordinal framework for measuring the geologic time. The Paleogene time scale of *Hardenbol and Berggren (1978)*, emphasizes this approach.

Recent advances in magnetostratigraphic studies on exposed marine deposits in the Mediterranean region (*Lowrie et al., 1982*), and deep sea sediments recovered from the DSDP hydraulic piston core (*Poore et al., 1982, 1983*) have resulted in direct correlation between plankton biostratigraphy and magnetic polarity stratigraphy for the entire Cenozoic period. Thus the geochronology of this era requires integration of radiochronologic, magnetostratigraphic and biostratigraphic approaches in the construction of a consistent time scale. The time scales of *Ryan et al. (1974)* and *Lowrie and Alvarez (1981)* followed such an integrated approach. Following the integrated approach, *Berggren et al. (1985)* proposed Cenozoic geochronology based on magnetostratigraphy incorporating the magneto-biostratigraphic correlations for both marine and non marine sections and the age calibration data in the middle Cenozoic from radiometrically dated polarity stratigraphy.

4.2.1 SELECTION OF GEOMAGNETIC POLARITY TIME SCALE FOR THE MODEL STUDIES

The criterion for selection of suitable time scale as a reference for the model studies mainly depends on the range of anomalies expected in the study area and the degree of resolution desired. The time scales tied to the radiometric dates would be most accurate. However, these can be used only for the very young period. In most of the time scales, the resolution is higher at the younger ages as this period is well calibrated with the availability of radiometric dates. In the analysis of the older anomalies, the time scale with calibration points within the expected anomalies is desirable. The anomalies expected from the present study area are between A21 to A26, corresponding to the age of about 50 to 60 Ma.

The time scales based on radiochronology (Cox, 1969), marine magnetic anomalies (Hirtzler *et al.*, 1968) and the integrated approach (LaBrecque *et al.*, 1977; Berggren *et al.*, 1985) are shown in Figure 4.2. The normal polarity intervals of these time scales are listed in Tables T4.1, T4.2 and T4.3. The time scale proposed by Berggren *et al.*, (1985) was used for the generation of synthetics in the model studies, as it is well calibrated and tied to the high temperature K-Ar dates at anomalies 2A, 5, 12, 21 and 34.

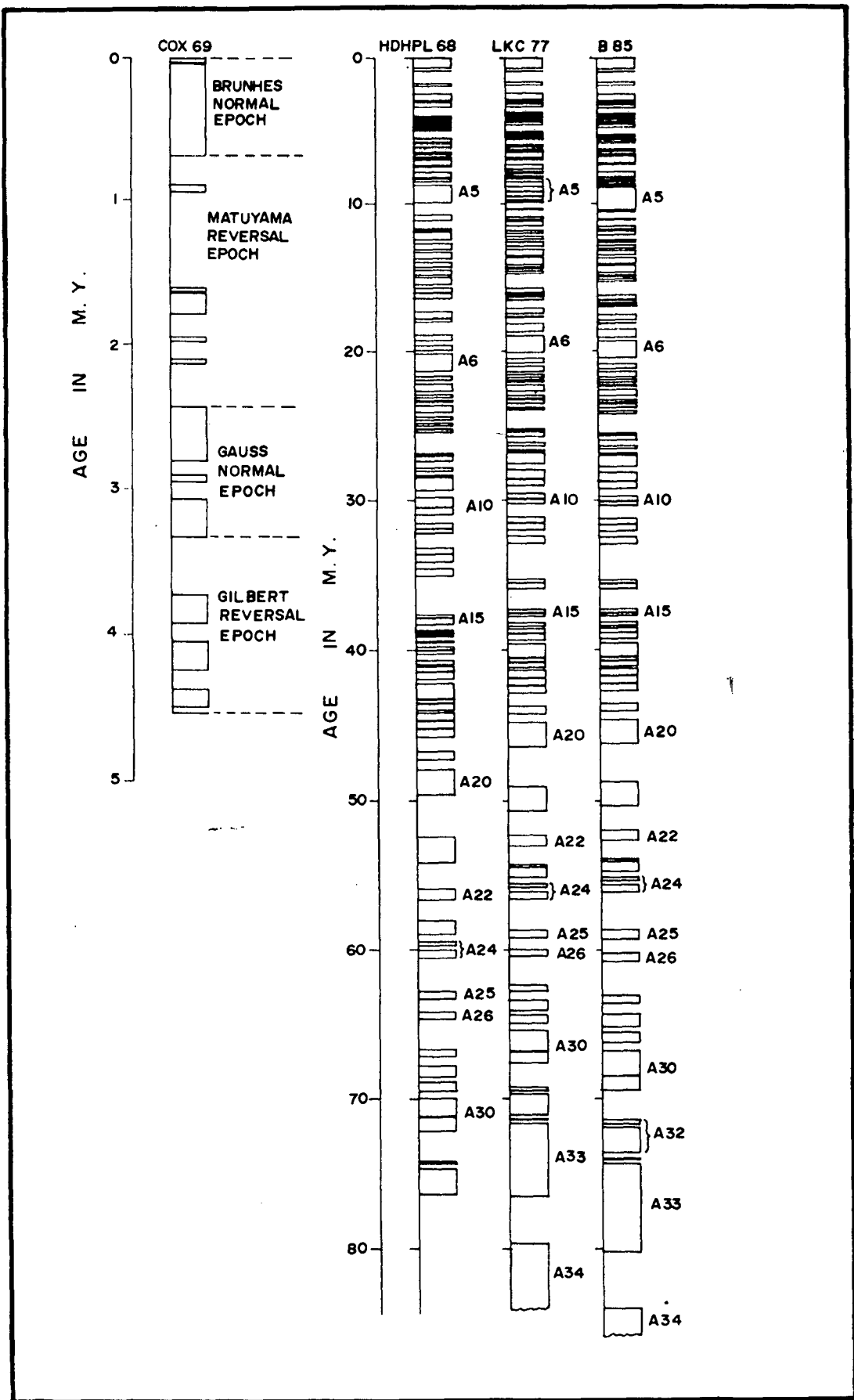


Figure 4.2 The geomagnetic polarity time scales of Cox (1969), Heirtzler et al. (1968), LaBrecque et al. (1977) and Berggren et al. (1985). The blocks indicate normal polarity events, anomaly numbers are shown.

TABLE T4.1

GEOMAGNETIC POLARITY TIME SCALE FOR
CENOZOIC and LATE CRETACEOUS
(Heirtzler et al., 1968)

INTERVALS OF NORMAL POLARITY (m.y)

00.00- 0.69	11.93-12.43	25.25-25.43	40.03-40.25	67.77-68.51
00.89- 0.93	12.72-13.09	26.86-26.98	40.71-40.97	68.84-69.44
01.78- 1.93	13.29-13.71	27.05-27.37	41.15-41.46	69.93-71.12
02.48- 2.93	13.96-14.28	27.83-28.03	41.52-41.96	71.22-72.11
03.06- 3.37	14.51-14.82	28.35-28.44	42.28-43.26	74.17-74.30
04.04- 4.22	14.98-15.45	28.52-29.33	43.34-43.56	74.64-76.33
04.35- 4.53	15.71-16.00	29.78-30.42	43.64-44.01	
04.66- 4.77	16.03-16.41	30.48-30.93	44.21-44.69	
04.81- 5.01	17.33-17.80	31.50-31.84	44.77-45.24	
05.61- 5.88	17.83-18.02	31.90-32.17	45.32-45.79	
05.96- 6.24	18.91-19.26	33.16-33.55	46.76-47.26	
06.57- 6.70	19.62-19.96	33.61-34.07	47.91-49.58	
06.91- 7.00	20.19-21.31	34.52-35.00	52.41-54.16	
07.07- 7.46	21.65-21.91	37.61-37.82	55.92-56.66	
07.51- 7.55	22.17-22.64	37.89-38.26	58.04-58.94	
07.91- 8.28	22.90-23.08	38.68-38.77	59.43-59.69	
08.37- 8.51	23.29-23.40	38.83-38.92	60.01-60.53	
08.79- 9.94	23.63-24.07	39.03-39.11	62.75-63.28	
10.77-11.14	24.41-24.59	39.42-39.47	64.14-64.62	
11.72-11.85	24.82-24.97	39.77-40.00	66.65-67.10	

TABLE T4.2

GEOMAGNETIC POLARITY TIME SCALE FOR
CENOZOIC and LATE CRETACEOUS
(LaBrecque et al., 1977)

Magnetic Normal		Magnetic Normal		Magnetic Normal		Magnetic Normal		Magnetic Normal	
Anomaly	Polarity	Anomaly	Polarity	Anomaly	Polarity	Anomaly	Polarity	Anomaly	Polarity
No.	Interval	No.	Interval	No.	Interval	No.	Interval	No.	Interval
	(m.y.)		(m.y.)		(m.y.)		(m.y.)		(m.y.)
1	00.00-00.70	5	08.54-08.86	5D	17.67-17.69	11	31.11-31.47	23	54.29-54.44
	00.89-00.95	5	08.87-09.15	5E	18.13-18.67	11	31.53-31.96	23	54.50-55.13
2	01.62-01.83	5	09.18-09.46	6	18.95-20.07	12	32.37-32.82	24	55.58-55.81
2A	02.41-02.84	5	09.48-09.74	6A	20.52-20.80	13	35.26-35.45	24	56.11-56.60
2A	02.91-03.00		09.86-09.91	6A	21.03-21.36	13	35.52-35.86	25	58.67-59.16
2A	03.10-03.32		10.36-10.43		21.56-21.72	15	37.26-37.48	26	59.97-60.41
3	03.76-03.85	5A	10.91-11.09		21.92-22.02	15	37.50-37.71	27	62.30-62.72
3	03.97-04.10	5A	11.22-11.49	6B	22.24-22.65	16	38.14-38.38	28	63.34-64.03
3	04.24-04.31		11.84-11.87	6C	22.96-23.13	16	38.55-38.84	29	64.34-64.90
3	04.40-04.59		11.96-12.01	6C	23.25-23.49	16	38.89-39.31	30	65.37-66.76
3A	05.12-05.29		12.23-12.41	6C	23.75-23.92	17	39.60-40.52	31	66.84-67.57
3A	05.43-05.62		12.61-12.87	7	25.24-25.35	17	40.59-40.80	32	69.20-69.43
	06.06-06.18		13.11-13.52	7	25.42-25.72	17	40.87-41.22		69.65-71.00
4	06.37-06.44		13.64-14.11	7A	26.14-26.33	18	41.40-41.85	32	71.34-71.38
4	06.51-06.90	5B	14.32-14.42	8	26.63-26.71	18	41.93-42.37	33	71.62-76.48
4	06.97-07.02	5B	14.59-14.73	8	26.79-27.54	18	42.44-42.88	34	79.65-108.19
4A	07.39-07.68	5C	15.72-16.02	9	27.96-28.56	19	43.77-44.24		
4A	07.87-07.95	5C	16.06-16.24	9	28.62-29.04	20	44.85-46.40		
5	08.15-08.23	5C	16.31-16.50	10	29.57-29.88	21	49.04-50.67		
5	08.34-08.50	5D	17.11-17.45	10	29.94-30.19	22	52.31-53.00		

TABLE T4.3

GEOMAGNETIC POLARITY TIME SCALE FOR
CENOZOIC and LATE CRETACEOUS
(Berggren et al., 1985)

Magnetic Normal		Magnetic Normal		Magnetic Normal		Magnetic Normal		Magnetic Normal	
Anomaly No.	Interval (m.y.)	Anomaly No.	Interval (m.y.)	Anomaly No.	Interval (m.y.)	Anomaly No.	Interval (m.y.)	Anomaly No.	Interval (m.y.)
1	00.00-00.73		10.54-10.59	6A	21.38-21.71	13	35.54-35.87	25	58.64- 59.24
	00.91-00.98		11.03-11.09	6AA	21.90-22.06	15	37.24-37.46	26	60.21- 60.75
2	01.66-01.88	5A	11.55-11.73	6AA	22.25-22.35	15	37.48-37.68	27	63.03- 63.54
2A	02.47-02.92	5A	11.86-12.12	6B	22.57-22.97	16	38.10-38.34	28	64.29- 65.12
2A	02.99-03.08		12.46-12.49	6C	23.27-23.44	16	38.50-38.79	29	65.50- 66.17
2A	03.18-03.40		12.58-12.62	6C	23.55-23.79	16	38.83-39.24	30	66.74- 68.42
3	03.88-03.97	5AA	12.83-13.01	6C	24.04-24.21	17	39.53-40.43	31	68.52- 69.40
3	04.10-04.24	5AB	13.20-13.46	7	25.50-25.60	17	40.50-40.70	32	71.37- 71.65
3	04.40-04.47	5AC	13.69-14.08	7	25.67-25.97	17	40.77-41.11	32	71.91- 73.55
3	04.57-04.77	5AD	14.20-14.66	7A	26.38-26.56	18	41.29-41.73		73.96- 74.01
3A	05.35-05.53	5B	14.87-14.96	8	26.86-26.93	18	41.80-42.23	33	74.30- 80.17
3A	05.68-05.89	5B	15.13-15.27	8	27.01-27.74	18	42.30-42.73	34	84.00-118.00
	06.37-06.50	5C	16.22-16.52	9	28.15-28.74	19	43.60-44.06		
4	06.70-06.78	5C	16.56-16.73	9	28.80-29.21	20	44.66-46.17		
4	06.85-07.28	5C	16.80-16.98	10	29.73-30.03	21	48.75-50.34		
4	07.35-07.41	5D	17.57-17.90	10	30.09-30.33	22	51.95-52.62		
4A	07.90-08.21	5D	18.12-18.14	11	31.23-31.58	23	53.88-54.03		
4A	08.41-08.50	5E	18.56-19.09	11	31.64-32.06	23	54.09-54.70		
	08.71-08.80	6	19.35-20.45	12	32.46-32.90	24	55.14-55.37		
5	08.92-10.42	6A	20.88-21.16	13	35.29-35.47	24	55.66-56.14		

4.3 MODEL STUDIES : MARINE MAGNETIC ANOMALIES

4.3.1 FACTORS INFLUENCING THE MARINE MAGNETIC ANOMALIES

Modeling of the marine magnetic anomalies are carried out based on the concept of Vine and Matthew's block model in the present investigations. The method involves the computation of synthetic magnetic anomaly resulting from normal and reversely magnetized parallel blocks representing the magnetized oceanic crust. The vertical thickness of the magnetized layer is taken as constant and it is assumed to be within the basaltic layer (layer 2 of the oceanic crust). It is conceivable that thickness of the magnetized layer varies and may extend up to the Curie isotherm which is about 580 °C (*Vine, 1968*), for the magnetite. If we consider the thickness of the oceanic lithosphere based on thermal evolution models, the isotherm defining 580 °C may reach a thickness of about 30.0 km for a lithosphere of 40 Ma age (*Arkani-Hamed and Strangway, 1986*). This observation suggests that the region shallower than the depth of the 580 °C isotherm may contribute to the observed magnetic anomalies (*Arkani-Hamed, 1991*). As the ocean basins are about 4.0 km deep, the shapes of the anomalies are not seriously affected by the assumed thickness of the model (*Vacquier, 1972*). There is no general agreement on the thickness and susceptibility of the basaltic layer which produces the magnetic anomalies (*Talwani et al., 1971; McKnezie and Sclater, 1971*). Susceptibility measurements of the pillow basalts dredged from the ridge axes (*Irving et al., 1970; Marshall and Cox, 1971*) have shown

an average susceptibility of 0.05 cgs units and these studies have suggested that a model with a thickness of 200-400 m would be sufficient to produce the observed anomalies. The susceptibility of the dredged samples appears to vary within a given region. In general, the susceptibilities of the rock specimens from the central valley of the ridge axis have shown higher values of about 0.0574 cgs units and decreases to about 0.0092 cgs units away from the ridge axis (*Irving et al.*, 1970). In a region of unknown magnetization and magnetic layer thickness, relatively thick blocks with low magnetization or thin blocks with large magnetization can be ascribed to generate the synthetic anomalies (*Talwani et al.*, 1971). A constant thickness and magnetization parameters are preferred. *Cande and Kent* (1976) have proposed a two layer approximation of the basaltic layer and suggested that the rapidly cooled top 500 m of the 2 km thick upper layer contributes to about three quarters of total amplitude of the magnetic anomalies. Whereas the slowly cooled lower layer which experiences delayed acquisition of magnetization contributes one quarter.

Model studies are carried out by varying the thickness and susceptibility of the magnetized blocks. In the first case, the thickness of the blocks are varied with a constant assumed susceptibility and in the second case the susceptibility is varied by keeping the block thickness constant. Figures 4.3 and 4.4 show the synthetic anomalies generated with various assumed thickness and susceptibilities of the magnetized blocks. These studies have shown that the variations in the assumed susceptibility and thickness values

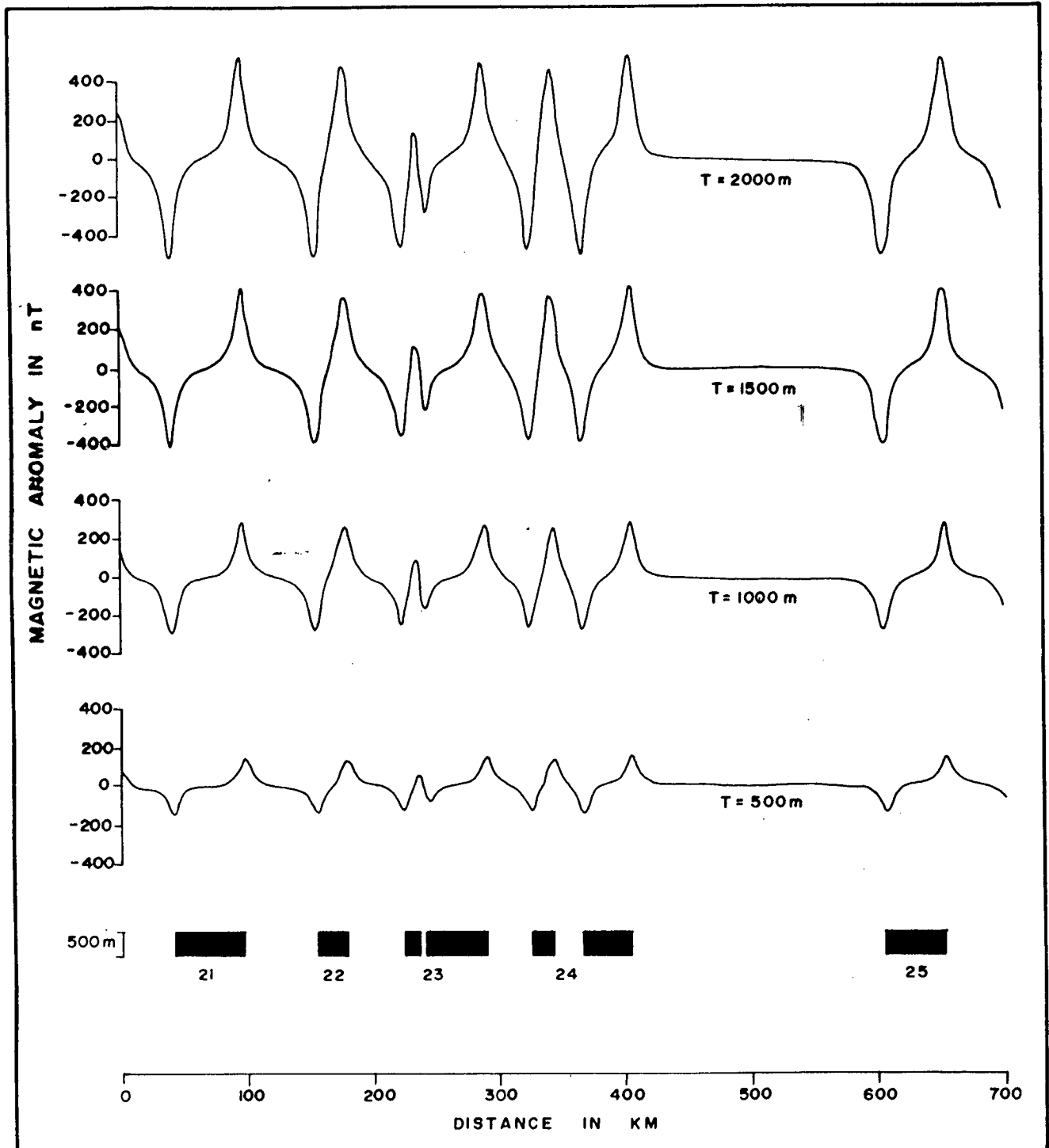


Figure 4.3 Synthetic magnetic anomalies generated by varying the thickness of the assumed blocks of the model. A constant susceptibility of 0.01 cgs units is used.

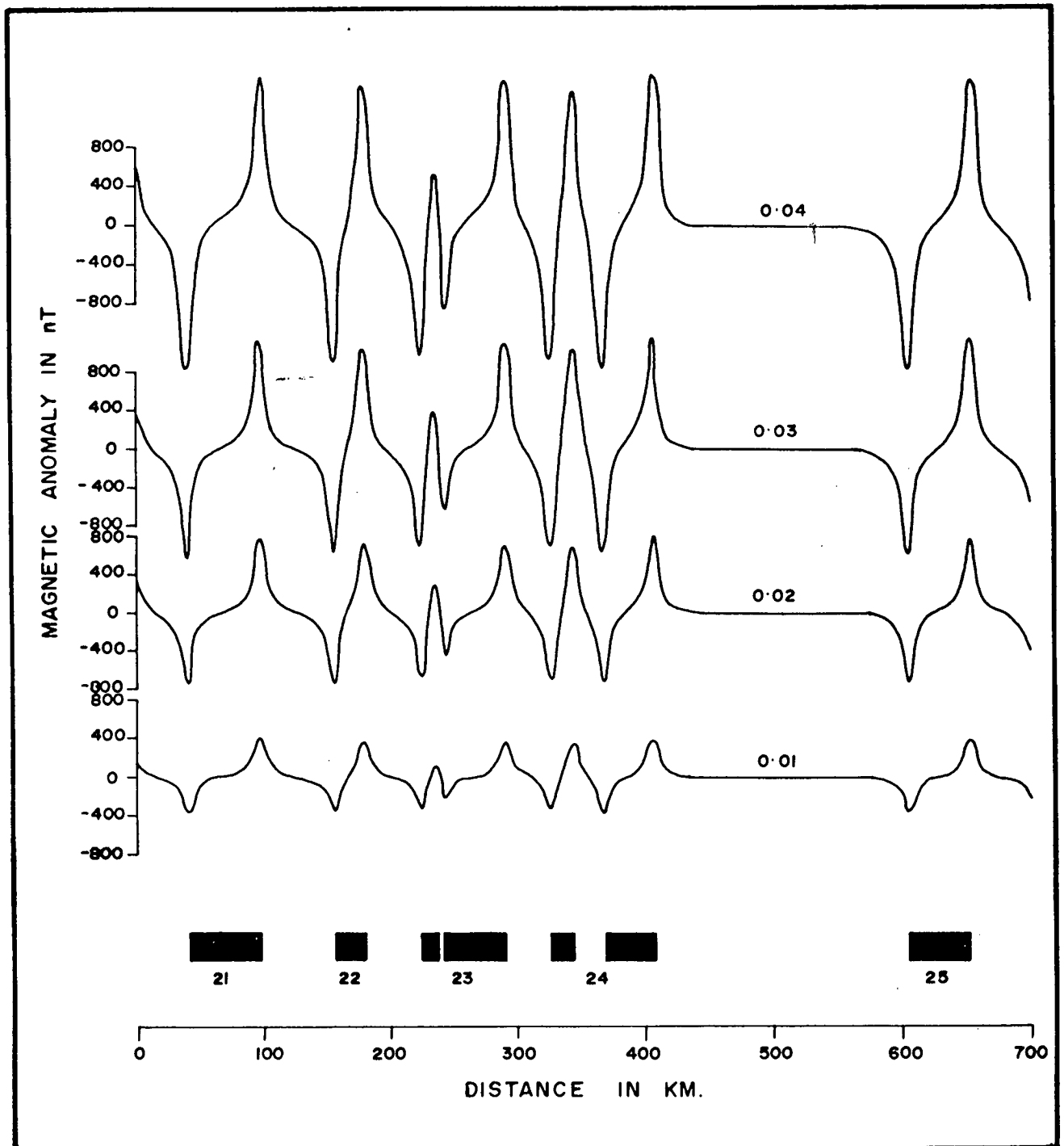


Figure 4.4 Synthetic magnetic anomalies generated by varying the susceptibility of the model blocks. The thickness of the blocks is kept constant at 500m.

primarily affect the amplitude of the anomalies, while the shape and sequence of the anomalies is a function of the Vine and Matthew's model and the geomagnetic polarity scale. In the present study, a constant thickness of 500 m (*Talwani et al.*, 1971) and a susceptibility of 0.01 cgs units (*McKenzie and Sclater*, 1971) was used in conjunction with the geomagnetic polarity scale of *Berggren et al.* (1985), to generate the synthetic magnetic anomalies. As the primary aim of the present studies is to identify the magnetic anomalies and not to estimate the thickness of the magnetized layer, the selection of these parameters prevailed.

The shape of the anomalies is also dependent on the azimuth of the profile and the latitude at which the source layer got magnetized. As long as the spreading is in E-W direction and the generated crust does not drift north or south, the pattern of the observed anomalies remain same, as there is no change in the magnetic inclination at the time of generation and observation of the anomalies. If the magnetized crust moves in the N-S direction as a result of spreading process and the re-orientation of the ridge axis, then the shape of the observed anomalies will be affected by the change in the magnetic inclination at the time of generation and observation of the anomalies. In the Indian Ocean, the ancient spreading was in the N-S direction and it is required to take into account the magnetic parameters existed at the time of generation of the anomalies. *McKenzie and Sclater* (1971), suggested a modification to the two dimensional strip model initially developed by *Talwani and Heirtzler* (1964), to account for the changes in

latitude and azimuth between the epochs of generation and observation of the anomalies. The modified program which is adopted to run on the ND 570 system was used for the generation of synthetic anomalies in the present study. Figure 4.5 illustrates a hypothetical case depicting the variation in the shape of the anomalies produced by E-W spreading at 40 °S and drifted north and observed at various latitudes. It can be seen that the crust generated by E-W spreading observed at magnetic equator produces no anomalies as the horizontal and vertical components become equal to zero. When seafloor moves across the magnetic equator positively magnetized blocks give rise to negative anomalies when observed in the northern hemisphere (Figure 4.5). These factors were taken into consideration while carrying out the model studies.

The observed and computed profiles are compared. The shape of the anomalies are considered more important while identifying the anomalies due to the various reasons discussed above. Synthetic profiles were generated with assumed spreading rates and at various paleolatitudes. The parameters used for the computed profile that fits best are considered as the one representing the paleogeographic position during the generation of the anomaly.

All the 15 profiles were modeled in this manner and each profile along with the corresponding model is shown in Figures 4.6 to 4.20.

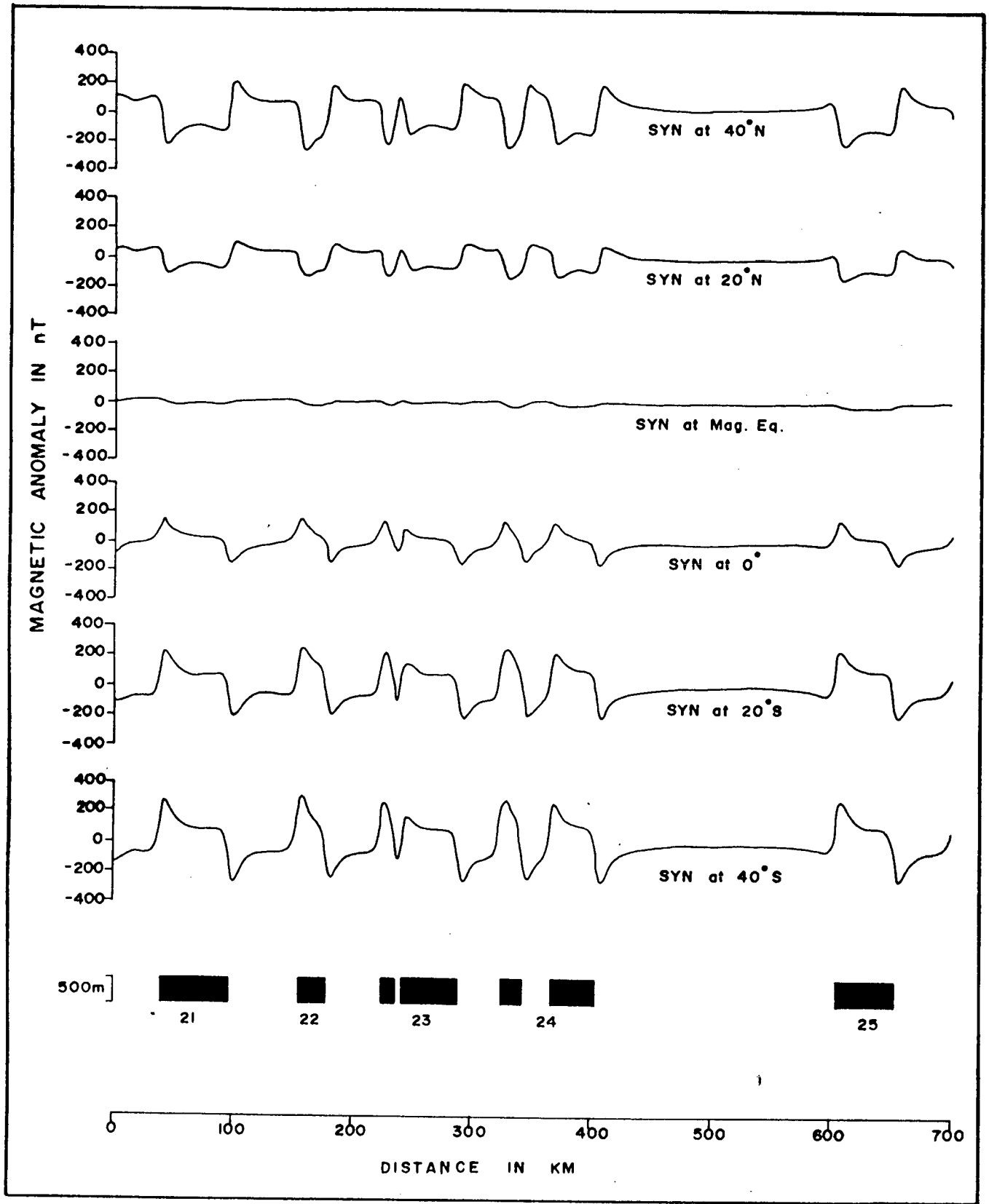


Figure 4.5 Synthetic magnetic anomalies as observed at various latitudes (see text for explanation). Note that the positively magnetized blocks give rise to negative anomalies when observed in the northern hemisphere.

Total field?

4.3.2 DESCRIPTION OF THE OBSERVED MAGNETIC ANOMALIES AND BATHYMETRY. IDENTIFICATION OF MARINE MAGNETIC ANOMALIES

The observed anomalies within the study area when viewed along with the earlier observation of *McKenzie and Sclater* (1971), in the near vicinity, suggested that they belong to the older anomalies in the range A21 to A26. Synthetic anomalies are generated with assumed spreading rates and at various paleolatitudes. The synthetics generated assuming that the anomalies were generated by an E-W trending ridge at 35 °S resulted in the best fit. A variable spreading rate of 3.6 cm/yr between anomalies A21 and A23 and 8.0 cm/yr between anomalies A23 and A26 was derived by matching the observed and computed anomalies.

In general, the observed profiles exhibited long wave length anomalies and the amplitude varied from 300 to 400 gammas. All the 15 profiles are modeled and the characteristics of individual profiles are described below. The locations of these profiles numbered from *CB-1* to *CB-15* are shown in the track chart (Figure 2.7).

i Profile CB-1

Along this profile the characteristic feature of the anomaly A23 is conspicuous with a narrow low amplitude anomaly followed by a broad and

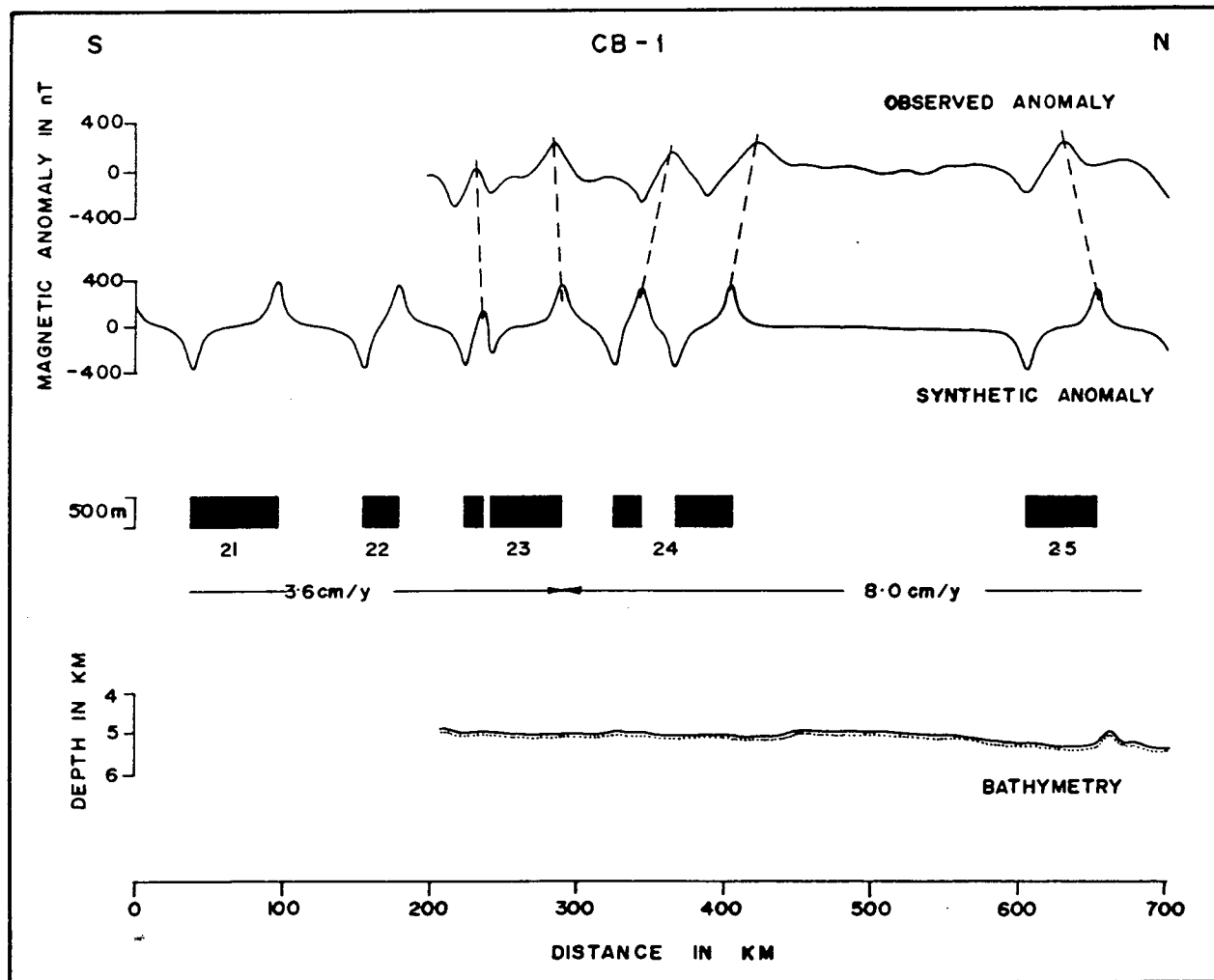


Figure 4.6 The synthetic anomalies generated by assuming the ridge axis to be at 35°S . Susceptibility of the model blocks is assumed to be 0.01 cgs units and the thickness of the block is kept at 500m (McKenzie and Slater, 1971; Taiwani et al., 1971). A variable spreading rate of 3.6 cm/yr between anomalies A21 and A23 and 8.0 cm/yr between anomalies A23 and A25 were inferred. Berggren et al. (1985) time scale was used to generate the synthetic anomalies. The observed magnetic anomaly profile CB-1 and the bathymetry are shown.

higher amplitude anomaly. This characteristic feature is identified as the anomaly A23. The anomaly A23 is followed by the twin peaked anomaly A24 and a long reversal between A24 and A25 (Figure 4.6). The bathymetry along the profile is gentle with an abyssal hill at the northern end of the profile. The average depth is in the range of 4800 to 5000m.

ii Profile CB-2

The anomaly signature along this profile is very much similar to the profile *CB-1*. The anomalies A23, A24, A25 and A26 can be easily identified (Figure 4.7). The bathymetry is gentle with the average depth ranging from 5000 to 5300 m.

iii Profile CB-3

Along this profile in addition to the anomalies A23 to A26, the anomaly A22 is also observed. The anomaly A26 is not fully recorded due to the limited length of the profile. The bathymetry is smooth with the average depth around 5000m (Figure 4.8).

iv Profile CB-4

The anomalies A22, A23 and A24 can be identified along this profile. A seamount of 700m is observed in the middle of the profile and this feature appears to have distorted the anomaly signature of A23 (Figure 4.9).

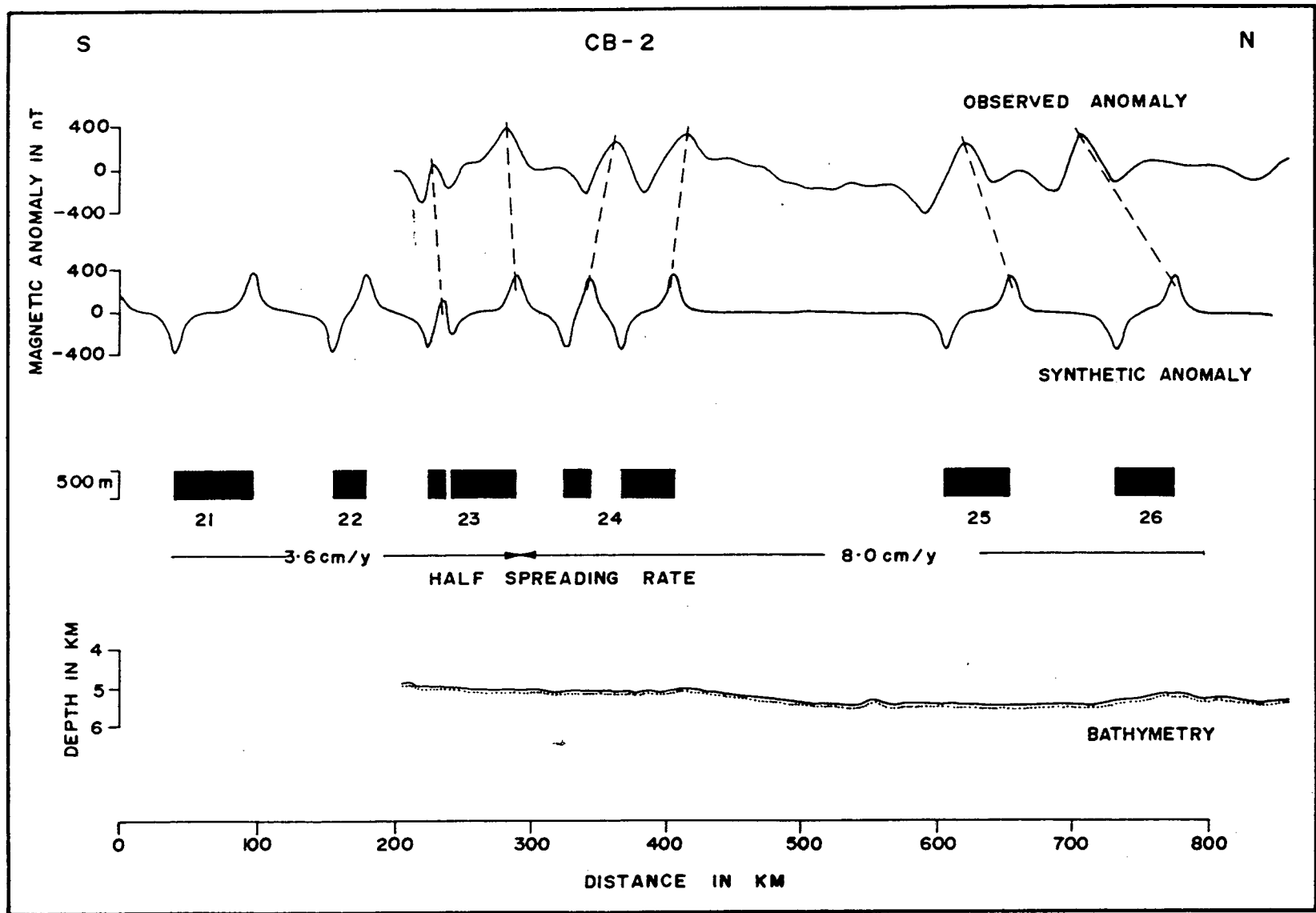


Figure 4.7 Observed magnetic anomaly and bathymetry along the profile CB-2 along with the synthetic anomalies and the model. Model parameters are same as mentioned in figure 4.6

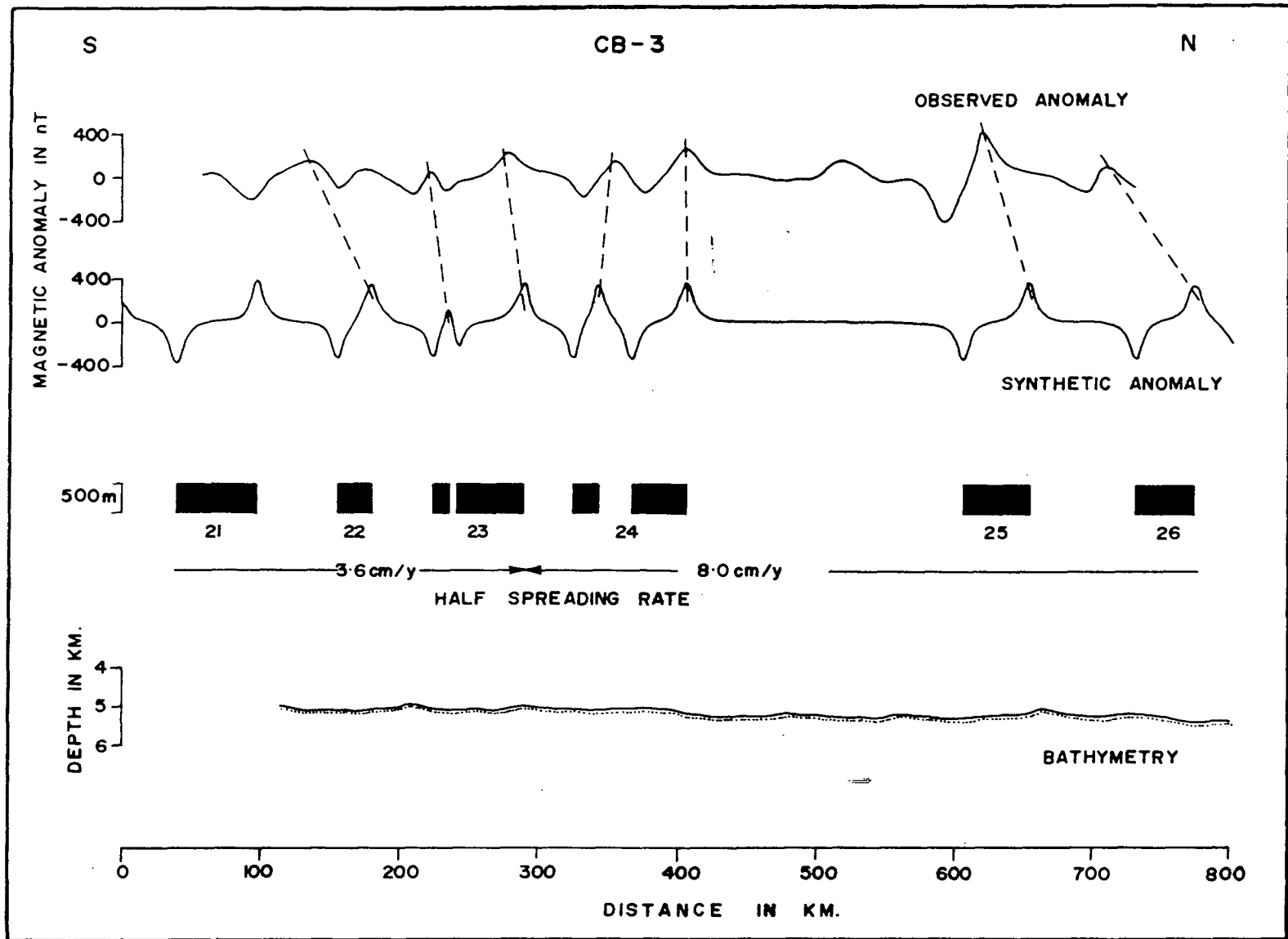


Figure 4.8 Observed magnetic anomaly and bathymetry along the profile CB-3 along with the synthetic anomalies and the model. Model parameters are same as mentioned in figure 4.6

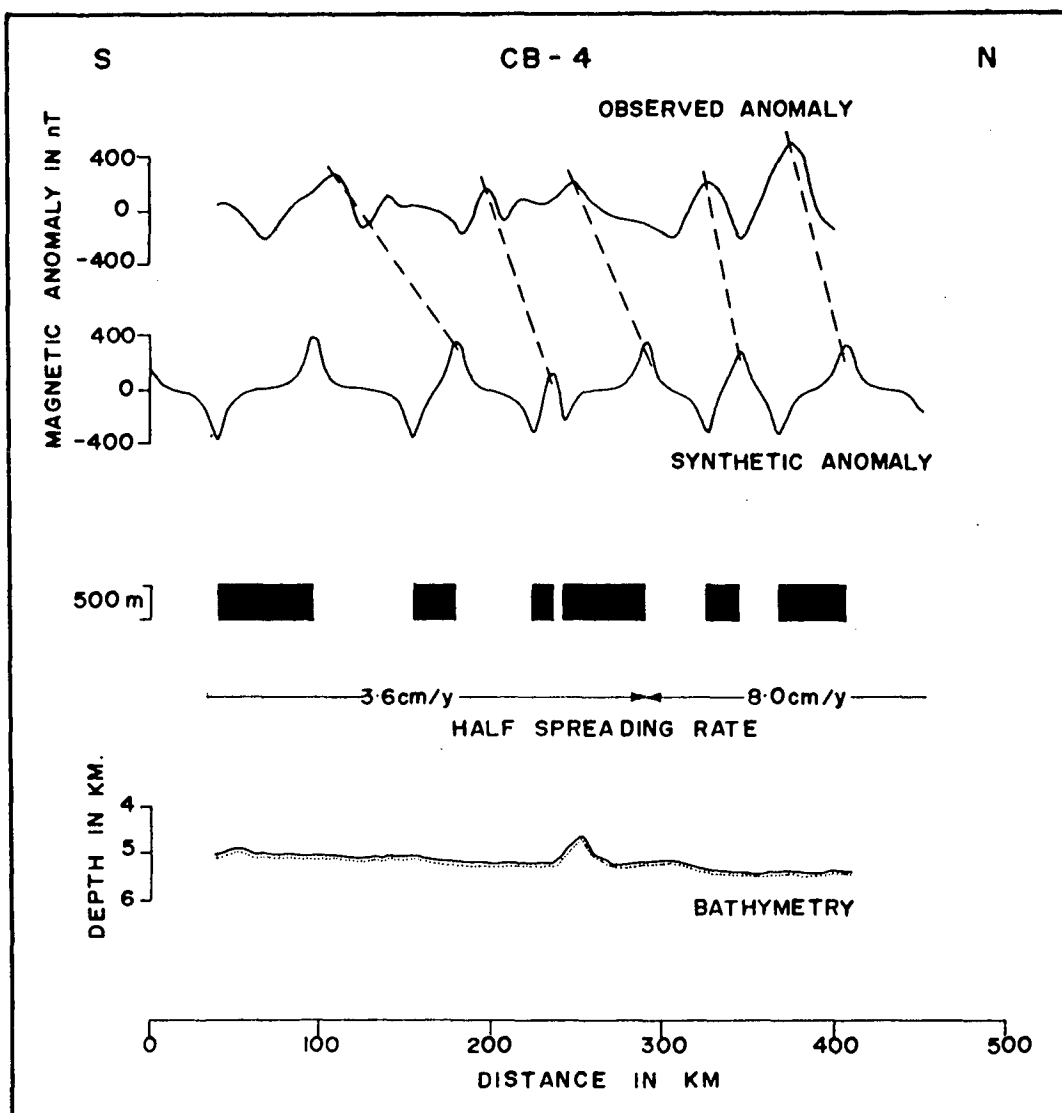


Figure 4.9 Observed magnetic anomaly and bathymetry along the profile CB-4 along with the synthetic anomalies and the model. Model parameters are same as mentioned in figure 4.6

v Profile CB-5

The anomaly A24 is more pronounced along this profile compared to the anomalies A22 and A23 (Figure 4.10). At the southern end of the profile the expression of A21 is also noticed. The bathymetry is smooth with average depth around 5000 m. An abyssal hill of 200 m is observed at about 150 kms from the southern end of the profile.

vi Profile CB-6

Along this profile anomaly A24 can be identified without difficulty but the anomaly signature of A23 is distorted (Figure 4.11). The bathymetry is rugged compared to the profiles to the east with undulations of about 100 m, the average depth is 5000 m.

vii Profile CB-7

The anomalies A22, A23 and A24 are well defined along this profile. Bottom topography is rugged with a valley like feature at about 150 km from the southern end of the profile. This bathymetric feature is reflected in the magnetics between anomalies A22 and A23 (Figure 4.12).

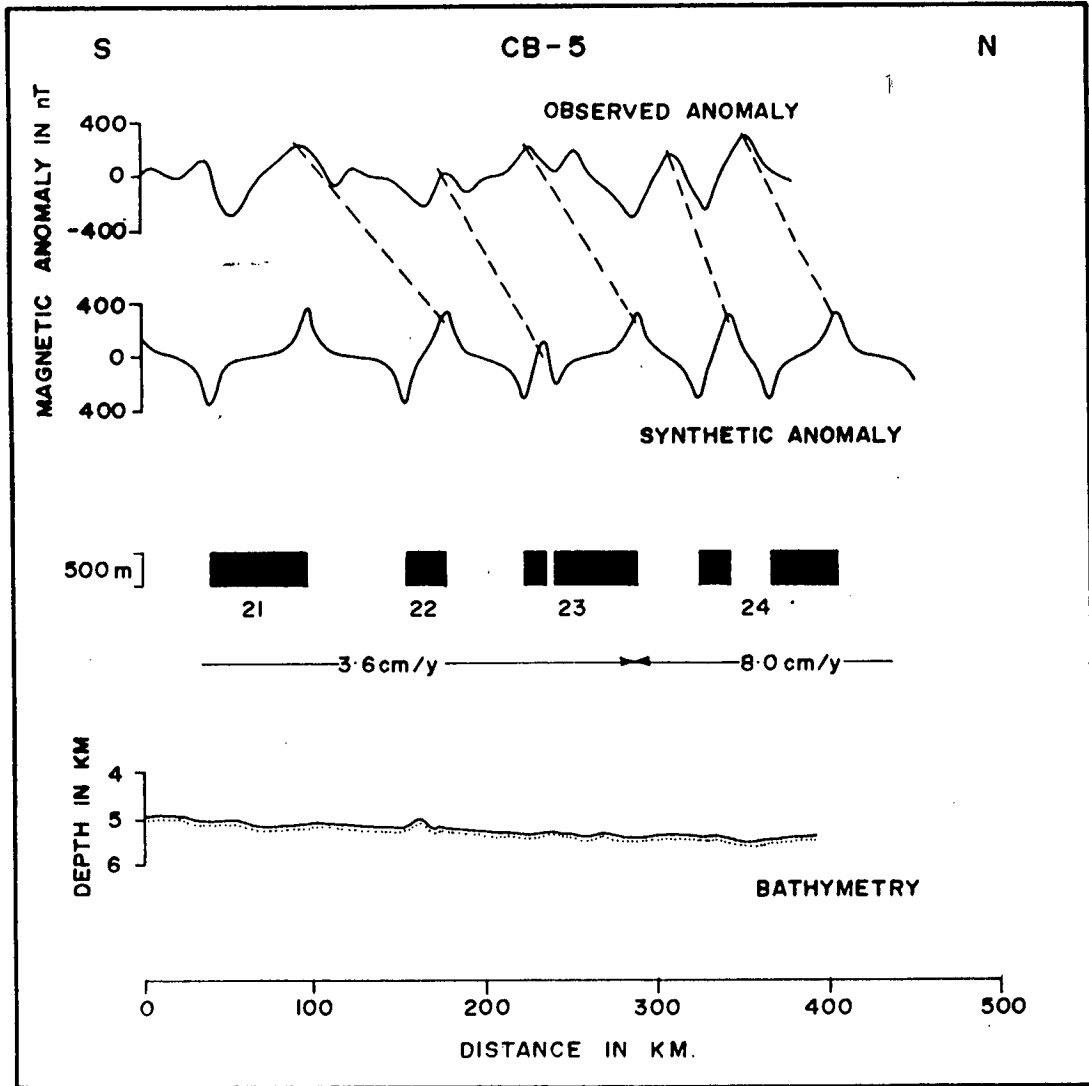


Figure 4.10 Observed magnetic anomaly and bathymetry along the profile *CB-5* along with the synthetic anomalies and the model. Model parameters are same as mentioned in figure 4.6

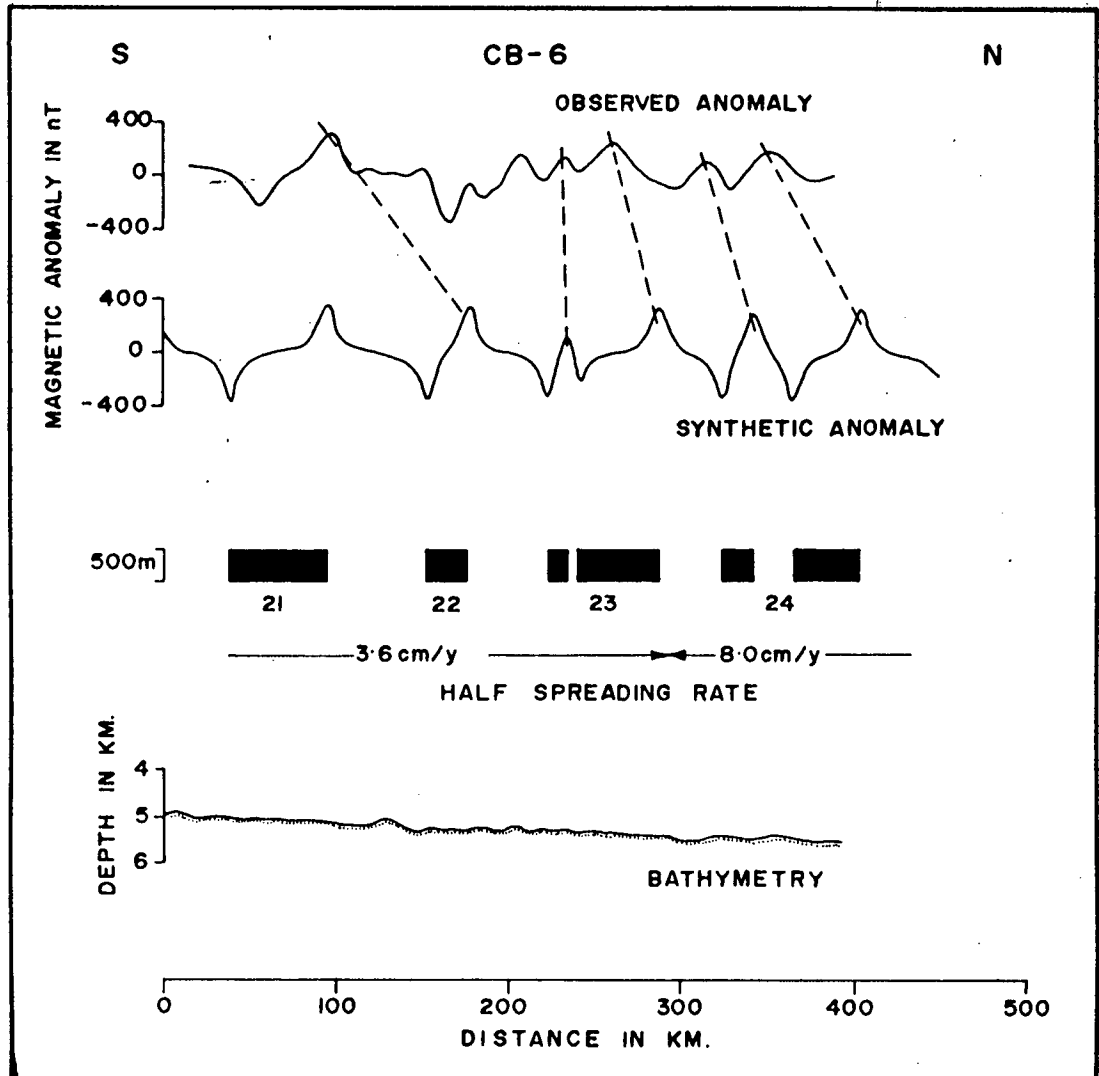


Figure 4.11 Observed magnetic anomaly and bathymetry along the profile *CB-6* along with the synthetic anomalies and the model. Model parameters are same as mentioned in figure 4.6

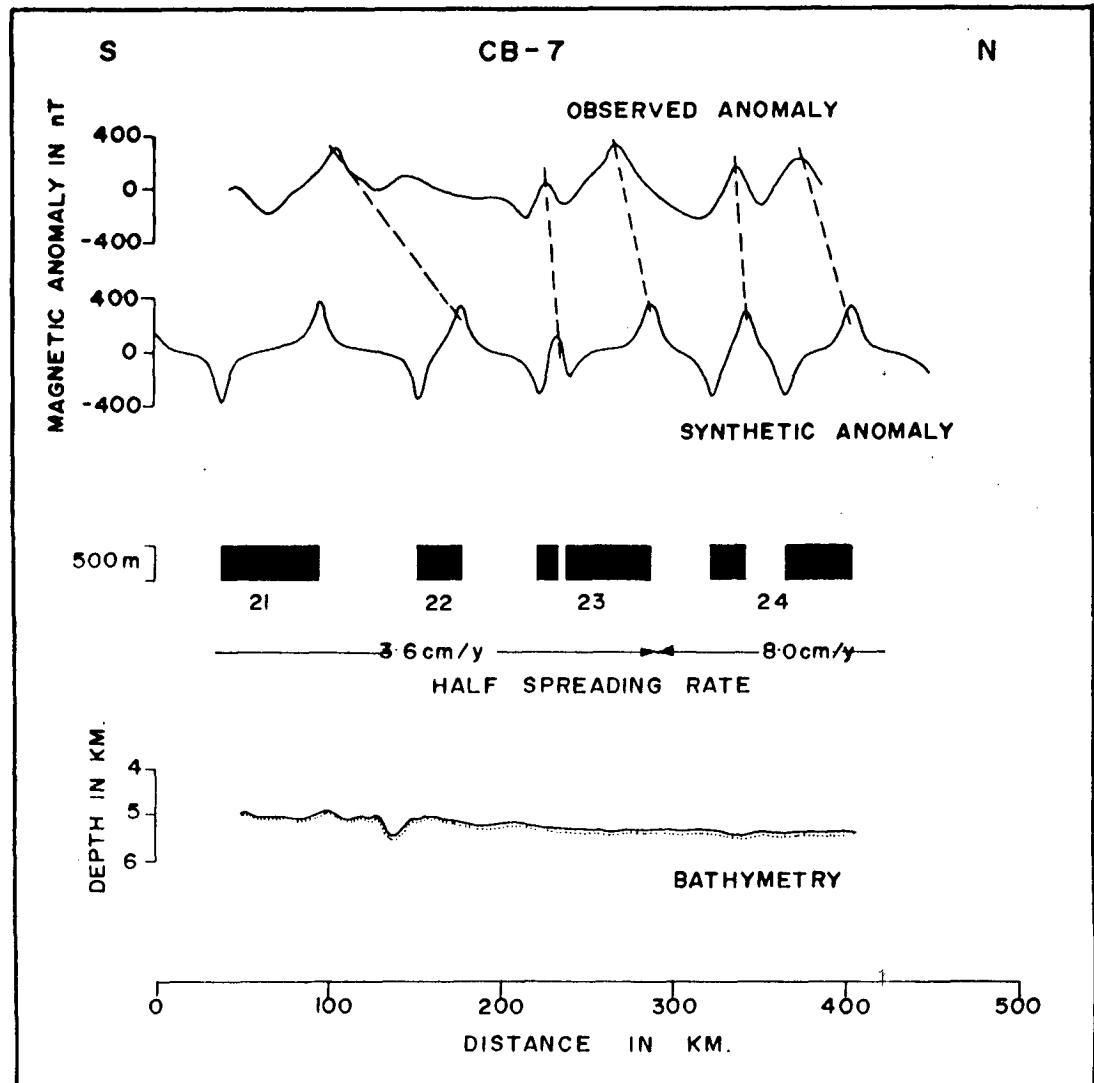


Figure 4.12 Observed magnetic anomaly and bathymetry along the profile CB-7 along with the synthetic anomalies and the model. Model parameters are same as mentioned in figure 4.6

viii Profile CB-8

The anomalies A21, A22 and A23 can be recognized on this profile, these anomalies are well defined with their characteristic features. At the southern end of the profile near anomaly A21 the bottom topography is rugged with a valley and hill like features (Figure 4.13). The depth along this profile varies from 4500 to 5500 m, the maximum variation occurring at the southern end of the profile.

ix Profile CB-9

Along this profile the anomalies A22, A23, A24 can be identified and the anomaly signature of A21 is very subdued. The anomaly A24 is characterized by the twin peaks observed at the northern end of the profile. Bathymetry along the profile is moderately smooth with an average depth of 5000 m (Figure 4.14).

x Profile CB-10

The anomaly identifications are difficult along this profile, as the anomaly signatures are subdued. However, based on the anomaly identifications on the adjacent profiles the anomalies are marked. The bathymetry is smooth with abyssal hills of about 400m at the southern end and towards north of the profile (Figure 4.15).

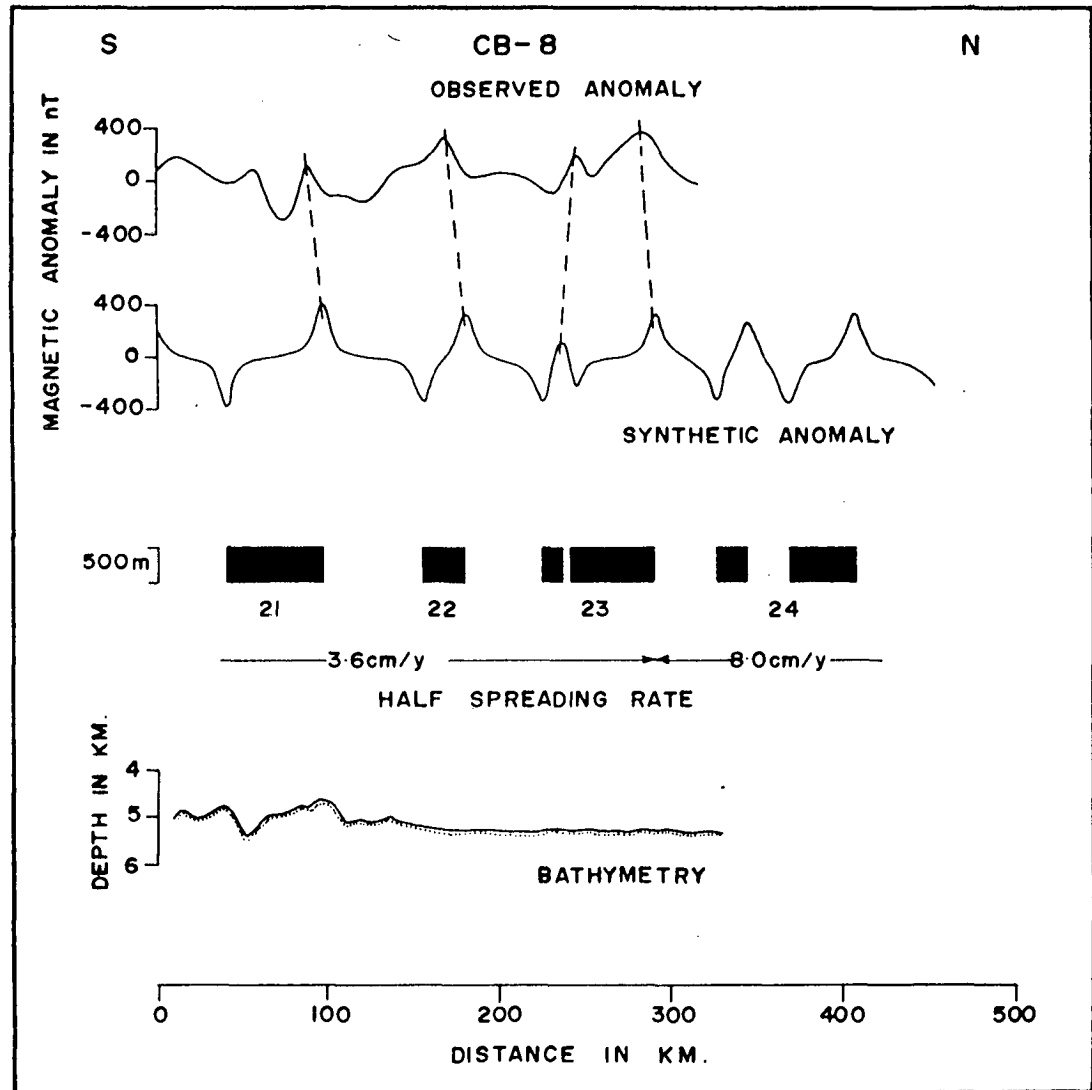


Figure 4.13 Observed magnetic anomaly and bathymetry along the profile *CB-8* along with the synthetic anomalies and the model. Model parameters are same as mentioned in figure 4.6

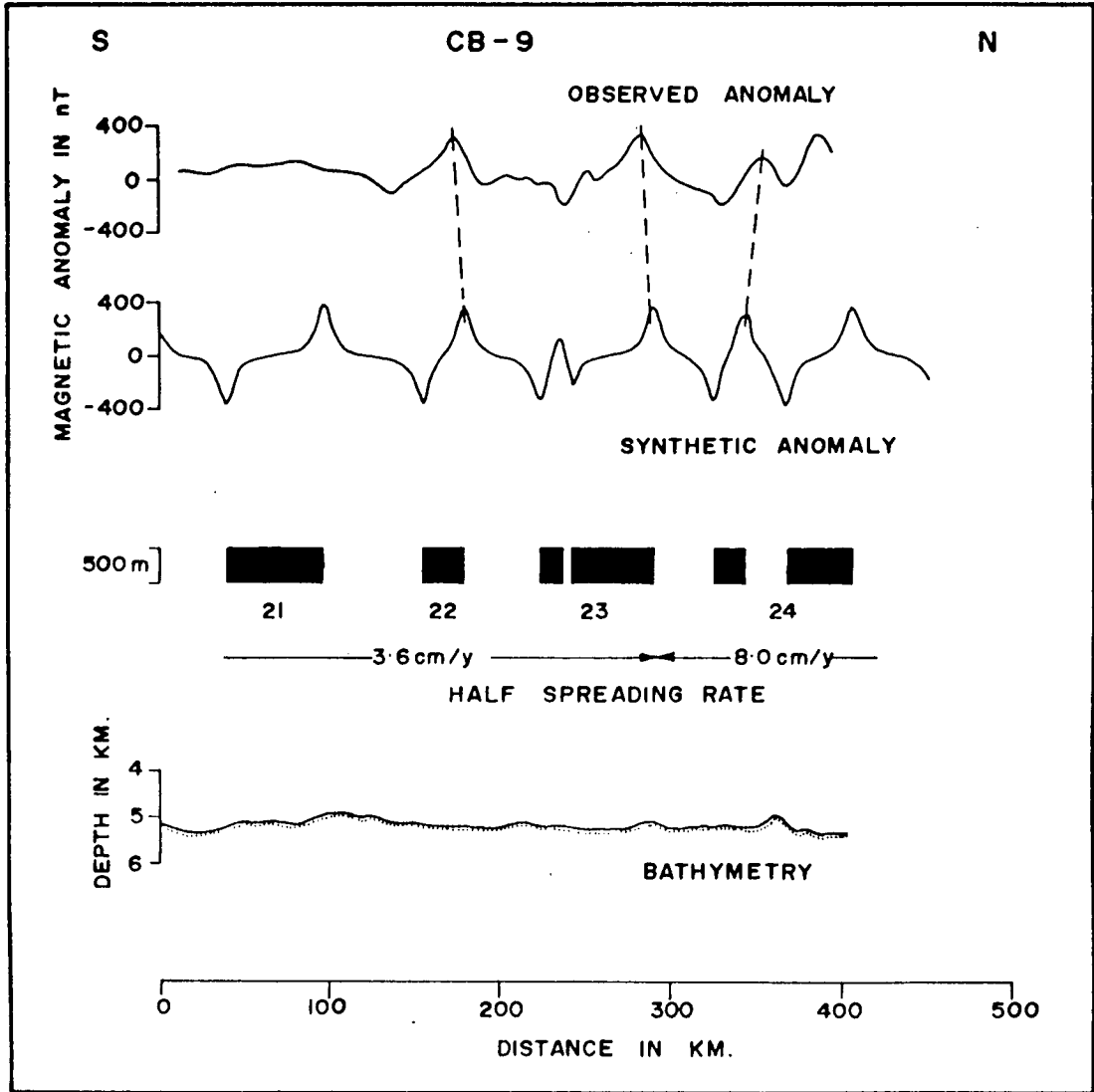


Figure 4.14 Observed magnetic anomaly and bathymetry along the profile *CB-9* along with the synthetic anomalies and the model. Model parameters are same as mentioned in figure 4.6

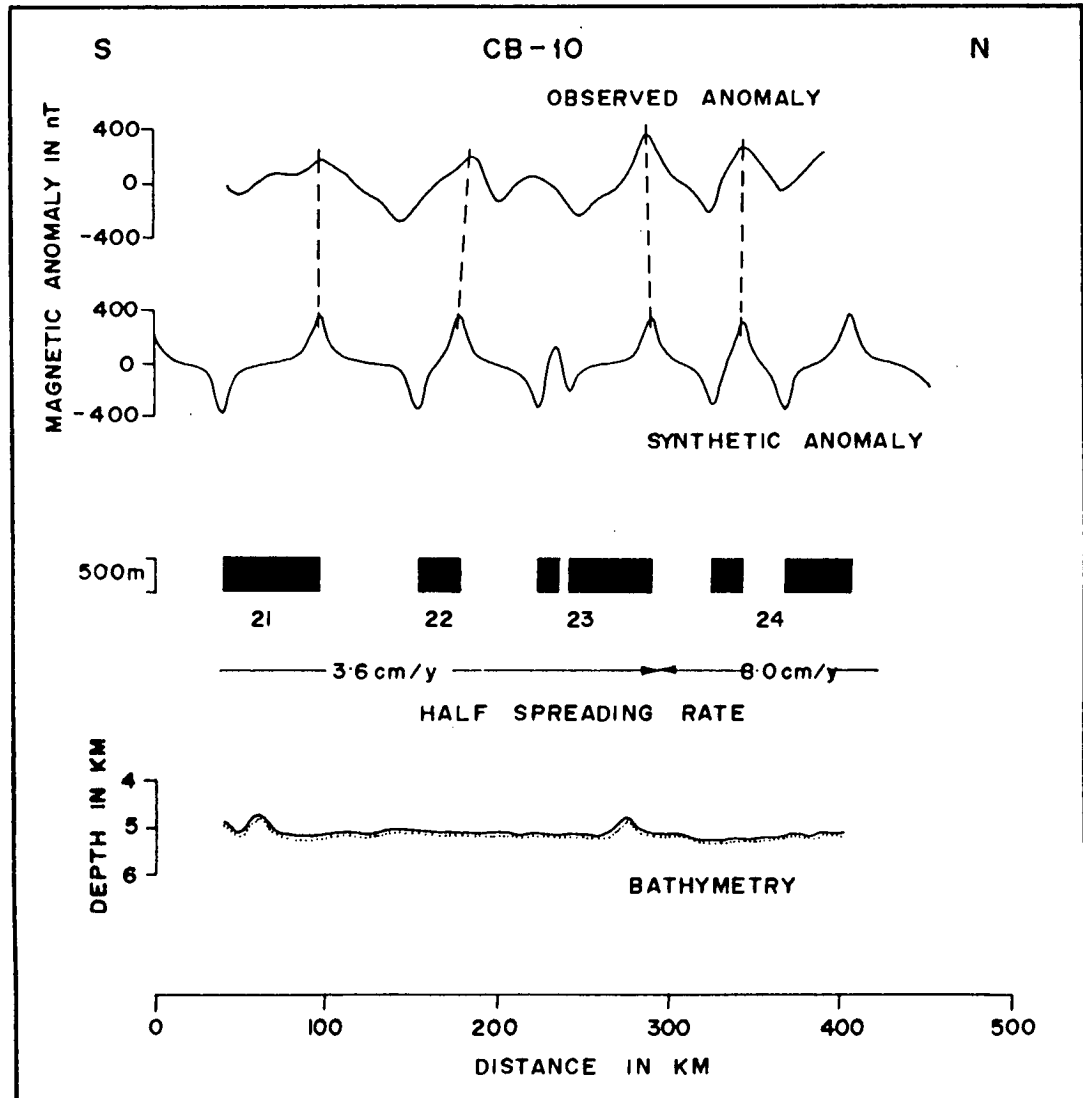


Figure 4.15 Observed magnetic anomaly and bathymetry along the profile CB-10 along with the synthetic anomalies and the model. Model parameters are same as mentioned in figure 4.6

xi Profile CB-11

The anomalies A22 and A23 are identified along this profile by their characteristic sequence of a low amplitude anomaly bounded on either side by high amplitude anomalies (Figure 4.16). The anomaly A24 is identified even though a single peak only is recorded. The bathymetry is moderately rugged with small scale undulations and a prominent broad low of about 500m at the southern end of the profile.

xii Profile CB-12

Along this profile the anomalies A22, A23, A24 are identified without difficulty as the characteristic features are well reflected in the observed anomalies. The anomaly A21 is not very clear. Towards the northern end of the profile following anomaly A24 no identifiable anomaly is observed. The expected anomaly A25 appears to be located further north. The bathymetry along the profile is smooth with the average depth around 5000 m (Figure 4.17).

xiii Profile CB-13

The profile *CB-13* is much similar to the profile *CB-12*. The anomalies A22, A23, A24 are identified on the profile. The bathymetry is smooth with a long wavelength elevated feature of about 500 m at the northern end of the

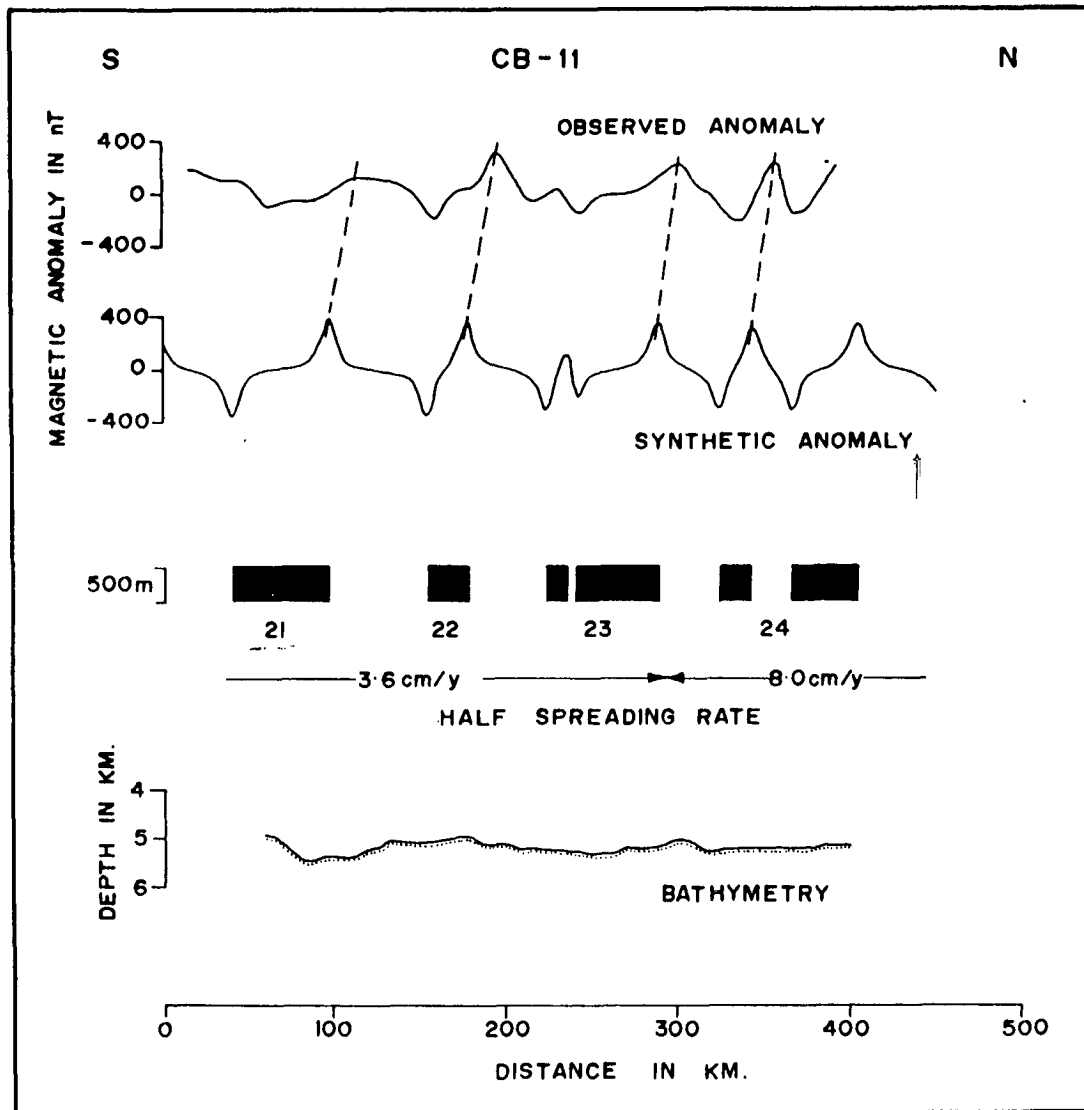


Figure 4.16 Observed magnetic anomaly and bathymetry along the profile *CB-11* along with the synthetic anomalies and the model. Model parameters are same as mentioned in figure 4.6

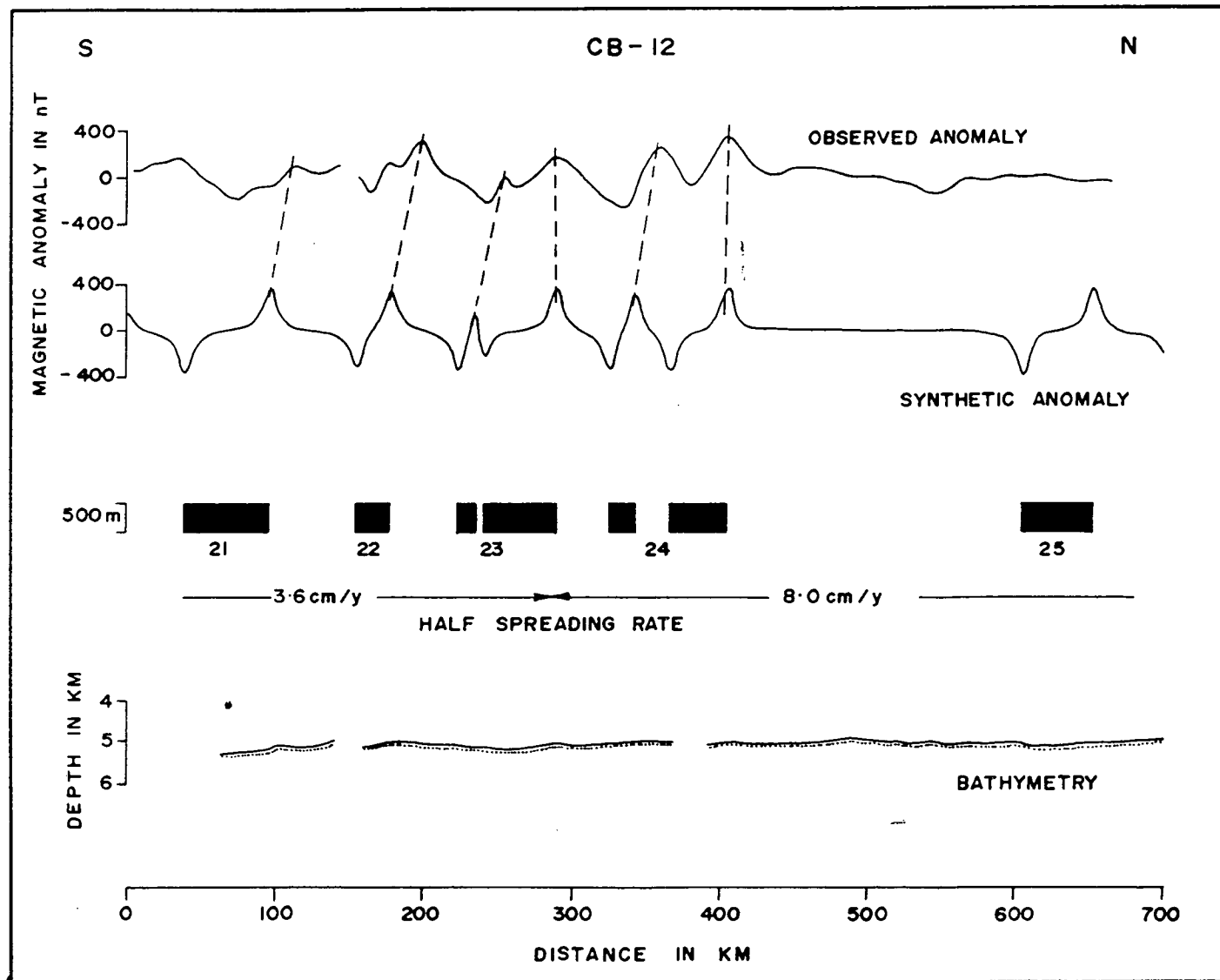


Figure 4.17 Observed magnetic anomaly and bathymetry along the profile CB-12 along with the synthetic anomalies and the model. Model parameters are same as mentioned in figure 4.6

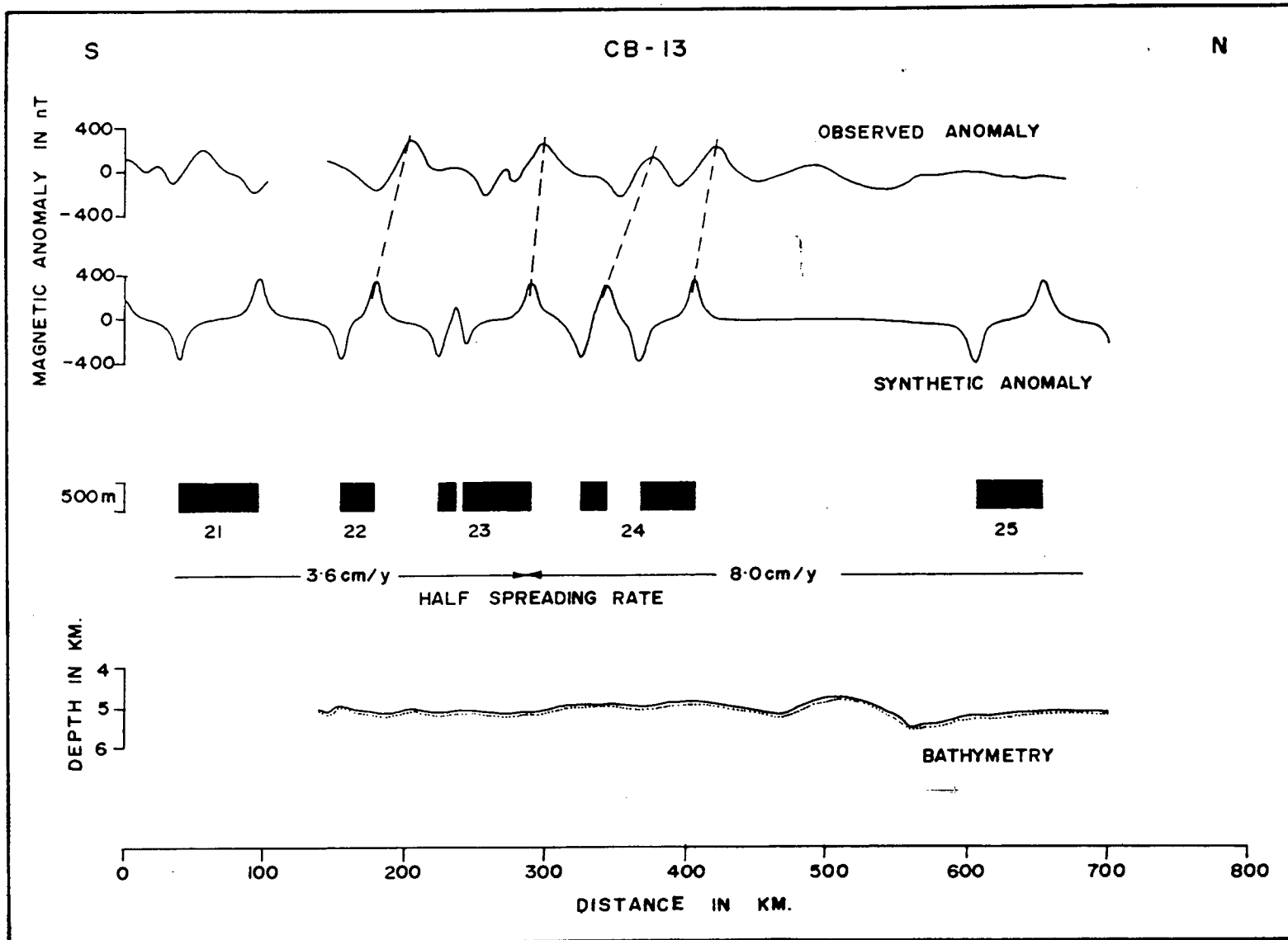


Figure 4.18 Observed magnetic anomaly and bathymetry along the profile CB-13 along with the synthetic anomalies and the model. Model parameters are same as mentioned in figure 4.6

profile. A corresponding response in the magnetic signature can be noticed north of anomaly A24 (Figure 4.18).

xiv Profile CB-14

The magnetic signature along this profile is very much distorted and consequently no anomaly identifications could be made (Figure 4.19). This abrupt change in the anomaly signature may be due to the presence of a feature disturbing the seafloor spreading sequence. The bathymetry along the profile is very rugged with undulations ranging from 500m to 1200m. A step like feature at the northern end of the profile is very pronounced.

xv Profile CB-15

Along this profile the overall amplitude is subdued. The anomalies A21, A22 and A24 can be clearly observed, the anomaly A23 is not well defined. The bathymetry is very rugged with sharp peaks and troughs (Figure 4.20) ranging from 500 to 1000 m. The depth decreases to about 2600 m towards the northern end of the profile.

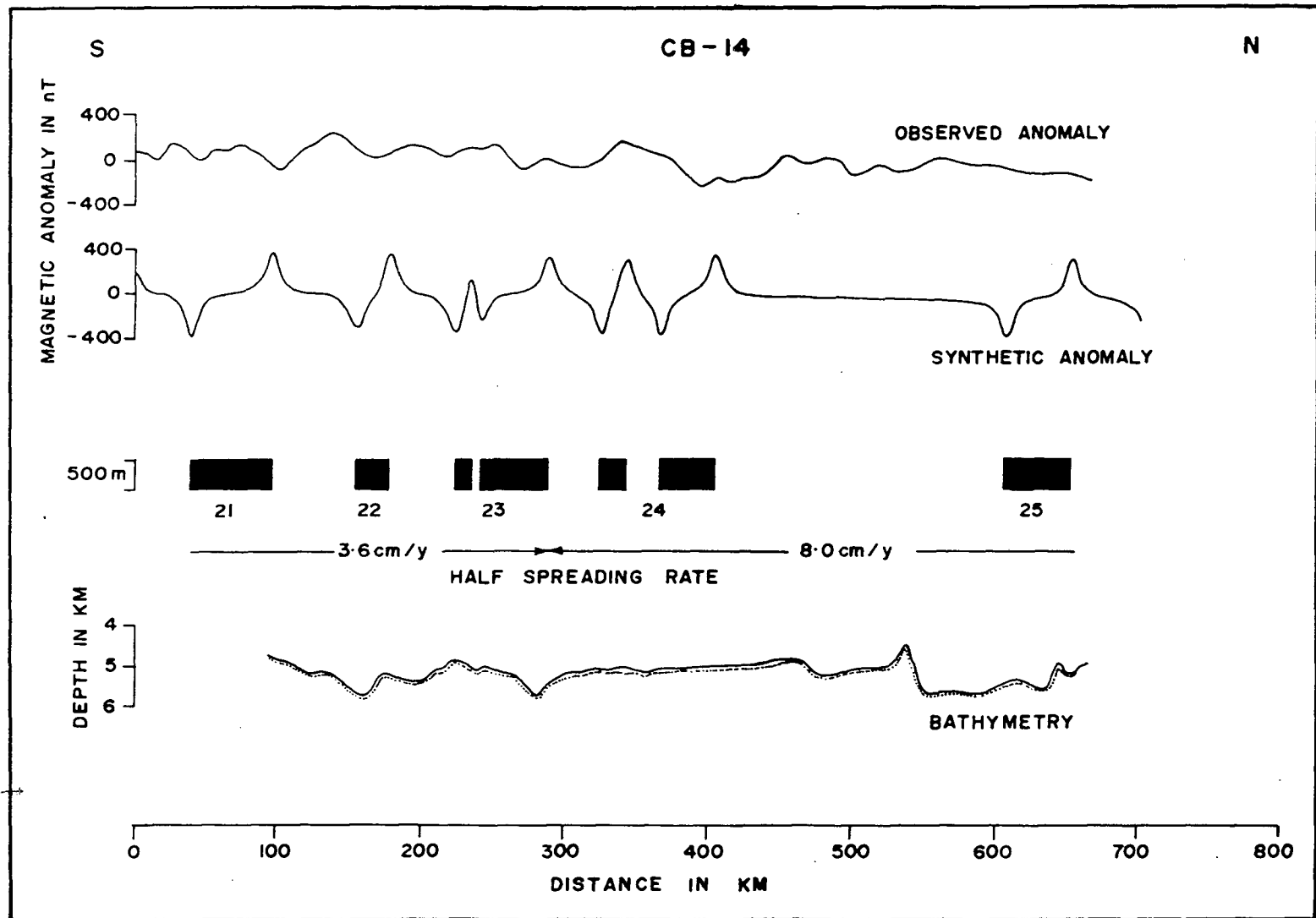


Figure 4.19 Observed magnetic anomaly and bathymetry along the profile *CB-14* along with the synthetic anomalies and the model. Model parameters are same as mentioned in figure 4.6

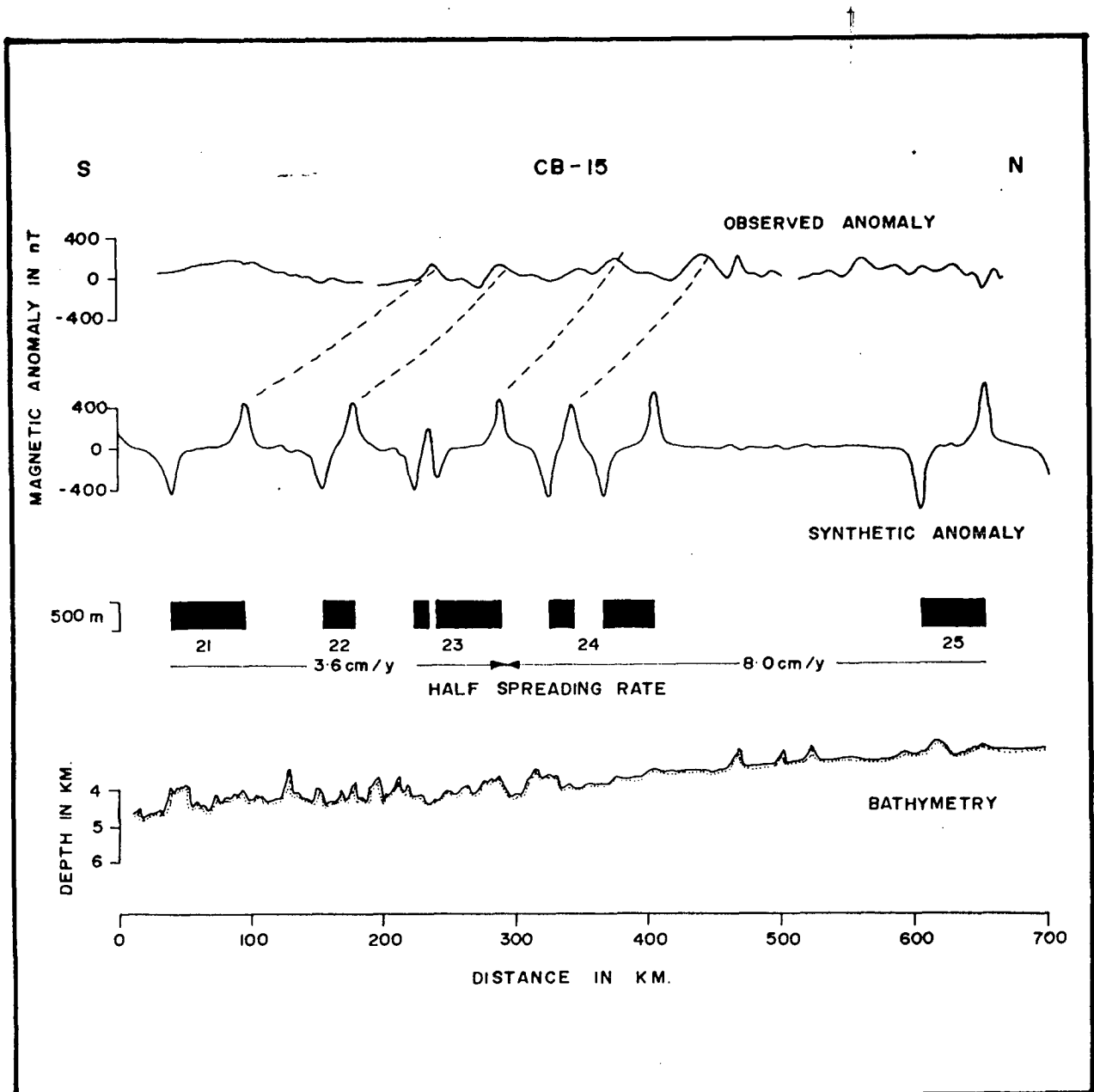


Figure 4.20 Observed magnetic anomaly and bathymetry along the profile *CB-15* along with the synthetic anomalies and the model. Model parameters are same as mentioned in figure 4.6

4.4 DELINEATION OF TECTONIC FEATURES FROM THE MAGNETIC ANOMALY IDENTIFICATIONS AND BOTTOM TOPOGRAPHY

The oceanic magnetic anomalies studied within the frame work of Vine and Matthews hypothesis has been the basis for reconstructing the evolutionary history of the ocean basins. Magnetic anomaly patterns can be used to identify various tectonic features even with less detailed bathymetric data. Several fracture zones have been identified in world oceans based on observed offsets in the magnetic lineations. The initial compilation of magnetic anomalies from the world oceans by *Pitman et al.* (1974), revealed several tectonic features. In the Indian Ocean, in particular, the studies by *McKnezie and Sclater* (1971) and *Schlich* (1982) have delineated major tectonic lineations. The following sections describe in detail the delineation of the tectonic features within the study area.

4.4.1 STACKED MAGNETIC ANOMALIES

The observed magnetic anomalies are stacked and depicted along with the synthetic magnetic anomaly in Figure 4.21. The stacked magnetic anomalies plotted perpendicular to the cruise tracks is presented in Figure 4.22. A remarkable correlation of the anomalies between the profiles is observed. These anomalies form magnetic lineations which trend at about 96°E. The anomalies A23, A24 and A25 are continuous between the profiles

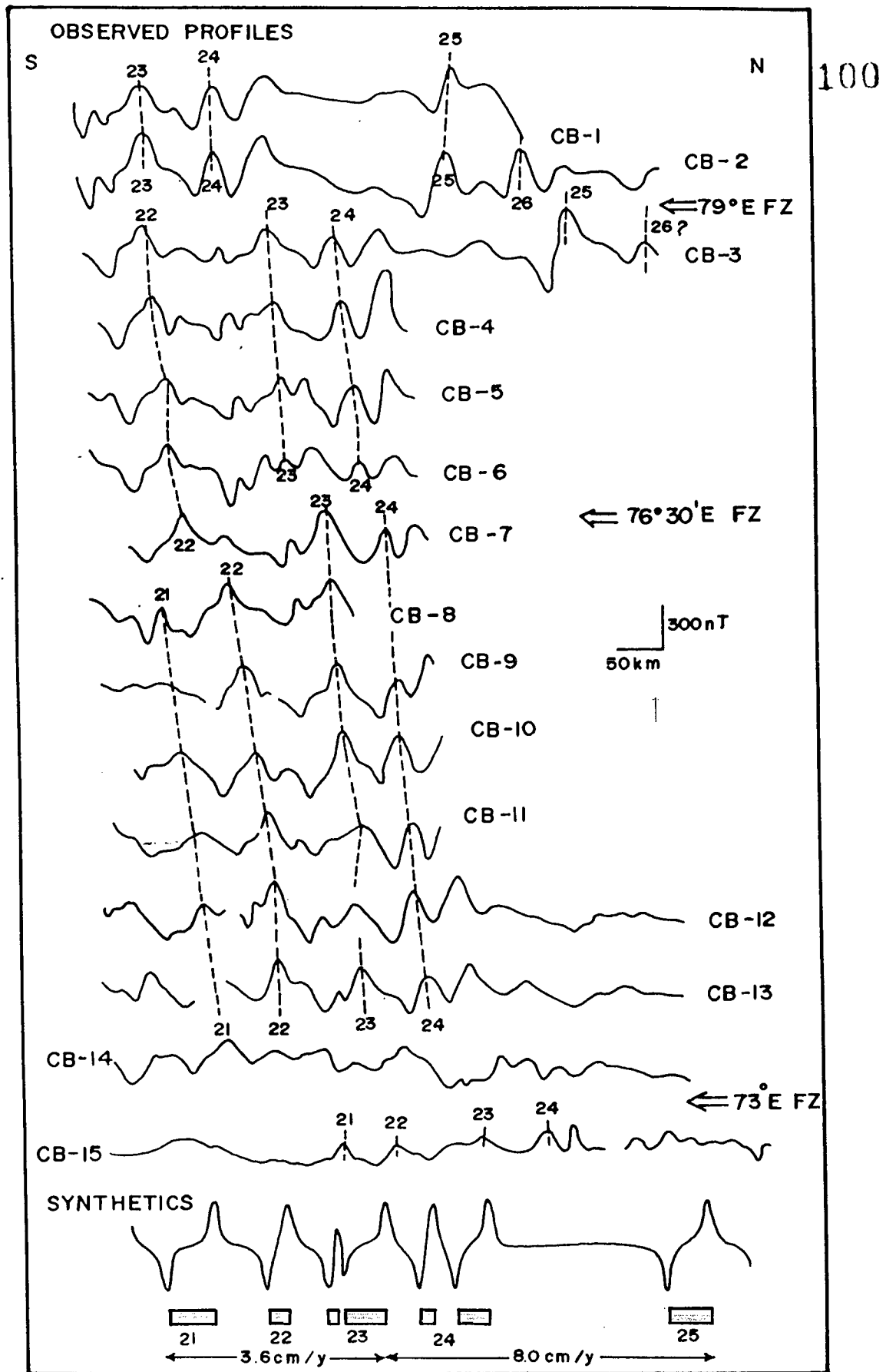


Figure 4.21 The observed magnetic anomalies stacked with respect to position. Synthetic anomalies and model are shown at the bottom. Identified magnetic anomalies are indicated with dashed line, inferred fracture zones are marked.

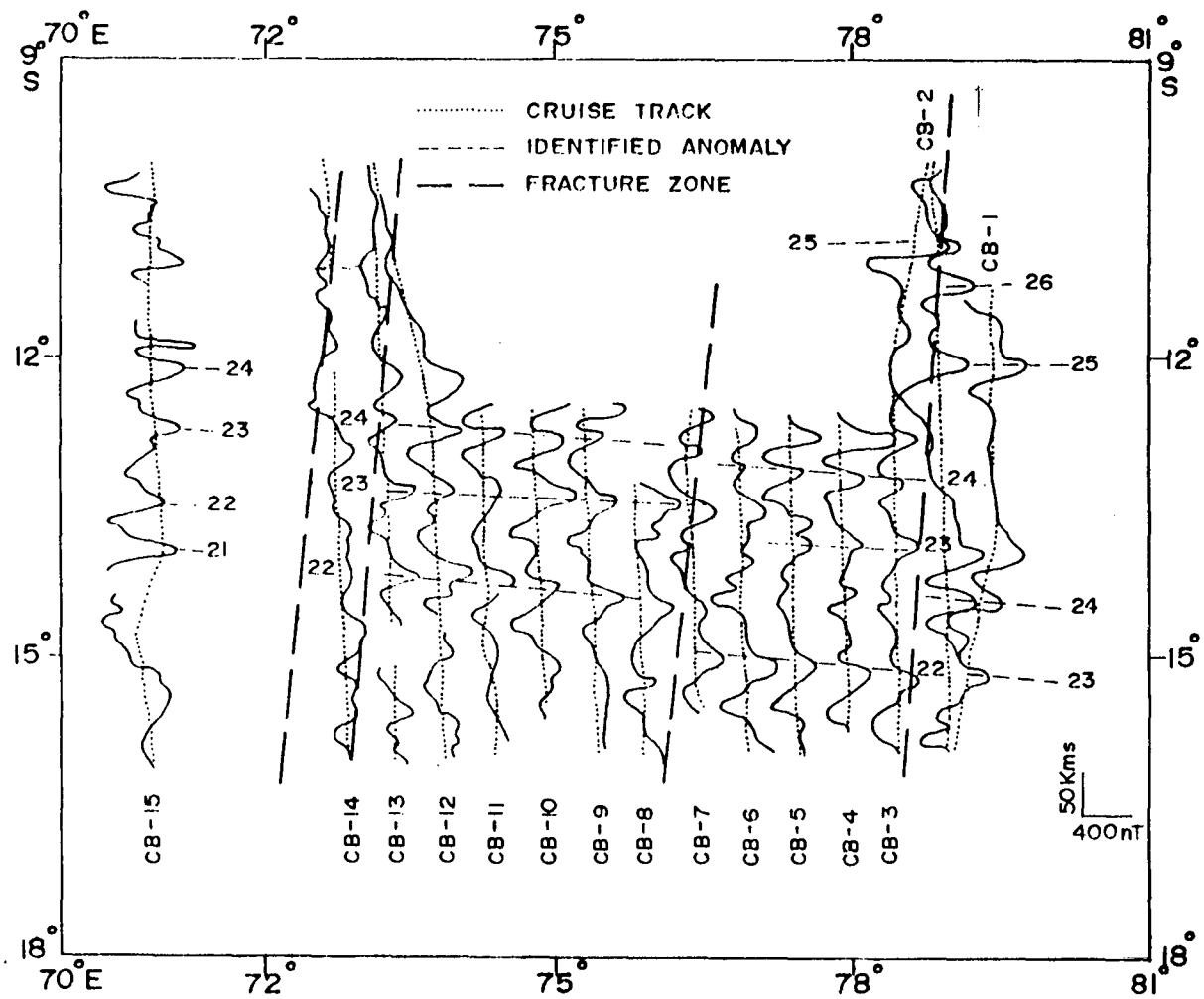


Figure 4.22 Observed magnetic anomalies plotted perpendicular to the cruise tracks. The identified magnetic lineations and fracture zones are indicated.

CB-1, *CB-2* and there is an offset between the anomalies when compared with those identified along the profile *CB-3*. The offset is about 135 kms and this offset displaces the magnetic lineations right laterally towards south. A fracture zone is inferred in this region from these observed offsets in the magnetic lineations. The inferred fracture zone trends at $N5^{\circ}E$ and roughly aligns along $79^{\circ}E$ longitude (Figure 4.22). The feature thus delineated forms the southern extension of the $79^{\circ}E$ fracture zone. McKenzie and Sclater, (1971) have earlier identified this fracture zone in the north between $2^{\circ}S$ and $7^{\circ}S$ and tentatively named it as *Indrani* fracture zone.

Further west between the profiles *CB-3* to *CB-12* the correlations of identified anomalies are continuous. An offset distorting the continuity of the magnetic anomalies between the profiles *CB-6* and *CB-8* is noticed. The offset in the magnetic lineations at this place displacing the magnetic lineations in a right lateral sense is interpreted as due to a fracture zone along $76^{\circ}30'E$ longitude. The observed offset is about 50 km. The offset between the identified magnetic anomalies decreases towards north while the maximum displacement is observed in the south between anomalies A21 and A22. This fracture zone along $76^{\circ}30'E$ longitude trending at about $N5^{\circ}E$ is a new feature being reported for this region.

The magnetic signature along the profiles *CB-13* and *CB-14* is very much disturbed. No anomaly identifications could be made along the profile *CB-14*. If we correlate the magnetic lineations east of profiles *CB-13* and

CB-14 with that of the anomalies along *CB-15*, there is an offset in the observed magnetic lineations marking the presence of a fracture zone, which is along 73°E longitude. *Munschy and Schlich* (1989) have shown a pair of fracture zones in this region, however, no magnetic anomalies are shown confirming this feature. The profile *CB-14* along which very disturbed magnetic signature is observed, lies within the fracture zone region (Figure 4.22). The presence of the 73°E fracture zone is confirmed with the identification of anomalies A21 to A24 along *CB-15* and the observed offsets in the magnetic lineations. The observed offset between the identified magnetic anomalies across this fracture zone is 70 km and the fracture zone trends at about N5°E

The observed magnetic anomalies are contoured at an interval of 100 gammas and presented in Figure 4.23. The magnetic anomaly contour map reflects the alternate bands of magnetic highs and lows clearly depicting near E-W trending magnetic lineations. The contour map is prepared using the profiles *CB-1* to *CB-14*, the profile *CB-15* is not considered as there is large gap between the profiles *CB-14* and *CB-15*.

4.4.2 BOTTOM TOPOGRAPHY

The stacked bathymetric profiles and the bathymetric contour map are shown in Figures 4.24 and 4.25. There are no obvious correlations of bathymetric features between the profiles. The lack of correlations may be

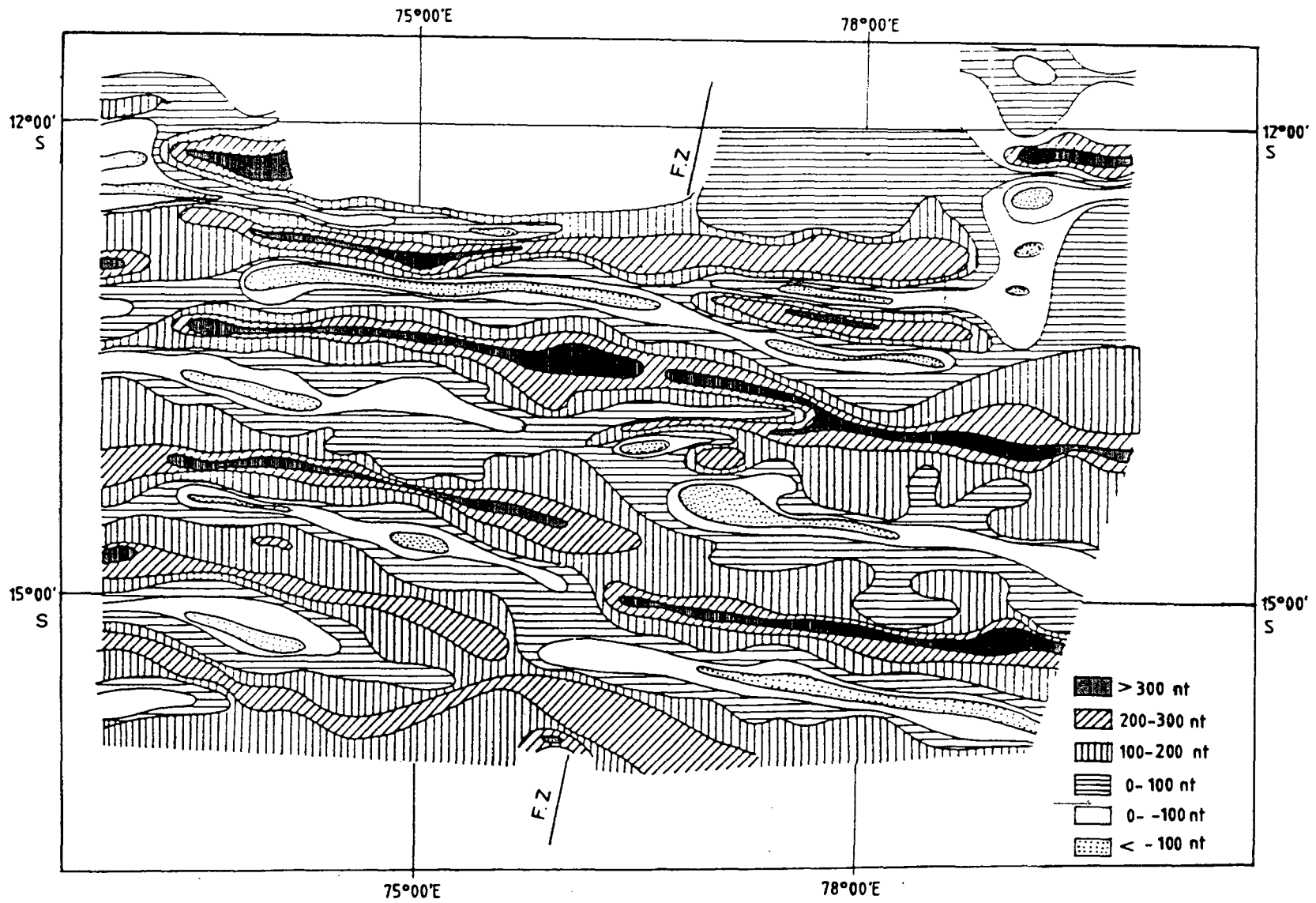


Figure 4.23 Magnetic anomaly contour map depicting well defined near E-W lineations. Contour interval is 100 nT.

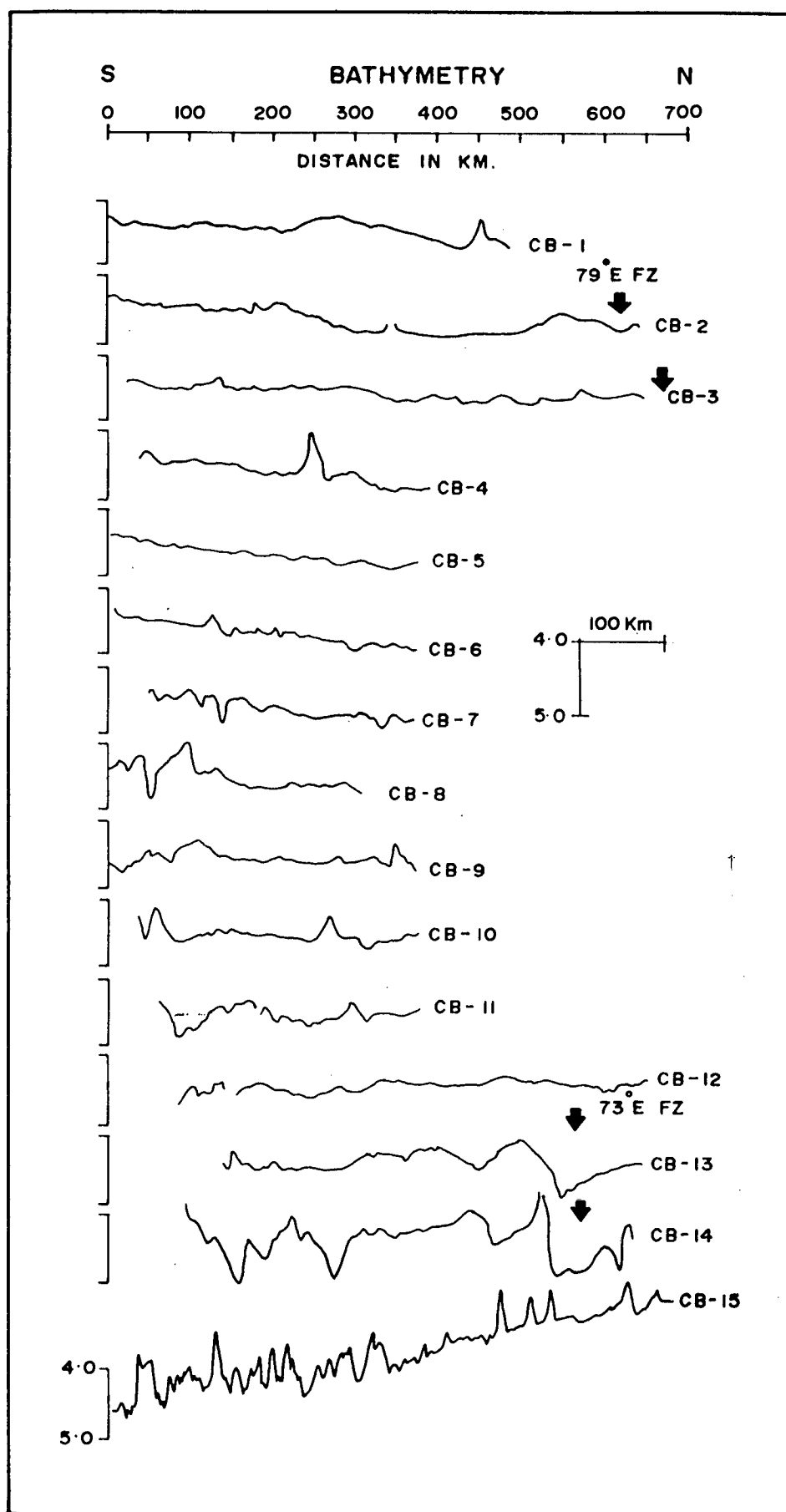


Figure 4.24 Bathymetric profiles stacked with respect to position.

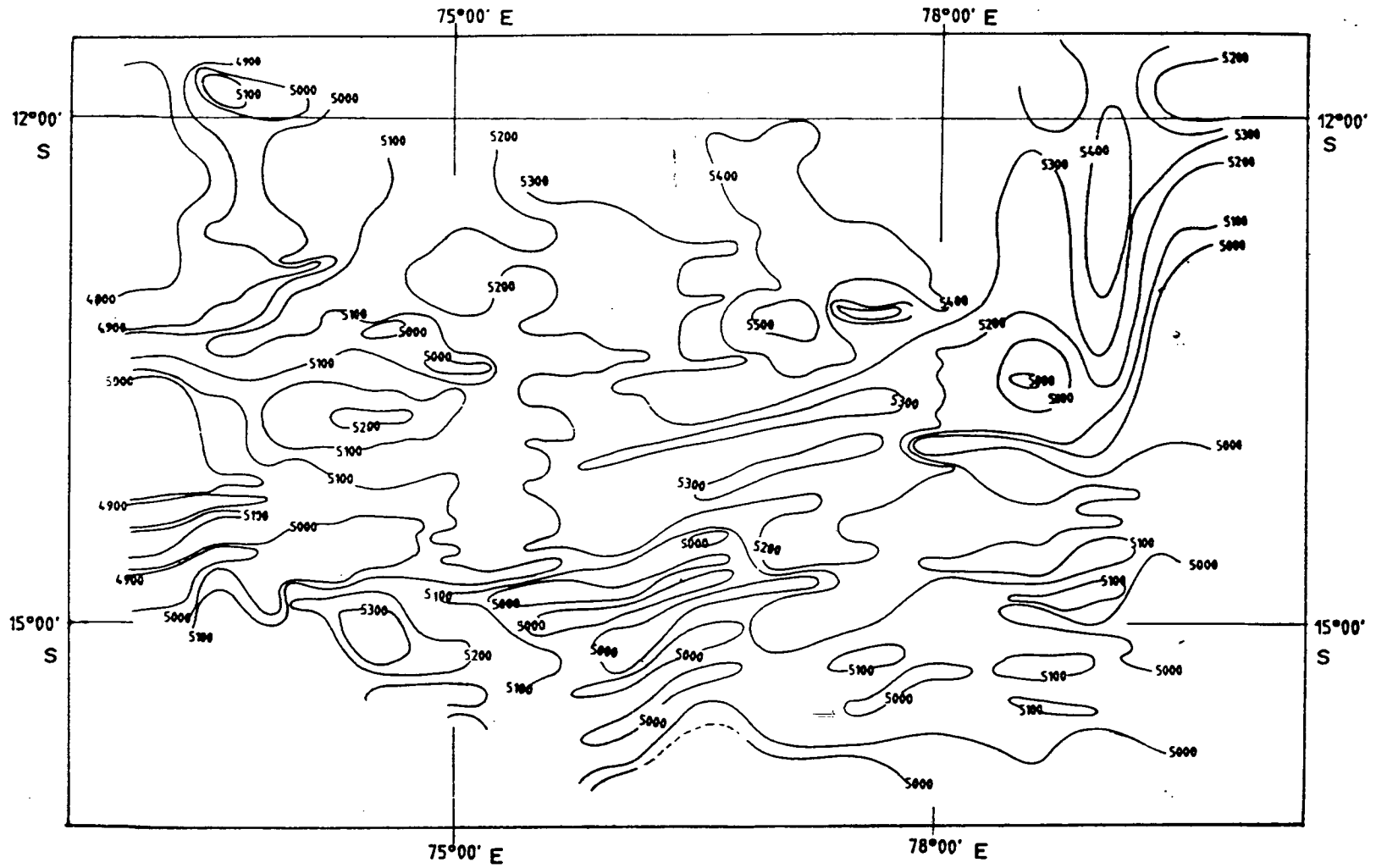


Figure 4.25 Bathymetric contour map. Contour interval 100 m.

due to the wide spacing of the lines. However, the expression of the major fracture zones identified on the basis of the offsets in the magnetic lineations can be noticed. The rugged topography along the profiles *CB-1*, *CB-2* and *CB-3*, probably is an expression of the 79°E fracture zone. A step like feature associated with a seamount at the northern end of the profile *CB-1* and the bathymetric highs and lows noticed on profiles *CB-2* and *CB-3* are indicative of the 79°E fracture zone. Along the profiles *CB-13* and *CB-14* also very rugged bottom topography is observed with a pronounced step like feature at the northern end of the profiles and prominent valleys and highs along profile *CB-14* (Figure 4.24). These bathymetric features represent the presence of 73°E fracture zone. Along the profile *CB-15* the decrease in the depth to about 2600 m towards the north may be due to the proximity to the Chagos Bank.

The bathymetric contour map is prepared using the profiles *CB-1* to *CB-14*, the profile *CB-15* is not used as this is inducing excessive interpolation due to the large gap between profiles *CB-14* and *CB-15*. It can be observed from the contour map (Figure 4.25), that the western part of the study area is more rugged than the eastern part. Subtle E-W bathymetric lineations can be noticed in the central part of the area. The bathymetric expression of 79°E fracture zone is pronounced in the northeastern corner of the area with a conspicuous bathymetric low of 5400 m. This feature extends to about 125 km, flanked by topographic elevations on either side.

4.5 SUMMARY

The results from the studies of marine magnetic anomalies and the bottom topography are summarized below.

The marine magnetic anomalies A21 to A26 are identified in the study area based on the model studies. Variable spreading rates of 3.6 cm/yr between anomalies A21 to A23 and 8.0 cm/yr between anomalies A23 and A26 were inferred from these studies. These identifications suggest that the age of the oceanic crust in the region ranges from about 48 Ma (A21) in the southwestern part to 60 Ma (A26) in the northeast.

The E-W magnetic lineations are mapped on the basis of correlation of magnetic anomalies between the profiles. The trend of these magnetic lineations is about 96°E . The observed offsets in the magnetic lineations are interpreted as due to the fracture zones. Fracture zones at 79°E , $76^{\circ}30'\text{E}$ and 73°E have been identified. The general trend of these fracture zones is near N-S and the E-W magnetic lineations are offset in a right lateral sense across these fracture zones. The northward age progression of the oceanic crust is expressed interspersed with fracture zones. These inferences suggest that the anomalies identified in the region are produced by the east-west trending Southeast Indian Ridge. The Southeast Indian Ridge was further south and was trending E-W during the Paleocene and Early Eocene periods (*Fisher et al.*, 1971; *Patriat and Segoufin*, 1988).

The fracture zones at 79°E and 73°E are associated with topographic expression where as the fracture zone at 76°30'E has no conspicuous bathymetric expression. The absence of bathymetric expression of the 76°30'E fracture zone may be due to the diminished offset across the magnetic lineations and very low age contrast across the fracture zone.

CHAPTER V

**MULTIBEAM BATHYMETRY AND
FREE-AIR GRAVITY OBSERVATIONS
IN THE VICINITY OF 79 °E FRACTURE ZONE**

CHAPTER V

**MULTIBEAM BATHYMETRY AND FREE-AIR GRAVITY
OBSERVATIONS IN THE VICINITY
OF 79°E FRACTURE ZONE**

5.1 INTRODUCTION

The multibeam bathymetric data were collected using the Krupp Atlas Electronics (Germany) made *Hydrosweep* system. Gravity data were collected using *KSS30 Bodenseewerk* marine gravimeter. Details of these systems are outlined in the Chapter 2.

Hydrosweep data were post-processed using the *Hydromap* system (EPR-1300 computer) onboard and the depth contour maps and cross profiles were prepared. Depth contour maps generated at a contour interval of 25 m were used for the delineation of various morphotectonic features. A regional scale bathymetric map at 100 m contour interval color coded for every 300 m (Figure 5.1), a simplified depth contour map along with identified magnetic anomalies (Figure 5.2) and the magnetic anomalies (Figure 5.3) are presented. Detailed bathymetric maps at 25 m contour interval depicting the E-W lineations and a part of the fracture zone are shown in Figures 5.4 and 5.5. Isometric view of a part of the 79 °E fracture zone is presented in

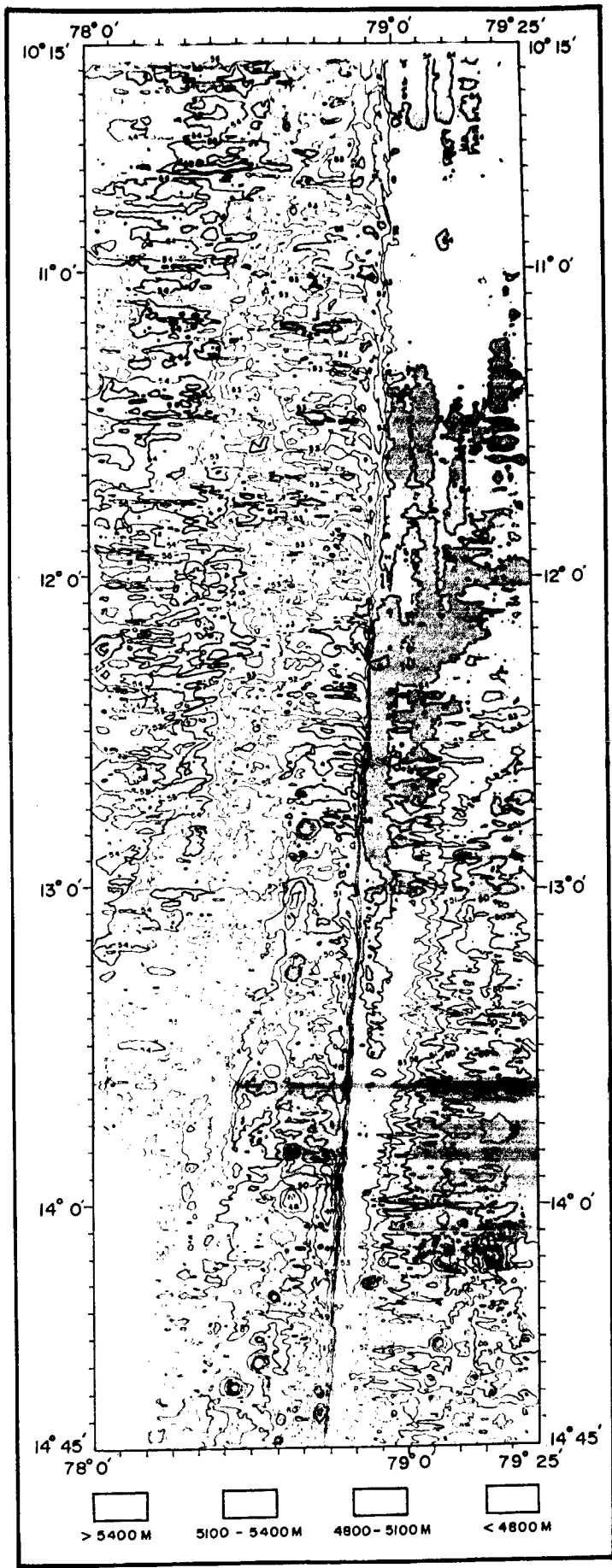


Figure 5.1 Colour coded bathymetric contour map generated by using multibeam sonar data. Contour interval 100 m, colour change at every 300 m.

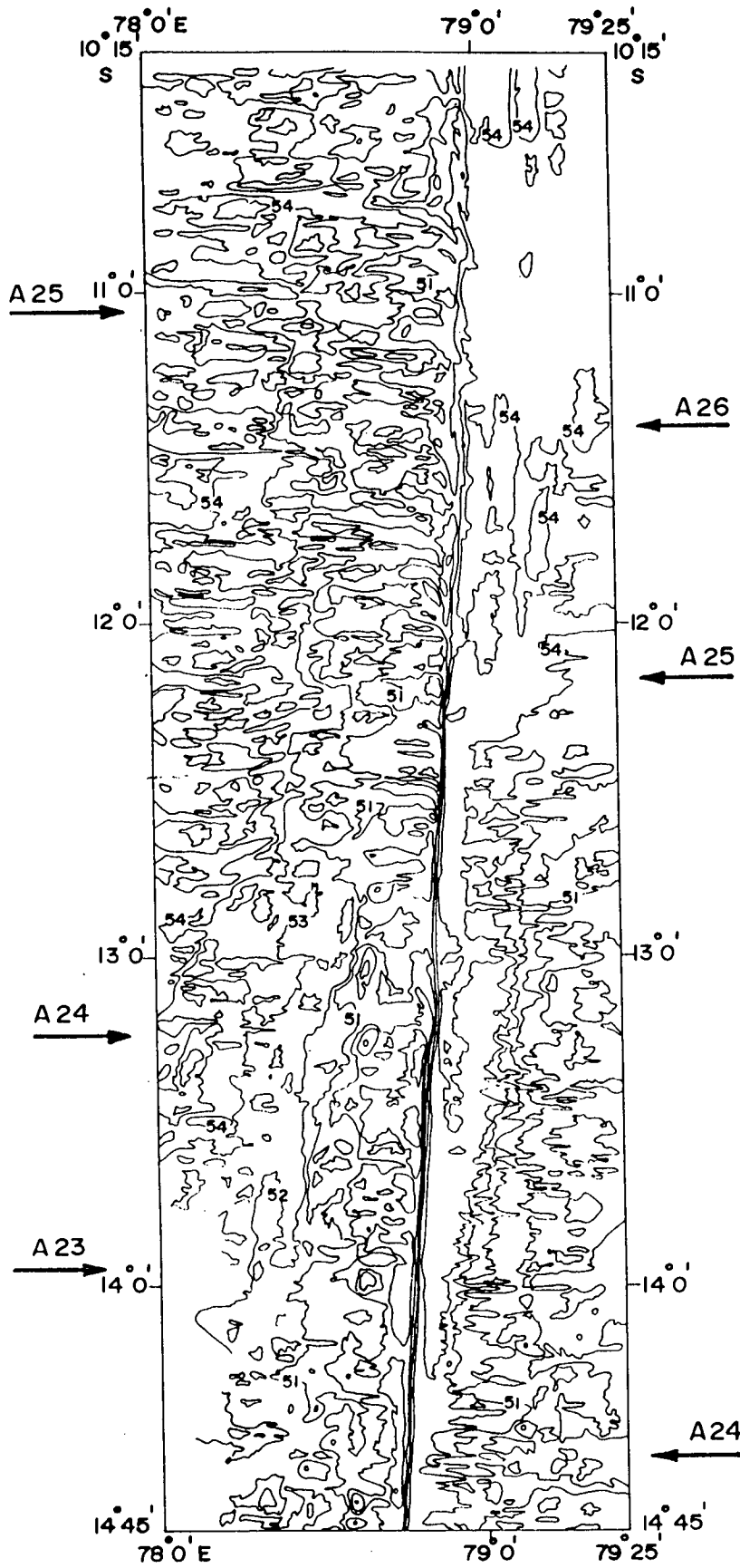


Figure 5.2 Simplified bathymetric map of multibeam sonar data along with the magnetic anomaly markings. Contour interval 100 m.

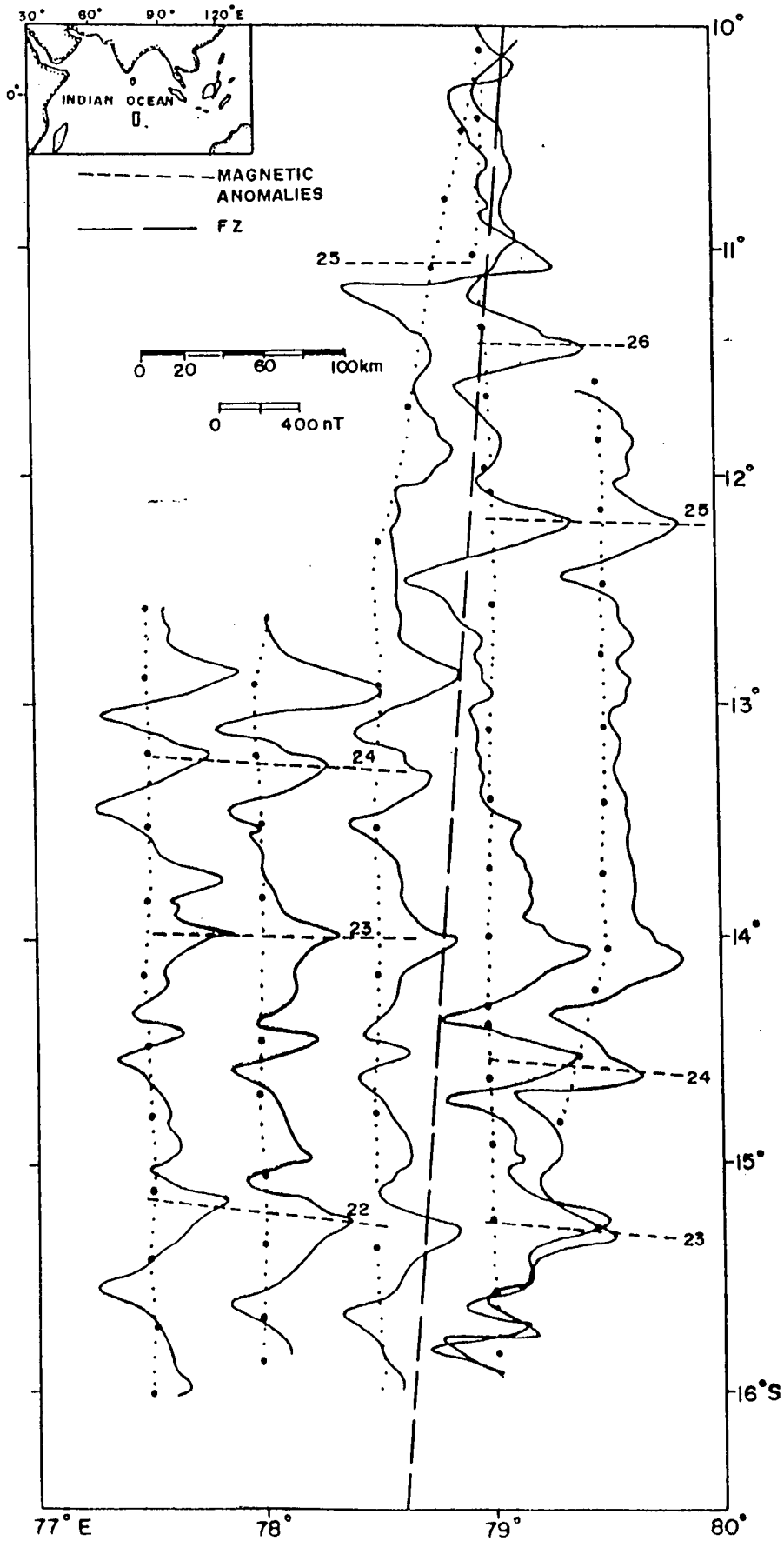


Figure 5.3 Magnetic anomalies plotted perpendicular to the cruise tracks in the vicinity of 79°E fracture zone.

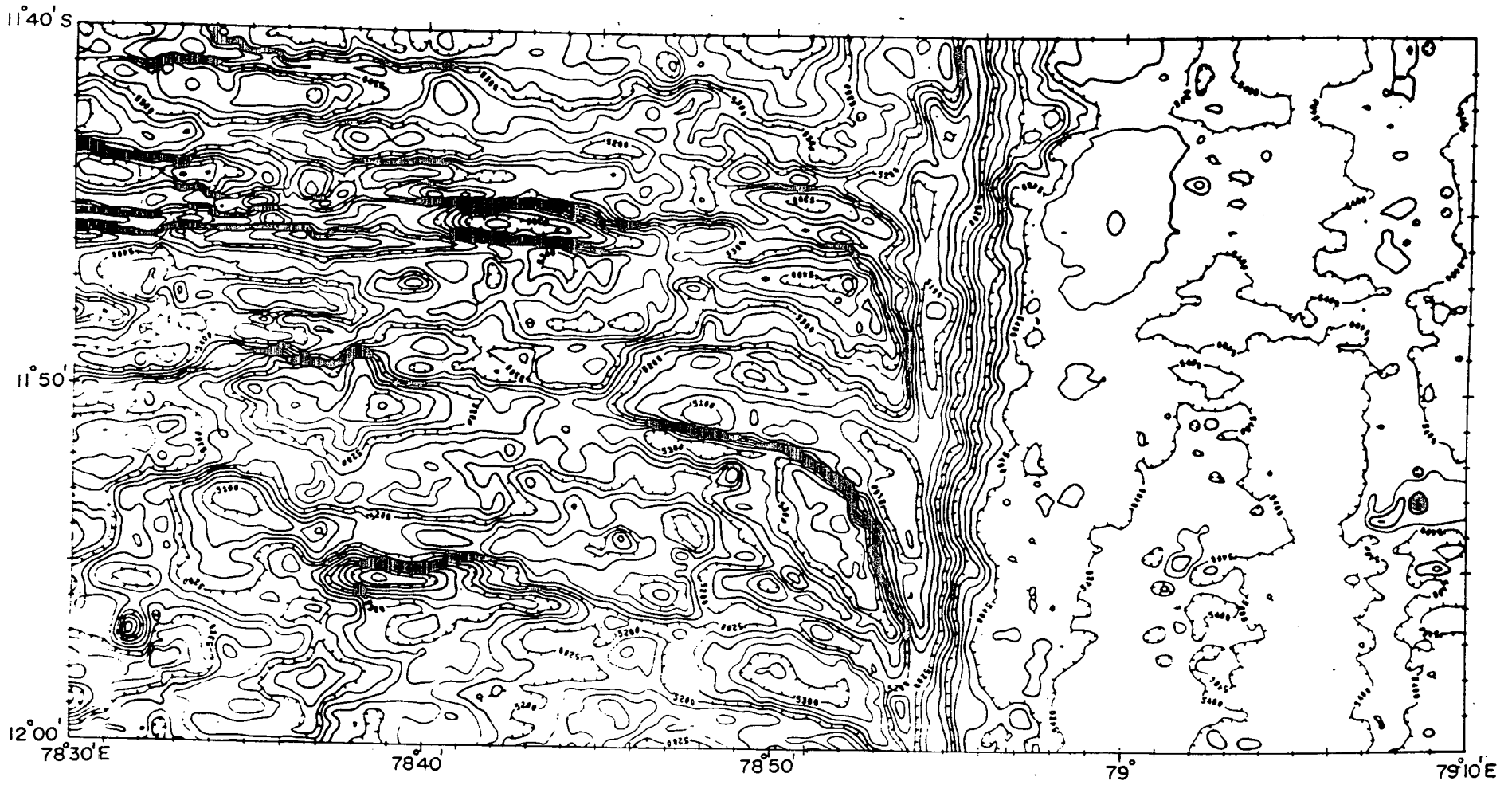


Figure 5.4 High resolution bathymetric map at 25 m contour interval, depicting prominent E-W bathymetric lineations and bending of these lineations into the fracture zone.

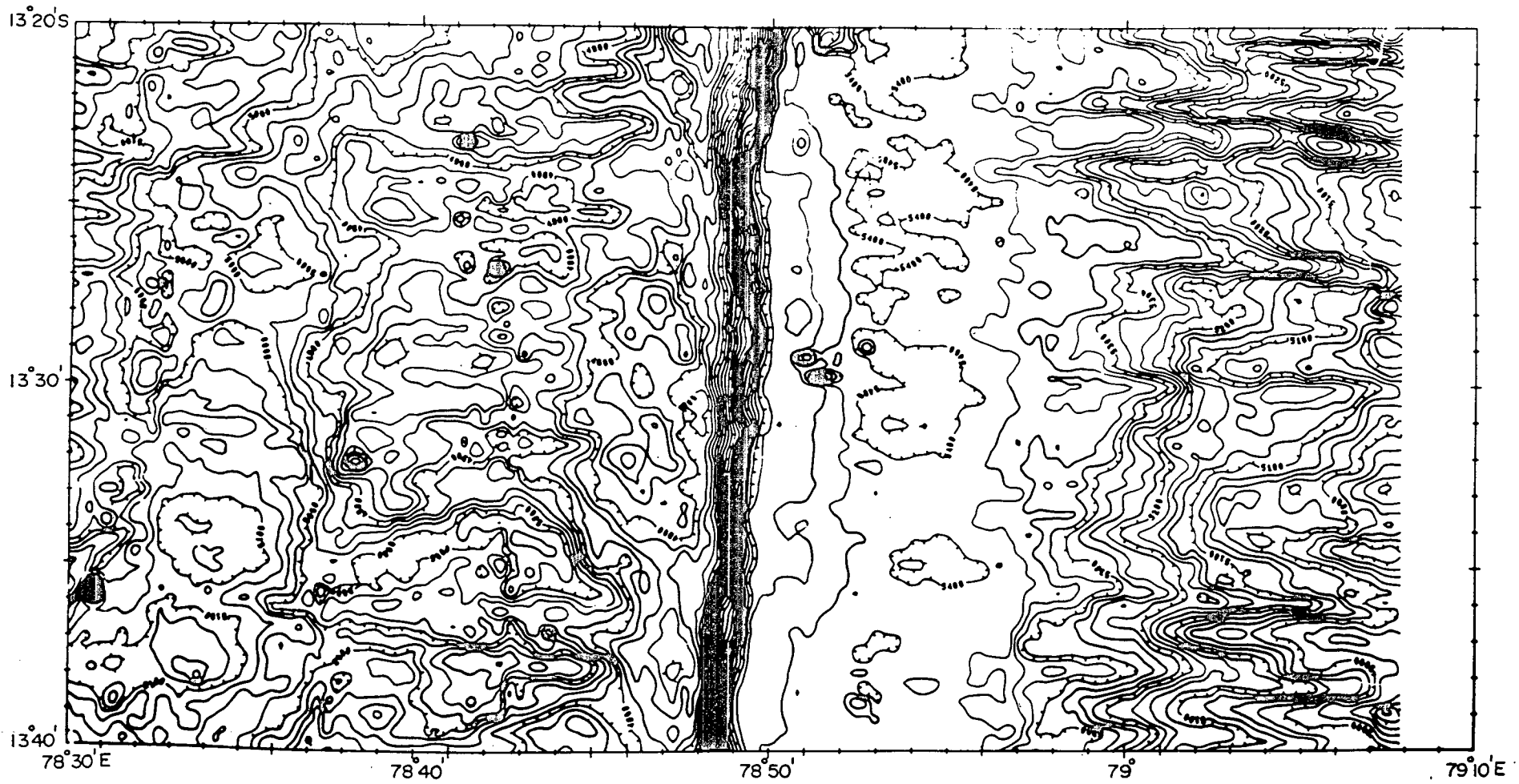


Figure 5.5 High resolution bathymetric map at 25 m contour interval, depicting steep gradient expression of the fracture zone.

Figure 5.6. Bathymetry of a multi-peaked seamount is displayed at 50 m contour interval in Figure 5.7.

5.2 MORPHOTECTONIC ELEMENTS

A regional bathymetric map was constructed from the *Hydrosweep* data collected along 16 profiles (Figure 2.8). An area of 73000 km² was covered between latitudes 10°15'S to 14°45'S and 78°E to 79°25'E longitudes. The area covered encompasses the magnetic anomalies A23, A24, A25, and A26 (Figure 5.3), and the age of the oceanic crust corresponding to these anomalies varies between 53.88 to 60.75 Ma. The average depth in the region varies from 5100 to 5400 m.

Evaluation of the color coded regional bathymetric map (Figure 5.1), the detailed high resolution maps (Figures 5.4 and 5.5) and the E-W profiles generated from the grid file (Figure 5.8) revealed the following features.

- i) Ridge and trough topographic expression of the 79 °E fracture zone.
- ii) The flexural topographic expression.
- iii) Prominent east west trending bathymetric lineations.
- iv) Bending of the bathymetric lineations.
- v) Seamounts.

Grid Name : A242	Center: 78 D 40.00 M East	Viewing Direction: 355 Deg	KRUPP ATLAS I
Cell Width: 500 m	13 D 45.00 M South	Vertical Aspect : 20 Deg	HMS 1300 / I

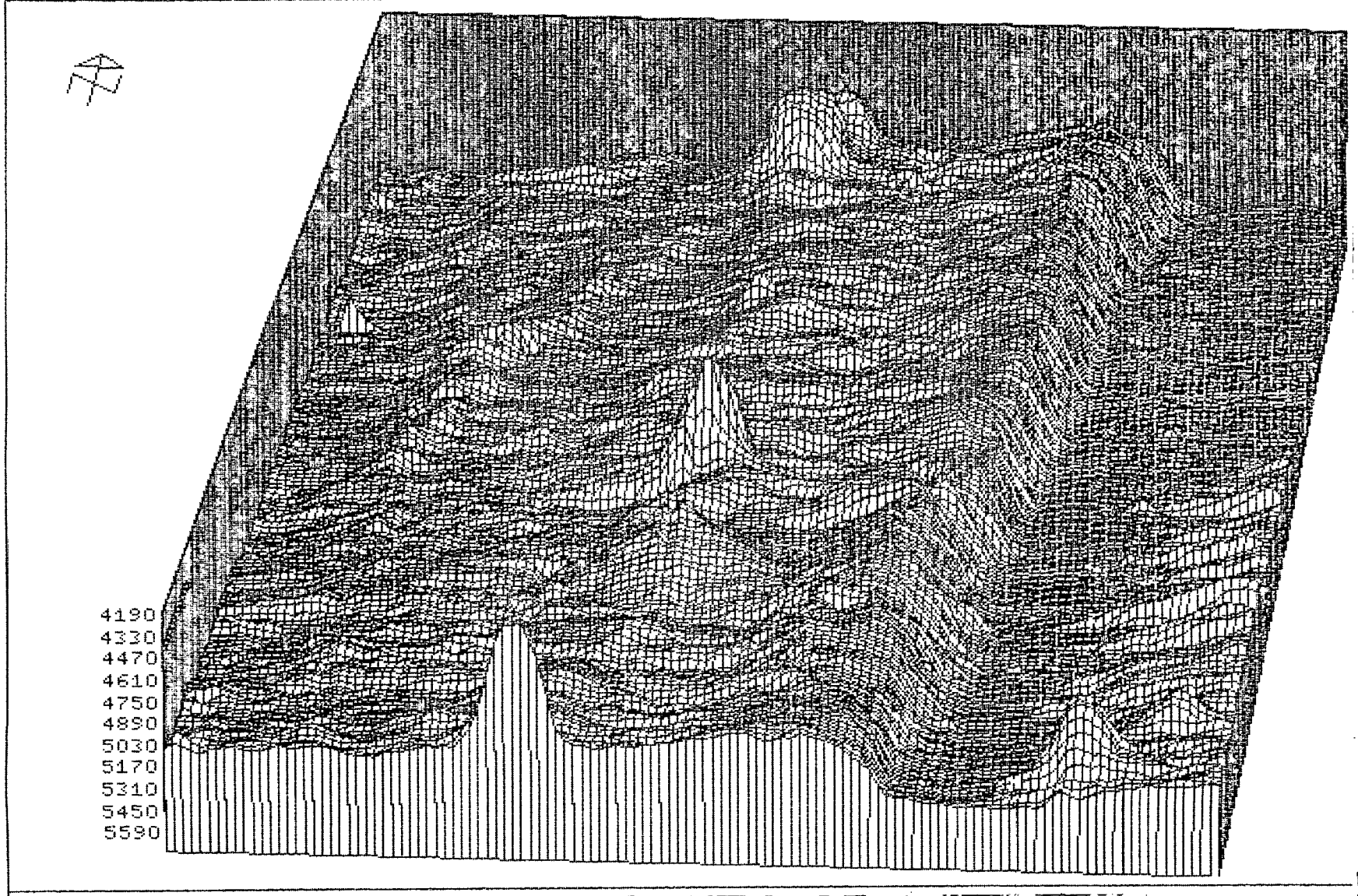


Figure 5.6 Isometric view of a part of the 79°E fracture zone generated from the Hydrosweep data.

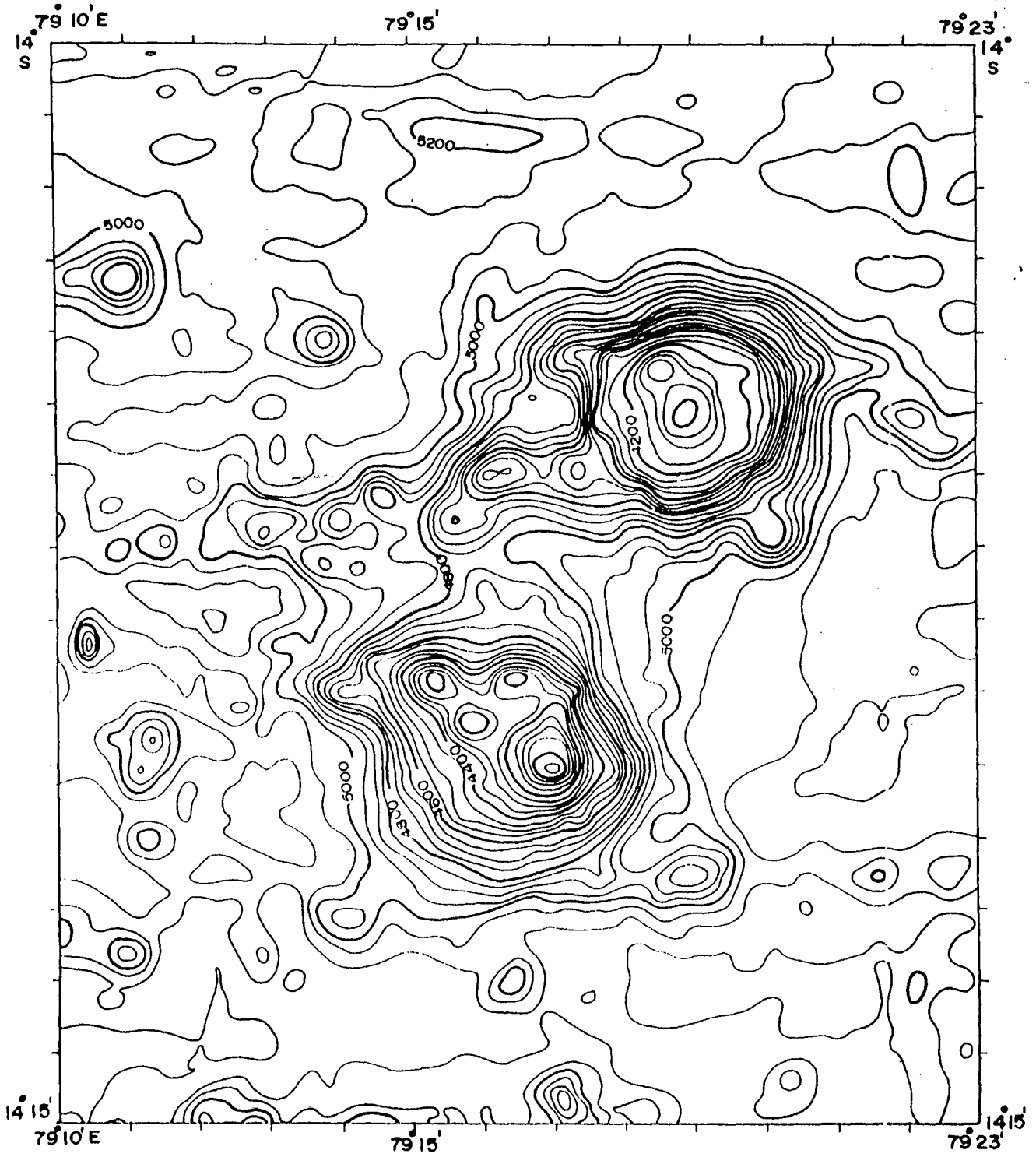


Figure 5.7 Multipeaked seamount. Contour interval 50 m.

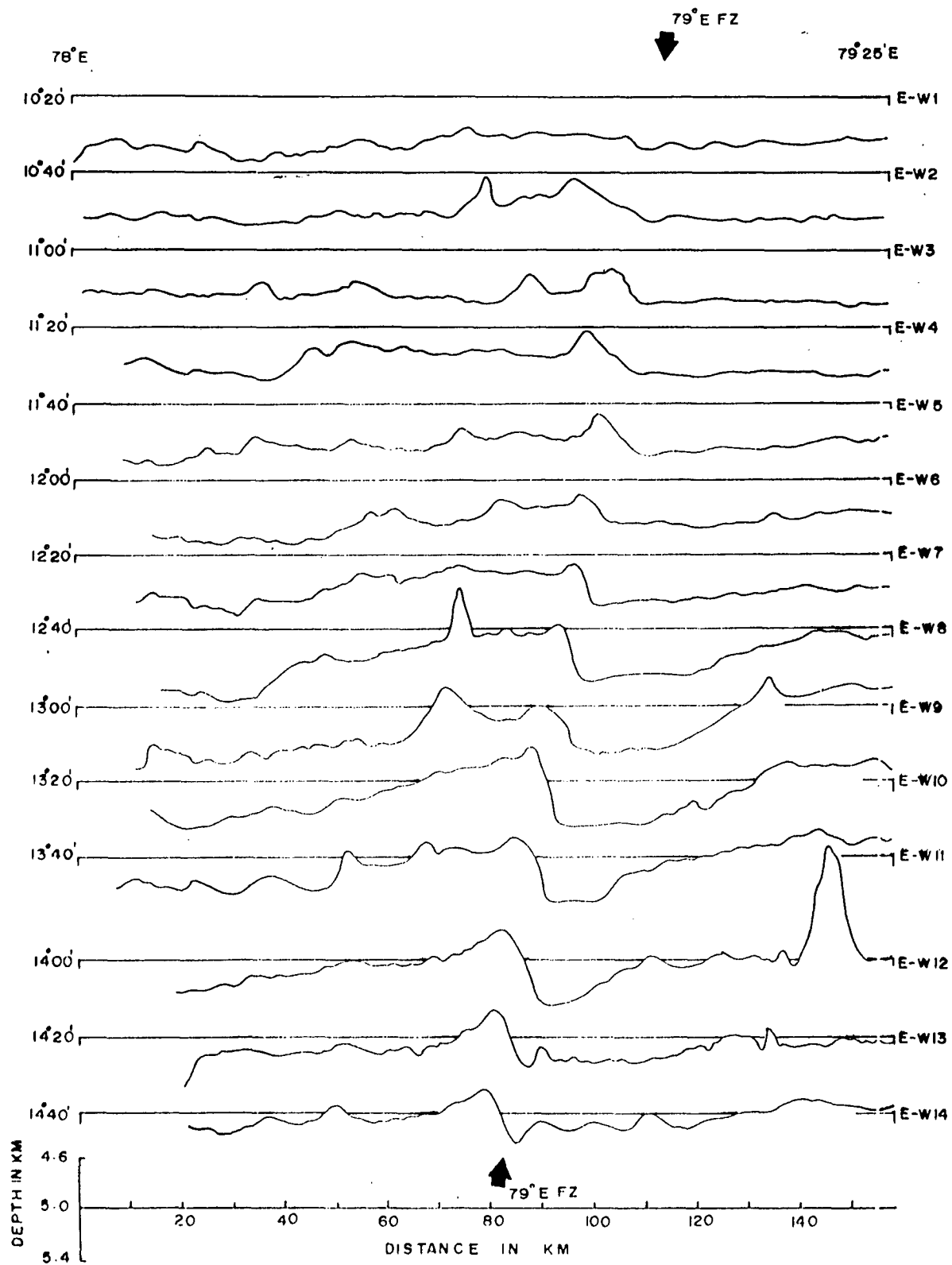


Figure 5.8 Bathymetric profiles generated from the gridded depth data.

The above listed broad morphotectonic features are described in detail in the following sections with reference to their tectonic implications. These morphotectonic features are compared with those observed along the fracture zones in the Pacific ocean.

1 Ridge and Trough Topography of 79 °E Fracture Zone

The most striking feature of the region is the linear trend of the contours along 79°E longitude. This feature coincides with the southern extension of the 79°E fracture zone delineated from the studies of magnetics. The seafloor on the western flank of the fracture zone, in general, is shallower than that of eastern flank. To the west of the 79 °E fracture zone the depth is around 5100 m and it increases to about 5400 m to the east of the fracture zone with a high gradient as depicted by the linear N-S trending bathymetric contours (Figures 5.1, 5.2 and 5.5). Topographic high is observed along the fracture zone with the depth decreasing to a minimum of 4800 m followed by a deep extending up to 5400 m. This feature marks the typical ridge and trough feature associated with the fracture zone. *Sandwell and Schubert* (1982) from the studies on Pacific ocean fracture zones concluded that the ridge and trough topographic expression is a characteristic feature of the fracture zones. The persistence of this topographic expression over thousands of kilometers along the fracture zones is attributed to the lithospheric flexure controlled by the thermal structure of the oceanic lithosphere at the fracture zones. The ridge and trough bathymetric

expression of 79°E fracture zone in the present study is much similar to the features associated with the Pacific fracture zones.

Bathymetric profiles are plotted with the depths obtained from the center beam (Figure 5.9). The N-S profiles HS1-1 to HS1-7 depict abrupt change in the bathymetric signature, showing a transformation from very rough to smooth topography across the fracture zone. Along the profiles HS1-6 and HS1-7 the smooth topographic zone is bordered by the rough topographic expression on both southern and northern sides of the profile. Whereas, along the profiles HS1-1 to HS1-5, the smooth topographic expression continues till the end of the profile. Along the remaining profiles from HS1-8 to HS1-16, abrupt change of bathymetric signature is not seen. The locations of the occurrence of change in the bathymetric signature along the profiles HS1-1 to HS1-7 define a zone of smooth bathymetry along the fracture zone trough widening towards north. The bathymetric expression of the trough associated with the fracture zone widens towards north as depicted by the 5400 m isobath in the northeastern portion of the area (Figure 5.2). The widening of the bathymetric trough towards north and the diminished bathymetric step at the fracture zone may be due to the in-fill of the sediments in the trough. The studies at the Clipperton transform in the East Pacific Rise (Gallo *et al.*, 1986; Wessel and Haxby, 1990) have indicated that the sediment in-fill in the trough resulted in reduced bathymetric step and the corresponding geoid anomalies.

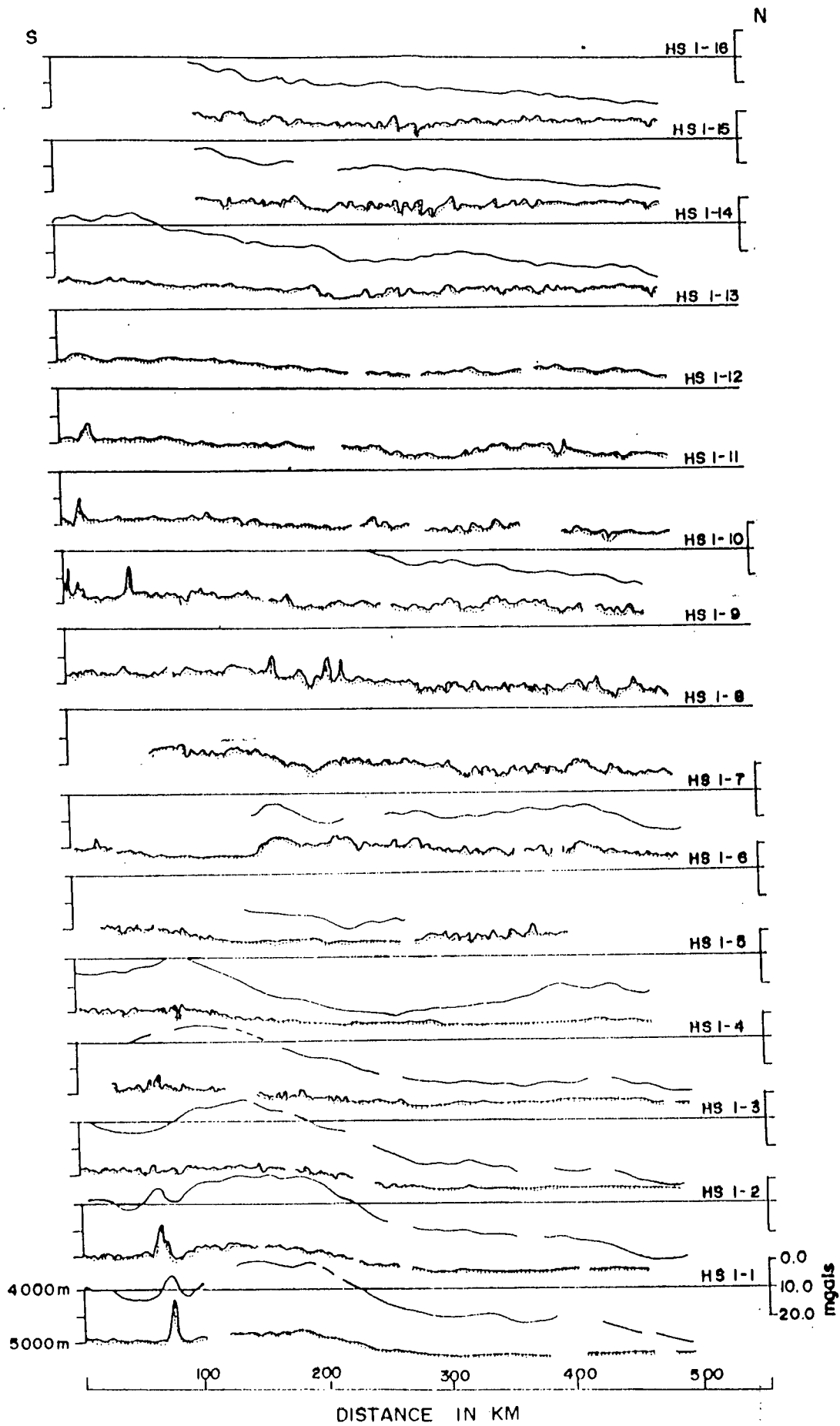


Figure 5.9 Free-air gravity and center beam depth along the tracks of multibeam sonar survey. See figure.2.8 for the location of the tracks.

ii Flexural Topographic Expression

Bathymetric profiles across the fracture zone in the E-W direction were generated from the gridded depth values using the grid file (Figure 5.8). These profiles highlight the ridge and trough topography of the fracture zone. The amplitude of the topographic variations are prominent in the southern part and decrease towards north. The magnitude of the bathymetric step varies from about 500 m in the south to 200 m in the north. Flexural response of the topography can be observed along these E-W bathymetric profiles perpendicular to the trend of the fracture zone. The younger western side flexes at a shorter wave length than the older eastern side of the fracture zone. The amplitude and the wave length of the flexural response depends on the thermal structure of the lithosphere (*Sandwell and Schubert, 1982, Sandwell, 1984*). The thermal structure of the lithosphere across the fracture zones is dealt in the following Chapter.

iii East-West Bathymetric Lineations

Prominent E-W bathymetric lineations are observed in the area which can be seen on the regional bathymetric maps (Figure 5.1 and 5.2) and also in the high resolution detailed maps (Figures 5.4 and 5.5). These lineations extend up to 20-30 km in length, define numerous ridges and intervening

trenches with a relief of 200-300 m (Figure 5.4). These features result from the spreading center parallel topography formed by the seafloor spreading process. During the anomaly times of A23 to A26 (anomalies identified in the region from magnetics), the South East Indian Ridge was trending east west (*McKenzie and Sclater, 1971; Fisher et al., 1971; Patriat and Segoufin, 1982*). Therefore prominent E-W bathymetric lineations documented here can be interpreted as the ridge-parallel (trending N95 °E) topographic fabric of the Southeast Indian Ridge during Paleocene-Eocene times. Similar kind of morphological character is observed over the East Pacific Rise across the Clipperton transform fault (*Gallo et al., 1986*). Multibeam sonar studies near Galapagos rift have shown the ridge parallel bathymetric lineations on either side of the rift (*Allmendinger and Riis, 1979*).

The formation of these lineaments is due to the emplacement of magma and its subsequent solidification parallel to the spreading center. These lineaments are frozen in the near vicinity of the ridge and move along with the plate. The relief of these lineaments reduce due to the processes of subduction and thermal contraction. The pattern of these lineaments is controlled by the factors influencing the spreading center morphology.

The morphology of the spreading center depends on the rate of plate separation and the rate of magma supply (*Macdonald et al., 1991*). It has been observed that at slow spreading rates the ridge axis is characterized by a rift valley and at fast spreading ridges there is an axial high (*Hall et al.,*

1986). At intermediate spreading rates the crest of the ridge axis may have either an axial high or a rift valley depending on the rate of magma supply (Macdonald, 1986; Sempere *et al.*, 1991). Thus it is expected that at faster spreading centers the magma source is shallower than for a slower ridge. Seismic images of magma chamber at fast spreading East Pacific Rise have shown shallow magma chamber with a thin brittle lid of about 2 km. Whereas at slower spreading Mid Atlantic Ridge such a structure is not found and the lithosphere is about 10 km thick (Lin, 1992).

The ridge-parallel grain is well-defined in the northwestern and southeastern quadrants of the area across the 79°E fracture zone (Figure 5.1 and 5.2). Whereas in the southwestern quadrant ridge-parallel topographic fabric is not significant. In the northeastern quadrant the bathymetry is very smooth depicting a broad trough probably indicating sediment in-fill in the fracture zone.

The magnetic model studies conducted during the present investigation indicate that the segment of 79°E fracture zone in this region, has evolved in two spreading episodes. The slow spreading (3.6 cm/yr) episode between A21-A23 and the fast spreading (8.0 cm/yr) episode between A23-A26. Therefore, the prominent E-W lineations observed in the northwestern and southeastern quadrants are a consequence of the accretion processes in a faster spreading regime. After the anomaly A23 the spreading rate has

decreased resulting in the slow spreading regime giving rise to less significant E-W lineations.

Bathymetric character of the lineations in the northwestern quadrant between 11°S and 12°S and in the southeastern quadrant between 13°S and 14°S latitudes are similar (Figures 5.1 and 5.2). These lineations show a correlation of the bathymetric signature with the crustal age (anomaly A24) and indicate the right lateral offset of the oceanic crust across the 79°E fracture zone.

iv Bending of the Bathymetric Lineations

The E-W trending bathymetric lineations bend towards south against the 79°E fracture zone in the west especially in the near vicinity of fracture zone. The magnitude of the curvature tend to reduce towards south (Figure 5.2). The bending of the bathymetric lineations into the fracture zone can be seen more clearly on the detailed high resolution map (Figure 5.4). The change in strike of the lineations near fracture zones is commonly observed at ridge transform boundaries (*Karson and Dick, 1983; Searle, 1983; OTTER Scientific team, 1984*). *Gallo et al. (1986)* explained this morphometric signature to be the mimic of the ridge-transform intersection (RTI) morphology. As the transform boundary approaches, the trend of the ridge axes turn sharply into and merge with the trend of the transform. Deep tow investigations near Vema transform fault in the Mid Atlantic by *Macdonald et*

al. (1986), depicted curving of the faults in the direction of transform. The curving of the extensional structures into the transform are suggested to be the transmission of transform related stresses.

v Seamounds in the Vicinity of 79 °E Fracture Zone

The detailed high resolution multibeam bathymetric surveys carried out in the vicinity of 79°E fracture zone have revealed several new seamounds in the region which are highlighted on the regional bathymetric map (Figure 5.1). The region is dotted with 14 conspicuous seamounds whose heights range from 500m to 1200m.

The southern part is dominated by the occurrence of seamounds (Figure 5.2). In sharp contrast in the northern part of the area, the seamounds are absent. Seamounds on the western side show a linear trend parallel to the fracture zone and are in general, more circular, conical and single peaked. These seamounds overlie the transform-parallel ridge on the west side of the fracture zone. The seamounds to the east of the fracture zone between 14 °S to 14°15'S are of irregular shape and multi-peaked while the rest are steep and have single peak. Detailed bathymetry at a contour interval of 50m of one of the multi-peaked seamound, whose highest point is at 14 °10'S and 79°17'E, is shown in Figure 5.7.

Seamount clusters in the southern portion of the area may be related to the fracture zone. Fracture zones provide easy conduits for seamounts (*Batiza, 1982*). Although, fracture zones are not necessary for seamount formation, there may be local perturbations to the plumbing system or other zones of weakness in the crust that control the location of seamounts (*Epp and Smoot, 1989*). It appears probable that the fracture zone at 79 °E provided conduits for seamount formation. The bathymetric expression of the fracture zone is confined to 9-11 km in the south and widens to over 56 km in the north. One can speculate that the concentration of the seamount clusters on either side of the fracture zone in the south may probably be related to the narrower width of the fracture zone.

5.3 FREE-AIR GRAVITY OBSERVATIONS

NEAR 79°E FRACTURE ZONE

Gravity data were collected along 11 N-S profiles (Figure 5.9). The gravity observations are tied to the Marmugao base and the free-air gravity values are computed.

The free-air gravity values vary from 0.0 to -45.0 mgals in the region. Along these profiles, as expected, the free-air gravity followed closely the bottom topography (Figure 5.9). Towards the southern end of the profiles HS1-1 and HS1-2, a seamount, with a relief of 750 m, is reflected by an anomaly of 10 mgals amplitude. A broad, relative free-air gravity high of

about 20 mgals amplitude which has a width of about 150 km is observed consistently along the profiles HS1-1 to HS1-5. This gravity high followed by a low, corresponds to the abrupt changes in the bathymetric signature (Figure 5.9) marking the presence of 79°E fracture zone. This anomaly with an amplitude of 20 mgals resembles the edge effect anomaly across the fracture zones (*Sibuet et al.*, 1974). A small scarp of about 400 m relief observed along the profile HS1-7 towards south merging into the smooth topography is associated with 8-10 mgals free-air anomaly.

The free-air gravity anomalies across the 79°E fracture zone are modeled to predict the probable density structure and to estimate the lithospheric thickness. The modeling studies were carried out taking into consideration the thermal structure of the lithosphere. These aspects are dealt in detail in the Chapter 6.

5.4 DISTRIBUTION OF SEAMOUNTS IN THE CENTRAL INDIAN BASIN

It has long been recognized that the distribution of seamounts in the ocean basins provide useful constraints on the models of plate evolution and the nature of volcanism (*Menard*, 1964, 1969; *Udintsev et al.*, 1976). Based on the studies of the distribution of seamounts in the Pacific, it was suggested that the abundance of seamount distributions are influenced by the characteristics of the underlying lithosphere. These characters include

the lithospheric thickness, the state of stress and the fracture zone patterns (Vogt, 1974, 1979; Batiza, 1982). These studies relied on the existing bathymetric charts and conventional echosounding data. With these data sets even in the extensively covered Pacific ocean, the seamount abundance estimates are considered to be incomplete (Batiza, 1982). It becomes exceedingly difficult to accurately map the smaller size seamounts whose heights range between 500 to 2000 m, with the conventional echosounding data due to the wide spacing of the survey tracks and limited coverage.

In the Central Indian Basin multibeam swath bathymetric data helped in identifying several hitherto unknown seamounts. In the present study multibeam data available for the entire study area has been considered to identify the seamounts. Some of these seamounts were earlier reported by Mukhopdhyay and Khadge (1990) based on conventional echosounding data. In the present study seamounts which are more than 500 m height are considered. A total number of 80 seamounts are identified in the region whose heights range from 500 m to 1850 m. The locations of these seamounts are shown in Figure 5.10. Seamounts identified based on echosounding data are represented by solid circles whereas the triangles represent seamounts identified based on *Hydrosweep* data. The identified fracture zones are also shown. As can be seen on the Figure 5.10 the trends of the seamounts follow the flow line pattern parallel to the fracture zones. The tectonic implications of the distribution of these seamounts in relation to the fracture zones are discussed in Chapter 7.

Why not
from both
the data
sets?

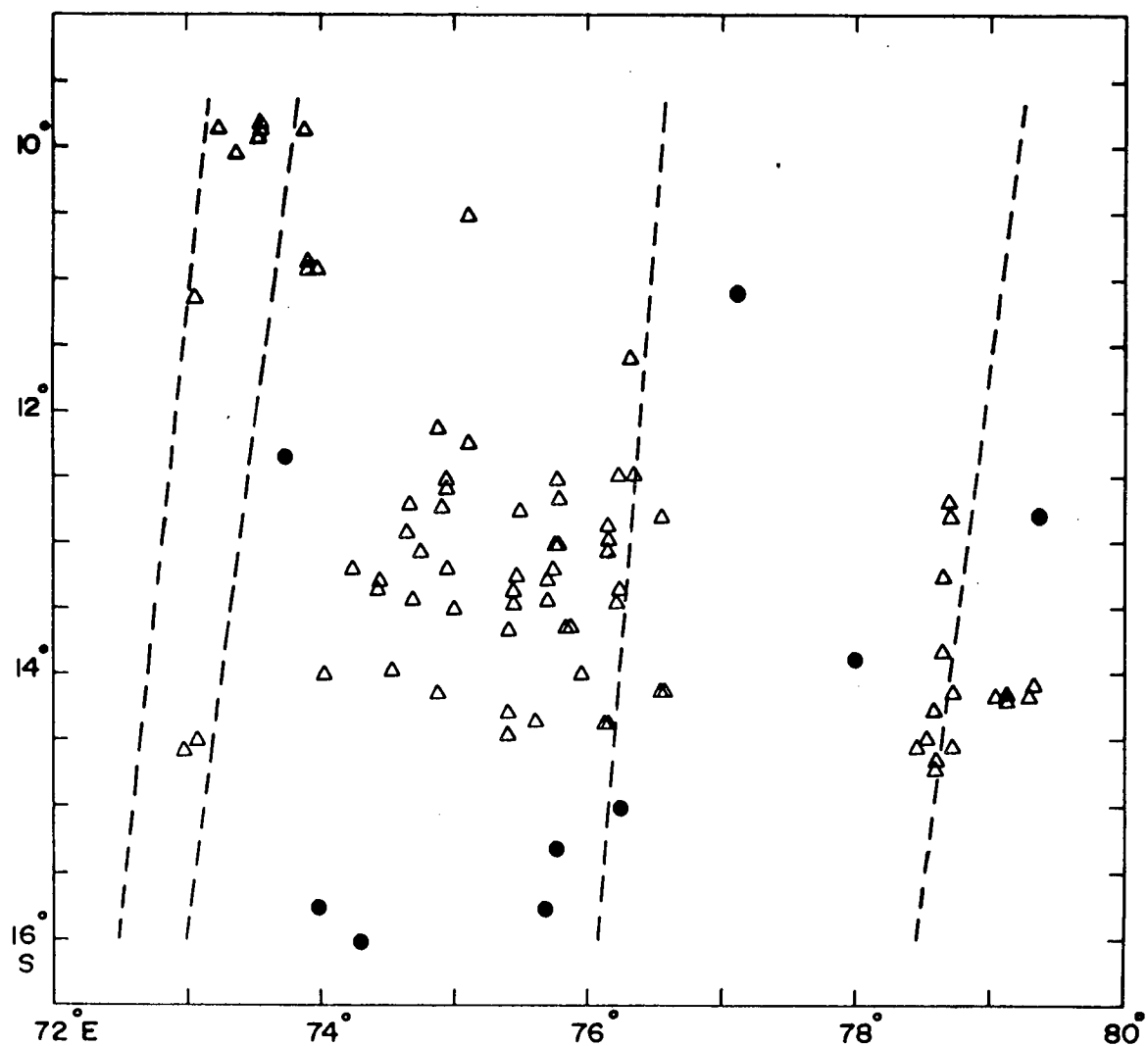


Figure 5.10 Map showing the distribution of seamounts in the Central Indian Basin. Open triangles represent the locations of the seamounts identified based on multibeam data and the solid dots from echosounding data. The inferred fracture zones are shown with dashed line.

CHAPTER VI

MODEL STUDIES: THERMAL STRUCTURE OF THE OCEANIC LITHOSPHERE AND FREE-AIR GRAVITY MODEL STUDIES AT 79°E FRACTURE ZONE

*CHAPTER VI***MODEL STUDIES: THERMAL STRUCTURE OF THE
OCEANIC LITHOSPHERE AND FREE-AIR GRAVITY
MODEL STUDIES AT 79°E FRACTURE ZONE****6.1 THERMAL MODELS OF OCEANIC LITHOSPHERE**

The broad structure of the oceanic lithosphere was initially derived from the regional ocean floor topography and heat flow data. Based on these data, models have been proposed which fall into two categories. One class of models (plate model) are represented by a slab of finite and constant thickness which cools with distance from the axis of accretion with the base of the slab held at a constant temperature (*McKenzie, 1967; Sclater and Francheteau, 1970*). The second category (boundary layer model) assumes that the lithosphere is a semi-infinite half space, which increases in thickness with age (*Parkér and Oldenburg, 1973; Forsyth, 1977*). These models have explained the general decrease in heat flow with age and the increase in depth away from the ridge axis. The raw heat flow data are highly scattered, hence more emphasis has been placed on the ocean floor topography in developing the quantitative models of the oceanic lithosphere. *Sclater et al. (1971)* have shown that most mid ocean ridges are at a depth of 2500 m and the depth increases with age indicating a general subsidence. It was shown that for the crust younger than 80 Ma the depth increases linearly with the

square root of age (*Davis and Lister, 1974*). This relation is not valid for older ocean floor and it was found that beyond 80 Ma the depth increases exponentially to a constant value of 6400 m (*Parsons and Sclater, 1977*). This two stage relationship between the depth and age was explained in terms of formation of a thermal boundary layer. The magma cools as it moves away from the spreading center and the thickness of the rigid layer thus created increases (Figure 6.1). *Parker and Oldenburg (1973)*, predicted that the thickness of the rigid layer increases as the square root of age. Further more *Parsons and Sclater (1977)* have demonstrated that for the crust younger than 80 Ma, both plate and boundary layer models approximate each other in defining the isothermal surfaces and they differ principally in their lower boundary conditions (Figure 6.1). The boundary layer cooling model predicts an error function geotherm which is a good approximation of the actual geotherm for ages less than 70 Ma (*Parsons and Sclater, 1977*).

As per the thermal models the lower boundary of the lithosphere can be represented by an isotherm T_M , at temperature greater than T_M mantle rocks behave like fluid and at temperature below T_M , the rocks of the mantle and crust are essentially rigid at low stress levels (*Turcotte and Oxburgh, 1967, 1972*). The value of T_M was suggested to be about $1000^\circ \pm 200^\circ\text{C}$ and the average thickness of the lithosphere ^{is} about 100 km (*Turcotte, 1974*).

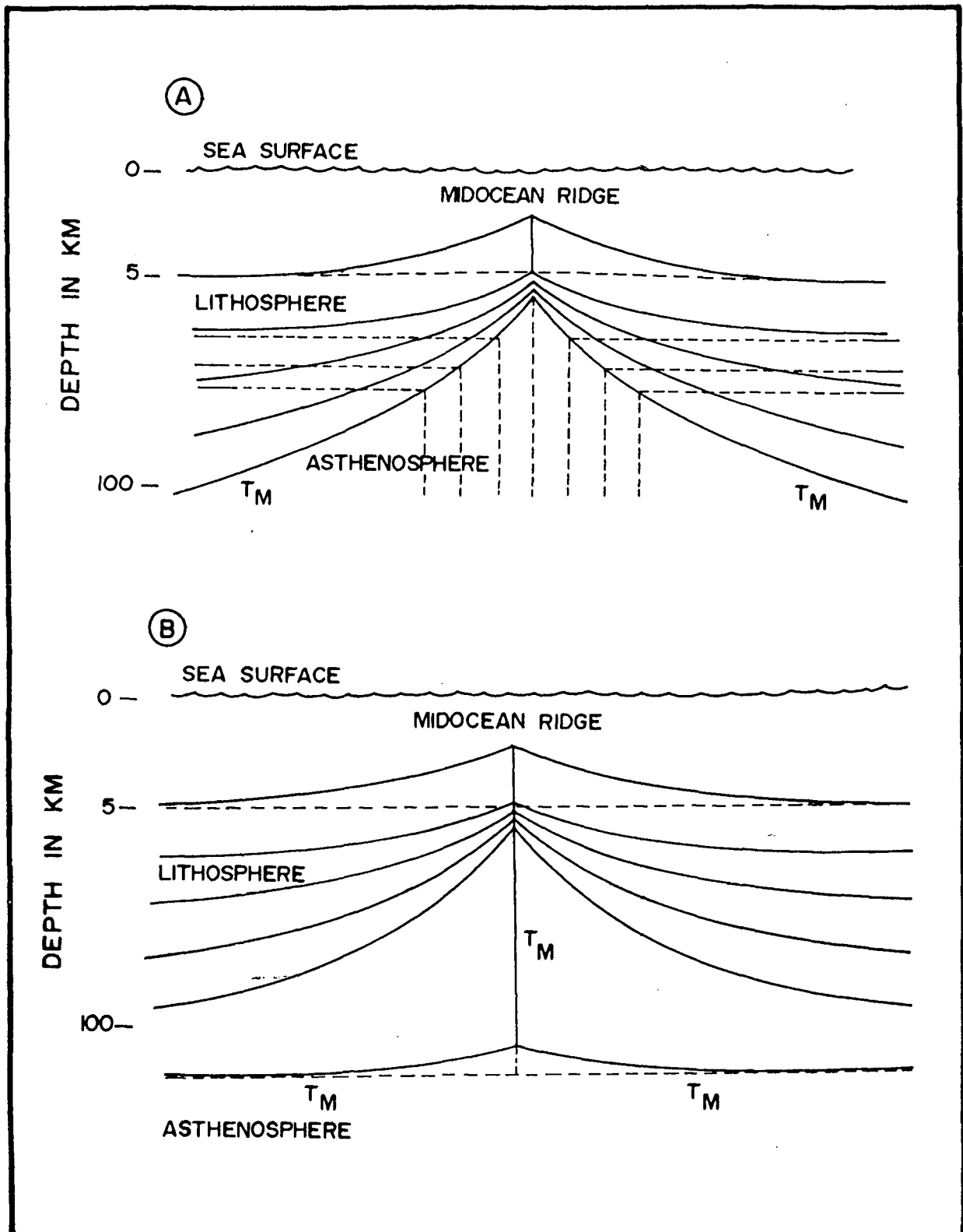


Figure 6.1 Schematic thermal models of the oceanic lithosphere. A) Boundary layer model. B) Constant plate model. (after *Slater et al.*, 1980). T_M indicates the deep mantle temperature. The solid lines represent isothermal surfaces within the cooling lithosphere.

Studies of lithospheric bending at Hawaii (*Walcott, 1970*) and at trenches (*Hanks, 1971*) have shown that the oceanic lithosphere exhibits elastic behavior on time scales of millions of years. Based on flexural rigidity values it was suggested that the upper 25 km of the lithosphere behaves like an elastic brittle material on geological time scales. In the depth range 25-100 km the oceanic lithosphere exhibits plastic behavior, at low stress levels this region acts as a stress guide and plastic deformation takes place when subjected to large stress (above 10 k bars) (*Wallcott, 1970*). The boundary of the top layer of the lithosphere which behaves like an elastic brittle material can be represented by an isotherm T_E , the value of T_E was suggested to be about 300°C (*Turcotte, 1974*). Based on these observations, *Turcotte (1974)* proposed a broad division of the oceanic lithosphere (away from the ridge axis) depending on the deformation mechanism. The thickness of the elastic brittle layer is termed as the effective elastic thickness (H_E) of the lithosphere.

DEPTH RANGE IN km	DEFORMATION MECHANISM
0 - 25	<i>Elastic Brittle</i>
25 - 100	<i>Plastic</i>
> 100	<i>Fluid</i>

Thus the oceanic lithosphere can be viewed as a combination of mechanical and thermal boundary layers (*Sclater et al.*, 1980; *Parsons and McKenzie*, 1978).

Mechanical models have been further refined from the studies of flexure of the oceanic lithosphere at Hawaiian- Emperor chain (*Watts*, 1978; *Caldwell and Turcotte*, 1979; *Watts et al.*, 1980; *Bodine et al.*, 1981). These studies have shown that the effective elastic thickness of the lithosphere is approximately proportional to the square root of the age.

6.2 THERMAL STRUCTURE OF THE LITHOSPHERE AT FRACTURE ZONES

The various thermal and mechanical models of the lithosphere discussed above demonstrate a prominent age dependent thermal structure of the lithosphere. Fracture zones in the ocean basins which represent inactive traces of the transform faults depict unique asymmetrical contact between separate sections of the same lithospheric plate having substantially different thermal structures. The difference in the thermal structures arises from the age offset of the lithospheric sections which are in contact at the fracture zones. Topography along the fracture zones consist of long ridges, troughs and scarps which separate regions of different depth (*Menard and Atwater*, 1969). This topographic expression of the fracture zone is preserved and can be traced for thousands of kilometers. The persistence of the

topographic expression suggests that the generation and evolution of the oceanic lithosphere proximal to the transform boundaries is different from the normal oceanic lithosphere (*Gallo et al.*, 1986). Even though there is persistence of the topography due to the relative vertical subsidence of the crust with age, if there is sufficient sedimentation the fracture zone may get buried. The diminished bathymetric signature of the Clipperton fracture zone in the Pacific ocean is due to the sediment in-fill and this in turn resulted in small amplitude geoid anomalies (*Wessel and Haxby*, 1990). The persistence of ridge and trough topography along the fracture zones has been attributed to the thermomechanical interactions in the lithosphere driven by the age contrast across the fracture zone (*Sandwell and Schubert*, 1984). Figure 6.2 shows the thermomechanical model of the lithosphere at a fracture zone.

6.2.1 FLEXURAL RESPONSE OF THE LITHOSPHERE

As a consequence of the differential subsidence due to the age contrast across the fracture zone, the lithosphere adjacent to the fracture zone undergoes flexure and maintains the topographic expression (*Sandwell and Schubert*, 1982). These authors have demonstrated that the lithospheric flexure occurs across the Pioneer and Mendocino fracture zones in the north west Pacific. Figure 6.3 , illustrates the evolution of the fracture zone and the flexural response of the lithosphere. At the ridge axis (A-A', Figure 6.3) the newly created lithosphere on the younger side separates the older

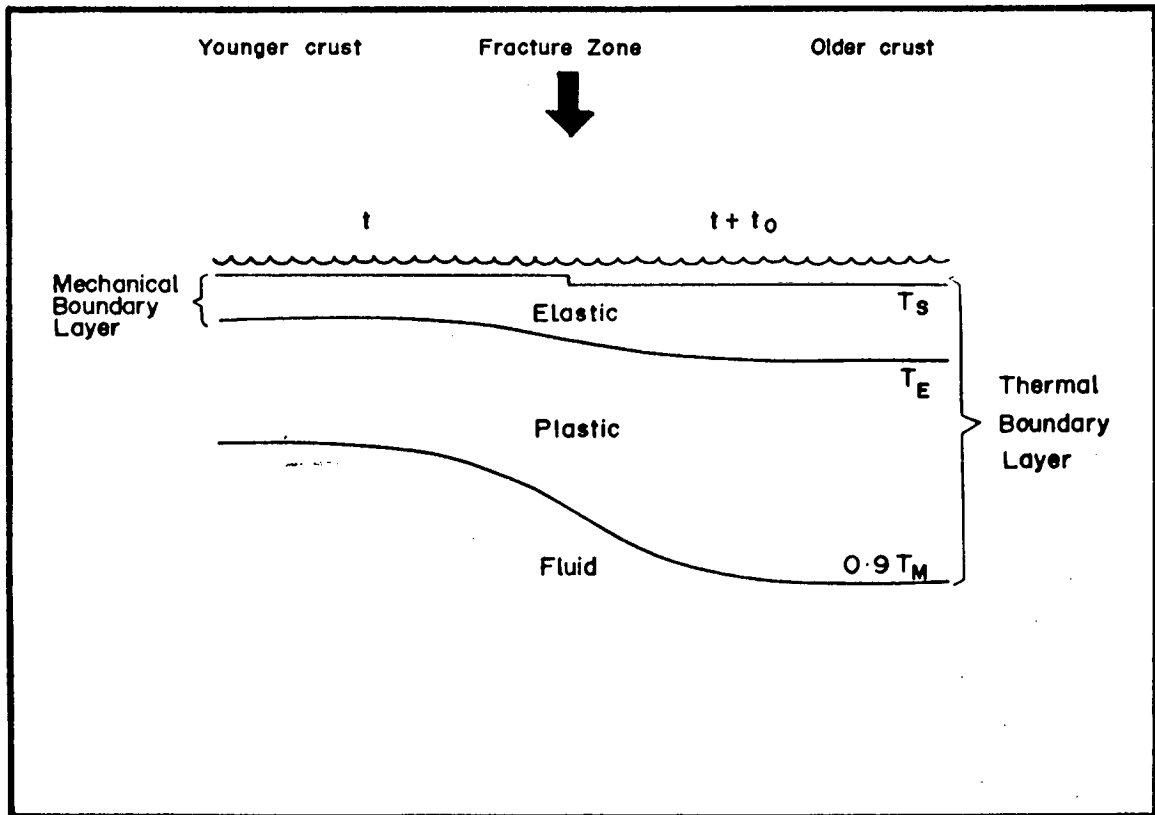


Figure 6.2 Thermomechanical model of the oceanic lithosphere at a fracture zone (after Sandwell, 1984).

lithosphere. As the crust generated by the two segments evolve to B-B' (Figure 6.3), the depth far from fracture zone on the younger lithospheric segment increases at a higher rate than the depth far from fracture zone on the older segment (*Menard and Atwater, 1969; Delong et al., 1977; Sibuet and Mascle, 1978*). This mechanism is depicted by the subsidence curves shown at the right side of the Figure 6.3. By the time the two segments evolved to B-B' the overall change in depth **across the fracture zone**, h_B is less than the initial bathymetric step h_A . However, the height of the scarp **at the fracture zone** remains equal to h_A . If there is no vertical slip at the fracture zone, the lithosphere must flex to maintain the expression of the scarp as shown on the lower portion of the Figure 6.3. The amplitude of this flexure δ_B is the change in the differential subsidence from A to B, ie., $h_A - h_B$.

The shape of the flexural topography depends on the effective elastic thickness H_E of the lithosphere (*Sandwell and Schubert, 1982*). Since H_E is proportional to the square root of the age, the flexure is asymmetric about the fracture zone with the younger lithosphere flexing at a shorter wave length than the older lithosphere. The effective elastic thickness again depends on the thermal structure controlled by the depth to the isotherm T_E . These observations suggests that the thermal structure across the fracture zone strongly influences the overall fracture zone topography.

If the lithosphere is in local isostatic equilibrium, the effects of lateral heat conduction and local isostasy results in rapid smoothing of the topography with age. However, it is found that the topographic expression

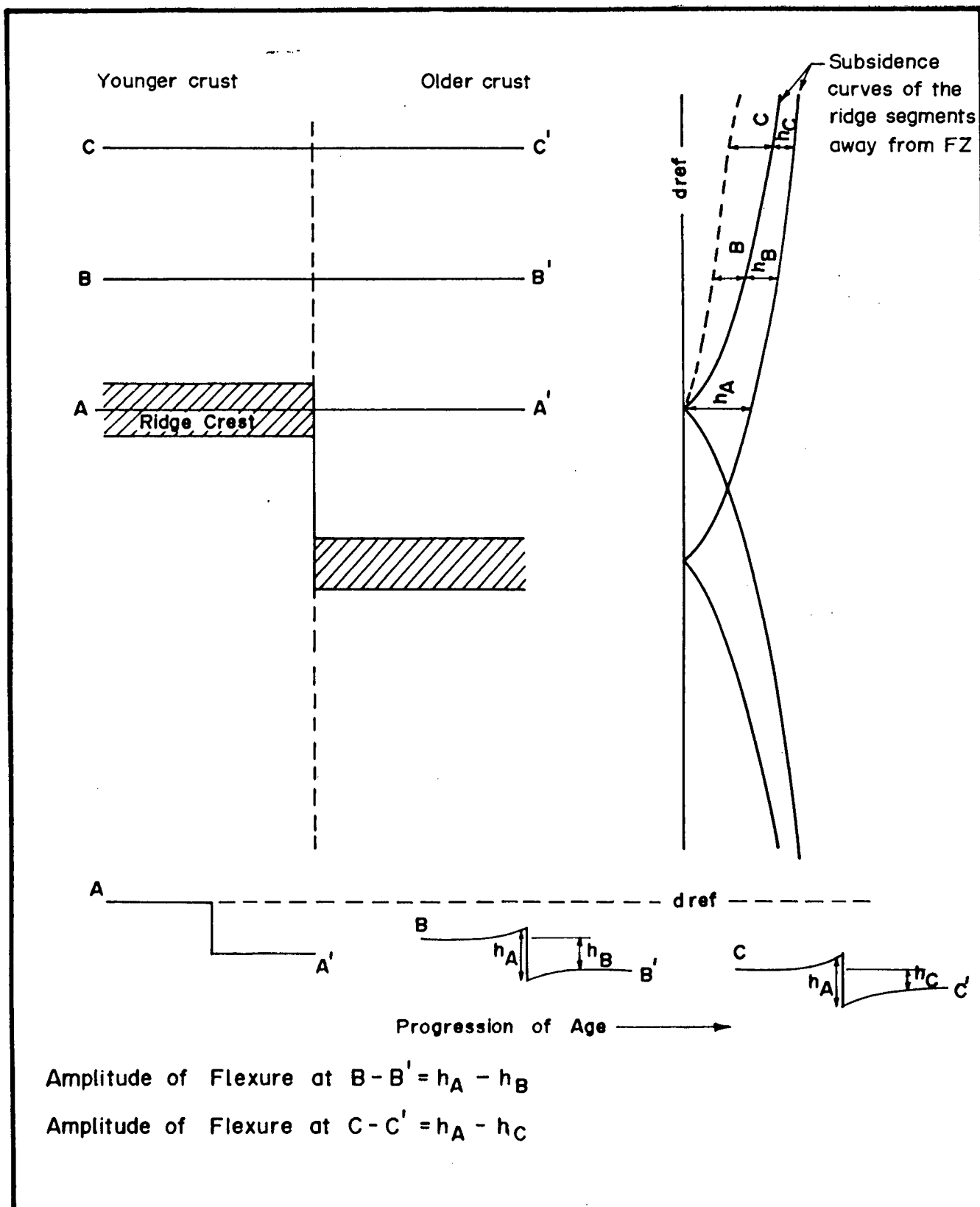


Figure 6.3 Schematic illustration of the flexural response of the lithosphere at a fracture zone. Subsidence curves of the ridge segments are shown at the right.

persists along the fracture zones. Component of lithospheric flexure is responsible for the persistence of ridge and trough topography (*Sandwell, 1984*). Lithospheric flexuring implies that the isostatic compensation is regional rather than local.

The density structure within the lithosphere is sensitive to the temperature changes. In the present study the thermal structure of the lithosphere is computed to predict the probable density variations within the lithospheric section considering a thermomechanical model (Figure 6.2) of the fracture zone.

6.3 COMPUTATION OF THERMAL STRUCTURE AT A FRACTURE ZONE

In this section the thermal structure of the oceanic lithosphere at the fracture zone is computed based on the thermomechanical model considering the lateral heat conduction across the fracture zone, following the methods proposed by *Louden and Forsyth (1976)* and *Sandwell (1984)*.

In the region outside the active transform fault, the two dimensional thermal structure is found by solving the time dependent heat conduction equation :

$$\frac{\partial^2 T}{\partial X^2} + \frac{\partial^2 T}{\partial Z^2} = \frac{1}{k} \frac{\partial T}{\partial t} \quad \text{--- (1)}$$



Where k is the thermal diffusivity, which is assigned a value of 8×10^{-7} sq. m per sec. (*Parsons and Sclater, 1977*).

Initially at $t=0$ age, at the ridge axis near the transform fault, the geotherm on the right side of the fracture zone (Figure 6.2) corresponds to an age of t_0 and the left side has a constant temperature T_M . Thus, initially, the thickness of the elastic layer on the left (younger) side is zero and a continuous elastic layer develops across the fracture zone away from the transform fault as the fracture zone evolves.

The initial temperature distribution is:

$$T(x, z, t_0) = \begin{cases} T_S + (T_M - T_S) \operatorname{erf} \left[\frac{z}{2\sqrt{kt_0}} \right] & x > 0 \\ T_M & x < 0 \end{cases} \quad \text{--- (2)}$$

The surface boundary condition is $T(x, 0, t) = T_S$

Where T_S is the sea water temperature ($\approx 0^\circ\text{C}$), T_M is the temperature of the deep mantle, 1365°C (*Parsons and Sclater, 1977*) and t is the time.

Away from the initial conditions the thermal structure across the fracture zone is a function of the age contrast. At a given depth and distance from the fracture zone, the isotherms can be computed.

For the initial temperature distribution given above, the convolution integral can be evaluated analytically (*Sandwell and Schubert, 1982*), and is:

$$T(x, z, t) = T_S + \frac{(T_M - T_S)}{2} \left[\operatorname{erfc} \left[\frac{-x}{2\sqrt{k(t-t_0)}} \right] \operatorname{erf} \left[\frac{z}{2\sqrt{kt}} \right] + \operatorname{erfc} \left[\frac{x}{2\sqrt{k(t-t_0)}} \right] \operatorname{erf} \left[\frac{z}{2\sqrt{k(t-t_0)}} \right] \right] \quad \text{--- (3)}$$

The equations (2) and (3) are modified from that of *Sandwell (1984)* by changing the sign of x , in order to simulate the effects of a right laterally offset fracture zone, wherein, the right side of the fracture zone represents older crust (Figure 6.4).

The function $\operatorname{erfc}(x)$ ranges from 2 to 0 as x varies from $-\infty$ to ∞ . Thus, far from the fracture zone the geotherm follows the error function of the boundary layer convection model (*Turcotte and Oxburgh, 1967*). As a result of lateral heat conduction, temperatures vary continuously across the fracture zone (*Louden and Forsyth, 1976*).

The base of the lithosphere is an isotherm equal to a fraction of the mantle temperature, given as $0.9T_M$ (Sandwell, 1984). The base of the elastic layer as defined by the stress relaxation temperature T_E , is suggested to be in the range of 300°C to 600°C (Watts *et al.*, 1980). A value of 450°C for T_E (Sandwell and Schubert, 1982) has been considered in the present study.

In Figure 6.4, the computed isotherms $0.9 T_M$ and T_E , obtained from the equation (3), for an age offset of 2.08 My across the 79°E fracture zone are shown. The physical constants and the model parameters are summarized in Table 6.1

6.3.1 FLEXURAL RIGIDITY

The elastic properties of the lithosphere are usually expressed in terms of flexural rigidity (Cochran and Talwani, 1979). The flexural rigidity can be computed using the relation:

$$D = \frac{E H_E^3}{12(1-\nu^2)} \quad \text{--- (4)}$$

Where,

D - Flexural Rigidity

E - Young's Modulus

H_E - Effective elastic layer thickness

ν - Poisson's ratio

The variations of the flexural rigidity across the 79 °E fracture zone are computed using the above relation. The effective elastic thickness of the lithosphere was obtained from the isotherm defining T_E and the constants Young's modulus and Poisson's ratio were assumed (Table 6.1). The variation of the flexural rigidity of the lithosphere across 79 °E fracture zone is shown at the bottom part of the Figure 6.4.

6.3.2 DENSITY STRUCTURE

The variations in the density are related to the temperature changes, due to the thermal expansion. The following equation of state is used to compute the density variations corresponding to the temperature changes.

$$\sigma(x, z, t) = \sigma_M [1 - \alpha (T(x, z, t) - T_M)] \quad \text{--- (5)}$$

TABLE T6.1

Physical constants and model parameters used

Parameter	Definition	Value/ Units	Reference
α	Thermal expansion coefficient	$3.1 \times 10^{-5} \text{K}^{-1}$	Parsons and Sclater (1977)
E	Young's modulus	6.5×10^4 MPa	Sandwell and Schubert (1982)
T_E	Stress relaxation temperature	450°C	Watts et al. (1980)
T_M	Mantle temperature	1365°C	Parsons and Sclater (1977)
T_S	Surface temperature	0°C	
ν	Poisson's ratio	0.25	
D	Flexural rigidity	newton-meter	
δ	Flexural amplitude	meters	
H_E	Effective elastic thickness	meters	
E	Young's modulus	megapascals	

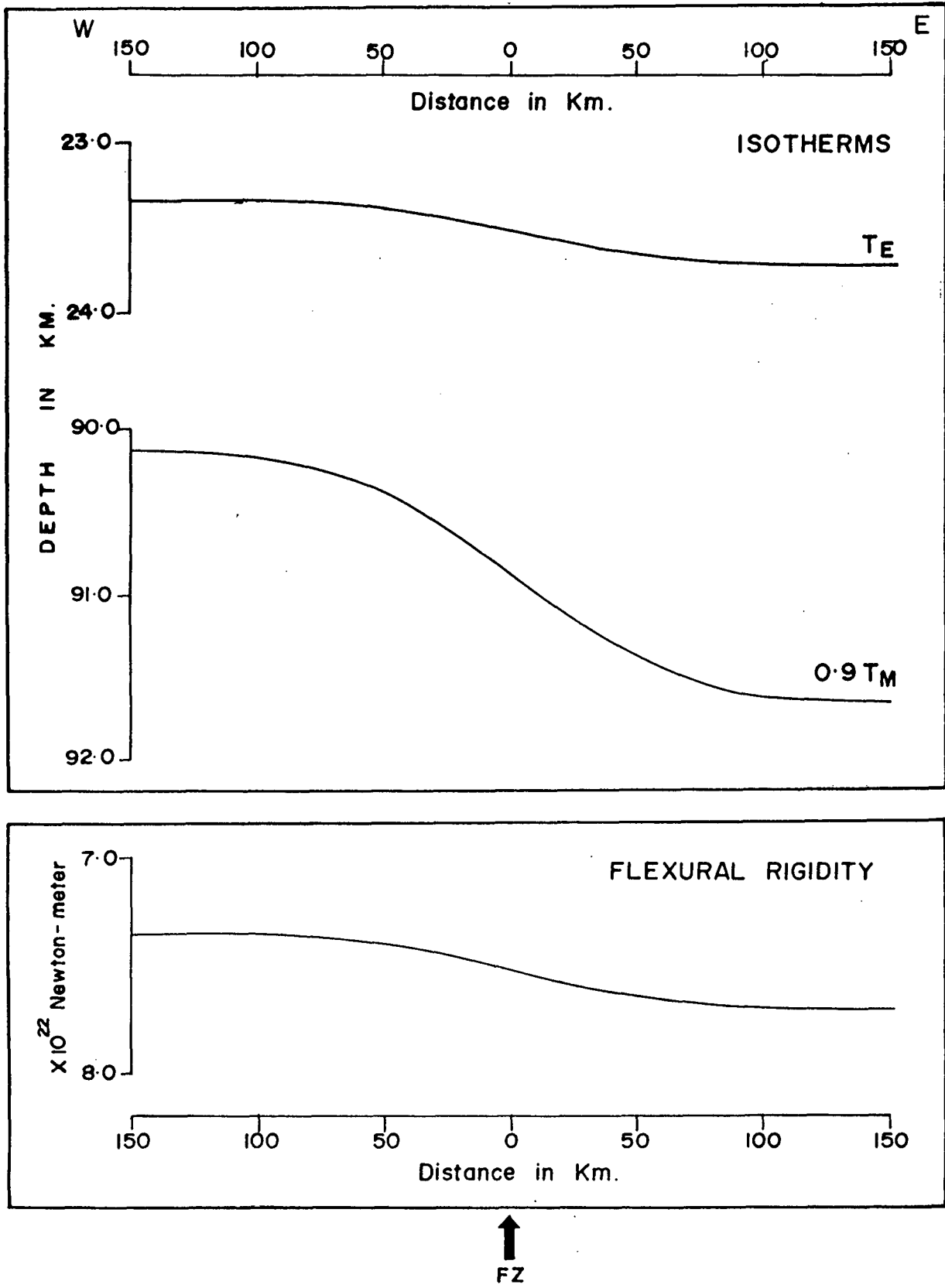


Figure 6.4 Computed isotherms at 79°E fracture zone. Stress relaxation temperature (T_E) 450°C and deep mantle temperature (T_M) 1365°C are considered. The bottom part of the figure shows the variation in flexural rigidity across the 79°E fracture zone.

Where σ_M is the density of the mantle at temperature T_M , and is assumed to be 3400 kg/m^3 , and α is the thermal expansion coefficient and is considered as $3.1 \times 10^{-1} \text{ K}^{-1}$ (*Parsons and Sclater, 1977*).

Densities obtained from the above relation are utilized to model the free-air gravity anomaly to deduce probable density structure and to estimate lithospheric thickness across 79°E fracture zone.

6.4 FREE-AIR GRAVITY MODEL STUDIES

The response of the differential subsidence and the lithospheric flexure across the fracture zone result in step like free-air gravity anomalies (*Sibuet et al., 1974*) and the geoid anomalies (*Parmentier and Haxby, 1986; Sandwell, 1984; Wessel and Haxby, 1990*). Several authors have suggested the use of gravity anomalies as a means of predicting the probable density structure and thickness of the lithosphere, associated with the cooling plate model (*Le Pichon et al., 1973; Sibuet et al., 1974; Dorman, 1975; Sibuet and Mascle, 1978*).

The free-air gravity anomalies observed across the 79°E fracture zone are modeled following the procedure of *Talwani et al., (1959)*, assuming two dimensional bodies. The gravitational edge effect anomalies that are observed across the fracture zones are best reflected over profiles perpendicular to the strike of the fracture zone. Therefore, data along an E-W

line (AA-AA', Figure 2.8) was considered by retrieving the observed gravity and water depth values from the closely spaced (5 miles) N-S lines for the purpose of model studies. The free-air gravity along the profile AA-AA' (Figure 6.5) thus represents data points spaced at 9.2 km and reflects long wavelength character. The average depth on the western and eastern sides of the fracture zone are 5250 and 5400 m respectively. The age of the oceanic crust as derived from the magnetic studies along this profile are 59.47 Ma on the western (younger side) and 61.55 Ma on the eastern (older) side of the fracture zone. The age offset across the fracture zone along the profile AA-AA' is 2.08 Ma.

The gravity effect of the lithospheric section is computed by assuming three layers, the sediment, the oceanic crust and the upper mantle. In the absence of any refraction data a sediment layer of 500 m with a density of 2260 kg/m^3 was assumed. These values are assumed considering the sediment thickness reported at the DSDP sites 214 and 238. The sediment layer is followed by the oceanic crust for which a crustal thickness of 6.0 km and a density of 2800 kg/m^3 was assumed. Global average thickness of the oceanic crust was suggested to be about 6.0 km by *Spudich and Orcutt* (1980). The remaining part of the lithospheric section is divided into layers of constant density differing by 10 kg/m^3 starting from 3400 Kg/m^3 (Figure 6.5), following a similar approach as that of *Sibuet et al.* (1974).

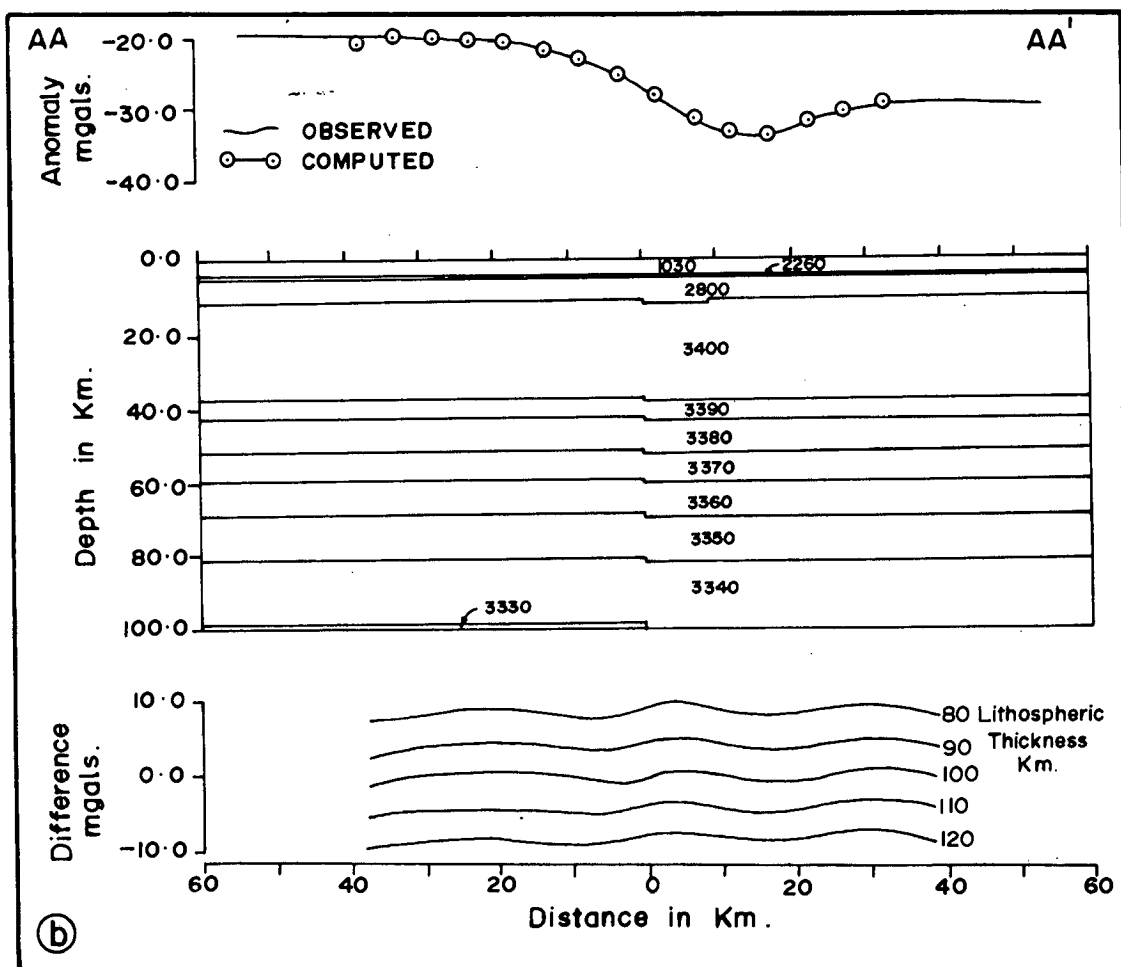
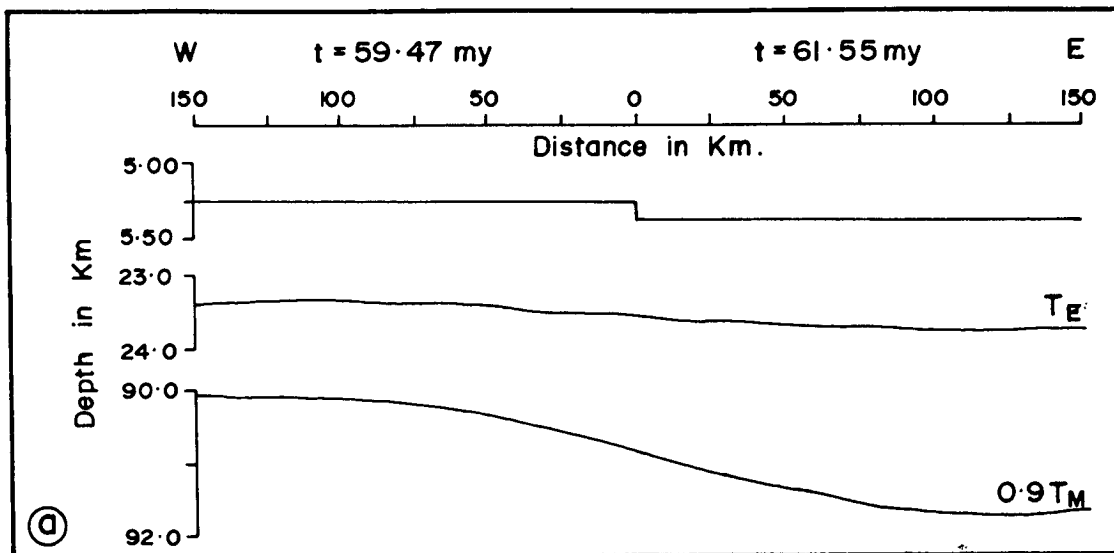


Figure 6.5 Free-air gravity model showing the lithospheric section at 79°E fracture zone. (a) The isotherms of T_E and T_M are shown. (b) Computed and observed free-air gravity along a profile AA-AA' (see figure 2.8). The bottom part of the figure shows the difference between the computed and observed free-air gravity for different assumed thicknesses of the lithosphere.

The average layer thickness within the upper mantle was constrained by the thermal structure. The depth at which a given density occurs has been determined by successive iterations using the thermal model equations (2) and (3) and the corresponding density by eq. (5). These density and layer thicknesses were incorporated in the model and a best fit was obtained (Figure 6.5). In order to satisfy the gravity low at the fracture zone more thickness of the sediment and crustal layers were invoked.

After having achieved the probable density structure and the lithospheric thickness estimate, the response of the computed gravity for various assumed thicknesses of the lithosphere was tested. These tests were made by varying the thickness of the lithosphere, while all other parameters were kept constant. The bottom part of the Figure 6.5 shows the difference between the observed and the computed gravity values, for various assumed thicknesses of the lithosphere. The least difference is observed for a lithosphere with a thickness of 100 km (Figure 6.5).

Parker and Oldenburg, (1973) proposed an empirical relationship to estimate the lithospheric thickness as $Z = 9.4 (\text{age})^{1/2}$. This relationship approximates the lithospheric thickness within ± 25 km. In the present study area the thickness of the lithosphere works out to 72.48 km for a crustal age of 59.47 Ma, using this empirical relation. The estimated lithospheric thickness obtained from the thermal and free-air gravity model is 100 km.

Sibuet et al. (1974) demonstrated that the estimates of lithosphere thickness can be obtained from the observed gravitational edge effect across the fracture zone. Estimations of lithospheric thickness were obtained across the Mendocino fracture in the Pacific (*Sibuet et al.*, 1974) and Romanche and Chain fracture zones in Atlantic (*Sibuet and Mascle*, 1978), using the thermal conduction model, with the assumption of no horizontal heat conduction across the fracture zones. In the present study, the estimates of lithospheric thickness were computed from the gravitational edge effect observed across the 79°E fracture zone, considering the thermal structure including the effects of horizontal heat conduction. These estimates give a thickness of about 100 km, which within the acceptable limits, matches the value obtained by the empirical formula suggested by *Parker and Oldenberg* (1973). More realistic estimates can be achieved by including the crustal information, from seismic refraction studies.

CHAPTER VII

DISCUSSION

CHAPTER VII
DISCUSSION

The results obtained from the present investigations are discussed in the context of the evolution of the Indian ocean in general and the evolution of the Central Indian Basin in particular. Before going into the detailed discussions pertaining to the evolution of the Central Indian Basin, a brief overview of evolution of the Indian ocean from the breakup of Gondwanaland to Present is outlined.

7.1 EVOLUTION OF THE INDIAN OCEAN

The evolution of the Indian ocean according to the observed magnetic lineation patterns can be summarized as a consequence of the processes involved in three main phases. These phases include the breakup of Gondwanaland (Late Jurassic to Late Cretaceous), Late Cretaceous to Middle Eocene period and the Middle Eocene to the Present.

7.1.1 BREAKUP OF GONDWANALAND (LATE JURASSIC TO LATE CRETACEOUS)

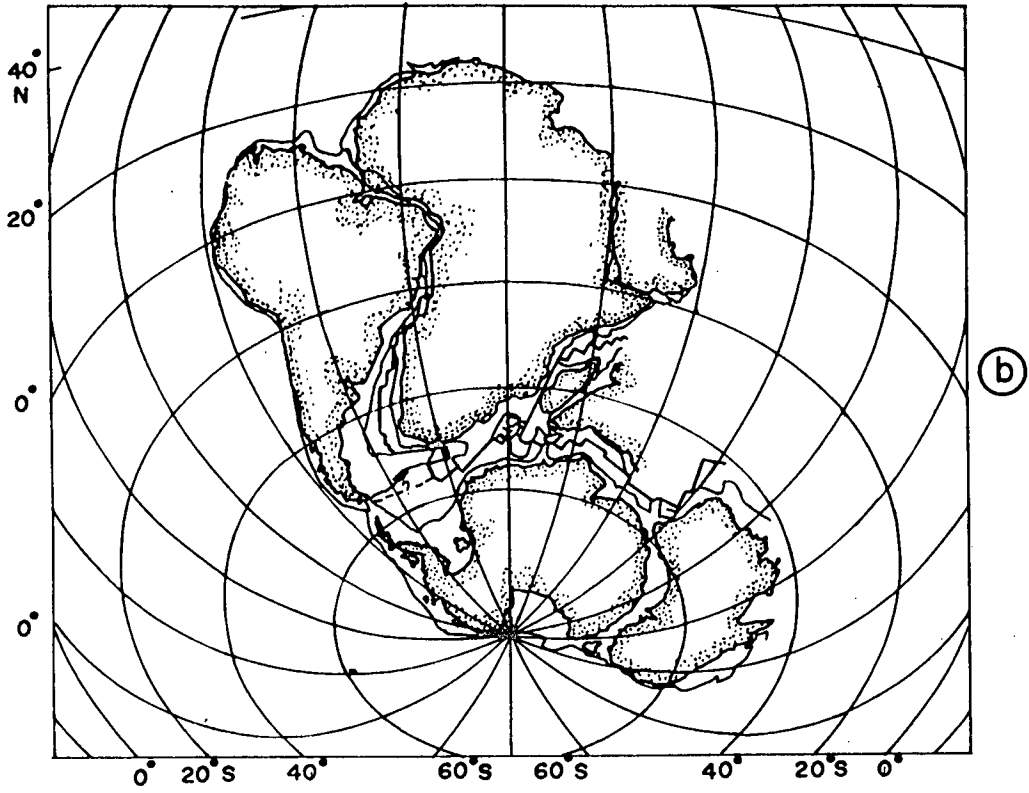
The initial breakup of Gondwanaland during the Late Jurassic period at about 152 Ma (anomaly M22), resulted in the separation of Africa from

Madagascar and Antarctica. During this process, the western Somali Basin (*Segoufin and Patriat, 1980; Rabinowitz et al., 1983; Coffin and Rabinowitz, 1987; Cochran, 1988*), the symmetric Mozambique Basin and the basin off Droning Maud land, Antarctica (*Segoufin, 1978; Simpson et al., 1979; Bergh, 1977, 1987*) have formed.

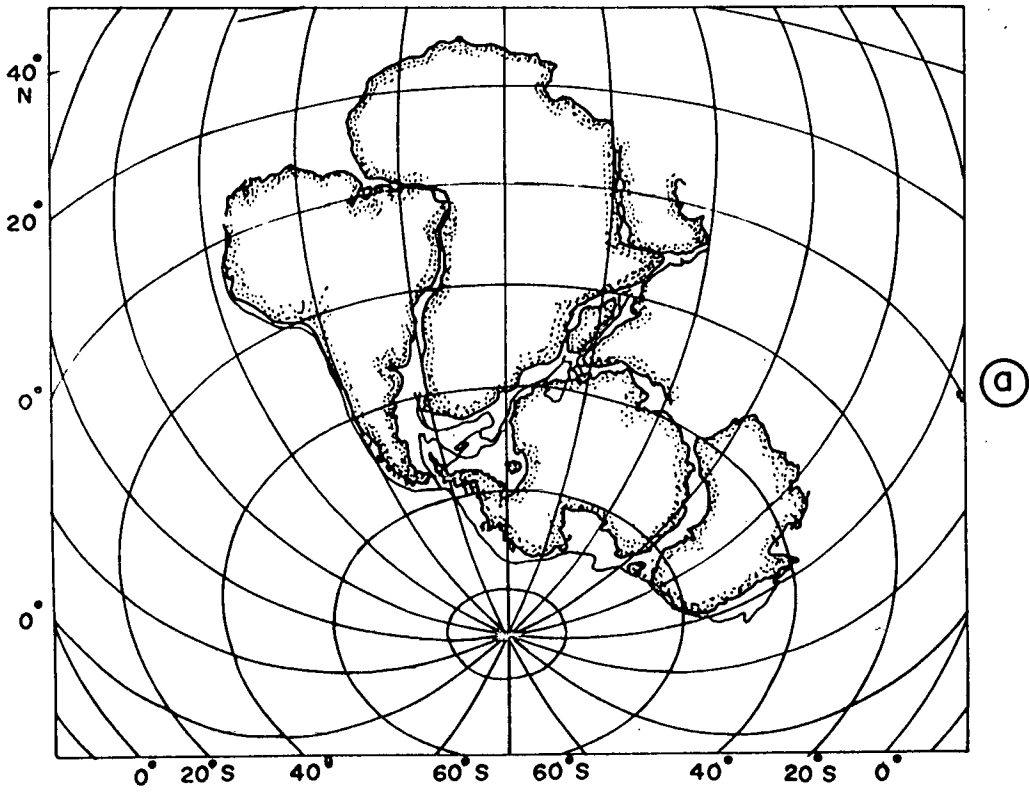
Subsequent to the initial break up, during the Early Cretaceous period at about 127 Ma (anomaly M11), the South Atlantic started to form (*Larson and Ladd, 1973; Rabinowitz, 1976*) and probably during the same period India and Madagascar separated from Antarctica creating Mesozoic basins along the western margin of Australia (*Markl, 1974, 1978; Larson et al., 1979; Veevers et al., 1985*). The movement between Africa and Madagascar ceased some time in the Early Cretaceous (*Norton and Sclater, 1979*). Figures 7.1a and 7.1b illustrate the initial position of the southern continents before breakup and the reconstruction during the Early Cretaceous period respectively.

7.1.2 LATE CRETACEOUS TO MIDDLE EOCENE

This period recorded the rapid northward drift of Indian plate towards Asia. As a consequence of this process major portion of the Indian ocean has evolved and resulted in the formation of ocean basins. India left Madagascar in the Late Cretaceous period (80-90 Ma). This event was recorded in a suite of lavas along the east coast of Madagascar (*Vallier,*



(b)



(a)

Figure 7.1 (a) Initial position of the southern continents before breakup (b) Reconstructed positions of the continents during Early Cretaceous (after Norton and Slater, 1979).

1974). *Norton and Sclater* (1979), opined that similar volcanism, if existed on the west coast of India, probably got masked by the later Deccan trap events. The seafloor spreading record of the first few reversals after the Cretaceous normal suggested very high spreading rates (up to 15 cm/yr, half rate) in the Latest Cretaceous (*Norton and Sclater, 1979*). *Larson et al.*, (1978) suggested a major reorganisation of spreading direction between India and Antarctica during the Late Cretaceous following the separation of India from Madagascar (Figure 7.2).

In the Early Paleocene, the ridge axis between Madagascar and India jumped towards India and separated Seychelles platform from India and formed the Chagos-Laccadive transform (*Norton and Sclater, 1979; Patriat and Segoufin, 1988*). The Early Paleocene reconstruction indicating the separation of Seychelles from India is shown in Figure 7.3a.

In summary, during this period (Late Cretaceous to Middle Eocene) the basins between Africa-Madagascar and Antarctica (*Bergh and Norton, 1976; Patriat, 1979; LaBrecque and Hayes, 1979; Sclater et al., 1981; Fisher and Sclater, 1983*); the Madagascar and Mascarene Basins, the eastern Somali Basin and the Arabian sea between Africa-Madagascar and India have evolved (*McKenzie and Sclater, 1971; Whitmarsh, 1974; Schlich, 1975, 1982*). The mirrored Central Indian Basin and Crozet Basins between India and Antarctica (*McKenzie and Sclater, 1971; Sclater and Fisher, 1974; Schlich, 1975, 1982*) and Wharton Basin between India and Australia

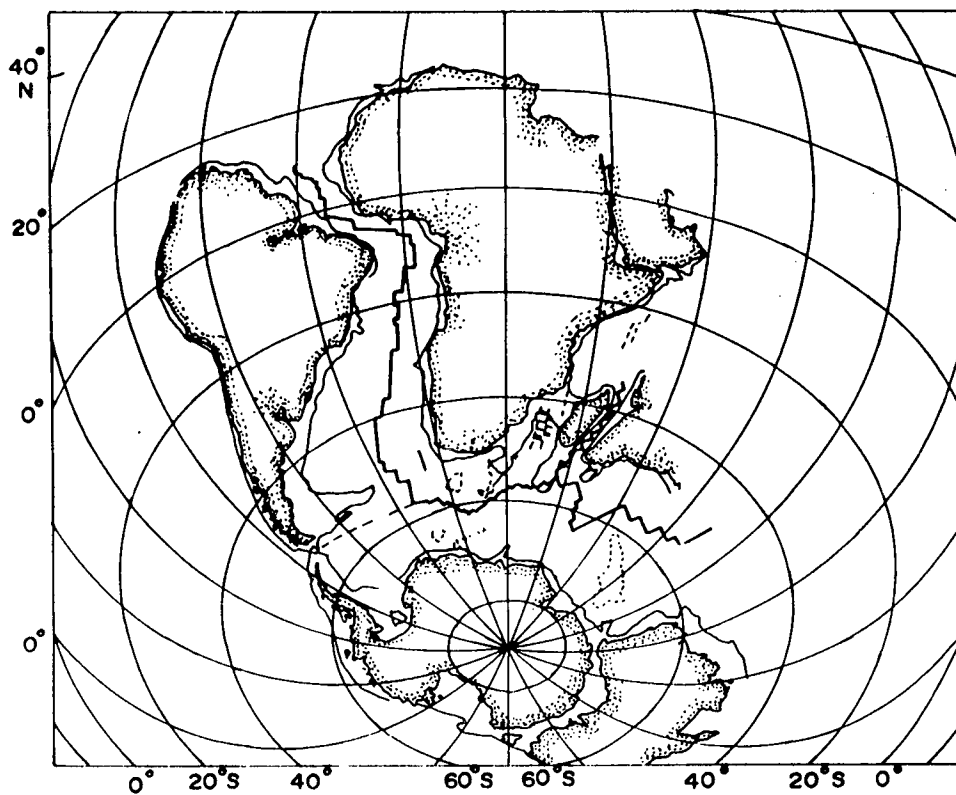


Figure 7.2 Reconstruction during Late Cretaceous (80 Ma) (after Norton and Sclater, 1979).

(*Sclater and Fisher, 1974; Liu et al., 1983*) were also formed during this period.

In addition to the formation of these basins, Australia and Antarctica commenced to separate during the Eocene (*Weissel and Hayes, 1972; Cande and Mutter, 1982*).

7.1.3 MIDDLE EOCENE

The latest period in the evolution of the Indian ocean started with a major reorganization of the spreading centers consequent to the collision of India with Asia in the Middle Eocene.

Indian plate collided with Asia in the Middle Eocene about 43 Ma (anomalies A19, A20) (*Patriat and Achache, 1984*). The collision initiated a major plate reorganisation and the spreading rates decreased dramatically along the Central Indian Ridge and the Southeast Indian Ridge. The spreading direction on the Southeast Indian Ridge changed from near north-south to northeast direction.

During this phase the seafloor spreading ceased in Wharton Basin. Major changes in the direction and rate of spreading occurred in the Central Indian Basin and Crozet Basin, the Madagascar Basin, the eastern Somali

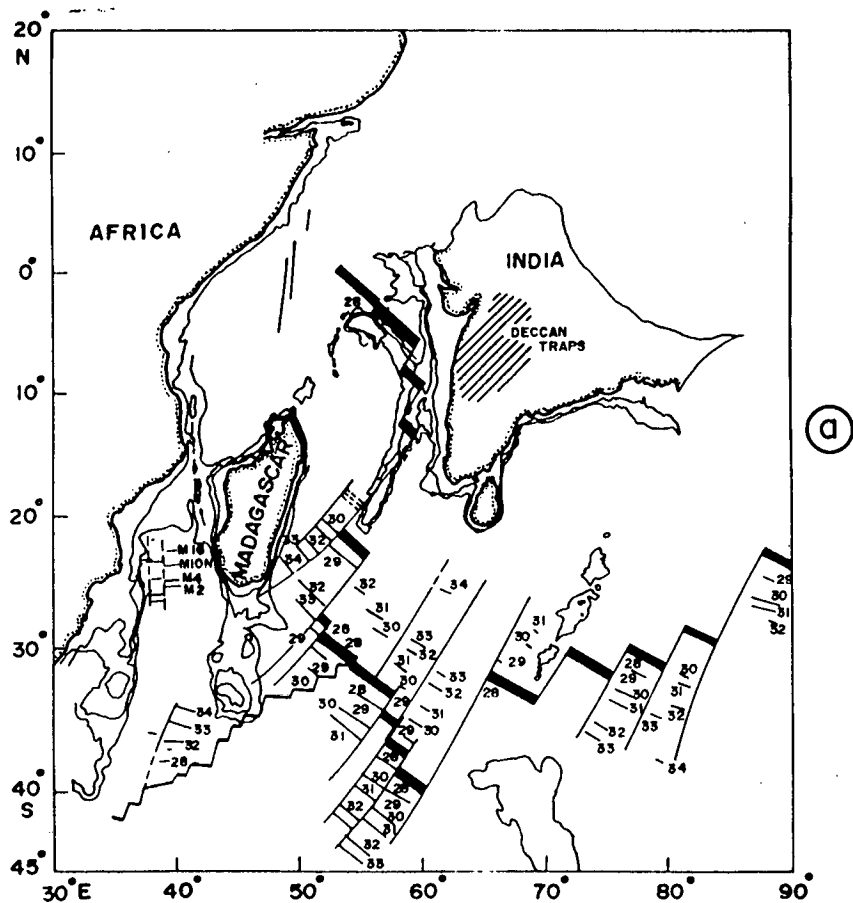
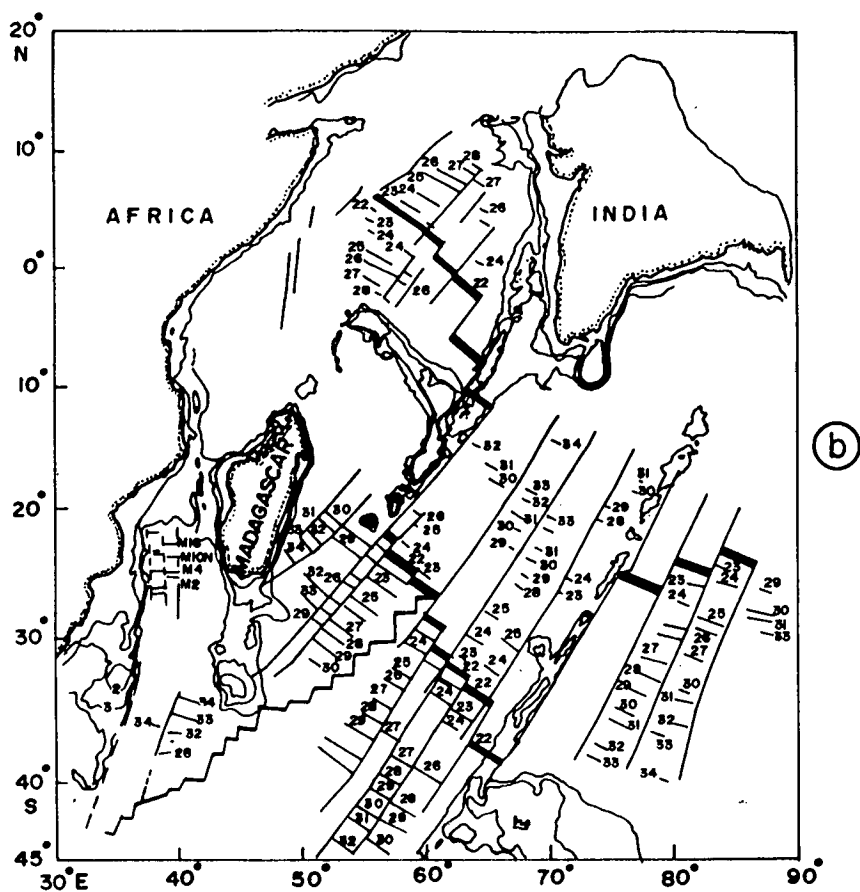


Figure 7.3 (a) Early Paleocene (65 Ma) reconstruction indicating the separation of Seychelles from India. (b) Reconstructed positions during Early Eocene (53 Ma) (after Norton and Sclater, 1979).

Basin and the Arabian Sea (*Patriat and Achache, 1984; Patriat and Segoufin, 1989*).

The Australian-Antarctic Basin, the southern Central Indian Basin and the northern Crozet Basins were created during this period (*Weissel and Hayes, 1972; Sclater et al., 1976a; Schlich, 1975*).

The Mascarene plateau and the Chagos-Laccadive Ridge were separated (*Fisher et al., 1971; McKenzie and Sclater, 1971*) and the Gulf of Aden opened (*Laughton et al., 1970*). Because of the differential motion along the Central Indian Ridge and the Southeast Indian Ridge, the South West Indian Ridge propagated rapidly towards east (*Tapscott et al., 1980; Sclater et al., 1981; Patriat, 1987a*). Figure 7.3b illustrates the reconstructions during the Early Eocene.

7.1.4 MIDDLE EOCENE TO PRESENT

During this tectonic epoch, the plate boundaries in the Indian ocean assumed the present status. The strike slip motion along the Ninetyeast Ridge has ceased, Australia drifted rapidly away from the Antarctica.

In this period the Reunion hotspot crossed beneath the Central Indian Ridge and transferred from Indian plate to the African plate (*Patriat and*

Segoufin, 1988). The transfer of the Reunion hotspot resulted in the ending of the development of Chagos-Laccadive archipelago.

Figures 7.4a and 7.4b illustrate the reconstructions during Early Oligocene (anomaly 16, 38 Ma) and the Present positions of the continents, respectively.

7.2 EVOLUTION OF THE CENTRAL INDIAN BASIN

7.2.1 TECTONIC IMPLICATIONS OF MAGNETIC LINEATIONS, SPREADING RATES AND FRACTURE ZONES

The identified magnetic anomalies A21 to A26 in the study area define near E-W magnetic lineations (Figure 4.22). Fracture zones at 73°E , $76^{\circ}30'\text{E}$ and 79°E are delineated based on the offsets of the magnetic lineations (see section 4.4).

The near E-W trend of the magnetic lineations indicates that these magnetic lineations originated from an E-W trending ridge which was spreading in N-S direction. *McKenzie and Sclater* (1971) suggested that the Central Indian Basin was formed further south and since has drifted to the present position. The paleo-position of the Southeast Indian Ridge as proposed by the reconstructions of *Fisher et al.* (1971) indicated that the ridge existed further south and was trending in E-W direction during the

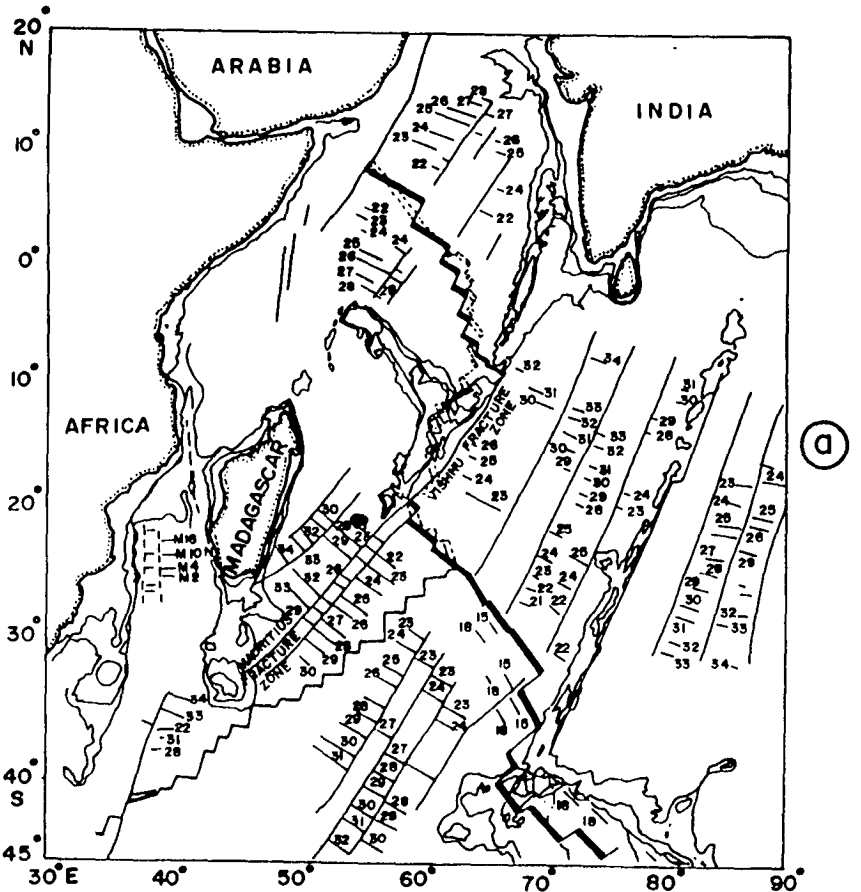
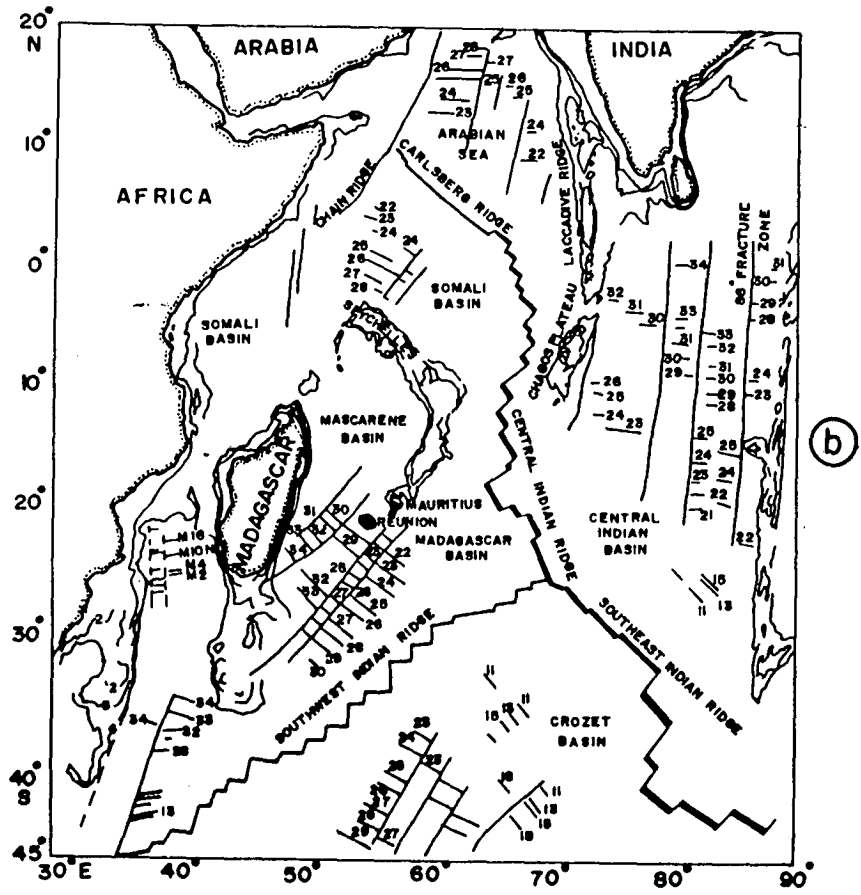


Figure 7.4 Reconstructed positions during (a) Early Oligocene (38 Ma) and (b) Present day positions (after Norton and Sclater, 1979).

geological past. Figure 7.5 illustrates the past position and orientation of the Southeast Indian Ridge at 51 Ma, 35 Ma and at Present. The near N-S orientation of the identified fracture zones and the E-W magnetic lineations observed in the Central Indian Basin suggest the dominant N-S spreading during the period A21 to A26 from the E-W trending Southeast Indian Ridge. The model studies have indicated a spreading rate of 8.0 cm/yr (half spreading rate) between anomalies A26 to A23 and 3.6 cm/yr between anomalies A23 to A21.

The Cenozoic rapid northward drift of the Indian plate followed three successive phases (Figure 7.6). In the first phase, down to anomaly A23 Indian plate drifted with a mean velocity of 15 to 20 cm/yr (full spreading rate). Then between anomalies A23 to A13 (36 Ma) the motion of the Indian plate was rather erratic, showing several changes in the spreading direction and the velocity decreased to <10 cm/yr. In the third and the latest phase, from anomaly A13 to present, the Indian plate motion resumed to a stable northward direction with respect to the Eurasian plate, with full spreading rate less than 5 cm/yr (*Patriat and Achache, 1984*). The spreading rates inferred from the model studies undertaken in the present investigations have documented the Indian plate movement during a part of the first and second phases. The inferred spreading rate of 8.0 cm/yr (half spreading rate) between anomalies A26 to A23, fits in to the first phase. The dramatic decrease in the spreading rate to 3.6 cm/yr half rate (ie., 7.2 cm/yr full rate),

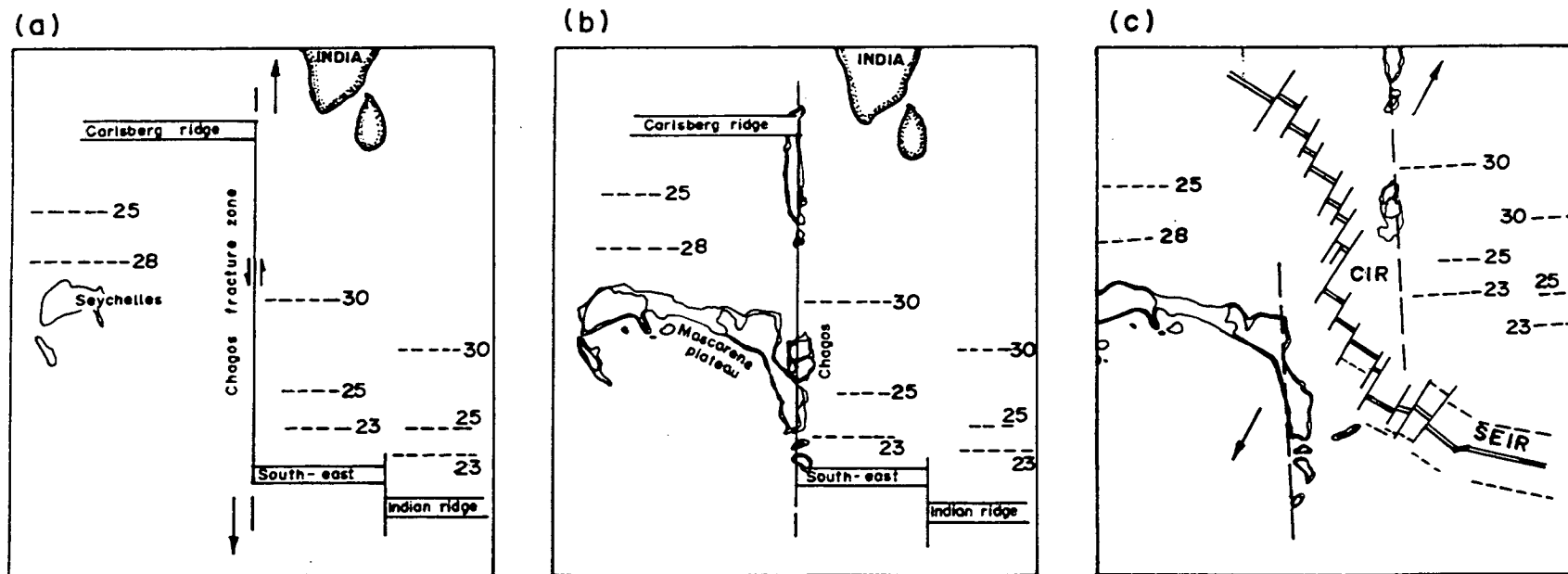


Figure 7.5 Paleoposition of the Southeast Indian Ridge during a) Eocene b) Oligocene and c) Present (Fisher et al., 1971).

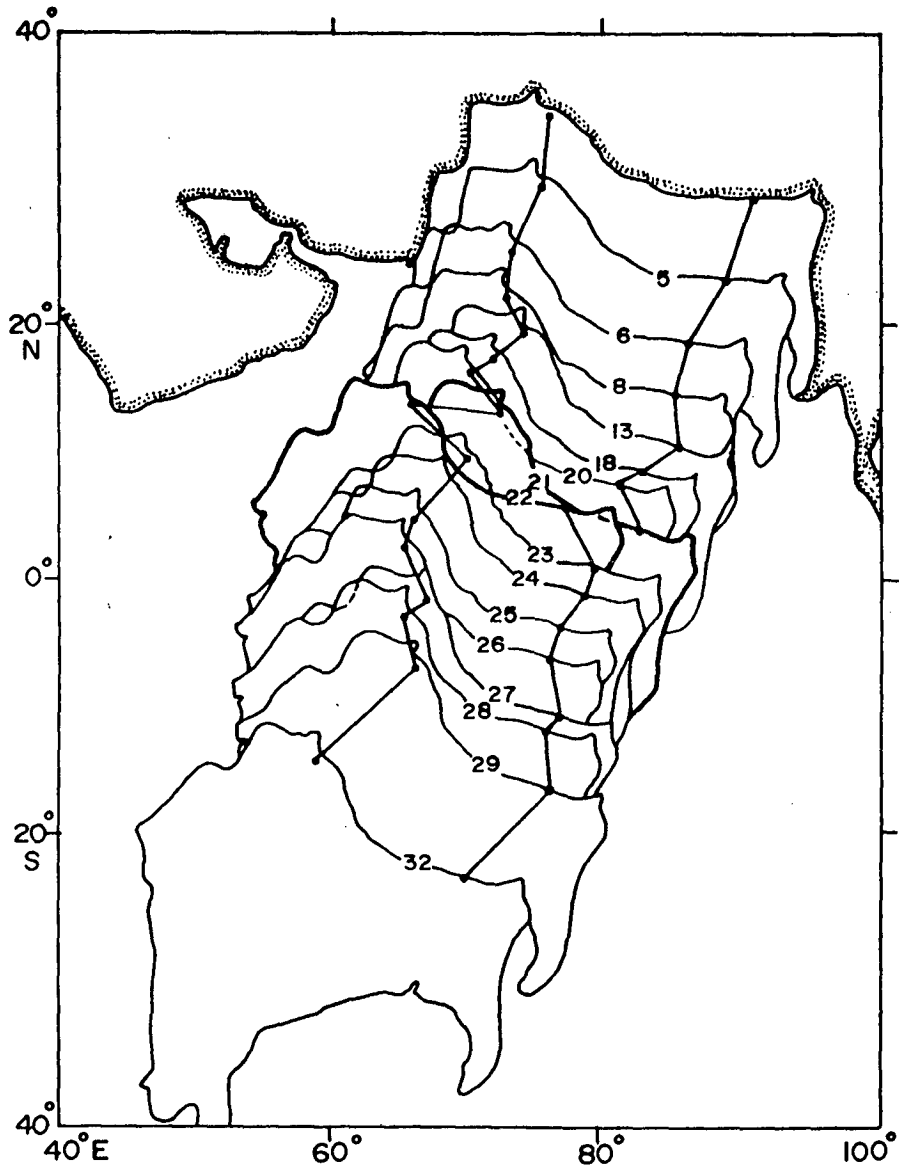


Figure 7.6 The Indian plate movement during the geological past. The magnetic anomalies corresponding to various stages are marked (*Patriat and Achache, 1984*).

corresponds to the initial stages of the second phase of the Indian plate movement.

The initial decrease in the spreading rates at anomaly A23 (53 Ma) may indicate a 'soft' collision that has occurred between the Indian plate and the Eurasian plate which was followed by the 'hard' continent-continent collision in the later period. The initial result of the ODP Leg 116 suggested this process (*Shipboard scientific party, Leg 116, 1987*). Based on the detailed studies of the ODP Leg 116 results, *Cochran (1990)* proposed that the Tethyan oceanic crust at the northern portion of the Indian plate was consumed in a subduction zone along the southern margin of Eurasia. He further suggested that the northern continental margin of India encountered the subduction zone in the Eocene. The present location of the volcanic arc associated with the subduction zone is marked by the Trans-Himalayan granitic batholith, which extends over 2500 km to the north of Indus-Tsangpo suture zone (*Tapponnier et al., 1981; Brookfield and Reynolds, 1981; Honegger et al., 1982*).

The studies carried out on the Southeast Indian Ridge by *Royer and Schlich (1988)*, between the Amsterdam and St.Paul islands indicated several fracture zones on this segment. These detailed kinematic studies have shown that the fracture zones tracked in the Crozet Basin can be traced in the north in the Central Indian Basin. The inferred fracture zones from the

studies of magnetics and bathymetry in the study region are suggested to be the traces of the transform faults on the Southeast Indian Ridge.

The fracture zone at $76^{\circ}30'E$ is reported for the first time in the Central Indian Basin based on the offsets observed in the magnetic lineations. This fracture zone was earlier predicted from the studies of reconstruction models by *Patriat and Segoufin* (1988). These predictions were based on the observed offsets in the magnetic anomalies A20-A22 in the Madagascar Basin and the reconstruction of the same isochrons on the Indian plate (*Patriat and Segoufin*, 1988). However, earlier predictions indicated that the fracture zone at $76^{\circ}30'E$ could have originated either from Southeast Indian Ridge or from Central Indian Ridge. In the present studies the observed anomalies in the region are modeled assuming that these anomalies have originated from the Southeast Indian Ridge and the fit is reasonable. Thus the model studies and the trends of the $79^{\circ}E$ and $83^{\circ}E$ fracture zones suggest that the $76^{\circ}30'E$ fracture zone also originated from the Southeast Indian Ridge.

Studies by *Sclater et al.*, (1976), have shown that the trend of the fracture zone at $86^{\circ}E$, changes from $N12^{\circ}E$ to $N45^{\circ}E$ during the anomaly times A18 to A20, as a consequence of the reorientation of the Southeast Indian Ridge from east-west to northwest-northeast during Eocene. The trends of the fracture zones at $73^{\circ}E$, $76^{\circ}30'E$ and $79^{\circ}E$ which are identified in the present study might have undergone similar changes.

Several changes in the spreading rate and direction are observed in the vicinity of the Southeast Indian Ridge (*Schlich and Patriat, 1971; Schlich, 1974*). The changes in the spreading rate and direction are noticed over the crust generated by all the three ridges (Figure 7.7) (*Patriat and Segoufin, 1988*). One common feature of these observations is that the spreading rate and direction changes are more prominent on the Central Indian Ridge and the Southeast Indian Ridge than on the Southwest Indian Ridge. The Southwest Indian Ridge along which very slow spreading rates (< 1 cm/yr) were observed was believed to have evolved as a consequence of the eastward migration of the Indian Ocean Triple Junction (*Tapscott et al., 1980; Sclater et al., 1981; Fisher and Sclater, 1983*). A detailed discussion of the influence of the triple junction on the evolution of the Central Indian Basin, is given in the following section. One more important observation from the changes of spreading rate and direction (Figure 7.7) is that these changes have occurred between A18 to A20 during the Eocene period. These major changes have been attributed to the global plate reorganisation that took place in the Indian Ocean as a consequence of the collision of the Indian plate with the Eurasian plate (*Schlich et al., 1976; Patriat and Achache, 1984; Royer and Schlich, 1988*). The plate reorganisation is believed to have taken place immediately before anomaly A20 near 45 Ma and was completed before anomaly A19 near 44 Ma (*Patriat and Achache, 1984*). Consequent to the major plate reorganisation, the spreading rates have dramatically

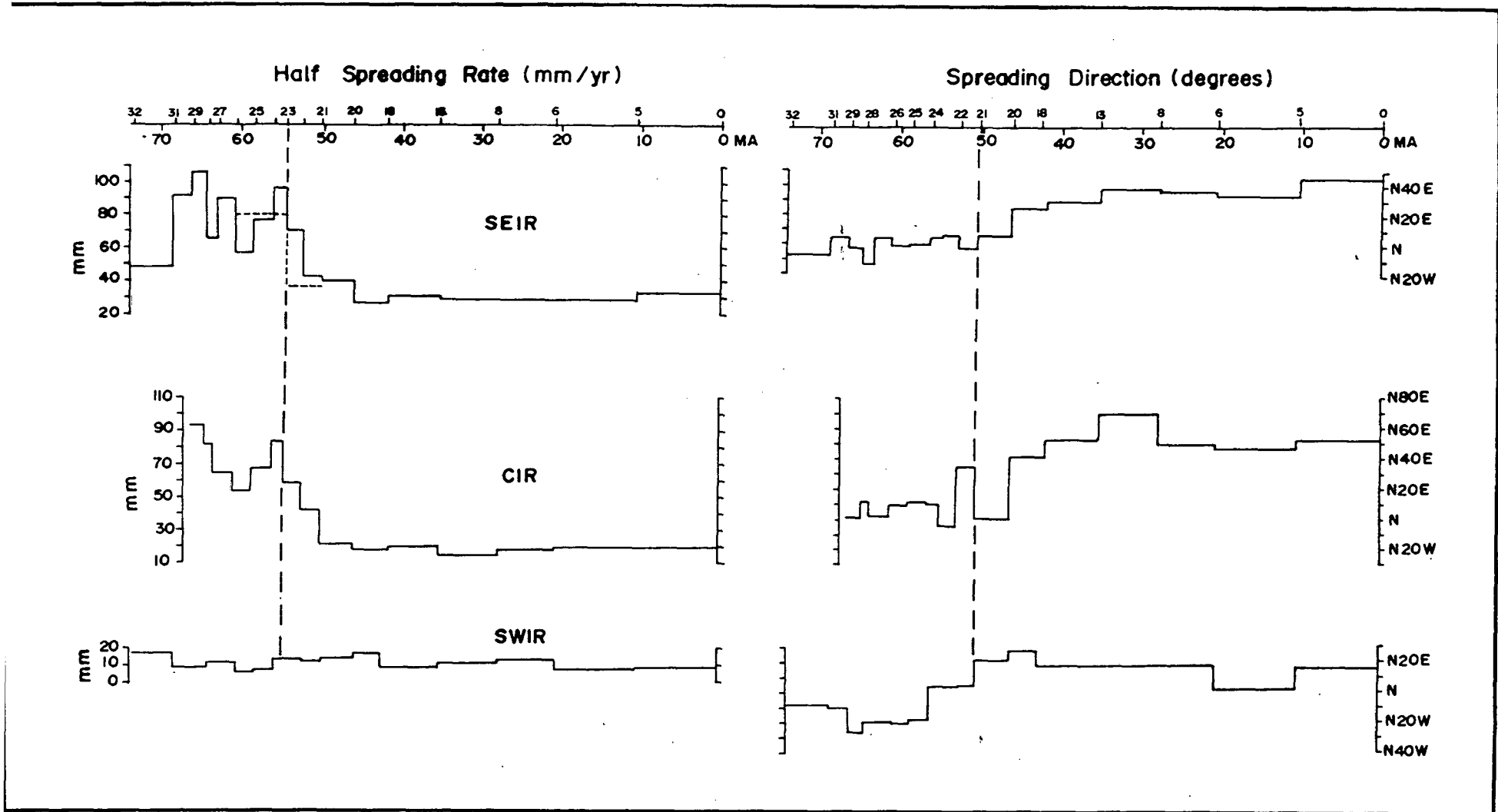


Figure 7.7 The computed spreading direction and spreading rates with respect to Central Indian, Southeast Indian and Southwest Indian Ridges (*Patriat and Segoufin, 1988*). The inferred spreading rates in the present study are shown with small dashed line. Note the sudden decrease in spreading rate around anomaly 23.

decreased. The model studies in the present investigations have indicated these variable spreading rates in the Central Indian Basin.

The above discussion highlights the erratic spreading direction changes of the Indian plate movement subsequent to anomaly A20, the suggestion of a 'soft' collision as indicated by the ODP Leg 116 results and the sudden decrease in the spreading rate as observed in the present study, at anomaly A23. These observations suggest that even though the major global plate reorganization took place during the A20 and A19 anomaly times (Middle and Late Eocene period), the effects of 'soft' collision were felt during anomaly time A23 (Early Eocene period) as documented by the decrease in spreading rate.

7.2.2 INFLUENCE OF INDIAN OCEAN TRIPLE JUNCTION

Contemporaneous to the evolution of the oceanic crust in the study area, another major tectonic process that has been active in the region is the evolution of the Indian ocean triple junction. Shortly before 80 Ma, the ridge axis that had existed north of Madagascar jumped south (Figure 7.2), changed direction and commenced to separate Madagascar from India (Tapscott *et al.*, 1980; Fisher and Sclater, 1983). An RRR (Ridge-Ridge-Ridge) triple junction was created at the southern extremity of the Madagascar Ridge, joining the newly formed Central Indian Ridge spreading center to the already active Southwest and Southeast Indian Ridges (Figure

7.2) that had been separating Africa and Antarctica and India and Antarctica respectively (*Fisher and Sclater, 1983*). At this stage the Southwest Indian Ridge which was spreading at a very slow rate (<1.0 cm/yr, *Bergh, 1971*), was coupled with faster spreading Central Indian and Southeast Indian Ridges. The Southwest Indian Ridge had been spreading consistently slower than the other two ridges forming the triple junction. The varied spreading rates lead to the eastward migration of the triple junction while the Central Indian Ridge and Southwest Indian Ridges migrated away from Africa and Antarctica. Between 80 and 64 Ma India and Madagascar continued to separate as did India and Antarctica and the triple junction moved both east and south. By 53 Ma (anomaly 22), the triple junction moved further east and to the north (*Fisher and Sclater, 1983*). At about 44 Ma (anomaly 19), as noted in the previous section, major spreading rate and direction changes have occurred on Central Indian Ridge and Southeast Indian Ridge. No contemporaneous major change was noticed on the Southwest Indian Ridge. Between 44 Ma to present rapid eastward migration of the triple junction was reported by *Tapscott et al. (1980)* and *Sclater et al. (1981)*.

During the anomaly times A26 to A21 i.e., from about 60 to 50 Ma, which corresponds to the period documented in the present study, the eastward migration of the triple junction had been taking place. The trace of the triple junction separates the crust generated at different ridges and these traces can be mapped on the Indian, African and Antarctic plates. From the

study of kinematics of the three ridges the triple junction traces were predicted on the Indian, African and Antarctic plates (*Sclater et al.*, 1981).

The triple junction trace as delineated by *Sclater et al.* (1981) extends into the present study area (Figure 7.8). The triple junction trace is typically marked by the change in the bathymetric character demarcating the crust generated by the different spreading centers. The recent SEABEAM surveys in the vicinity of the triple junction (*Patriat and Larson*, 1989; *Munsch and Schlich*, 1989) have mapped the triple junction trace. The reconstructions of the triple junction (*Sclater et al.*, 1981; *Tapscott et al.*, 1980; *Fisher and Sclater*, 1983), suggest rapid eastward migration of the triple junction. In order to maintain the RRR configuration the triple junction undergoes jumps and induces offsets along the ridges forming the junction (*Munsch and Schlich*, 1989).

The offset near anomaly A24 is very much less when compared to the observed offsets across anomalies A21 and A22 (Figure 7.8) across the 76°30'E fracture zone. The observed decrease in the offsets of the magnetic lineations across the 76°30'E fracture zone, when examined in the light of the triple junction trace on the Indian plate, indicates that the study area was affected by the evolution of the Indian ocean triple junction. Thus, it is implied that the seafloor in the study area which was generated by the fast spreading Southeast Indian Ridge, was influenced by the slower Central Indian Ridge

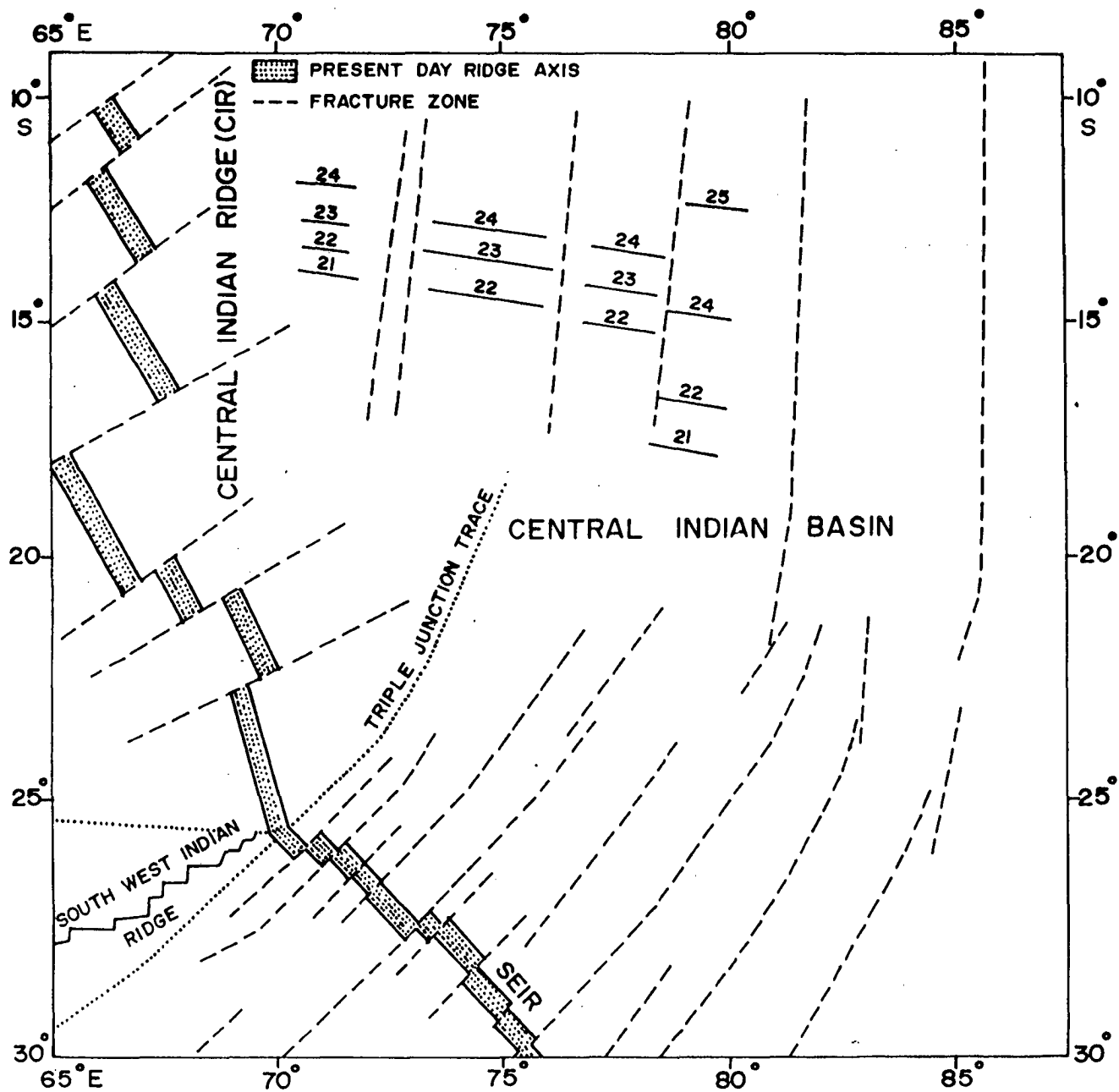


Figure 7.8 The identified magnetic lineations and fracture zones during the present study. The triple junction trace as delineated by *Slater et al. (1982)* and the fracture zone trends on Southeast Indian Ridge (*Royer and Schlich, 1988*) are shown.

and was subjected to modifications as a consequence of the evolution of the triple junction.

7.3 IMPLICATIONS OF SEAMOUNT DISTRIBUTION

A total number of 80 seamounts are identified in the region based on echosounding data and multibeam sonar data. The heights of the seamounts range from 500m to 1850m. Locations of these seamounts are shown in Figure 5.9. The morphological features of some of these seamounts are studied in detail by *Kodagali (1989)* and *Mukhopadhyay and Khadge (1990)*. These seamounts are situated on a lithosphere, with crustal ages varying from 50 to 60 Ma. As can be seen from the Figures 5.9 and 7.9, within the study area seamounts follow the fracture zone-trends. The 79°E fracture zone has distinct bathymetric expression as revealed by the *Hydrosweep* data (Figures 5.1 and 5.2), where as the 76°30'E fracture has very little bathymetric expression and is only manifested by a small offset in the magnetic lineations. It was observed that in areas where detailed magnetic surveys have been made, the seamounts are located either on or very close to the fracture zones, even though the fractures have little bathymetric expression (*Vogt, 1974; McNutt and Batiza, 1980*). Based on seamount distribution in the Pacific Ocean, *Batiza (1982)*, observed that the non-hotspot volcanoes have preferentially occurred either on or very near to the fracture zones and suggested that fracture zones may provide easy conduits for the seamounts. Although fracture zones are not necessary for the

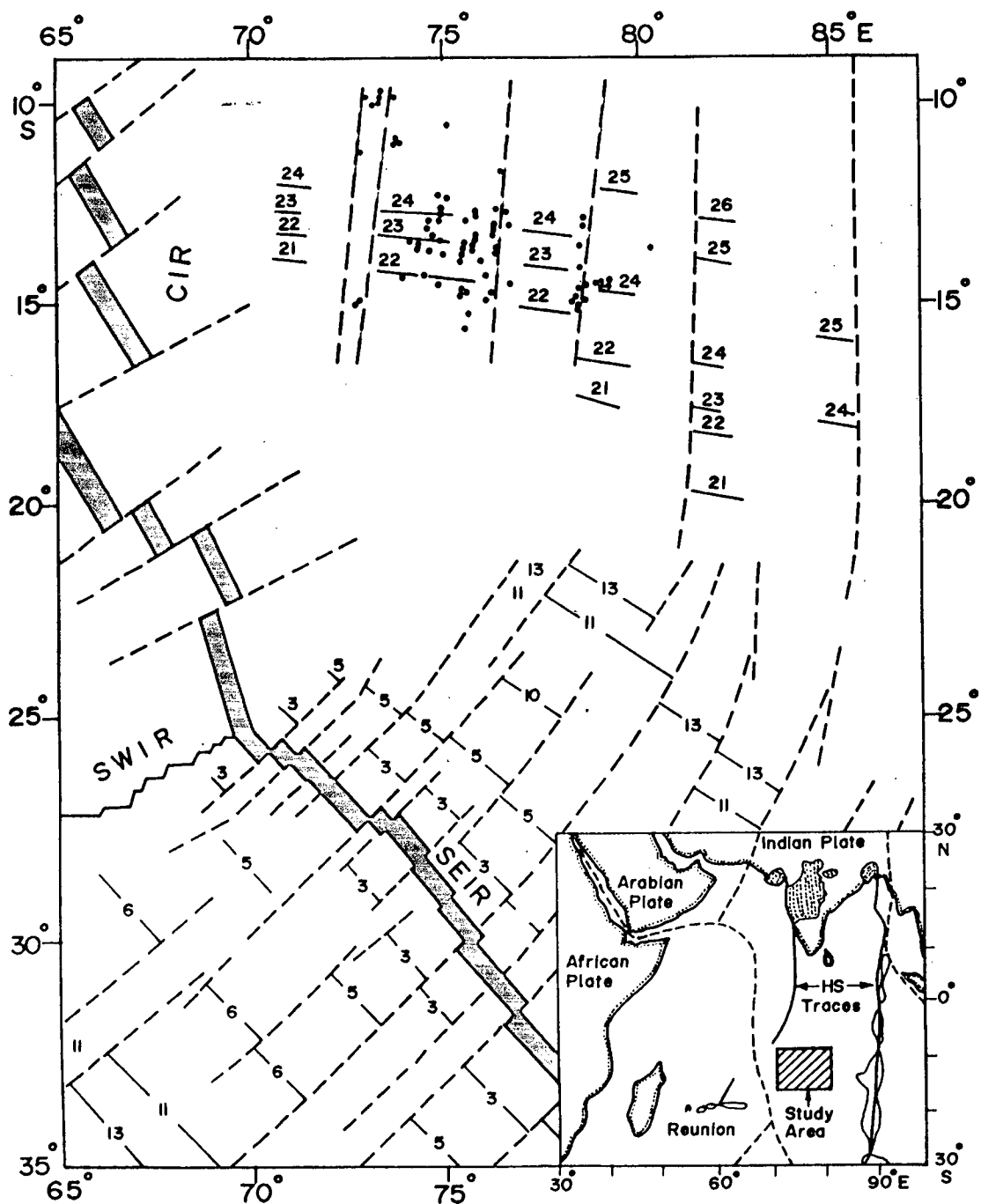


Figure 7.9 Summary tectonic map showing the results from the present study with magnetic lineations, fracture zones and seamount locations along with results from other studies. The magnetic lineations along SEIR are from *Royer and Schlich* (1988). The inset shows the traces of the Reunion and Kerguelen hot spot traces in the Indian Ocean (after *Duncan and Richards*, 1991).

formation of seamounts, there may be local perturbations to the plumbing system or other zones of weakness that control the location of seamounts (*Epp and Smoot, 1989*).

Seamount distribution in the Central Indian Basin can be viewed with respect to the known hotspot traces in the Indian Ocean (inset, Figure 7.9). The reconstructions of the Indian plate considering the relative plate motions (*Molnar et al., 1987; Royer and Sandwell, 1989*) assuming fixed hotspot reference frame, resulted in the Indian plate motion which can be compared to the Reunion and Kerguelen hotspot traces (*Duncan and Richards, 1991*). Recent studies of the legs 115 and 121 of the Ocean Drilling Program have shown evidences to suggest that the Chagos-Laccadive ridge system and Ninetyeast Ridge are the traces of the Reunion and Kerguelen hotspots, respectively (*Duncan and Richards, 1991*).

At present it is not clear whether the seamounts identified in the study area are related to the hotspot activity or they are of non-hotspot type. The magnetic signature along the line *CB-14* is disturbed and the anomalies are uncorrelatable. This may be due to the presence of the 73°E fracture zone. Furthermore, the region along the 73°E fracture zone, which was further south and west during the geological past, could have come under the influence of the Reunion hotspot. The disturbed and uncorrelatable magnetic signature along the 73°E fracture zone over a wide zone, the reconstructions of the Indian plate, and the proximity of the Reunion hotspot trace suggests

that the seamounts in the vicinity of 73°E fracture zone probably originated from the Reunion hotspot. Whereas, the seamount clusters along 76°30'E and 79°E fracture zones, which occur preferentially along the fracture zones appear to be controlled by the fracture zones.

It was suggested that the hotspot generated seamount chains will tend to form a mosaic of smaller chains along the fracture zones (*Vogt, 1974*) and the oceanic volcanoes belonging either to the hotspot or non-hotspot type may share a common genetic source (*Batiza, 1982*).

On the basis of the high resolution seismic tomographic models *Anderson et al. (1992)*, have indicated that the hotspots may not be a narrow pipe like features but have wider sublithospheric dimensions as represented by broad low velocity anomalies (LVA's) within the upper mantle and suggested that the mantle upwelling is controlled by appropriate lithospheric stress conditions.

The fracture zones in the study area could have provided suitable lithospheric conditions for the formation of seamounts. Based on these observations it is suggested that the seamount chains observed along the fracture zones at 73°E, 76°30'E and 79°E represent smaller chains of major hotspots.

7.4 MORPHOTECTONICS OF THE 79°E FRACTURE ZONE

The detailed high resolution swath bathymetric data has revealed various morphotectonic elements in the vicinity of the 79 °E fracture zone as detailed in Chapter 5.0. Integration of these results with other geophysical data and corroboration of the tectonic processes observed at various fracture zones enabled to decipher the detailed morphotectonics of the 79 °E fracture zone.

Studies of microseismicity at the intersections of transform faults, spreading ridges and fracture zones demonstrate that while numerous microearthquakes occur along the transform faults and spreading ridges, the fracture zones are seismically inactive (*Francis et al.*, 1978; *Forsyth and Rowlett*, 1979; *Rowlett*, 1981). It was also suggested that fracture zones are not the zones of weakness and the fractured crust is only a remnant surface expression of past tectonic activity along the transform faults. Furthermore, it was also shown that there is no significant slip along the fracture zones and that the lithosphere bends in the vicinity of the fracture zone, in order to contain the topographic expression (*Sandwell and Schubert*, 1982). The thermal contrast across the lithospheric sections at the fracture zone setup a small-scale convection cell in the underlying asthenosphere. The upwelling limb of the convection cell uplifts the hot younger side, while the downwelling limb depresses the colder older side resulting in a ridge trough topography along the fracture zone (*Craig and MacKenzie*, 1986).

The curvature of the bathymetric contours, seen on the maps (Figures 5.2 and 5.4), reflect the surface expression of the ridge-transform intersection (RTI) topographic signature. The clay cake deformation experiments of Macdonald et al., (1986) illustrated the development of riedel shears at the transforms. These riedel shears accommodate significant dip-slip component and evolve into normal faults that curve at the RTI resulting in sharply curved bathymetric scarps.

Multibeam bathymetric studies using *Seabeam* near a slow slipping transform fault (Vema fracture zone), (Macdonald et al., 1986) and fast slipping transform boundary (Clipperton transform fault), (Gallo et al., 1986) have shown the existence of a transform tectonized zone of varying dimensions along the length of the active transform fault. The transform tectonized zone (TTZ) as delineated at various transform faults represents a zone that had experienced strains associated with strike slip tectonism during the passage along the plate boundary. The TTZ contains braided network of small-scale faults and intrusive contacts of different ages. The width and geometry of the TTZ will vary as a function of regional changes that arise due to the pole of relative motion behavior and the local changes that include adjustments in slip geometry due to the structural incompatibilities in the transform fault environment (Fox and Gallo, 1989). A zone of smooth topography along the 79°E fracture zone has been delineated from the swath bathymetry is shown on the tectonic summary map (Figure 7.10). The varying width of the zone of smooth topographic expression, perhaps

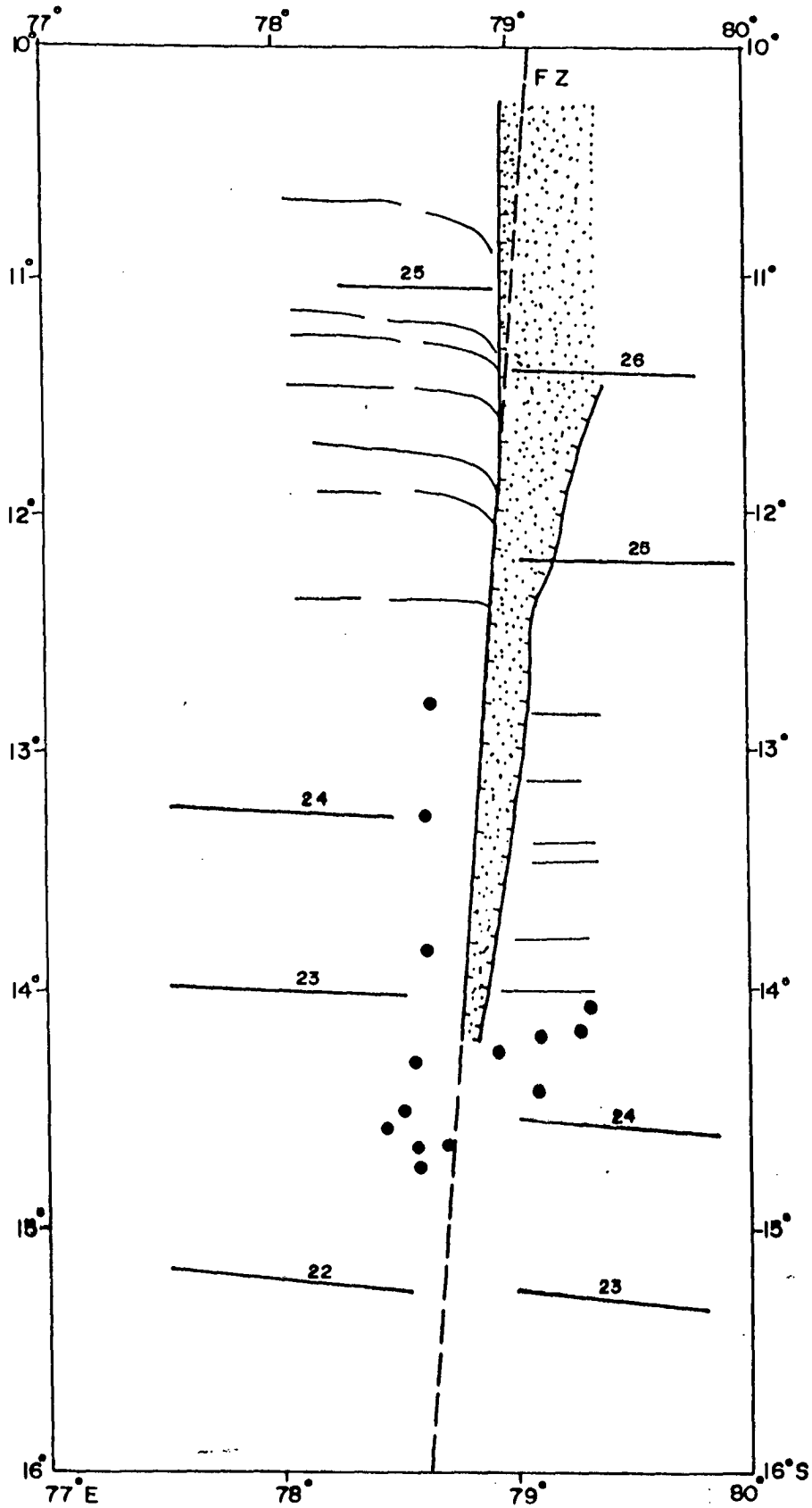


Figure 7.10 Summary tectonic map of the area encompassing the 79°E fracture zone. Bathymetric lineations as delineated from the multibeam bathymetric study, the identified magnetic anomalies (numbered solid lines), the fossil transform tectonized zone (stippled area) and the location of seamounts (solid dots) are shown.

resulted from the fracturing in the transform fault environment and subsequent sedimentation, represent a fossil transform tectonized zone.

The prominence of the bending of E-W bathymetric lineations in the northern portion of the 79°E fracture zone area in comparison to the southern portion (Figures 5.1, 5.2 and 7.10), indicates principal difference in the formation of these features. The features observed at the 79 °E fracture zone are compared with fast slipping transform faults like Clipperton (slip rate 110 km Ma⁻¹) (*Gallo et al.*, 1986) and Siqueiros (slip rate 126 km Ma⁻¹) (*Fornari et al.*, 1989) and the slow slipping Vema transform fault (slip rate 24km Ma⁻¹) (*Macdonald et al.*, 1986). In order to do this, a situation is visualized in which the present fracture zone was a part of active transform fault system. *Macdonald et al.*, (1986) proposed that the transform fault evolves from having young newly accreted lithosphere on one side which is thin and easily deformed to having old, thick lithosphere on both sides which does not deform easily and acts as a strain guide to confine the transform to a narrow zone. The detailed multibeam studies of fast slipping transform faults in the Pacific (*Fox and Gallo*, 1989) and slow slipping transforms in the north Atlantic (*Fox and Gallo*, 1986) have described the processes occurring at a wide range of slow (< 30 km Ma⁻¹), intermediate (60 km Ma⁻¹) and fast slipping (> 60 km Ma⁻¹) transforms. The slow slipping and large offset (> 10 Ma) transforms exhibit relatively simple geometry and the accretionary processes are constrained by thick lithosphere edges, proximal to these ridge transform intersections (RTI's) (*OTTER, scientific team*, 1985;

Langmuir and Bander, 1984; Macdonald et al., 1986; Fox and Gallo, 1986; Pockalny et al., 1988). The tectonic characters of the small offset (< 2 Ma) and fast slipping (>60 km Ma⁻¹) transforms are governed by thin, hot and weak edges of the lithosphere at the RTI. At these transforms the shear zone geometries exhibit complex patterns and the accretionary processes are not significantly perturbed by the thin edge of the lithosphere (*Searle, 1983, 1986; Gallo et al., 1986; Madsen et al., 1986; Kastens et al., 1986; Langmuir et al., 1986; Gallo et al., 1989*).

Based on the identified magnetic anomalies and the spreading rates inferred in the present study, the fracture zone segment between A23-A26 evolved during a fast slipping transform fault environment with a slip rate of 160 km Ma⁻¹, where as the segment between A22-A23 fits into a medium rate transform fault with a slip rate of 72 km Ma⁻¹. In this scenario the oblique extensional features which are prominent in the segment with fast slipping rate transform fault environment can be considered as due to the strong coupling at the RTI. The thin and hot lithospheric edges at the fast slipping transform which are easily deformed, facilitate strong coupling. Where as the subtle presence of the oblique extensions in the south which is the result of a medium rate slipping transform fault can be attributed to the weak coupling at the RTI. In this case the relatively cold and thick lithospheric edges are encountered at the RTI resulting in weak coupling. In the case of strong coupling at the RTI, the curvature of the riedel shear faults is more prominent and result in curved bathymetric scarps that are oblique to the transform,

where as spreading center parallel features develop when the coupling is weak. It was also suggested that the temporal variations of shear coupling at RTI may vary with the waxing and waning of axial magma chamber (Macdonald *et al.*, 1986). In case of Clipperton transform fault the oblique extensional features were delineated at the fracture zone adjacent to the transform fault zone (TFZ) on a seafloor of 0.5 Ma (Gallo *et al.*, 1986). Similar features existing on older lithosphere (53 Ma) in the present study area indicate the clear preservation of these morphotectonic features.

Because of the thin sediment cover, it has been possible to clearly document various morphotectonic features over the fracture zone. In general, sediment thickness of about 100 m was reported in the Central Indian Basin (Geological map of the Indian Ocean, Heezen *et al.*, 1978). Sediment thickness varying from 0.5 to 0.8 km with a decreasing trend towards south has been inferred based on the multichannel seismic data, north of the study area around 5°S (Bull, 1990). However, pulses of ancient sediment injection from the Bengal Fan have been found as far south as 7°S (Emmel and Curray, 1984) and geochemical evidence suggest the terrigenous input down to 10°S (Nath *et al.*, 1989; Martin-Barajas *et al.*, 1991). These studies suggest that in the study area, the northern portion can be expected to have more sediment thickness. The subdued topographic expression of the fracture zone in the north is therefore probably due to the sediment infill.

7.5 FACTORS INFLUENCING THE EVOLUTION OF MORPHOTECTONIC FEATURES AT A FRACTURE ZONE

Fracture zones in the ocean basins represent a unique asymmetrical contact between two sections of the same lithospheric plate. The wide range of spreading rates and age contrasts under which the fracture zones evolve result in markedly different lithospheric sections with substantially different thermomechanical structures.

Studies of seismicity at transform faults, mid-ocean ridges and fracture zones indicate that fracture zones are seismically inactive. It is therefore considered that the fracture zones are the inactive traces of the transform faults. The various morphotectonic features that were formed in the transform fault domain remain along the fracture zones. It is expected that the nature of these morphotectonic expressions undergo minor modifications due to the processes of subsidence and contraction with age. It is therefore possible to relate the evolution of various morphotectonic features observed at fracture zones, as a consequence of the tectonic processes that took place during the ridge-transform-ridge (RTR) environment. An RTR plate boundary represents a complex and dynamic interface. Along the RTR, strike slip strains are accommodated and the accretionary processes such as, asthenosphere upwelling, melt generation and melt emplacement are truncated. The interplay of these tectonic processes determines the overall morphology of the RTR boundary. These parameters affect the lithosphere on either side of

the transform fault. Expression of these processes can be found along the fracture zones and can be mapped with high resolution swath bathymetric tools.

As discussed in the earlier sections the morphotectonic characters at a fracture zone are primarily dependent on the plate tectonic setting under which it evolves. The plate tectonic setting can be inferred from the regional geophysical data such as magnetics and conventional bathymetry. The offset distance between the magnetic lineations, the age of the ocean floor and the spreading rates can be measured.

The age contrast across the fracture zone leads to the formation of intraplate lithospheric sections with different thermal structure and thickness. The differences in the age and thermal structure subject the lithospheric sections to differential subsidence on either side of the fracture zone. The contrast in rate of subsidence of the lithospheric sections coupled with the thermomechanical interactions, result in flexure of the lithosphere at the fracture zone.

The thermal contrast between the lithospheric sections across the fracture zone would also induce small scale convection cells within the asthenosphere with the hot upwelling limb on the younger side and the downwelling limb on cold, older side. Formation of these small scale

convection cell uplifts the younger side and depresses the older side and contributes to the persistence of ridge trough pair along the fracture zone.

Spreading rate and the rate of magma supply at various stages of evolution of the fracture zone control the coupling at the RTI. The coupling at the ridge transform intersection between the cold older lithospheric section and the newly accreted younger side depends on the mantle weld. During the faster spreading regimes the accretionary processes are in general faster and provide strong coupling at RTI. For the segment evolved in a slow spreading episode the coupling is weak. These factors lead to the presence or absence of bending of the bathymetric lineations at the fracture zone.

A model for the evolution of morphotectonic features at a fracture zone is proposed and the factors influencing the evolution are summarized in Figures 7.11a and 7.11b.

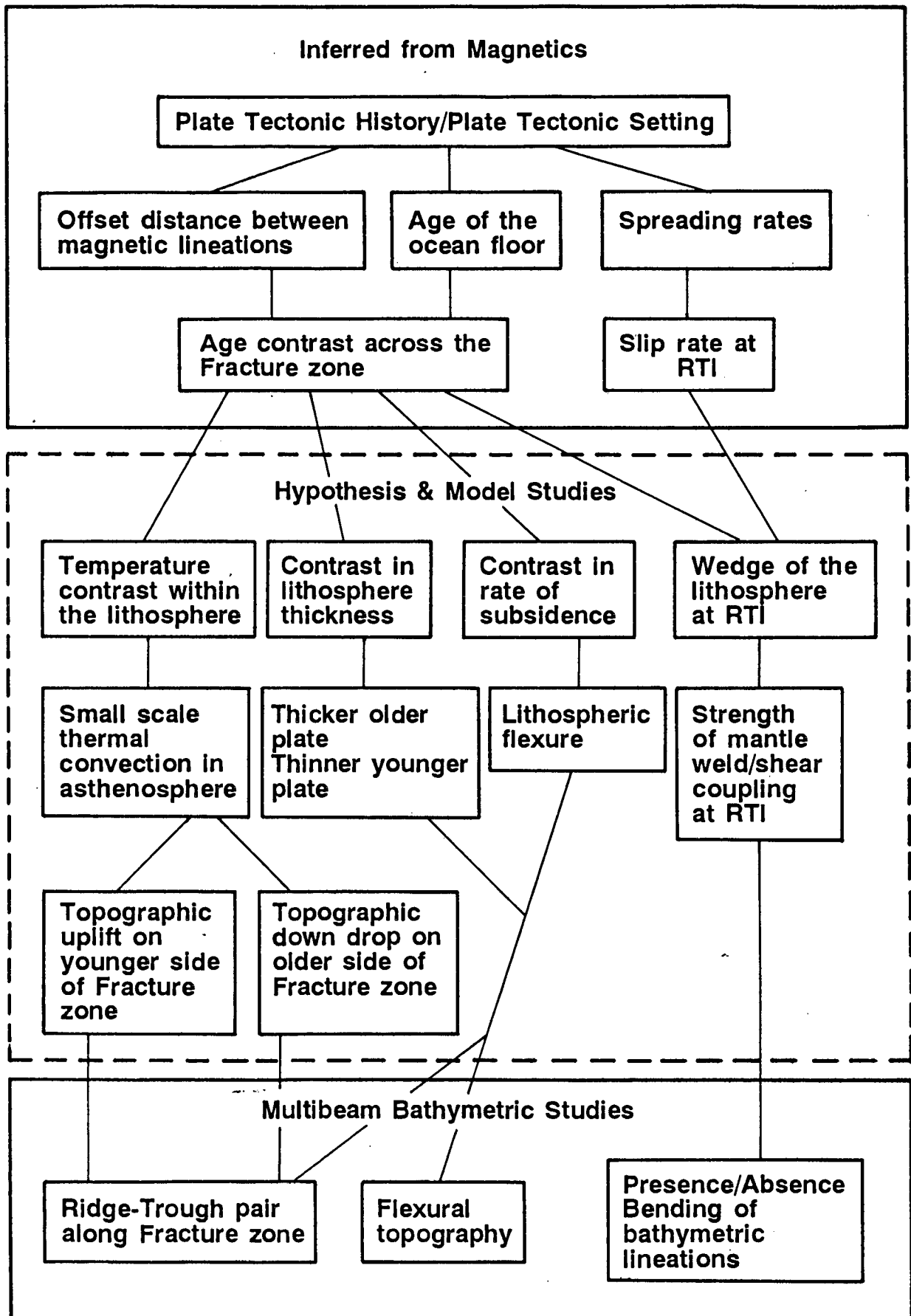


Figure 7.11 (a) The proposed model: summary of factors influencing the morphotectonics at a fracture zone.

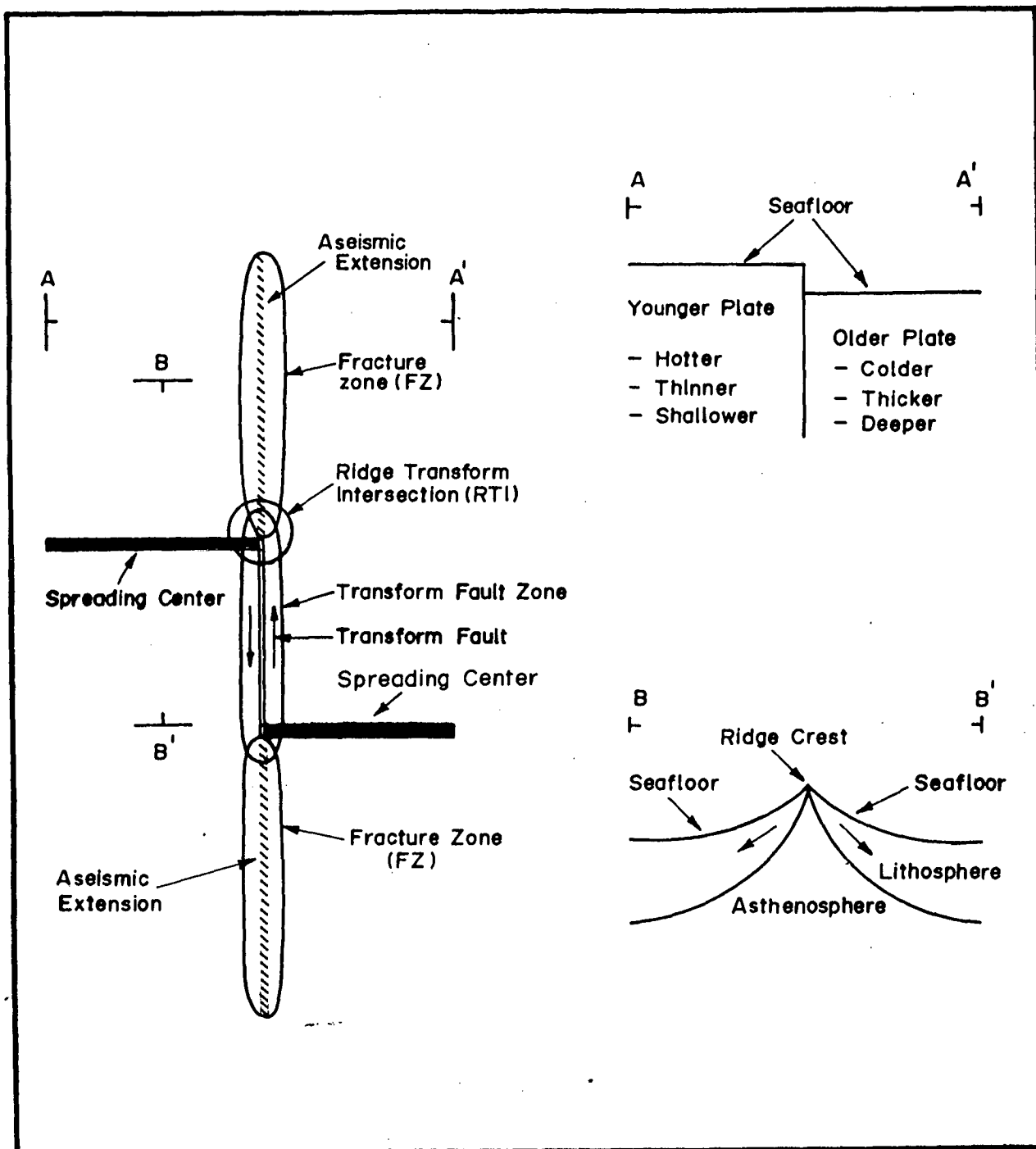


Figure 7.11 (b) Schematic illustration of the evolution of the fracture zone.

CHAPTER VIII

SUMMARY AND CONCLUSIONS

CHAPTER VIII
SUMMARY AND CONCLUSIONS

8.1 SUMMARY

The present investigations were carried out between latitudes 10 °S and 16°S and 71°E and 80°E longitudes as a part of the *National Institute of Oceanography* (NIO)'s major program to explore and delineate polymetallic nodule rich areas in the middle part of the Central Indian Basin. The region is extensively studied with closely spaced survey tracks using magnetics and bathymetric data. A part of the area encompassing the 79 °E fracture zone, between latitudes 10°15'S to 14°45'S and 78°E to 79°20'E longitudes is selected for detailed investigations using multibeam bathymetric, gravity and magnetic data.

The broad objectives of the present study are 1) to decipher the evolution of the southern part of the Central Indian Basin, in terms of the geodynamic processes at work in the region and 2) to delineate morphotectonic features associated with 79°E fracture zone by employing multibeam swath bathymetric techniques and to study their tectonic implications.

i Data

The data set comprise of 1) about 8494 lkms of magnetic and bathymetric data collected along 15 N-S profiles and 2) 4100 lkms of gravity and 73000 km² multibeam sonar data collected in the vicinity of 79 °E fracture zone.

The multibeam sonar data collected using the *Hydrosweep* system was processed using onboard *Hydromap* system and the other underway data were processed using computers onboard *ORV Sagarkanya* and the *ND 570* system at NIO. The navigation data were corrected for the uncertainties in the position information. Magnetic anomalies were computed by applying *IGRF* correction to the field data at each observation point, Matthew's correction was applied to the bathymetric data and the Eotvos and Free-air corrections were applied to the gravity data to compute free-air anomalies.

ii Magnetic and Bathymetric Studies

Seafloor spreading model studies have been carried out using *Berggren et al.* (1985) time scale, assuming a 500m thick blocks with a susceptibility of 0.01 cgs units. Magnetic anomalies A21 to A26 were identified along the 15 profiles based on the synthetic anomalies generated using the above model. Variable spreading rates of 3.6 cm/yr between A21 to A23 and 8.0 cm/yr

between A23 to A26 were inferred. The model studies have indicated that the anomalies were generated by an E-W trending Southeast Indian Ridge. A stacked magnetic anomaly map was prepared. This map has displayed a remarkable correlation of the magnetic anomalies. The identified magnetic anomalies define magnetic lineations which trend at about 96°E .

The spreading rates determined from the model studies have documented the movement of the Indian plate. The sudden decrease in spreading rate from 8.0 cm/yr between A26-A23 to 3.6 cm/yr between A23-A21, indicate the onset of collision between the Indian plate and the Eurasian plate. It was suggested that major plate reorganization in the Indian ocean took place during the anomaly times A19-A21 as a consequence of the collision between Indian plate and Eurasian plate resulting in the reorientation of the Southeast Indian Ridge from E-W to NW-SE direction and the upliftment of Himalayas. The sudden decrease in the spreading rate at anomaly A23 supports the contention of a 'soft' collision between the northern continental margin of India and the Eurasia prior to the process of 'hard' continent to continent collision at a later time (A19-A21). The recent results of the ODP leg 116 results also indicate similar process.

Based on the offsets in the magnetic lineations, fracture zones at 79°E , $76^{\circ}30'\text{E}$ and 73°E have been identified. These fracture zones are near parallel to the 83°E and 86°E fracture zones and trend at about $\text{N}5^{\circ}\text{E}$ and offset the magnetic lineations right laterally.

The 79°E fracture zone demarcated in the present study represents the southern extension of the Indrani fracture zone. The offset between the identified magnetic lineations across this fracture zone is about 135 km.

The 76°30'E fracture zone is represented by a small offset of about 50 km. This feature is identified for the first time in this region. The offset of the magnetic lineations across this fracture zone decrease towards north. The differential offsets in the magnetic lineations observed across this fracture zone are explained in terms of the evolution of the Indian Ocean triple junction. The study has further suggested that the southern part of the Central Indian Basin is influenced by the evolution of the Indian Ocean triple junction.

The offsets in the magnetic lineations near 73°E longitude, the disturbed magnetic signature along the profile *CB-14*, together with the very rugged topography observed in the region indicate the presence of 73°E fracture zone. This fracture zone is characterized by a pair of fractures encompassing broader area. Magnetic anomalies A21 to A24 identified west of the fracture zone along 71°E longitude (along profile *CB-15*) suggest that the crust generated in the region is a consequence of the seafloor spreading along the Southeast Indian Ridge. This observation implies that the crust generated by the Central Indian Ridge may be located towards west of the 71°E longitude in this region.

Bathymetric profiles and contour map prepared for the region display rugged topography in the western part and smooth towards east. The central part of the area is characterized by subtle E-W lineations. The expression of the 79°E and 73°E fracture zones can be noticed on the contour map and on the profiles. The bathymetric expression of the 76°30'E fracture zone is not conspicuous, which has been attributed to the very less age contrast across the fracture zone.

The identified fracture zones in the region are suggested to have originated from the ridge jumps along Southeast Indian Ridge. The age of the ocean floor is well constrained with clearly defined magnetic anomalies. The age of the ocean floor in the study area, inferred from these studies varies between 48 to 60 Ma.

These studies indicate that the evolution of the Indian ocean triple junction and the reorientation of the Southeast Indian Ridge are the major tectonic processes that controlled the evolution of the study area.

iii Multibeam Bathymetric Studies

After having established the detailed tectonic framework of the region based on the magnetic and bathymetric data, detailed multibeam bathymetric and gravity studies encompassing the 79°E fracture zone were carried out.

About 73000 km² area insonified by the swath bathymetric data and about 4100 lkms of gravity data were analysed.

High resolution multibeam bathymetric data revealed several morphotectonic features associated with 79°E fracture zone. A fossil transform tectonized zone of varying width from 9-11 km in the south to 56 km in the north along the fracture zone is delineated. The other major morphotectonic features identified include the ridge and trough topographic expression of the fracture zone, the conspicuous E-W bathymetric lineations and their bending into the fracture zone.

The ridge and trough bathymetric expression of the 79 °E fracture zone is similar to the topographic expression of some of the Pacific fracture zones. The evolution of the ridge and trough expression found along the 79 °E fracture zone is attributed to the combined effect of lithospheric flexure and formation of small scale convection cells within the asthenosphere. It is suggested that the lithosphere in the near vicinity of the fracture zone flexes leading to the persistence of the ridge and trough topographic expression. Small scale convection cells form in response to the temperature contrast between the lithospheric sections on either side of the fracture zone. The upwelling limb on the younger, hotter side uplifts, while the downwelling limb on the colder, older side depresses the lithosphere and imparts the ridge trough topography.

Prominent closely spaced E-W bathymetric lineations were observed in the northwestern and southeastern quadrants of the area corresponding to the anomaly times A24-A26. In the region belonging to the anomaly times A21-A23, the bathymetric lineaments are not very prominent. These lineations represent the ridge parallel topographic grain. The Southeast Indian Ridge was trending in E-W direction during Eocene and it is suggested that the E-W bathymetric lineations were generated by this ridge.

The configuration of these lineaments is a function of the spreading center morphology which in turn depends on the spreading rate and the rate of magma supply. It is inferred that the fracture zone segment evolved in two episodes of spreading between A21-A23 (3.6 cm/yr, half rate) and A23-A26 (8.0 cm/yr, half rate). The slow spreading rate during A21-A23 resulted in decreased amounts of magma emplacement and impeded the formation of prominent bathymetric lineations. Whereas, during fast spreading episode, the shallow magma chamber and robust magma supply rate support faster accretion resulting in closely spaced, well defined bathymetric lineations.

The E-W bathymetric lineations bend into the fracture zone forming curved bathymetric extensional features. The magnitude of the bending is more prominent in the north and it is absent in the southern part. The prominence of these features and their subtle presence in the southern part are explained in terms of the shear coupling at the ridge-transform intersection (RTI).

The intensity of coupling at the RTI between the hot, thin younger lithosphere and the cold, thick older lithosphere depends on the mantle weld and the magma supply rate. These factors, are controlled by the slip rate in the transform fault domain which is a function of the spreading rate. The present fracture zone segment evolved in intermediate and fast slip rates during anomaly times A21-A23 and A23-A26 respectively. It is suggested that at fast slip rate, the RTI encountered thinner lithospheric edges which had facilitated stronger coupling eventually resulting in the formation of bending of the bathymetric lineations in the fracture zone segment. At slow slip rates the coupling is weak as in this case relatively thicker lithospheric edges are encountered, consequently the bending features did not develop.

The smooth bathymetry and the diminished relief observed in the northeastern corner of the region indicates sediment infill in the fracture zone trough. The sediment infill in the region probably resulted from the influx of Bengal fan sediments.

iv Distribution of Seamounts

A total number of 80 seamounts ranging in heights from 500 m to 1850 m have been identified in the study area based on conventional echosounding and the multibeam sonar data. The tectonic implications of the seamount distribution has been studied.

The seamounts cluster along the fracture zones. The seamount distribution is viewed with respect to the reconstructions of the Indian plate and the traces of the Reunion and Kerguelen hotspots. It was suggested that the fracture zones provide conduits for the formation of the seamounts. The hotspot field is much wider at the sub-lithospheric level as indicated by the seismic tomographic images and the hotspots generate chains of smaller seamounts when appropriate stress conditions of the lithosphere are encountered. The fracture zones in the study region could have provided suitable conditions for the formation of seamounts. It is therefore suggested that the seamounts in the study area represent smaller seamount chains of major hotspot.

v Thermal Structure of the Oceanic Lithosphere and Free-Air Gravity Model Studies

Thermal structure of the lithosphere has been computed from the age contrast across the fracture zone and the thermal conduction. The thermal model represented the isotherm defining the stress relaxation temperature (T_E) 450°C and the elastic thickness of the plate (H_E), is inferred to be about 23 km. The isotherm defining the base of the lithosphere is represented by $0.9T_M$ ($T_M = 1365^\circ\text{C}$), occurred at about 91 km. The density and flexural rigidity parameters were computed from the thermal model.

The observed edge effect free-air gravity anomaly across the 79°E fracture zone was modeled to estimate the thickness of the lithosphere and to obtain probable density structure. Two dimensional model studies have been carried out by assuming three layers, the sediment, the oceanic crust and the upper mantle. The upper mantle is divided into layers which vary in density and thickness. The density and thickness of the layers within the upper mantle section is constrained by the thermal structure of the lithosphere. A lithospheric thickness of about 100 km was determined from the free-air gravity model.

A generalized model has been proposed summarizing the various factors that are responsible for the evolution of morphotectonic features at a fracture zone.

8.2 CONCLUSIONS

- 1) Marine magnetic anomalies A21 to A26 are identified in the study area based on model studies.
- 2) The identified magnetic anomalies define magnetic lineations with a trend of about 96°E.
- 3) Variable spreading rates of 3.6 cm/yr between anomalies A21-A23 and 8.0 cm/yr between anomalies A23-A26 were determined.

inferred

- 4) The inferred spreading rates indicate that the region has evolved as consequence of fast and inter-mediate spreading episodes.
- 5) Based on the magnetic anomaly identifications it is suggested that the age of the ocean floor in the study area is in the range of 48 Ma to 60 Ma.
- 6) The sudden decrease in the spreading rate at anomaly A23 indicates the onset of collision between Indian plate and Eurasian plates, prior to the 'hard' continent to continent collision that took place during anomaly times A21-A19.
- 7) Based on the observed offsets in the magnetic lineations and the bottom topography, fracture zones at 79°E , $76^{\circ}30'\text{E}$ and 73°E are identified. These fracture zones offset the magnetic lineations in a right lateral sense.
- 8) The identified fracture zones are suggested to have originated from the Southeast Indian Ridge as a consequence of ridge jumps.
- 9) These fracture zones appear to have changed their trend from near N-S to NE-SW as a consequence of the reorientation of the Southeast Indian Ridge during Eocene time. The change in the trend of the fracture zones may be located further south.

- 10) Identification of the older anomalies A21 to A24 towards west of the 73°E fracture zone along 71°E longitude indicates that the crust generated by the Central Indian Ridge lies west of 71 °E longitude in the region.
- 11) Variable offsets observed in the magnetic lineations across the 76 °30'E fracture zone, suggests that the crust in the study area was influenced by the evolution of the Indian Ocean triple junction.
- 12) The evolution of the triple junction and the reorientation of Southeast Indian Ridge resulting in major spreading rate and direction changes in the Central Indian Basin are the major tectonic processes that controlled the evolution of the study area.
- 13) Detailed multibeam bathymetric studies over 79 °E fracture zone provided unmistakable bathymetric evidence of the southern extension of the fracture zone.
- 14) The 79°E fracture zone is characterized by ridge trough topography with an overall relief of about 300m. The topography of this fracture zone is similar to the Pacific fracture zones.

- 15) Bathymetric profiles generated from the grided depth data exhibited the signature of flexure at the fracture zone. The amplitude of the flexure is prominent in the south. The flexural topography is indicative of the lithospheric flexure at the fracture zone. Lithosphere at the fracture zone flexes to maintain the ridge trough topography.
- 16) Formation of small scale convection cells within the asthenosphere is also suggested to be one of the mechanism resulting in the persistence of ridge trough topography along the fracture zone.
- 17) Prominent E-W bathymetric lineations were delineated. These lineations define the ridge parallel topographic grain of the Southeast Indian Ridge.
- 18) The prominence of the E-W bathymetric lineations in the northwestern and southeastern quadrants of the region is attributed to the processes related to the spreading center morphology at a fast spreading ridge.
- 19) The presence of conspicuous bending of the bathymetric lineations into the fracture zone in the northern part and their absence in the southern part are related to the strong and weak shear coupling at the RTI during various stages of evolution of the fracture zone.
- 20) A fossil transform tectonized zone of varying width is delineated along the fracture zone. This zone has a width of about 9-11 km in the south and 56 km in the north.

- 21) The smooth bathymetry and diminished relief observed in the northeastern corner of the region is indicative of sediment infill in the fracture zone trough, probably resulted from the influx of Bengal fan sediments.
- 22) It is suggested that the fracture zones have provided conduits for the formation of seamounts in the region.
- 23) The overall distribution of seamounts in the study area, when examined in the light of the hotspot traces over the Indian Plate suggest that these seamounts represent smaller chains of major hotspot.
- 24) Thermal structure evaluated at the 79 °E fracture zone indicated that the thickness of the elastic plate as defined by the stress relaxation temperature is about 23 km.
- 25) The base of the lithosphere as defined by the $0.9T_M$ isotherm is found to be at 91 km.
- 26) The free-air gravity model studies carried out at the 79 °E fracture zone indicated a lithospheric thickness of about 100 km.
- 27) Considering the thermal structure of the lithosphere at the fracture zone and the multibeam bathymetric observations, various factors that influence the evolution of morphotectonic features are summarized.

- 28) The well defined morphotectonic features observed at the fracture zone segment on a moderately old ocean floor of about 55 Ma, indicate the preservation of these features. These observations further suggest that these features are not significantly altered after their initial formation in the transform fault environment.

REFERENCES

REFERENCES

- Adams, R.D. and Christoffel, D.A., 1962. Total magnetic field surveys between New Zealand and the Ross Sea, *J. Geophys. Res.*, 67, 805-813.
- Allmendinger, R. and Riis, F., 1979. The Galapagos rift at 86 °W, 1. Regional morphological and structural analysis, *J. Geophys. Res.*, 84, 5379-5388.
- Anderson, D.L., Tanimoto, T. and Zhang, Y.-S., 1992. Plate tectonics and hotspots: The third dimension, *Science*, 256, 1645-1651.
- Arkani-Hamed, J. and Strangway, D.W., 1986. Effective magnetic susceptibility of the oceanic upper mantle derived from MAGSAT data, *Geophys. Res. Lett.*, 13, 999-1002.
- Arkani-Hamed, J., 1991. Thermoremanent magnetization of the oceanic lithosphere inferred from a thermal evolution model: Implications for the source of marine magnetic anomalies, *Tectonophysics*, 192, 81-96.
- Batiza, R., 1982. Abundance, Distribution and size of volcanoes in the Pacific Ocean and implications for Origin of non-hotspot volcanoes, *Earth Planet. Sci. Lett.*, 60, 195-206.
- Berggren, W.A., Kent, D.V., Flynn, J.J. and Van Couvering, J.A., 1985. Cenozoic geochronology, *Geol. Soc. Am. Bull.*, 96, 1407-1418.
- Bergh, H.W., 1971. Seafloor spreading in the southwest Indian Ocean, *J. Geophys. Res.*, 76, 6276-6282.
- Bergh, H.W., 1977. Mesozoic seafloor off Dronning Maud Land, Antarctica, *Nature*, 269, 686-687.
- Bergh, H.W., 1987. Underlying fracture zone nature of Astrid Ridge off Antarctica's Queen Maud land, *J. Geophys. Res.*, 92, 475-484.
- Bergh, H.W., and Norton, I.O., 1976. Prince Edward fracture zone and the evolution of the Mozambique Basin. *J. Geophys. Res.*, 81, 5221-5239.
- Bergman, E. A. and Solomon, S. C., 1985. Earthquake source mechanisms from body-waveform inversion and intraplate tectonics in the northern Indian Ocean, *Phys. Earth Planet. Inter.*, 40, 1-23.

- Blakely, R.J. and Cox, A., 1972. Evidence for short geomagnetic polarity intervals in the early Cenozoic, *J. Geophys. Res.*, 77, 7065-7072.
- Blakely, R.J., 1974. Geomagnetic reversals and crustal spreading rates during Miocene, *J. Geophys. Res.*, 79, 2979-2985.
- Bodine, J.H., Steckler, M.S. and Watts, A.B., 1981. Observations of flexure and the rheology of the Oceanic Lithosphere, *J. Geophys. Res.*, 86, 3695-3707.
- Brookfield, M.E. and Reynolds, P.H., 1981. Late Cretaceous emplacement of the Indus suture zone Ophiolitic melanges and an Eocene-Oligocene magmatic arc on the northern edge of the Indian plate, *Earth Planet. Sci. Lett.*, 55, 157-167.
- Brunhes, B., 1906. Recherches sur la direction d'aimantation des roches volcaniques, *J. Physique*, 5, 705-724.
- Bull, J. M., 1990. Structural style of intraplate deformation, Central Indian Ocean Basin: Evidence for the role of fracture zones, *Tectonophysics*, 184, 213-288.
- Bull, J. M. and Scrutton, R. A., 1990. Fault reactivation in the Central Indian Ocean and the rheology of oceanic lithosphere, *Nature*, 344, 855-858
- Caldwell, J. G., and Turcotte, D.L., 1979. Dependence of the thickness of the elastic oceanic lithosphere on age, *J. Geophys. Res.*, 83, 7572-7579.
- Cande, S.C. and Mutter, J.C., 1982. A revised identification of the oldest seafloor spreading anomalies between Australia and Antarctica, *Earth Planet. Sci. Lett.*, 58, 151-160.
- Cann, J.R., and Vine, F.J., 1966. An area on the crest of the Carlsberg Ridge: Petrology and magnetic survey. *Phil. Trans. Roy. Soc.*, A259, 198-217.
- Carter, D. J. T., 1980. Echosounding correction tables (formerly Matthew's tables), *Hydrographic Department, Ministry of Defence, Taunton*.
- Chaubey, A.K., Krishna, K.S., Subba Raju, L.V.S., and Gopala Rao, D., 1990. Magnetic anomalies across the southern Central Indian Ridge: Evidence for a new transform fault. *Deep-Sea Res.*, 37, 647-656.

- Cochran, J.R., 1988. Somali Basin, Chain Ridge and the origin of the Northern Somali Basin gravity and geoid low, *J. Geophys. Res.*, 93, 11985-12008.
- Cochran, J.R., 1990. Himalayan uplift, sealevel, and the record of Bengal fan sedimentation at the ODP Leg 116 sites. In: Cochran, J.R., Stov, D.A.V. et al., (Editors), *Proceedings of the Ocean Drilling Program, Scientific Results*, Vol. 116, 397-414.
- Coffin, M.F. and Rabinowitz, P.D., 1987. Reconstruction of Madagascar and Africa: evidence from the Davie fracture zone and western Somali Basin, *J. Geophys. Res.*, 92, 9385-9406.
- Cox, A., 1959. The remanent magnetization of some Cenozoic rocks, *Ph.D. thesis, Univ. of California, Berkeley*, 193p.
- Cox, A., 1969. Geomagnetic reversals, *Science*, 163, 237-245.
- Cox, A., Doell, R.R. and Dalrymple, G.B., 1963a. Geomagnetic polarity epochs and Pliocene geochronometry, *Nature*, 198, 1049-1051.
- Cox, A., Doell, R.R. and Dalrymple, G.B., 1963b. Geomagnetic polarity epochs: Sierra Nevada II, *Science*, 142, 382-385.
- Cox, A., Doell, R.R. and Dalrymple, G.B., 1964. Reversals of the earth's magnetic field, *Science*, 144, 1537-1543.
- Cox, A., Doell, R.R. and Dalrymple, G.B., 1968. Radiometric time scale for geomagnetic reversals, *Geol. Soc. London, Quart. J.*, 124, 53-66.
- Craig, C. H. and McKenzie, D., 1986. The existence of a thin low viscosity layer beneath the lithosphere, *Earth Planet. Sci. Lett.*, 78, 420-426.
- Davis, E.L. and Lister, C.R.B., 1974. Heatflow measured over the Juan de Fuca Ridge on a quasi-regular grid, *J. Geophys. Res.*, 82, 4845-4853.
- Dietz, R.S., 1961. Continent and ocean basin evolution by spreading of the sea floor. *Nature*, 190, 854-857.
- Doell, R.R. and Dalrymple, G.B., 1966. Geomagnetic polarity epochs: a new polarity event and the age of the Brunhes-Matuyama boundary, *Science*, 152, 1060-1061.
- Doell, R.R., Dalrymple, G.B., Cox, A., 1966. Geomagnetic polarity epochs: Sierra Nevada data, *J. Geophys. Res.*, 71, 531-541.

- Dorman, L. M., 1975. The gravitational edge effect, *J. Geophys. Res.*, 80, 2949-2950.
- Duncan, R. A. and Richards, M.A., 1991. Hotspots, mantle plumes, flood basalts and true polar wander, *Revs. Geophys.*, 29, 31-50.
- Emmel, F. J., and Curray, J.R. 1984. The Bengal submarine Fan, Northeastern Indian Ocean, *Geo-Mar. Letts.*, 3, 119-124.
- Engel, C.G., and Fisher, R.L., 1969. Lherzolite, anorthosite, gabbro and basalt dredged from the Mid-Indian Ocean Ridge, *Science*, 166, 1136-1141.
- Engel, C.G., and Fisher, R.L., 1975. Granite to ultramafic rock complexes of the Indian Ocean ridge system, western Indian Ocean, *Geol. Soc. Am. Bull.*, 86, 1553-1578.
- Epp, D., and Smoot, N. C., 1989. Distribution of Seamounts in North Atlantic, *Nature*, 337, 254-257.
- Ewing, M., and Eittrheim, S., Truchan, M., and Ewing, J.I., 1969. Sediment distribution in the Indian Ocean, *Deep-Sea Res.*, 16, 231-248.
- Ewing, M., and Heezen, B.C., 1960. Continuity of mid-oceanic ridge and rift valley in the southwestern Indian Ocean confirmed., *Science*, 131, 1677-1678.
- Fairbridge, R.W., 1948. The juvenility of the Indian Ocean, *Scope*, 1, 29-35.
- Fairbridge, R.W., 1955. Some bathymetric and geotectonic features of the eastern part of the Indian Ocean, *Deep-Sea Res.*, 2, 161-171.
- Farquharson, W.I., 1935. Topography, *Sci. Rep. John Murray exped.*, 1933-1934, 1, 43-61.
- Fisher, R.L., and Sclater, J.G., 1983. Tectonic evolution of the southwest Indian Ocean since mid Cretaceous: Plate motion and stability of the pole of Antarctica / Africa for at least 80 Myr, *Geophys. J.R. Astron. Soc.*, 73, 553-576.
- Fisher, R.L., Engel, C.G., and Hilde, T.W.C., 1968. Basalts dredged from Amirante Ridge, western Indian Ocean, *Deep-Sea Res.*, 15, 521-524.
- Fisher, R.L., Jhonson, G.L., and Heezen, B.C., 1967. Mascarene plateau, western Indian Ocean, *Geol. Soc. Am. Bull.*, 78, 1247-1266.

- Fisher, R.L., Sclater, J.G., and McKenzie, D.P., 1971. Evolution of the Central Indian Ridge, western Indian Ocean, *Geol. Soc. Am. Bull.*, 82, 553-562.
- Fornari, D.J., Gallo, D.G., Edwards, M.H., Madsen, M.R., Perfit, J.A. and Shor, A.N., 1989. Structure and topography of the Siqueiros transform fault system: Evidence for development of intra-transform spreading centres, *Mar. Geophys. Res.*, 11, 263-299.
- Forsyth, D. and Rowlett, H., 1979. Microearthquakes and recent faulting at the intersection of the Vema fracture zone and the Mid Atlantic ridge (abstract), *Eos Trans. AGU*, 60, 376.
- Forsyth, D.W., 1977. The evolution of the upper mantle beneath mid ocean ridges, *Tectonophysics*, 38, 89-118
- Fox, P.J., and Gallo, D.G., 1984. A tectonic model for ridge-transform-ridge plate boundaries: Implications for the structure of the Oceanic lithosphere, *Tectonophysics*, 104, 205-242.
- Fox, P.J. and Gallo, D.G., 1986. The geology of North Atlantic transform plate boundaries and their aseismic extensions, In: B. Tucholke and P.R. Vogt (Editors), *The geology of the North America: The western North Atlantic region*, *Geol. Soc. Am., Vol. M.*, 157-172.
- Fox, P.J. and Gallo, D.G., 1989. Transforms of the eastern Pacific, In: E.L. Winterer, D.M. Hussong and R.W. Decker (Editors), *The Geology of North America: The eastern Pacific ocean and Hawaii*, *Geol. Soc. Am., Vol. N*, 111-124.
- Francis, T.J.G., Porter, I.T. and Lilwall, R.C., 1978. Microearthquakes near eastern end of St. Paul fracture zone, *Geophys. J. R. Astron. Soc.*, 53, 201-217.
- Gallo, D. G., Fox, P.J. and Macdonald, K.C., 1986. A Seabeam investigation of the Clipperton transform fault: The morphotectonic expression of a fast slipping transform boundary, *J. Geophys. Res.*, 91, 3455-3467.
- Garland, G. D., 1979. Introduction to geophysics. Mantle, Core and Crust. W. B. Saunders co., Toronto, Canada, 494pp.
- GEBCO, General Bathymetric Chart of the Oceans, 1975. *Canadian Hydrographic Service, Ottawa, Canada.*
- Geller, C. A., Weissel, J. K. and Anderson, R. N., 1983. Heat transfer and intraplate deformation in the Central Indian Ocean, *J. Geophys. Res.*, 88, 1018-1032.

- Grant, J.A. and Schreiber, R., 1990. Modern swathe sounding and sub-bottom profiling technology for research applications: The Atlas Hydrosweep and Parasound systems, *Mar. Geophys. Res.*, 12, 9-19.
- Gutberlet, M., and Schenke, H. W., 1989. Hydrosweep: New era in high precession bathymetric surveying in deep and shallow water, *Mar. Geod.*, 13, 1-23.
- Gutenberg, B., and Richter, C.F., 1954. Seismicity of the Earth. *Princeton University Press*, Princeton, 310pp.
- Hall, S.A., Casey, J.F. and Elthon, D.L., 1986. A possible explanation of gravity anomalies over mid-ocean ridges, *J. Geophys. Res.*, 91, 3724-3738.
- Hanks, T. C., 1971. The Kuril trench-Hokkaido rise system: large shallow earthquakes and simple models of deformation, *Geophys. J. Roy. Astron. Soc.*, 23, 173-189.
- Hardenbol, J. and Berggren, W.A., 1978. A new Paleogene numerical time scale. In: Cohee, G.V., Glaessner, M.F. and Hedberg, H.D. (Editors), Contributions to the geologic time scale, *American Association of Petroleum Geologists*, Special studies, Vol.6, 213-234.
- Heezen, B.C., Ewing, M. and Muller, E.T., 1953. Trans Atlantic profile of total magnetic intensity and topography, Dakar to Barbados, *Deep-Sea Res.*, 1, 25-33.
- Heezen, B.C., and Nafe, J.E., 1964. Vema Trench: western Indian Ocean. *Deep-Sea Res.*, 11, 79-84.
- Heezen, B. C., and Tharp, M., 1965. Physiographic diagram of the Indian Ocean (with descriptive sheet). *Geol. Soc. Am.*, New York.
- Heezen, B. C., Lynde, R. P.Jr., and Fornari, D.J., 1978. Geological Map of Indian Ocean, *Geological World Atlas*, Published by UNESCO, France.
- Heirtzler, J.R., Dickson, G.O., Herron, E.M., Pitman, W.C. and Le Pichon, X., 1968. Marine magnetic anomalies, geomagnetic field reversals and motions of the ocean floor and continents, *J. Geophys. Res.*, 73, 2119-2136.

- Hess, H.H., 1962. History of the Ocean Basins. In: Engel, A.E.J., James, H.L., and Leonard, B.F. (Editors), Petrologic studies, *Geol. Soc. Am.*, 559-620.
- Honegger, K., Dietrich, V., Frank, W., Gauser, A., Thoni, M. and Trommsdorf, V., 1982. Magmatism and metamorphism in the Ladakh Himalayas (The Indus-Tsangpo suture zone), *Earth Planet. Sci. Lett.*, 60, 253-292.
- Hospers, J., 1954. Magnetic correlation in volcanic districts, *Geol. Mag.*, 91, 352-360.
- IGAG, I Division study group, 1985. International Geomagnetic Reference Field, 1985, *J. Geoelectr.*, 27, 437-439.
- Kamesh Raju, K.A., 1990. Magnetic and bathymetric studies in the vicinity of the 73°E fracture zone, Central Indian Basin. *Mar. Geol.*, 95, 147-153.
- Kamesh Raju, K.A., 1993. Magnetic lineations, Fracture zones and Seamounts, Central Indian Basin. *Mar. Geol.*, 109, 195-201.
- Kamesh Raju, K.A., Ramprasad, T., Bhattacharya, G.C. and Kodagali, V.N., 1986. A system for the processing of underway geophysical and geological data (Abstract). XII annual convention and seminar on Exploration Geophysics, AEG souvenir vol. no. 54, a24-a25.
- Kamesh Raju, K.A., and Ramprasad, T., 1989. Magnetic lineations in the Central Indian Basin for the period A24-A21: A study in relation to the Indian Ocean Triple Junction trace. *Earth Planet. Sci. Lett.*, 95, 395-402.
- Kamesh Raju, K.A., Ramprasad, T., Kodagali, V.N., and Nair, R.R., 1993. Multibeam bathymetric, gravity, and magnetic studies over 79°E fracture zone: Central Indian Basin. *J. Geophys. Res.*, 98, 9605-9618.
- Kanaev, V.P., 1967. Relief of the Indian Ocean. In: Relief of the Earth (Morphostructure and Morphosculpture). *Nauka, Moscow*, pp 276-286.
- Karson, J.A. and Dick, H., 1983. Tectonics of ridge transform intersection at the Kane fracture zone, *Mar. Geophys. Res.*, 6, 51-98.
- Kastens, K.A., 1987. A compendium of causes and effects of processes at transform faults and fracture zones. *Revs. Geophys.*, 25, 1554-1562.

- Kastens, K.A., Ryan, W.F. and Fox, P.J., 1986. Structural and volcanic expression of a fast slipping ridge-transform-ridge plate boundary: Sea Marc I and photographic surveys at Clipperton transform fault, *J. Geophys. Res.*, 91, 3469-3488
- Keen, M.J., 1963. Magnetic anomalies over the mid-Atlantic ridge, *Nature*, 197, 888-890.
- Kharmov, A.N., 1957. Paleomagnetism the basis of a new method of correlation and sub division of sedimentary strata, *Acad. Sci. USSR Earth Sci. Sect.*, 112, 129-132.
- Klitgord, K.D., Huestis, S.P., Mudie, J.D. and Parker, R.L., 1975. An analysis of near-bottom magnetic anomalies: seafloor spreading and the magnetized layer, *Geophys. J. Roy. Astron. Soc.*, 43, 387-424.
- Kodagali, V.N., 1989. Morphology of an uncharted Seamount from Central Indian Basin, *Mar. Geod.*, 13, 83-90.
- LaBrecque, J.L. and Hayes, D.E., 1979. Seafloor spreading history of Agulhas Basin, *Earth. Planet. Sci. Lett.*, 45, 411-428.
- LaBrecque, J.L., Kent, D.V. and Cande, S.C., 1977. Revised magnetic polarity time scale for Late Cretaceous and Cenozoic time, *Geology*, 5, 330-335.
- Langmuir, C.H. and Bender, J.F., 1984. Chemical variations of MORB in the vicinity of transform faults: observations and implications, *Earth Planet. Sci. Lett.*, 69, 107-127
- Langmuir, C.H., Bender, J.F. and Batiza, R., 1986. Petrological and tectonic segmentation of the East Pacific Rise, 5°30'-14°30'N, *Nature*, 332, 422-429.
- Langseth, M.G., and Taylor, P.T., 1967. Recent heat flow measurements in the Indian Ocean. *J. Geophys. Res.*, 72, 6249-6260.
- Larson, R.L. and Ladd, J.W., 1973. Evidence for the opening of the South Atlantic in the Early Cretaceous, *Nature*, 246, 209-212.
- Larson, R.L., Mutter, J.C., Diebold, J.B. and Carpenter, G.B., 1979. Cuvier Basin: a product of ocean crust formation by Early Cretaceous rifting off western Australia, *Earth Planet. Sci. Lett.*, 45, 105-114.
- Laughton, A.S., Matthews, D.H., and Fisher, R.L., 1970. The structure of the Indian Ocean. In: *The Sea, Maxwell, A.E., (Editor)*, Vol.4, John Wiley Interscience, New York, 543-586.

- Le Pichon, X., and Heirtzler, J.R., 1968. Magnetic anomalies in the Indian Ocean and seafloor spreading. *J. Geophys. Res.*, 73, 2101-2117.
- Le Pichon, X., Franchetau, J. and Bonnin, J., 1973. In: *Plate Tectonics*, Elsevier, New York, 300 pp.
- Lin, J., 1991. The segmented Mid-Atlantic Ridge, *Oceanus*, 34, 11-18.
- Liu, C.S., Curray, J.R. and McDonald, J.M., 1983. New constraints on the tectonic evolution of the eastern Indian ocean, *Earth Planet. Sci. Lett.*, 65, 331-342.
- Louden, K. E., and Forsyth, D.W., 1976. Thermal conduction across fracture zones and the gravitational edge effect, *J. Geophys. Res.*, 81, 4869-4874.
- Lowrie, W. and Alvarez, W., 1981. One hundred years of geomagnetic polarity history, *Geology*, 9, 392-397.
- Lowrie, W., Alvarez, W., Napoleone, G., Perch-Nielsen, K., Premoli-Silva, I. and Toumarkine, M., 1982. Paleogene magnetic stratigraphy in Umbrian pelagic carbonate rocks: The Contessa section, Gubbio, *Geol. Soc. Am. Bull.*, 93, 414-432.
- Macdonald, K.C., 1986. The crest of the Mid-Atlantic Ridge: Models for crustal generation processes and tectonics. In: Vogt, P.R. and Tucholke, B.E., (Editors), *The geology of North America, Western north Atlantic region, Vol. M, Geol. Soc. Amer.* Boulder.
- Macdonald, K. C., Castillo, D.A., Miller, S. P., Fox, P.J., Kastens, K.A., and Bonatti, E., 1986. Deep-Tow studies of the Vema fracture zone 1. Tectonics of a major slow slipping transform fault and its intersection with the Mid-Atlantic ridge, *J. Geophys. Res.*, 91, 3334-3354.
- Macdonald, K. C., Scheirer, S.D. and Carbotte, M.S., 1991. Mid-Ocean Ridges: Discontinuities, segments and giant cracks, *Science*, 253, 986-994.
- Madsen, J.A., Fox, P.J. and Macdonald, K.C., 1986. Morphotectonic fabric of the Orozco transform fault: Results from Seabeam investigation, *J. Geophys. Res.*, 91, 3439-3454
- Markl, R.G., 1974. Evidence for breakup of Eastern Gondwanaland by the Early Cretaceous, *Nature*, 251, 196-200.
- Markl, R.G., 1978. Further evidence for the Early Cretaceous breakup of Gondwanaland off southern Australia, *Mar. Geol.*, 26, 41-48.

- Martin-Barajas, A., Lallier-Verges, E. and Leclaire, L., 1991. Characteristics of manganese nodules from the Central Indian Basin: Relationship with sedimentary environment, *Mar. Geol.*, 101, 249-265.
- Matthews, D. H., 1963. A major fault scarp under Arabian Sea displacing the Carlsberg Ridge near Socotra, *Nature*, 198, 950-952.
- Matthews, D.H., 1966. The Owen fracture zone and the northern end of the Carlsberg Ridge, *Phil. Trans. Roy. Soc.*, A259, 172-186.
- Matthews, D.H., Vine, F.J., and Cann, J.R., 1965. Geology of an area of the Carlsberg Ridge, Indian Ocean. *Bull. Geol. Soc. Am.*, 76, 675-682.
- Matuyama, M., 1929. On the direction of magnetization of basalt in Japan, Tyosen and Manchuria, *Japan Academy Proceedings*, 5, 203-205.
- McDougall, I. and Chamalaun, F.H., 1966. Geomagnetic polarity scale of time, *Nature*, 212, 1415-1418.
- McKenzie, D.P., 1967. Some remarks on heat flow and gravity anomalies, *J. Geophys. Res.*, 72, 6261-6273.
- McKenzie, D.P., and Sclater, J.G., 1971. The evolution of the Indian Ocean since late Cretaceous, *Geophys. J. R. Astron. Soc.*, 25, 437-528.
- McNutt, M. and Batiza, R., 1980. Paleomagnetism of northern Cocos seamounts: Constraints on absolute motion, *Geology*, 9, 148-154.
- Menard, H.W., 1954. Topography of the northeastern Pacific seafloor (abstract). *Bull. Soc. Am.*, 65, 1284.
- Menard, H.W., 1964. *Marine Geology of the Pacific*, McGraw Hill, New York.
- Menard, H.W., 1969. Growth of drifting volcanoes, *J. Geophys. Res.*, 74, 4827-4837.
- Menard, H.W., and Chase, J.E., 1968. Fracture zones. In: Maxwell, A.E. (Editor), *The Sea, Vol.4*, John Wiley Interscience, New York, 421-443.
- Menard, H. W., and Atwater, T., 1969. Origin of Fracture topography, *Nature*, 222, 1037-1040.
- Mercanton, P.L., 1926. Inversion de l'inclinaison magnetique terrestre aux ages gologiques, *J. Geophys. Res.*, 31, 187-190.

- Mitchell, N.C., 1991. Disturbed extension at the Indian Ocean Triple Junction. *J. Geophys. Res.*, 96, 8019-8043.
- Molnar, P., Pardo-Casas, F. and Stock, J., 1987. The Cenezoic and Late Cretaceous evolution of the Indian Ocean Basin: Uncertainties in the reconstructed positions of the Indian, African and Antarctic plates, *Basin Res.*, 1, 23-40.
- Mukhopadhyay, R. and Khadge, N.H., 1990. Seamounts in the Central Indian Ocean Basin: indicators of the Indian Plate movement, *Proc. Indian Acad. Sci. (Earth and Planet Sci.)*, 99, 357-365.
- Munsch, M., and Schlich, R., 1989. The Rodriguez Triple Junction (Indian Ocean): Structure and evolution for the past one million years, *Mar. Geophys. Res.*, 11, 1-14.
- Nath, B. N., Rao, V.P. and Becker, K.P., 1989. Geochemical evidence of terrigenous influence in deep sea sediments up to 8°S in the Central Indian Basin, *Mar. Geol.*, 87, 301-313.
- Neprochnov, Y. P., Levchenko, O. V., Merklin, L. R. and Sedov, V. V., 1988. The structure and tectonics of the intraplate deformation area in the Indian Ocean, *Tectonophysics*, 156, 89-106.
- Nettleton, L.L., 1976. Gravity and magnetics in oil prospecting. McGraw Hill, Inc., New York, 464pp.
- Norton, I.O., 1976. The present relative motions between Africa and Antarctica, *Earth Planet. Sci. Lett.*, 33, 219-230.
- Norton, I.O., and Sclater, J.G., 1979. A model for the evolution of the Indian Ocean and the breakup of Gondwana land, *J. Geophys. Res.*, 84, 6803-6830.
- OTTER, Scientific Team, 1984. The geology of the Oceanographer Transform: The eastern ridge-transform intersection, *Mar. Geophys. Res.*, 6, 109-141
- OTTER Scientific Team, 1985. The geology of the Oceanographer transform fault: The transform domain, *Mar. Geophys. Res.*, 7, 329-358.
- Parker, R. L., and Oldenburg, D.W., 1973. Thermal model of ocean ridges, *Nat. Phys. Sci.*, 242, 137-139.
- Parmentier, E.M., and Haxby, W.F., 1986. Thermal stresses in the oceanic lithosphere: Evidence from geoid anomalies at fracture zones, *J. Geophys. Res.*, 91, 7193-7204.

- Parsons, B. and McKenzie, D.P., 1978. Mantle convection and the thermal structure of the plates, *J. Geophys. Res.*, 83, 4485-4496.
- Parsons, B., and Sclater, J.G., 1977. An analysis of the variation of ocean floor bathymetry and heat flow with age, *J. Geophys. Res.*, 82, 803-827.
- Patriat, P., 1979. L'ocean Indien occidental: La dorsale ouest-Indienne, *Mem. Mus. Nat. Hist.*, 43, 49-52.
- Patriat, P., 1987. Reconstruction de l'evolution du systeme de dorsale de l'ocean Indien par les methodes de la cinématique des plaques, Publ. by *Territoire des Terres Australes et Antarctiques Francaises*, Paris, 308P.
- Patriat, P. and Achache, J., 1984. India-Eurasia collision chronology has implications for crustal shortening and driving mechanism of plates, *Nature*, 311, 615-621.
- Patriat, P., and Segoufin, J., 1988. Reconstruction of the Central Indian Ocean, *Tectonophysics*, 155, 211-234.
- Patriat, P. and Parson, L., 1989. A survey of the Indian ocean triple junction trace within the Antarctic plate. Implications for the junction evolution since 15 Ma, *Mar. Geophys. Res.*, 11, 89-100.
- Pitman, W.C. and Heirtzler, J.R., 1966. Magnetic anomalies over Pacific-Antarctic ridge, *Science*, 154, 1164-1171.
- Pockalny, R.A., Detrick, R.S. and Fox, P.J., 1988. The morphology and tectonics of the Kane transform from Seabeam bathymetric data, *J. Geophys. Res.*, 93, 3179-3193.
- Poore, R.Z., Tauxe, L., Percival, S.F.Jr. and LaBrecque, J.L., 1982. Late Eocene-Oligocene magneto-stratigraphy and biostratigraphy at South Atlantic DSDP site 527, *Geology*, 10, 508-511.
- Poore, R.Z., Tauxe, L., Percival, S.F.Jr., LaBrecque, J.L., Wright, R., Petersen, N.P., Smith, C.C., Tucker, P. and Hsu, K.J., 1983. Late Cretaceous - Cenezoic magnetostratigraphy and biostratigraphy correlations of the South Atlantic ocean, DSDP leg 73, *Palaeogeography Palaeoclimatology Palaeoecology*, 42, 127-149.
- Rabinowitz, P.D., 1976. Geophysical study of the continental margin of southern Africa, *Geol. Soc. Am. Bull.*, 87, 1643-1653.
- Rabinowitz, P.D., Coffin, M.F. and Falvey, D., 1983. The separation of Madagascar and Africa, *Science*, 220, 67-69.

- Rothe, J.P., 1954. La zone seismique mediane Indo-Atlantique. *Proc. Roy. Soc.*, A222, 387-399.
- Rowlett, I., 1981. Seismicity at intersection of spreading centres and transform faults, *J. Geophys. Res.*, 86, 3815-3820.
- Royer, J.Y., and Schlich, R., 1988. Southeast Indian Ridge between the Rodriguez Triple Junction and Saint Paul islands: Detailed kinematics for the past 20 m.y., *J. Geophys. Res.*, 93, 13524-13550.
- Royer, J.Y. and Sandwell, D.T., 1989. Evolution of the Eastern Indian Ocean since Late Cretaceous: Constraints from Geosat altimetry, *J. Geophys. Res.*, 94, 13755-13782.
- Royer, J.Y., Sclater, J.G., and Sandwell, D.T., 1989. A preliminary tectonic fabric chart of the Indian Ocean. *Proc. Indian Acad. Sci. (Earth and Planet Sci.)*, 98, 7-24.
- Ryan, W.B.F., Cita, M.B., Rawson, M.D., Bruckle, L.H. and Saito, T., 1974. A paleomagnetic assignment of Neogene stage boundaries and the development of isochronous datum planes between the Mediterranean, the Pacific and Indian Oceans in order to investigate the response of the world oceans to the Mediterranean "Salinity crisis", *Rivista Italiana Paleontologia*, 80, 631-688.
- Sandwell, D. T., 1984. Thermomechanical evolution of Oceanic fracture zones, *J. Geophys. Res.*, 89, 11401-11413.
- Sandwell, D.T., and Schubert, G., 1982a. Lithospheric flexure at fracture zones, *J. Geophys. Res.*, 87, 4657-4667.
- Sandwell, D.T., and Schubert, G., 1982b. Geoid height-age relation from Seasat altimeter profiles across the Mendocino fracture zone, *J. Geophys. Res.*, 87, 3949-3958.
- Schlich, R., 1974. Seafloor spreading history and deep sea drilling results in Madagascar and Mascarene Basins, In: *Initial Reports of the Deep Sea Drilling Project, U.S. Govt. Printing Press, Washington, D.C.*, Vol. 25, 663-678.
- Schlich, R., 1975. Structure et age de l'Ocean Indien occidental. Mem. hors-serie, *Soc. Geol. de France*, No. 6, 1-103.

- Schlich, R., 1982. The Indian Ocean: Aseismic ridges, spreading centers and ocean basins. In: Nairn, A.E.M., and Stehli, F.G., (Editors), *The Ocean Basins and Margins*, Vol. 6., Plenum press, New York, 51-147.
- Schlich, R., and Patriat, P., 1967. Profils magnetiques sur la dorsale mediooceanique "Indo-Pacifique". *Ann. de Geophys.*, 23, 629-633.
- Schlich, R., and Patriat, P., 1968. Interpretation possible de donnees geophysiques recueillies sur la dorsale medio-indienne entre 20° et 40° sud. *C.R. Acad. Sci., Paris*, 266(B), 820-822.
- Schlich, R., and Patriat, P., 1971a. Mise en evidence d'anomalies magnetique axials sur la branche ouest de la dorsale medio-indienne. *C.R. Acad. Sci., Paris*, 272(D), 700-703.
- Schlich, R., and Patriat, P., 1971b. Anomalies magnetiques de la branche et de la dorsale medio-indienne entre les iles Amsterdam et Kerguelen. *C.R. Acad. Sci., Paris*, 272(B), 773-776.
- Schmidt, J., 1932. *Dana's togt Omkring Jorden 1928-1930*. Copenhagen, 255pp.
- Sclater, J.G. and Francheteau, J., 1970. The implications of terrestrial heat flow observations on current tectonic and geochemical models of the crust and upper mantle of the earth, *Geophys. J. R. Astron. Soc.*, 20, 509-542.
- Sclater, J.G., and Harrison, C.G.A., 1971. Elevation of mid-ocean ridges and the evolution of the Southwest Indian Ridge. *Nature*, 230, 175-177.
- Sclater, J.G., and Fisher, R.L., 1974. Evolution of the east-central Indian Ocean, with emphasis on the tectonic setting of the Ninetyeast Ridge, *Geol. Soc. Am. Bull.*, 85, 683-702.
- Sclater, J.G., Anderson, R.N. and Bell, M.L., 1971. The elevation of ridges and evolution of central eastern Pacific, *J. Geophys. Res.*, 76, 7888-7915.
- Sclater, J.G., Bowin, C., Hey, R., Hoskins, H., Peirce, J., Phillips, J., and Tapscott, C., 1976a. The Bouvet Triple Junction, *J. Geophys. Res.*, 81, 1857-1869.
- Sclater, J.G., Luyendyk, B.P., and Meinke, L., 1976b. Magnetic lineations in the southern part of the Central Indian Basin, *Geol. Soc. Am. Bull.*, 87, 371-378.

- Sclater, J.G., Jaupart, C. and Galson, D., 1980. The heat flow through oceanic and continental crust and the heat loss of the earth, *Revs. Geophys.*, 18, 269-311.
- Sclater, J.G., Fisher, R.L., Patriat, P., Tapscott, C., and Parsons, B., 1981. Eocene to recent development of the Southwest Indian Ridge, a consequence of the evolution of the Indian Ocean Triple Junction. *Geophys. J. R. Astron. Soc.*, 64, 587-604.
- Searle, R.C., 1983. Multiple, closely spaced transform faults in fast slipping fracture zones, *Geology*, 11, 607-610
- Searle, R.C., 1986. GLORIA investigations of oceanic fracture zones, comparative study of the transform fault zone, *J. Geol. Soc.*, 143, 743-756
- Segoufin, J., 1978. Anomalies magnetiques mesozoiques dans le bassin de Mozambique, *C.R. Acad. Sci., Paris*, B287, 109-112.
- Segoufin, J. and Patriat, P., 1980. Existence d'anomalies mesozoiques dans le bassin de Somalie. Implications pour les relations Afrique-Antarctique-Madagascar, *C.R. Acad. Sci., Paris*, B291, 85-88.
- Sempere, J.C., Palmer, J., Christie, D.M., Morgan, J.P. and Shor, A.N., 1991. Australian - Antarctic discordance, *Geology*, 19, 429-432.
- Sibuet J.C., and Mascle, J., 1978. Plate kinematic implications of Atlantic Equatorial fracture zone trends, *J. Geophys. Res.*, 83, 3401-3421.
- Sibuet, J.C., Le Pichon, X. and Goslin, J., 1974. Thickness of lithosphere deduced from gravity edge effects across the Mendocino fault, *Nature*, 252, 676-679.
- Sigurgeirsson, Th., 1957. Direction of magnetization in Icelandic basalts, *Phil. Mag. Suppl.*, 6, 240-246.
- Simpson, E.S.W., Sclater, J.G., Parsons, B., Norton, I.O. and Meinke, L., 1979. Mesozoic magnetic lineations in the Mozambique Basin, *Earth Planet. Sci. Lett.*, 43, 260-264.
- Spudich, P., and Orcutt, J., 1980. A new look at the seismic velocity structure of the oceanic crust, *Revs. Geophys.*, 18, 627-645.
- Stein, C. A. and Weissel, J. K., 1990. Constraints on Central Indian Basin thermal structure from heat flow, seismicity and bathymetry, *Tectonophysics*, 176, 315-332.

- Subbaraju, L.V. and Sreekrishna, K., 1989. Establishment of gravity stations at various berths of Marmugao harbour, Goa, *Technical Report, N.I.O., Donapaula.*
- Talwani, M., Worzel, J.L. and Landisman, M., 1959. Rapid gravity computations for two-dimensional bodies with application to the Mendocino submarine fracture zone, *J. Geophys. Res.*, 64, 49-59.
- Talwani, M., Windisch, C.C. and Langseth, M.G., 1971. Reykjanes ridge crest: a detailed geophysical survey, *J. Geophys. Res.*, 76, 473-517.
- Tapponnier, P., Mercier, J.L., Proust, F. et al., 1981. The Tibetan side of the Indo-Eurasia collision, *Nature*, 294, 405-410.
- Tapscott, C., Patriat, P., Fisher, R.L., Sclater, J.G., Hoskins, H., and Parsons, B., 1980. The Indian Ocean Triple Junction. *J. Geophys. Res.*, 85, 4723-4739.
- Tisseau, J., 1978. Etude structurale du Golfe d'Aden et du bassin de Somalie (Ocean Indien occidentale nord), *These de doctrat, Universite de Paris.*
- Turcotte, D. L., 1974. Are transform faults thermal contraction cracks?, *J. Geophys. Res.*, 79, 2573-2577.
- Turcotte, D. L., and Oxburgh, E.R., 1967. Finite amplitude convective cells and continental drift, *J. Fluid. Mech.*, 28, 24-42.
- Turcotte, D. L., and Oxburgh, E.R., 1972. Mantle convection and the new global tectonics, *Ann. Rev. Fluid. Mech.*, 4, 33-68.
- Udintsev, G.B., 1965. New data on the bottom topography of the Indian Ocean, *Okeanologiya*, 5, 993-998.
- Udintsev, G.B., 1975. Geological-geophysical atlas of the Indian Ocean, Udintsev, G.B. (Editor), *Pergamon press, Oxford*, 1-151.
- Udintsev, G.B., Agapova, G.V., Larima, N.I. and Marova, N.A., 1976. Seamounts of the Pacific Ocean, general features of releif of Pacific Oceanfloor, In: H.Aoki and S.lizuka (Editors), *Volcanoes and Tectonosphere, Tokai University Press*, 7-34.
- Vallier, T.L., 1974. Volcanogenic sediments and their relation to landmass volcanism and seafloor-continent movements, western Indian ocean, In: *Initial Reports of the Deep Sea Drilling Project, U.S. Govt. Printing Press, Washington, D.C.*, Vol. 25, 513-542.

- Veevers, J.J., Tayton, J.W., Johnson, B.D. and Hansen, L., 1985. Magnetic expression of the continent-ocean boundary between the western margin of Australia and the eastern Indian ocean, *J. Geophys. Res.*, 56, 106-120.
- Vine, F.J. and Matthews, D.H., 1963. Magnetic anomalies over oceanic ridges, *Nature*, 199, 947-949.
- Vine, F.J., 1966. Spreading of the ocean floor : New evidence, *Science*, 154, 1405-1415.
- Vine, F.J., 1968. Magnetic anomalies associated with mid ocean ridges. In: Phinnet, R.A., (Editor), *The history of the earth's crust, Princeton University press*, 73-89.
- Vogt, P.R., 1974. Volcano spacing, fractures and thickness of the lithosphere, *Earth and Planet. Sci. Lett.*, 21, 235-252.
- Vogt, P.R., 1979. Volcano height and plate thickness, *Earth Planet. Sci. Lett.*, 23, 337-348.
- Wallcott, R. I., 1970. Flexure of the lithosphere at Hawaii, *Tectonophysics*, 9, 435-446.
- Watts, A.B., 1978. An analysis of isostasy in the world's oceans, 1, Hawaiian-Emperor Seamount chain, *J. Geophys. Res.*, 83, 5989-6004.
- Watts, A.B., Bodine, J.H. and Steckler, M.S., 1980. Observations of flexure and the state of stress in the Oceanic lithosphere, *J. Geophys. Res.*, 85, 6369-6376.
- Wegener, A., 1929. The origin of Continents and Oceans, 4th German edition, *Methuen and Co., London*, 248p.
- Weissel, J. K. and Hayes, D.E., 1992. Magnetic anomalies in the Southeast Indian ocean, In: D.E. Hayes (Editor), *Antarctic Oceanology II, The Australian-New Zealand section, Am. Geophys. Un. Ant. Res. Ser.*, 19, 165-196.
- Weissel, J. K., Anderson, R. N. and Geller, C. A., 1980. Deformation of the Indo-Australian plate, *Nature*, 287, 284-291.
- Wessel, P. and Haxby, W.F., 1990. Thermal stresses, differential subsidence, and flexure at oceanic fracture zones, *J. Geophys. Res.*, 95, 375-391.

- Whitmarsh, R.B., 1974. Some aspects of the plate tectonics in the Arabian Sea, In: Initial Reports of the *Deep Sea Drilling Project*, U.S. Govt. Printing Press, Washington, D.C., Vol. 23, 527-535.
- Wilson, J. T., 1965. A new class of faults and their bearing on continental drift, *Nature*, 207, 343-347.
- Wiseman, J.D.H., and Seymour-Sewell, 1937. The floor of the Arabian Sea, *Geol. Mag.*, 74, 219-230.

PUBLICATIONS OF THE AUTHOR

I. List of papers published in standard referred journals

1. **Kamesh Raju, K.A.** and Ramprasad, T., 1989. Magnetic lineations in the Central Indian Basin for the period A24-A21: a study in relation to the Indian Ocean Triple Junction Trace. *Earth and Planetary Science Letters*, 95, 395-402.
2. **Kamesh Raju, K.A.**, 1990. Magnetic and Bathymetric studies in the vicinity of 73°E fracture zone: Central Indian Basin. *Marine Geology*, 95, 147-153.
3. **Kamesh Raju, K.A.**, 1993. Magnetic lineations, fracture zones and Seamounts, Central Indian Basin, *Marine Geology*, 109, 195-201.
4. **Kamesh Raju, K.A.**, Ramprasad, T., Kodagali, V. N., and Nair, R.R., 1993. Multibeam Bathymetric, Gravity and Magnetic studies over 79°E fracture zone, Central Indian Basin. *Journal of Geophysical Research*, 98, 9605-9618.
5. Kodagali, V.N., **Kamesh Raju, K.A.**, Ramprasad, T., George, P., and Jaishankar, S., 1992. Bathymetry and morphology of the Central Indian Basin, *International Hydrographic Reviews*, LXIX, 143-150.
6. Subbaraju, L.V., **Kamesh Raju, K.A.**, Subrahmanyam, V. and Gopala Rao, D., 1990. Regional gravity and magnetic studies over the continental margins of Central West Coast of India. *Geo- Marine Letters*, 10, 31-36.
7. Ramana, M.V., Ramprasad, T., **Kamesh Raju, K.A.**, and Maria Desa, 1993. Magnetic studies across the Carlsberg Ridge, Indian Ocean, *Marine Geology* (in Press)
8. Subrahmanyam, V., Gopala Rao, D., Ramprasad, T., **Kamesh Raju, K.A.**, and Gangadhara Rao, M., 1991. Gravity anomalies and crustal structure of Western Continental margin off Goa and Mulki, India. *Marine Geology*, 99, 247-256.

9. Gopala Rao, D., Bhattacharya, G.C., Subbaraju, L.V., Ramana, M.V., Subrahmanyam, V., **Kamesh Raju, K.A.**, Ramprasad, T. and Chaubey, A.K., 1987. Regional Marine Geophysical Studies of the south western continental margin of India. In the book: *Contributions in Marine Sciences*, Dr. S.Z. Qasim Sastybdapurti felicitation volume, 427-437.
10. Gopala Rao, D., Ramana, M.V., Bhattacharya, G.C., Subba Raju, L.V., **Kamesh Raju, K.A.** and Ramprasad, T., 1992. Marine Geophysical studies along a transect across the continental margin off Bombay, India, In: *Oceanography of the Indian Ocean*, B.N. Desai (editor), Oxford Publ., New Delhi, 493-501.
11. Subrahmanyam, V., Gopala Rao, D., Ramprasad, T., **Kamesh Raju, K.A.**, and Gangadhara Rao, M., 1992. Gravity anomalies and crustal structure of Western Continental margin off Goa and Mulki, India, In: *Oceanography of the Indian Ocean*, B.N. Desai (editor), Oxford Publ., New Delhi, 511-517.

II List of papers published in Conference/Symposia/Seminars etc.

1. Subba Raju, L.V., **Kamesh Raju, K.A.**, Subrahmanyam, V. and Gopala rao, D., 1984. Regional gravity studies off Ratnagiri- West coast of India. Decinnial convention of Association of Exploration Geophysicists.
2. **Kamesh Raju, K.A.**, Ramprasad, T., Bhattacharya, G.C. and Kodagali, V.N., 1986. A System for processing of Underway Marine Geophysical and Geological data. XII annual convention and seminar on exploration geophysics. AEG souvenir vol no. 54, a24-a25.
3. Siddiquie, H.N., Gopalarao, D., Bhattacharya, G.C., Subbaraju, L.V., Ramana, M.V., Subrahmanyam, V., **Kamesh Raju, K.A.**, Ramprasad, T. and Chaubey, A.K., 1986. Geophysical studies of the south western continental margin of India. XII Annual convention and seminar on exploration geophysics. AEG souvenir vol no. 54, a36-a37.
4. Subrahmanyam, V., **Kamesh Raju, K.A.**, Ramprasad, T. and Gangadhara Rao, M., 1987. Marine gravity studies between Marmugao and Udipi, West Coast of India. XIII Annual convention and seminar on exploration geophysics of AEG.
5. Kodagali, V.N., **Kamesh Raju, K.A.**, Ramprasad, T., George, P., Jaishankar, S. and Nair, R.R., 1991. Bathymetry and morphology of the Central Indian Basin. International Symposium on Oceanography of the Indian Ocean, held at NIO, Goa.

6. Kodagali, V.N., **Kamesh Raju, K.A.**, Ramprasad, T, and Nair, R.R., 1991. Multibeam swath Bathymetric surveys in Central Indian Basin, Fourteenth annual convention of AEG, held at Hyderabad.
7. Gopala Rao, D., Ramana, M.V., Bhattacharya, G.C., Subba Raju, L.V., **Kamesh Raju, K.A.** and Ramprasad, T., 1991. Marine geophysical studies along a transect across the continental margin off Bombay, India, International Symposium on Oceanography of the Indian Ocean, held at NIO, Goa.
8. Subrahmanyam, V., Gopala Rao, D., Ramprasad, T., **Kamesh Raju, K.A.**, and Gangadhara Rao, M., 1991. Gravity anomalies and crustal structure of Western Continental margin off Goa and Mulki, India, International Symposium on Oceanography of the Indian Ocean, 1991, held at NIO, Goa.
9. Ramprasad, T. and **Kamesh Raju, K.A.**, 1992. Satellite altimeter technology for the study of tectonic features in the Indian Ocean, Symposium on Ocean Tecnology, held at NIO, Goa.
10. **Kamesh Raju, K.A.**, Ramprasad, T., Kodagali, V. N., and Nair, R.R. Multibeam Bathymetric, Gravity and Magnetic studies over 79°E fracture zone, Central Indian Basin. *EOS, Transactions of American Geophysical Union*, (in Press).
11. Kodagali, V.N., **Kamesh Raju, K.A.**, Ramprasad, T., Ranade, G.H., Chakraborty, B., Raju, Y.S.N. and Sudhakar, T., 1993. Multibeam mapping of the Central Indian Basin, *SEABEAM Workshop*, PACON, Biejing, China.

